



Durham E-Theses

Crustal deformation in extensional regimes: Iceland, Nevada and SW Turkey

Hodgkinson, Kathleen Marian

How to cite:

Hodgkinson, Kathleen Marian (1996) *Crustal deformation in extensional regimes: Iceland, Nevada and SW Turkey*, Durham theses, Durham University. Available at Durham E-Theses Online:
<http://etheses.dur.ac.uk/5438/>

Use policy

The full-text may be used and/or reproduced, and given to third parties in any format or medium, without prior permission or charge, for personal research or study, educational, or not-for-profit purposes provided that:

- a full bibliographic reference is made to the original source
- a [link](#) is made to the metadata record in Durham E-Theses
- the full-text is not changed in any way

The full-text must not be sold in any format or medium without the formal permission of the copyright holders.

Please consult the [full Durham E-Theses policy](#) for further details.

Academic Support Office, Durham University, University Office, Old Elvet, Durham DH1 3HP
e-mail: e-theses.admin@dur.ac.uk Tel: +44 0191 334 6107
<http://etheses.dur.ac.uk>

Crustal deformation in extensional regimes: Iceland, Nevada and SW Turkey

by

Kathleen Marian Hodgkinson

The copyright of this thesis rests with the author. No quotation from it should be published without the written consent of the author and information derived from it should be acknowledged.

**A thesis submitted in partial fulfilment of
the requirements for the degree of Doctor
of Philosophy**

**University of Durham
Department of Geological Sciences**

April 1996



3 APR 1998

Dedicated to my Mother and Father

Abstract

In 1991 a 23-point, 30 x 25 km, GPS geodetic network was established in the Hengill ridge-ridge-transform triple junction, SW Iceland. The GPS data were processed using the Bernese V3.2 software. The ambiguity-fixed solution yielded scaled formal errors of less than 1 cm in the horizontal and about 1 cm in the vertical. The effect of ocean loading on the vertical component of the GPS measurements, a hitherto ignored effect in GPS data, was examined and found to be negligible for surveys of this type.

Extensional deformation processes in the western Basin and Range province were studied by analysing the co- and postseismic deformation associated with the 1954 Rainbow Mountain - Fairview Peak - Dixie Valley sequence of $M > 6.0$ earthquakes. Levelling and triangulation data which constrain the coseismic deformation are fitted well by modelling uniform slip on rectangular planar dislocations embedded in an elastic half-space. The best-fitting fault geometries dip at 50° to 80° and extend to depths of 8 to 14 km. A simultaneous inversion of the triangulation and levelling data which spanned the coseismic period reveals that slip determined geodetically tends to be equal to, or greater than, the surface offsets. Using the single value decomposition method to invert the data allowed determination of where the coseismic slip was resolvable given the data distribution. The static stresses changes induced by each earthquake in the 1954 sequence were calculated using the source models derived from the geodetic modelling. After the first earthquake each event in the 1954 sequence was preceded by a static stress increase of 10^4 to 10^5 Pa. Thus, it appears that static stresses may have played an important role in triggering the later earthquakes.

The vertical postseismic deformation which followed the earthquakes was modelled assuming stress redistribution in the Earth's crust through viscous flow in the lower crust. Calculation of surface deformation caused by the anelastic response to a normal faulting earthquake was performed using the finite element method. The viscosity which best fit the postseismic levelling data was 1×10^{20} Pa s at depths of 10 to 30 km.

GPS measurements made between 1988 and 1992 show that north-south aseismic extension within SW Turkey is occurring at rates of 11.7 ± 5 mm/yr. The deformation extension was modelled along 2-dimensional north-south profiles using the finite element method. These calculations show that the postseismic deformation created by eight earthquakes of $M_s 6.5$ and greater within SW Turkey this century accounts for 10% of the north-south extension rate measured by GPS. The rest can be explained as postseismic deformation from earthquakes in earlier centuries. Modelling indicates that north-south extension rates decrease from west to east across the province. Reoccupation of the GPS network in the year 2000 will yield a clear regional strain signal, given the errors of the 1989 survey.

Acknowledgements

There are many people who helped me with this thesis and it is difficult to summarise my gratitude in a few lines. Gill Foulger made this project possible. By arranging a '6-month' visit to the Branch of Earthquake Geology and Geophysics at the US Geological Survey in Menlo Park she probably changed the course of my life. Gill helped me to pull the thesis together as she read and reread terrible first drafts of my confused thoughts. Over the last year of this thesis Gill proved a source of positive encouragement in what was a bewildering time for me.

Ross Stein was the guiding light behind a large percentage of this thesis. He taught me everything I now know about analysing and modelling geodetic data. For his patience, wisdom and willingness to help me in any way throughout this work, I will always be grateful. Working with Grant Marshall was a lot of fun. Grant backed up his help in analysing the Dixie Valley levelling data with beers after work.

I must thank the Branch of Earthquake Geology and Geophysics at the US Geological Survey in Menlo Park for allowing me to do my Ph. D. mostly there. I benefited from conversations with many of the people who work there. Bruce Julian was a great help. He showed me how to write shell scripts, use GMT, made freely available any of his own programs and was always ready to provide suggestions on how to proceed with the work. Wayne Thatcher explained the mysteries of single value decomposition and permitted me to work with his matrix inversion software. Greg Allen looked after my computer needs and always sorted out any problems I had with the UNIX machines.

I thank Rob Reilinger and Burc Oral of the MIT for making it possible for me to study the finite element method there for three months in 1994. Also, Kosuki Heki who showed me the intricacies of processing GPS data in my first year at Durham.

During the course of the Ph. D. I have made many friends at the survey and in Durham who made it all worth while: Michelle Hofton, Simon Williams, Charlotte Martin, Angus Miller, Lynn Dietz, Alwyn Ross, Brian Kilgore, Ruth Harris, Phill Dawson and John Hamilton. I also had much fun with the USGS GPS crew on fieldwork.

Finally there are Tim and Cassie without whose love I would be lost. Tim, my husband, pulled me out of my low points and gave me the confidence to continue. He selflessly gave up hundreds of hours of biking, running and skiing as I pursued my goal. I think Cassie deserves some kind of college credit as she spent most of the first year of her life sitting on my knees at the computer as I wrote this thesis. I thank her for her patience.

This project was funded by the Department of Education for Northern Ireland.

Contents

Abstract	iii
Acknowledgements	iv
Tables	xi
Figures	xii

Chapter 1: Regions of extensional Tectonics: Iceland, the Basin and Range Province and South West Turkey

1.1 Introduction and overview of the thesis.....	1
1.2 Iceland.....	3
1.2.1 Tectonics of Iceland.....	3
1.2.2 Crustal structure.....	6
1.2.3 Crustal deformation.....	6
1.2.4 The tectonics of the Hengill triple junction.....	7
1.3 The Basin and Range Province.....	8
1.3.1 Tectonic setting.....	8
1.3.2 Tectonic evolution.....	10
1.3.3 Current tectonism.....	10
1.3.4 Crustal structure.....	12
1.3.5 Seismicity.....	14
1.3.6 The Rainbow Mountain - Fairview Peak - Dixie Valley area.....	14
1.3.6.1 Tectonic setting.....	14
1.3.6.2 The 1954 Rainbow Mountain-Fairview Peak-Dixie Valley earthquake sequence.....	18
1.4 Turkey.....	21
1.4.1 Tectonic setting.....	21
1.4.2 Tectonic evolution of the Aegean and the Anatolian plate.....	23
1.4.3 Crustal structure.....	24
1.4.4 Southwest Turkey.....	24
1.4.4.1 Tectonics.....	24
1.4.4.2 Extension rates in western Turkey.....	26
1.5 Summary.....	27

CHAPTER 2: Principles of GPS Surveying and data processing

2.1 Introduction.....	29
2.2 The Global Positioning System.....	30
2.2.1 The space segment.....	30

2.2.2 The control segment	30
2.2.3 The user segment	30
2.3 GPS data types	31
2.3.1 Psuedorange code data	31
2.3.2 Carrier phase data	33
2.4 GPS data processing theory.....	33
2.4.1 Relative and absolute point positioning.....	33
2.4.2 Modelling the ionospheric effect.....	34
2.4.3 Single-, double- and triple-differenced data.....	35
2.4.4 Linear combinations of differenced observations	37
2.5 GPS data processing using the Bernese V3.2 software.....	39
2.5.1 Introduction	39
2.5.2 Data transfer	39
2.5.3 Orbit modelling	39
2.5.4 Outlier removal, cycle-slip detection and clock corrections.....	42
2.5.5 Ionosphere modelling	42
2.5.6 Parameter estimation	43
2.6 Network adjustment	44
2.7 Biases and errors	45
2.8 Summary	46

CHAPTER 3: A first epoch GPS survey of the Hengill Triple Junction and the effect of ocean tides

3.1 Introduction	48
3.2 Design and measurement of the network.....	50
3.2.1 Network design.....	50
3.2.2 Fieldwork	50
3.3 Data processing.....	54
3.3.1 Introduction	54
3.3.2 Processing procedure.....	54
3.4 Results.....	55
3.4.1 Ionospheric modelling.....	55
3.4.2 Ambiguity resolution	56
3.4.3 Comparison of ambiguity-free and ambiguity-fixed solutions.....	56
3.5 Earth tides and ocean loading.....	60
3.5.1 Effect of ocean loading on GPS measurements	60
3.5.2 Processing of the Hengill GPS data to determine the ocean loading effect.....	66
3.5.3 Results	66
3.6 Summary.....	67

CHAPTER 4: The triangulation and levelling data constraining the 1954 Rainbow Mountain - Fairview Peak - Dixie Valley earthquake sequence

4.1 Introduction	69
4.2 The data	71
4.2.1 Levelling.....	71
4.2.1.1 The levelling procedure	71
4.2.1.2 Accuracy of levelling	72
4.2.1.3 Sources of systematic errors in levelling	73
4.2.2 Triangulation.....	75
4.2.2.1 Triangulation surveying	75
4.2.2.2 Accuracy of triangulation surveying	77
4.3 Assessment of data quality.....	78
4.3.1 The levelling data.....	78
4.3.2 Non-tectonic errors and signals	79
4.3.2.1 Water withdrawal in the Fallon area.....	79
4.3.2.2 Systematic errors in the postseismic data.....	81
4.3.2.3 Error source of the 1967 levelling data.....	84
4.3.2.4 Assignment of errors	89
4.3.3 Triangulation data.....	90
4.3.4 Data quality	91
4.3.4.1 Misclosures in the data set	91
4.3.4.2 Assignment of errors.....	92
4.4 The measured coseismic and postseismic deformation.....	93
4.4.1 Data constraining coseismic movements	93
4.4.2 Data constraining postseismic movements.....	96
4.5 Summary.....	97

CHAPTER 5: Modelling of the coseismic deformation field of the 1954 Rainbow Mountain - Fairview Peak - Dixie Valley, Nevada earthquake sequence

5.1 Introduction.....	98
5.2 Fault geometries and slip estimates from previous geodetic analyses.....	99
5.3 Method.....	102
5.3.1 Calculating coseismic displacement fields.....	102
5.3.2 The optimum fault model.....	103
5.3.3 Inversion of a mixed-determined matrix	107
5.3.3.1 Single value decomposition.....	107
5.3.3.2 Determining coseismic slip.....	111
5.3.4 Frank's method of calculating shear strain.....	111
5.4 Results.....	112

5.4.1 Fault geometry.....	112
5.4.2 Coseismic slip.....	117
5.5 Summary.....	120

CHAPTER 6: The Rainbow Mountain-Fairview Peak-Dixie Valley earthquakes: Triggered seismicity

6.1 Introduction	122
6.2 Fault failure	124
6.2.1 Static stress changes.....	124
6.2.2 The Navier-Coulomb failure criterion.....	124
6.3 Calculation of static stress changes.....	127
6.3.1 Method of calculation	127
6.3.2 Stress changes on fault planes.....	128
6.3.2.1 Stress changes on a geodetically-inferred fault.....	128
6.3.2.2 Stress changes on optimally-orientated faults.....	129
6.4 Modelling the 1954 earthquake sequence	132
6.4.1 The method.....	132
6.4.2 The regional stress field	132
6.4.3 The coefficient of friction.....	133
6.5 Results	134
6.5.1 Stress changes preceding the Fairview Peak earthquake.....	134
6.5.1.1 Stress changes on the geodetically inferred faults.....	134
6.5.1.2 Stress changes on optimally-orientated faults.....	135
6.5.2 Stress change preceding the Dixie Valley event.....	138
6.5.2.1 Stress changes on geodetically inferred faults.....	138
6.5.2.2 Stress changes on optimally-orientated faults.....	139
6.5.3 Stress changes on optimally-orientated faults resulting from the 1954 earthquake sequence.....	139
6.6 Summary.....	141

CHAPTER 7: Analysis of the postseismic deformation that followed the Fairview Peak earthquake

7.1 Introduction	144
7.2 Postseismic deformation and Earth rheology.....	145
7.2.1 Postseismic deformation.....	145
7.2.2 The rheology of the crust and upper mantle	147
7.3 Finite element analysis.....	148
7.3.1 Overview of the method.....	148
7.3.2 The governing finite element equations.....	148
7.4 Relation between fault geometry and postseismic deformation.....	152

7.4.1 Finite element calculations of the postseismic signal	152
7.4.2 Factors affecting deformation following a normal earthquake	156
7.4.2.1 Dependence on fault depth	156
7.4.2.2 Dependence on the thickness of the elastic layer	156
7.5 Modelling the Dixie Valley postseismic deformation	159
7.5.1 The data	159
7.5.2 Method	161
7.5.2.1 The modelling approach	161
7.5.2.2 The finite element model of the Dixie Valley area	162
7.5.3 Results	163
7.5.3.1 Continued aseismic slip on the fault planes	163
7.5.3.2 Finite element modelling of the residual postseismic deformation	165
7.6 Summary	166

CHAPTER 8: Global Positioning System surveying and crustal deformation modelling in South West Turkey

8.1 Introduction.....	167
8.2 GPS Surveying within SW Turkey.....	168
8.2.1 GPS field surveys in SW Turkey.....	168
8.2.2 Relative plate motions in the eastern Aegean and deformation within SW Turkey, 1988-1992.....	171
8.3 Modelling the deformation within SW Turkey.....	172
8.3.1 The method and Earth structure used	172
8.3.2 The seismicity of SW Turkey	174
8.3.3 Deformation expected from a single event.....	175
8.3.3.1 The coseismic effect.....	175
8.3.3.2 The postseismic effect	177
8.4 Modelling results	178
8.4.1 Deformation associated with repeated Ms7 events	178
8.4.2 Deformation associated seismicity this century	180
8.5 Summary.....	184

CHAPTER 9: Discussion

9.1 GPS surveying in the Hengill triple junction.....	186
9.1.1 The 1991 survey	186
9.1.2 Possible future tectonic activity in the Hengill triple junction	186
9.1.3 Recent partial measurement of the network	187
9.2 Modelling of deformation associated with the 1954 Rainbow Mountain - Fairview Peak and Dixie Valley earthquakes.....	188
9.2.1 Geodetic data analysis	188

9.2.2 Modelling of coseismic deformation	189
9.2.3 Stress transfer between normal faults	191
9.2.4 Modelling of postseismic deformation	194
9.3 Extensional deformation in SW Turkey	196
9.4 Crustal extension in oceanic-type and continental-type environments	198
9.5 Conclusions	199
9.6 Future Work	200
References	200
Appendix 1: Hengill GPS site descriptions	213

Tables

Table 1.1 Location and magnitude of the 1954 events	19
Table 1.2 Geological and seismological parameters derived for the 1954 earthquake.....	20
Table 2.1 Summary of errors and biases	46
Table 3.1 Point occupation schedule for the Hengill survey, 10-27 August 1991	51
Table 3.2 Geographic coordinates (WGS84) of the Hengill network.....	61
Table 3.3 Repeatabilities and scaled formal errors of the Hengill 1991 survey.....	62
Table 4.1 Levelling and triangulation surveys made in the Dixie Valley area	78
Table 4.2 Areas where subsidence due to water withdrawal has been recorded.....	80
Table 4.3 Rod miscalibration coefficients.....	86
Table 4.4 Other surveys made using rods 312-347 and 312-383	88
Table 4.5 α and β tolerances for each of the Dixie Valley levelling surveys	90
Table 4.6 Average misclosures and probable error of the levelling surveys.....	92
Table 5.1 Previous studies of the 1954 earthquake sequence	100
Table 5.2 Fault parameters of Savage and Hastie (1969) and Snay <i>et al.</i> (1985)	101
Table 5.3 Fault parameters derived from the geodetic inversion	113
Table 5.4 Coseismic displacements and seismic moments	119
Table 6.1 Stress changes induced by the events in the 1954 earthquake sequence.....	135
Table 7.1 Slip estimates for the Fairview Peak and West Gate faults, 1955 to 1986.....	164
Table 8.1 Occupations of the SW Turkey GPS network	169
Table 9.1 Points within the Hengill network remeasured in May 1995.....	188

Figures

Figure 1.1	Regional tectonic map of Iceland	4
Figure 1.2	Schematic tectonic map of the Hengill Triple Junction	5
Figure 1.3	The Basin and Range province	9
Figure 1.4	The seismic model of the northern Basin and Range province	13
Figure 1.5	Seismic zones in western Nevada. shaded	15
Figure 1.6	The Rainbow Mountain-Fairview Peak-Dixie Valley area, Nevada.....	16
Figure 1.7	Interaction of the Eurasian, Arabian, African and Anatolian plates.....	22
Figure 1.8	The Gediz and Buyuk Menderes grabens of SW Turkey	25
Figure 2.1	Modulation of the carrier by PRN codes	32
Figure 2.2	A signal transmitted at time A in the SV clock time frame from is received at time B in the receiver clock time frame.....	32
Figure 2.3	Two receivers observe two SVS simultaneously	37
Figure 2.4	A flowchart of the Bernese V3.2 software	40
Figure 2.5	a) Example of a prange data file.....	41
Figure 2.5	b) Example of a phase data file.....	41
Figure 3.1	Locations of points of the Hengill GPS network.....	49
Figure 3.2	Schematic tectonic map of the Hengill triple junction	52
Figure 3.3	SV visibility over the Hengill area, August 1st, 1991	53
Figure 3.4	Repeatabilities of the horizontal and vertical components of the ambiguity-free and ambiguity-fixed solutions for the entire network.....	57
Figure 3.5	a) Scaled formal errors of each point for the Hengill-only network.....	58
Figure 3.5	b) Scaled formal errors of each point for the entire survey.....	59
Figure 3.6	Map showing the 1σ horizontal scaled formal error ellipsoids for points of the entire network for the best solution	61
Figure 3.7	The effect of ocean loading in Iceland.....	65
Figure 3.8	Predicted and observed variations in vertical positions relative to Nupafjall	67
Figure 4.1	The Dixie 1, Dixie2 and Dixie 3 levelling line.....	70
Figure 4.2	The levelling procedure	71
Figure 4.3	Directional angles measured	76
Figure 4.4	Elevation changes along line Dixie 1 for years 1934, 1955, 1967, 1986	79
Figure 4.5	Wells where water level drops have been recorded.....	81
Figure 4.6	Elevation changes between 1955 and 1934 along line Dixie 1	82
Figure 4.7	The elevation changes along line Dixie 1, calculated from the 1955, 1967, 1973, 1978 and 1986 survey.....	83
Figure 4.8	Elevation changes along line Dixie 2 levelling	84
Figure 4.9	Elevation changes along the first and last 20 km of the line Dixie 3	85
Figure 4.10	The elevation change per unit distance versus topographic gradient for elevation changes 1967-1955 and 1986-1967	87

Figure 4.11 a)The elevation changes along line Dixie 1, calculated from the 1955, 1986 and corrected 1967 surveys. b) The elevation changes along line Dixie 2, calculated from the 1955, 1986 and corrected 1967 surveys	88
Figure 4.12 Triangulation network	91
Figure 4.13 Coseismic deformation measured along Dixie 1, Dixie 2 and Dixie 3	94
Figure 4.14 Coseismic displacement vectors calculated by Miller (1967).	95
Figure 4.15 Postseismic deformation measured along line Dixie 1	96
Figure 5.1 Vertical displacement due to slip on a fault of length L and width $L/2$. a) upper fault depth = 0. b) upper fault depth = $L/4$	104
Figure 5.2 Horizontal displacement due to slip (u) on a fault of length L and width $L/2$. a) upper fault depth = 0, b) upper fault depth = $L/4$	105
Figure 5.3 a) A graphic illustration of a resolution matrix. b) The model fit versus number of eigenvalues	110
Figure 5.4 Best fitting fault geometry derived from the geodetic data.....	114
Figure 5.5 Normalised residuals from inversion of the geodetic data	115
Figure 5.6 Model fit versus number of eigenvalues curve, and illustration of the resolution matrices for the 12-eigenvalue problem	118
Figure 5.7 The coseismic deformation field calculated using the slip vectors determined from the data inversion	121
Figure 6.1 Shear and normal stresses in a coordinate system that has been rotated at θ to the x -axis.....	125
Figure 6.2 The Mohr diagram for stress in two dimensions.....	125
Figure 6.3 Mohr diagram showing how rock strength increases with mean stress.	126
Figure 6.4 Stress changes caused by slip on a source fault resolved onto a receiving fault.....	129
Figure 6.5 Coulomb stress change associated with 1 m slip on a normal fault	131
Figure 6.6 Spatial distribution of faults modelled.	132
Figure 6.7 Stresses induced by the Rainbow Mtn event resolved onto the Fairview Peak fault, the West Gate/Gold King fault, and the Dixie Valley fault.....	136
Figure 6.8 Coulomb stress change fields associated with slip on the Rainbow Mtn. fault	137
Figure 6.9 Coulomb stress changes across the Fairview Peak fault caused by slip on the Rainbow Mountain fault along profile AA'.....	138
Figure 6.10 Stress resolved onto the Dixie Valley fault caused by the Rainbow Mountain, Fairview Peak and West Gate/Gold King events.....	139
Figure 6.11 Coulomb stress-change fields associated with slip on the Rainbow Mountain, Fairview Peak and West Gate/Gold King faults.....	140
Figure 6.12 Variation in maximum Coulomb stress change with depth due to slip on all but the Dixie Valley fault.....	141
Figure 6.13 Regions of increased Coulomb stress caused by the 1954 earthquake sequence.....	142
Figure 7.1 Idealised rheological strength of the Earth's crust and upper mantle versus depth.	149
Figure 7.2 Split nodes.....	152

Figure 7.3	A simplified rheological model of the Earth's crust.	153
Figure 7.4	Comparison of coseismic offsets calculated using the finite element technique and the analytical equations of Okada (1992).	154
Figure 7.5	10, 50 and 100 years of cumulative, vertical, postseismic deformation following slip of 1 m on a 70°E dipping fault.	155
Figure 7.6	The horizontal postseismic deformation at 10, 50 and 100 years after the event.	155
Figure 7.7	Vertical peak-to-peak amplitude of the postseismic signal 30 years after the initial elastic offsets versus the fault depth : elastic thickness ratio.	155
Figure 7.8	Variation of the uplift with D/H ratio over the fault scarp	157
Figure 7.9	The uplift 30 years after the event for faults with 8 and 12 km depths	158
Figure 7.10	Variation of width of vertical deformation with increasing fault depth	158
Figure 7.11	Variation in peak-to-peak amplitude with increasing elastic thickness	158
Figure 7.12	Variation in width of deformation with elastic thickness	159
Figure 7.13	Postseismic deformation in the Fairview Peak area from levelling data taken in 1986, 1978, 1973 and 1955.	160
Figure 7.14	Postseismic deformation calculated by combining the 1986, 1978 and 1973 levelling data.	161
Figure 7.15	Model of shear strength versus depth for the Dixie Valley area.	163
Figure 7.16	The postseismic levelling data between 1955 and 1986.	164
Figure 7.17	Uplift over the Fairview Peak and West Gate faults modelled using the finite element model.	165
Figure 8.1	Map of the GPS network in SW Turkey	168
Figure 8.2	Deformation within the SW Turkey network, 1992-1988 measured using GPS	172
Figure 8.3	Finite element crustal model.	173
Figure 8.4	Seismicity of SW Turkey, 1899 to 1992 ($M_s > 5.5$).	174
Figure 8.5	Surface wave magnitude versus the log of the cumulative number of earthquakes for the 93-years- period 1899 to 1992.	176
Figure 8.6	Variations in postseismic, fault-normal displacement with time following one $M_s 6.5$ event.	177
Figure 8.7	Variations in horizontal, fault-normal displacement with earthquake magnitude.	178
Figure 8.8	The decay in horizontal, fault-normal velocity following an $M_s 6.5$ earthquake.	179
Figure 8.9	Cumulative deformation due to two thousand years of $M_s 7.0$ earthquakes repeating at 100-year intervals.	179
Figure 8.10	Displacements due to 3 $M_s 7.0$ earthquakes	180
Figure 8.11	Velocity along the western extremity of the Bozdag Horst	183
Figure 8.12	Velocity along the eastern extremity of the Bozdag Horst	183

CHAPTER 1

REGIONS OF EXTENSIONAL TECTONICS: ICELAND, THE BASIN AND RANGE PROVINCE AND SOUTH WEST TURKEY

1.1 INTRODUCTION AND OVERVIEW OF THE THESIS

The Earth's crust can accommodate extension through rifting, dyke injection, basin formation, earthquakes and postseismic deformation. Rifting and dyke injection processes tend to occur in oceanic environments where there is a magma source at shallow depths, such as on the sea floor and in Iceland. Large normal faulting earthquakes tend to occur in continental environments where there is little or no magma, such as in the Basin and Range province in the western United States and in southwest Turkey. Following rifting or faulting events, the high stresses induced locally in the crust are relaxed by the redistribution of stress to distant areas (*e.g.*, Foulger *et al.*, 1992; Reilinger, 1986; Thatcher and Rundle, 1984). The post-event stress redistribution thus contributes to the regional extensional deformation and to plate motions. How much earthquakes or rifting events contribute to the overall deformation of a region cannot be determined by a seismological investigation alone since this reveals coseismic motion only. Seismic monitoring must be coupled with geodetic monitoring of postseismic deformation to determine the full kinematic behaviour of a region.

The island of Iceland provides a unique opportunity to study oceanic-style extensional deformation on land. In Iceland crustal growth occurs primarily through rifting and dyke injections. Transform zones, which connect offset volcanic zones in Iceland to the mid-Atlantic spreading ridge, release strain through strike-slip faulting (Einarsson, 1991). Normal faults, which form sub-parallel to the rift zones, have near-vertical throws and are thought to be linked by dykes (Saemundsson, 1986). As part of the current research a 23 point GPS network was installed in the Hengill triple junction, southwest Iceland. The network is ideally placed to monitor extensional processes in south Iceland. The results of a first-epoch survey of this network are reported here, along with an analysis of the effect of ocean loading, a hitherto ignored source of noise in GPS results.

Extension within the continental crust is generally enacted by large normal-faulting earthquakes. Regions of continental extension are normally broad, up to several 100 km wide, and the associated seismicity is diffuse. Seismological investigations have revealed that normal faulting earthquakes within these regions occur on planar faults (*e.g.*, Doser, 1986; 1988; Barrientos and Stein, 1987; Eyidogan and Jackson, 1985). Both the Basin and Range province and SW Turkey are dominated topographically by wide, deep, grabens which trend perpendicular to the direction of maximum extension. The deformation within these regions is tectonically related to motion at the plate boundaries. Earthquakes along the western edge of the Basin and Range province are influenced by the right-lateral motion between the North American and Pacific plates. Extension in SW Turkey has been attributed to back-arc extension behind the subduction zone where the African plate plunges beneath the Eurasian plate (Kissel *et al.*, 1988; Sengor *et al.*, 1985; Atwater, 1970). It has been proposed that the large amount of extension observed in the Aegean region and in the Basin and Range province could be accommodated through listric faulting (Jackson and McKenzie, 1983; Wernicke and Burchfiel, 1982). Although seismic reflection data from the eastern Basin and Range province suggests the presence of such faults (Smith and Bruhn, 1984) they are not seismically active. Thus, if extension is occurring on such faults it must be aseismic.

The 1954 Rainbow Mountain, Fairview Peak and Dixie Valley earthquake sequence in Nevada, USA, provides a unique opportunity to study continental extensional tectonics within a plate interior. The events are amongst the largest to have been recorded geodetically and seismically in the western United States. Excellent spatial and temporal measurements of the geodetic network which spans the activated faults constrain the coseismic and postseismic deformation. In this research the subsurface fault geometry and coseismic slip estimates are calculated from the geodetic measurements. Such earthquake sequences have occurred in other continental extensional regions such as Greece and Turkey (*e.g.*, Jackson *et al.*, 1982; Eyidogan and Jackson, 1985). It has been proposed that increases in static stresses can trigger moderate-to-large events. As part of this research coseismic static stress changes are calculated to determine whether the events of the 1954 earthquake sequence were triggered.

The vertical, postseismic deformation following the Fairview Peak event and the interseismic, horizontal extension measured in southwest Turkey between 1989 and 1992 provide measurements of aseismic deformation in the continental crust. The measured deformation can be modelled using the finite element method and assuming a rheologically varied model of the Earth. In this study the data are used to study how

postseismic deformation contributes to the overall motion in an extending, continental environment.

1.2. ICELAND

1.2.1 Tectonics of Iceland

Iceland is a uniquely large, subaerial exposure of oceanic-type crust traversed by 700 km of accretionary plate boundary. The structure and tectonics of the island are controlled by the position of the mid-Atlantic ridge (MAR) and the hotspot that underlies east-central Iceland. The NUVEL-1A plate motion model gives a spreading rate of 1.8 cm/yr across the Icelandic plate boundary (DeMets *et al.*, 1994). Active deformation occurs along axial rift zones and along oblique or transverse fracture zones which connect offset rift zones. Throughout the island extensional features dominate. Iceland offers an unparalleled opportunity to study crustal deformation processes associated with oceanic-style crustal extension. Geodetic surveys using the Global Positioning System (GPS) have been conducted in Iceland almost annually since the system became usable for field surveying in 1986. Large, regional networks encompassing most of the country were installed and measured in 1986 and 1987, and remeasured and extended in 1989, 1990, 1991, 1992, 1993 and 1995 (Foulger *et al.*, 1987; 1993; Jahn *et al.*, 1989; Hackman, 1991; Jahn *et al.*, 1994; Sigmundsson *et al.*, 1992; Foulger *et al.*, 1992; Heki *et al.*, 1993).

The accretionary plate boundary comes onshore in Iceland at the Reykjanes Peninsula and strikes N70°E for 85 km, as far as Mt. Hengill (Figures 1.1 and 1.2). There, the ridge splits into the Western Volcanic Zone (WVZ), which continues the accretionary plate boundary into central Iceland, and the South Iceland Seismic Zone (SISZ). The SISZ forms a 90-km long east-west zone of historical destructive earthquakes connecting the southern ends of the WVZ and the Eastern Volcanic Zone (EVZ). To the north lies the Northern Volcanic Zone (NVZ) which is connected to the MAR by the Tjornes Fracture Zone (TFZ). Within each branch of the rift zone, deformation occurs in volcanic systems up to 100 km long. The volcanic systems usually comprise fissure swarms containing central volcanoes, along with evidence for shallow, fractionating, crustal magma chambers.

The WVZ and the EVZ are thought to be dying and propagating rifts respectively with the main locus of accretion currently moving from the WVZ to the EVZ. The EVZ appears to be propagating southward at a rate of 3.5 to 5 cm/yr away from the hotspot in east central Iceland (Einarsson, 1991). The absence of volcanic activity in the WVZ in

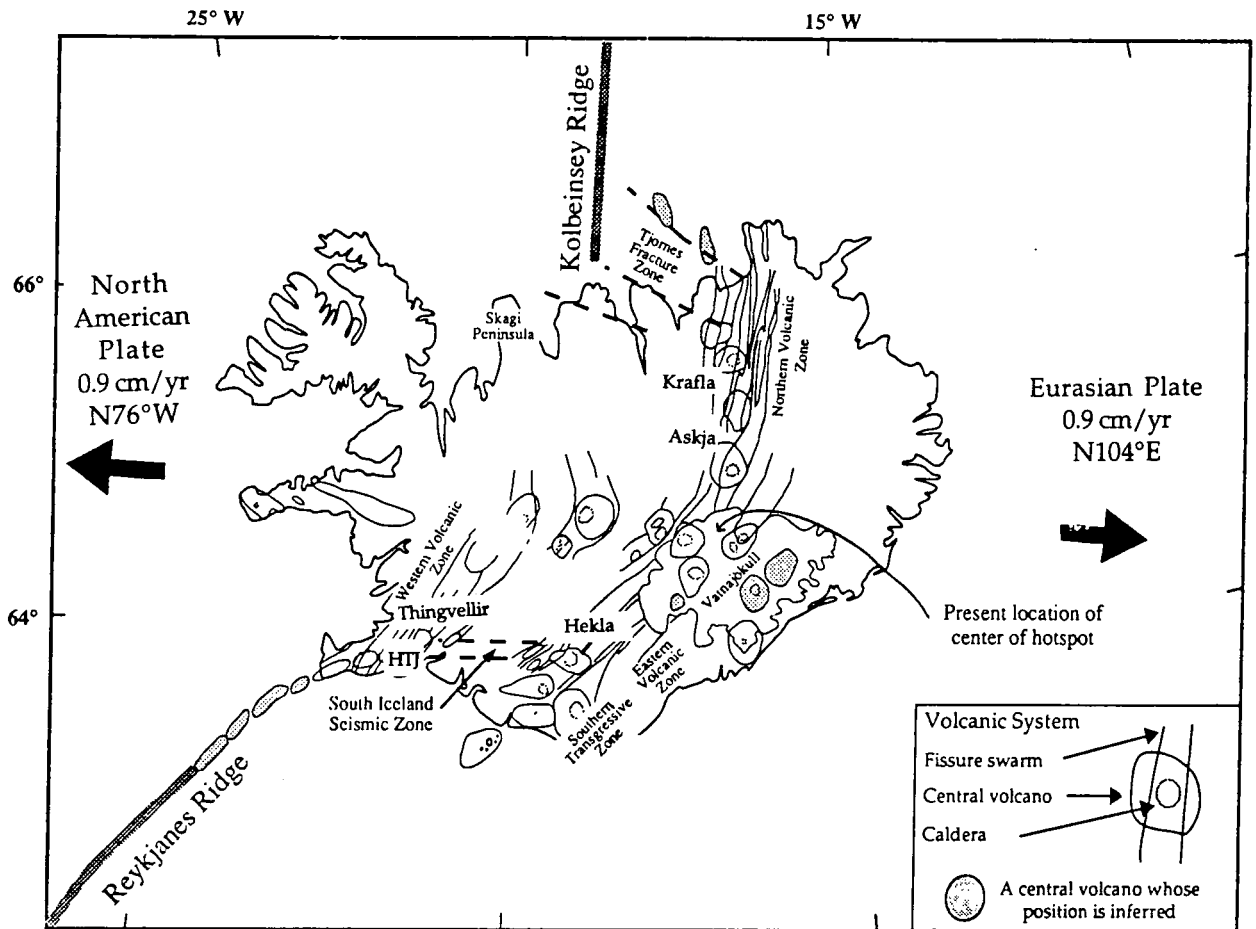


Figure 1.1 Regional tectonic map of Iceland, HTJ: Hengill Triple Junction. After Hackman *et al.*, 1990.

historic times, and the position of the SISZ well south of the Thingvellir graben (Figure 1.1) rather than further north, is cited as evidence that this rift zone is inactive. Part of the Thingvellir graben however, lies below sea level and is evidence of large-scale extension in the WVZ in the past (Figure 1.1). Normal faults that fracture the most recent 9000 years of lava indicate extensional rates of ~ 1 cm/yr across the zone. The WVZ has therefore accommodated at least half the spreading in the past 9000 years (Gudmundsson, 1987; Sigmundsson *et al.*, 1995). Strains of only 1.2×10^{-5} have been measured in the graben in the period 1967 to 1990, however (Tryggvason, 1990). The transfer of activity from one zone to another or “ridge jump” is believed to be caused by the westward drift of the plate boundary with respect to the hotspot.

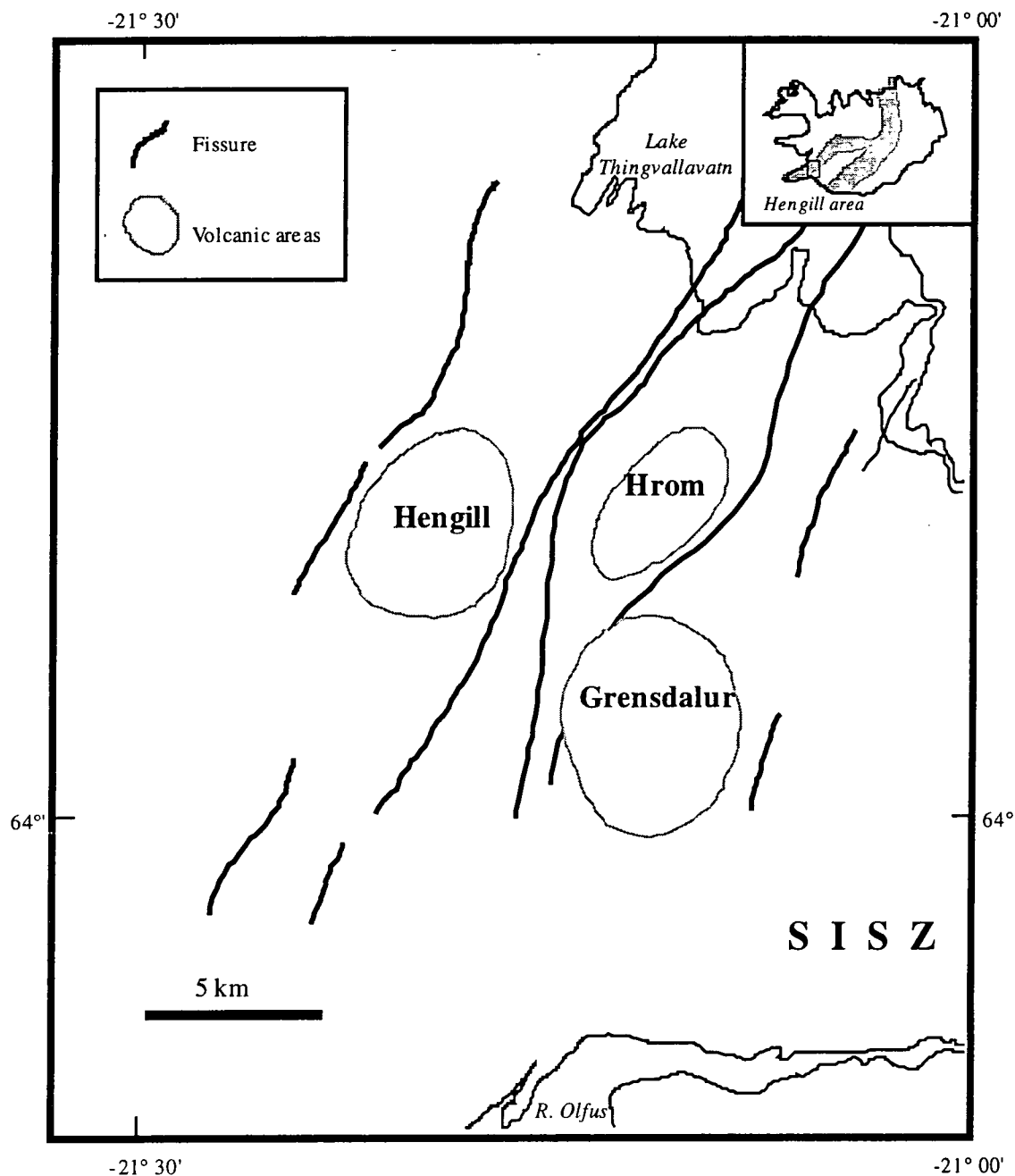


Figure 1.2 Schematic tectonic map of the Hengill Triple Junction showing the Hengill, Hromundartindur (Hrom) and Grensdalur systems. The shaded areas indicate the centres of greatest volcanism within each system. Inset shows the regional setting. SISZ: South Iceland Seismic Zone.

The transform zones in north and south Iceland connect the eastward-displaced rift zones to the MAR. The subdued surface morphology associated with these zones suggests the individual faults which comprise them may be transient. The SISZ releases strain that accumulates in the rotating microplate between the EVZ and the WVZ by dextral strike-slip movement on north-south faults (Einarsson, 1988; Foulger *et al.*, 1993). Historical records show that major earthquake sequences recur at 80 to 100 year intervals in the SISZ, the most recent sequences having occurred in 1732, 1784, and 1896 (Stefansson and Halldorsson, 1987). GPS measurements made in south Iceland between 1986 and 1992 indicate a relative plate velocity of 2.1 ± 0.4 cm/yr orientated at $N116 \pm 11^\circ E$ between

the two plates. This velocity is similar to the NUVEL-1A plate motion prediction of 1.8 cm/yr orientated at N104°E (Sigmundsson *et al.*, 1995).

1.2.2 Crustal structure

Temperatures close to the melting range of basalt are predicted at depths of 8 km in SW Iceland, the temperature gradient being about 100°C/km (Palmason *et al.*, 1971). Magnetotelluric measurements across the rift zones indicate a low-resistivity layer of 5 to 10 km thick at depths of 10 km increasing to 20 km east and west of the rift zones (Beblo and Bjornsson, 1980). Beblo and Bjornsson (1980) proposed that this low-resistivity layer corresponds to a layer of partially molten basalt. The temperatures at that depth are thought to be 1000° to 1100°C. P-wave velocities increase with depth to a 6.5 km/s isovelocity layer which lies at 1 to 3 km below central volcanoes and 3 to 6 km over most of the island (Palmason, 1971). Seismic velocities of 7.2 to 7.4 km/s below this are interpreted as an anomalous mantle which teleseismic residuals suggest may extend to a depth of 250 km. The brittle surface layer in Iceland is thus probably 10 km thick over the rift zones. The shallow, hot, anomalous mantle with partial melt beneath the whole island enables rapid stress redistribution following large events.

1.2.3 Crustal deformation

Crustal growth in Iceland is one of slow, continuous stretching and occasional rifting episodes when several metres of extension occur rapidly in the rift zones (Foulger *et al.*, 1992; Saemundsson, 1986). Within the NVZ, which is currently the locus of spreading in Iceland, rifting events have occurred at intervals of 100 to 150 years. The most recent spreading episode occurred in the Krafla volcanic system between 1975 and 1985 (Figure 1.1). The Askja volcanic system in northeast Iceland was active between 1874-1875. Earlier rifting events occurred in the Krafla volcanic system 1724-1729 and to the northwest of Krafla in 1618 (Tryggvason, 1984). The 10-year spreading episode in the Krafla volcanic system is probably representative of the rifting process along the Icelandic plate boundary. The rifting episode could be divided into two phases. From 1975 to 1979 extension was through dyke intrusion as magma was expelled from shallow magma chambers (Saemundsson, 1986). After 1980, as the extensional stress was gradually relieved, magma flowed out onto the surface. The accumulated rifting was up to about 8 m perpendicular to the plate boundary.

The regional post-rifting deformation field in north Iceland has been measured at approximately three- year intervals since 1987 using GPS and activity within the Krafla system has been monitored continuously since 1986 by a dense array of tiltmeters (Foulger *et al.*, 1992; Heki *et al.*, 1992; Tryggvason, 1994; Hofton, 1995). Differencing the 1992 and 1987 GPS measurements revealed that rift-normal expansion occurred at a

rate of 4.5 cm/yr near the rift zone and at a rate of 3 cm/yr at larger distances (Hofton, 1995). The horizontal spreading rate was thus more than twice the time averaged spreading rate of 1.8 cm/yr. The GPS data and tiltmeter data could be reasonably well modelled assuming the postseismic deformation was caused by the redistribution of stresses in the Earth's crust following the rifting event (Hofton, 1995).

The deformation was modelled using an Earth model of an elastic layer overlying a viscoelastic halfspace. Modelling the deformation in this way predicts rapid redistribution of stress in the few decades after the rifting followed by a period of relatively little motion. The viscosity of the viscoelastic layer which best fit the GPS and tiltmeter data ranged from $0.8-1.1 \times 10^{18}$ Pa s. Following a rifting event, little transient motion is predicted at distances of 0.1-1 km from the plate boundary with most of the deformation there occurring during the rifting episode. Between 15 and 150 km from the zone, the horizontal deformation field is variable with time. Shortly after the event extension occurs at ~ 35 cm/yr. After ~ 8 years this decays to ~ 5 cm/yr and after 85 years to 0.5 cm/yr (assuming a viscosity of 1.1×10^{18} Pa s). Subsidence is predicted following the rifting event reaching a maximum 58 years after the event at distances of 30 to 90 km from the zone. Close to the dike uplift occurs until 29 years after the event, at which time the area begins to subside.

Assuming such a viscoelastic relaxation model, and repeated rifting events through history, motion is predicted to be episodic in nature over a broad zone (Hofton, 1995). The width of the plate boundary zone, defined as the zone within which episodic extension occurs, is dependent on the viscosity of the viscoelastic halfspace and the recurrence interval of the rifting events. Assuming a viscosity of 1.1×10^{18} Pa s and a recurrence interval of 100 years, the plate boundary zone is predicted to be several 100 kms wide. Within 30 km of the rift zone most of the extension occurs at the time of dyking. From 30 to 90 km from the rift zone displacements reach a maximum at ~ 17 years and after ~ 50 years, motion has generally ceased. Outside of the plate boundary zone, deformation is a continuum as the effects of many events merge and episodicity is undetectable. The extensional process at oceanic spreading centers is thus predicted to be one of large coseismic displacements followed by a redistribution of stress with time. Extension is episodic in nature within a few 100 kms of the rift zone and the redistribution of stress causes regional, aseismic deformation over the following few decades.

1.2.4 The tectonics of the Hengill triple junction

The Hengill triple junction comprises the southernmost part of the N35°E trending WVZ and lies at the point where the Reykjanes Ridge, the SISZ and the WVZ meet (Figure

1.2). The Hengill area thus represents a very unusual kind of kind of triple junction. Crustal accretion within the triple junction currently occurs along the Hengill volcanic system which is dominated topographically by Mt. Hengill. A high-temperature geothermal area which is thought to be fueled by volcanic intrusions and partial melt encompasses the whole volcanic complex (Foulger, 1988a,b). The near-surface geothermal gradients range from $89^{\circ} \text{ km}^{-1}$ in the SISZ to $138^{\circ} \text{ km}^{-1}$ below the centre of the high-temperature geothermal area. The area is continuously seismically active and hypocenters lie in the 3-7 km depth range (Foulger, 1995). The focal mechanisms of about half of all the events recorded are normal or strike slip whereas the other half are non-double-couple with substantial explosive components (Foulger, 1988a,b). The non-double-couple events indicate extensional failure and are thought to result from circulating ground water causing cooling and contraction of the hot rock in the roots of the volcanoes. South of the volcanic complex the western end of the SISZ forms a zone of destructive historic seismicity.

Two older volcanic systems also lie within the Hengill triple junction, the Hromundartindur and Grensdalur systems, which have been rendered almost inactive by migration of volcanism and spreading to the Hengill system (Figure 1.2). The Grensdalur system was the main locus of accretionary activity prior to ~ 0.5 Ma. It is now extinct and the roots of the Grensdalur central volcano have been exposed by erosion (Foulger, 1988a). The Hengill volcanic system has been active since ~ 0.5 Ma. Five postglacial eruptions have occurred within the system. The Hromundartindur system is volcanically active at low levels, having produced one postglacial lava flow (Foulger, 1988a). It formed synchronously with the Hengill system and is now relatively inactive. Volcanic activity has thus migrated westerly through the Hengill triple junction over the past 0.5 Ma. Southerly migration of the SISZ through the Grensdalur volcanic system may have triggered this migration of spreading (Foulger, 1988a). Interaction of the discrete tectonic units that comprise the Hengill triple junction thus affect the seismicity, volcanism, spreading and consequently the deformation in the region.

1.3 THE BASIN AND RANGE PROVINCE

1.3.1 Tectonic setting

The Great Basin of the western United States contains almost all the state of Nevada, half of Utah and portions of California and Idaho (Figure 1.3). It is the northern half of a larger geological entity, the Basin and Range Province. The Great Basin is bounded to the east by the Colorado Plateau and to the west by the Sierra Nevada mountain range. The northern rim follows the Snake River plain of Oregon and Idaho. The province can be

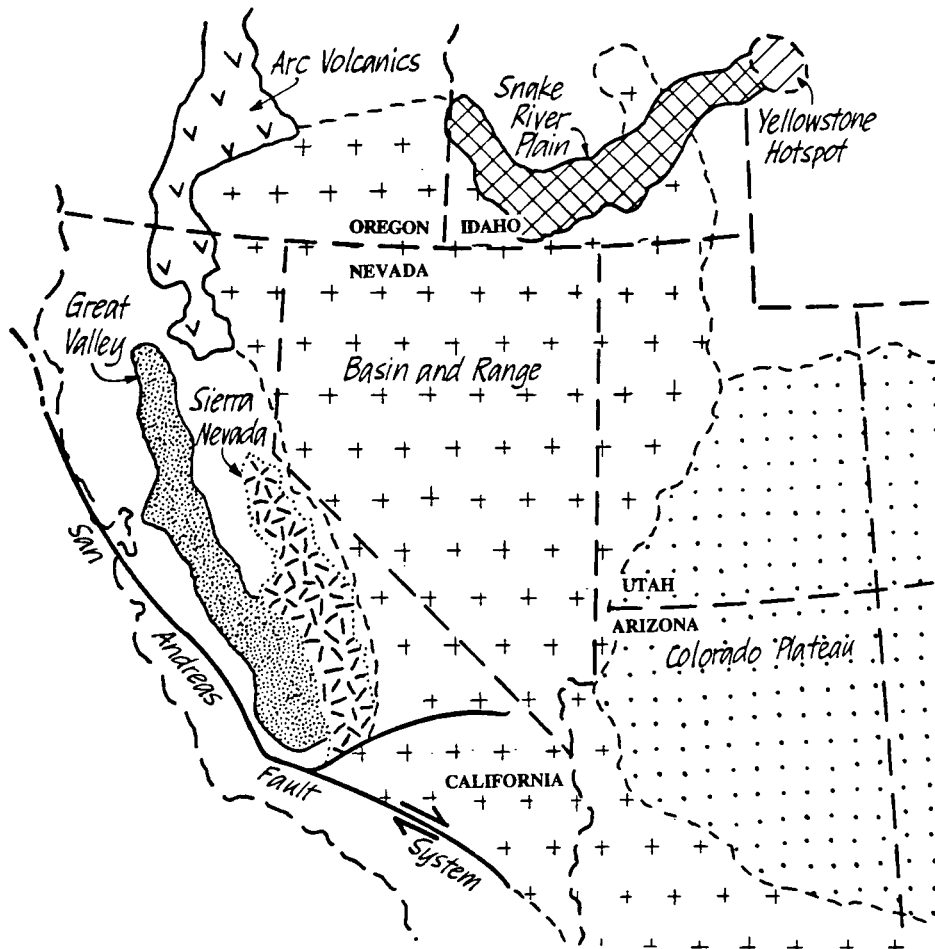


Figure 1.3 The Basin and Range province today and surrounding geological provinces. From Fiero (1986).

distinguished from neighbouring tectonic regions by its uplifted mountain ranges which separate long, sediment-filled valleys. The geophysical and physiographical characteristics of the Basin and Range province indicate large-scale extension over the past 20 Ma. The province is an area where active continental extensional deformation by normal faulting may be studied.

The geophysical properties of the Basin and Range province are similar to those of active rift zones: block faulting, high heat flow, active seismicity and high-amplitude, short-wavelength Bouguer gravity anomalies. It has been suggested that the Great Basin is an area of back-arc extension and superimposed on this is dextral shear in the same sense as the San Andreas fault regime (Atwater, 1970). This hypothesis is supported by observation that the direction of least principal stress has rotated from a southwest-northeast orientation to a northwest-southeast orientation, which would accommodate right-lateral motion. It has also been suggested that the East Pacific rise intersects the North American continent and extends under the Basin and Range province (Thompson, 1966).

1.3.2 Tectonic evolution

The distinctive topography of the Basin and Range province began to form at 17 Ma as a result of widescale continental extension (Zoback, 1989). The onset of extension coincided with the collision of the oceanic spreading centre to the west with the North American continent. A lateral transform system, now the San Andreas fault, began to develop to accommodate motion between the Pacific and North American plates along the western margin of the continent (Anderson *et al.*, 1989). In the Basin and Range province, northerly orientated faults formed in the brittle upper crust and mountain ranges were uplifted. Data on orientation of dyke-swarms and fault-slip vectors indicate the direction of extension was oriented northeast-southwest over most of the Basin and Range province in the mid-Miocene but had rotated clockwise to WNW - ESE by about 10 Ma (Zoback and Zoback 1980). The trends of the basins are normally perpendicular to the direction of least principal stress and therefore are an indication of the direction of spreading. Basins formed in Arizona and southeast California at 15-10 Ma show the least principal stress was oriented south-southwest then, while the topography of younger basins in Nevada and Utah suggests it was orientated east-west during their formation at ~10 Ma (Thompson *et al.*, 1989). Volcanic calderas and subvolcanic batholiths formed during the Cenozoic testify to the upward transfer of magma from deep source regions (Anderson, 1989). The crust of the province today has been uplifted, stretched and thinned.

1.3.3 Current tectonism

The Basin and Range province today is dominated by northwest to northeast trending sediment-filled basins bounded on each side by mountain ranges. In the west of the province faults generally dip to the east and the ranges are tilted to the west. In the east, faults tend to dip west and ranges tilt down to the east suggesting symmetry to the Basin and Range extensional structures. An inversion of focal mechanisms of historical earthquakes and slip-vector data from Quaternary fault scarps indicates an orientation of N64°W for the least principal stress in western Nevada (Zoback, 1989). Geodetic data from Very Long Baseline Interferometry (VLBI) observatories over the past 10 years, however, show that the direction of extension is now N34°W (Ward, 1990). It is probable that the geodetic data reflect the current orientation of the regional stress field while the geologic estimate reflects the average orientation over the past 10 Ma. The northwest orientation of current regional stresses within the province has been ascribed to the distribution of right-lateral shear across the western margin of the North American continent (Zoback, 1989).

Estimates of extension within the province vary from 10% to over 100%. The main difference in the estimates results from assumptions of fault geometry, *i.e.*, whether it is

listric or planar. Assuming a tilted-block geometry across the province with an average dip of 60° , the average extension is calculated to be $\sim 10\%$ (Stewart, 1971). Proffett (1977) estimated an extension of 30-35% across the province assuming listric fault structures which flatten at depth. Multiple superposition of near-horizontal faults in the Yerrington province of western Nevada, however, indicates over 100% extension (Proffett, 1977).

Normal extensional faulting characterises the deformation and controls the topography within the Basin and Range province. Three types of normal faults have been proposed: high-angle planar faults, listric faults and low-angle detachment faults, which are subhorizontal faults that underlie faulted, unmetamorphosed, upper-plate rocks. Seismic reflection and refraction profiles have shown that all three types exist. Seismic reflection data from Dixie Valley, Railroad Valley and Diamond Valley in Nevada show basins which are bounded by steep faults with little or no curvature (Anderson *et al.*, 1983; Okaya and Thompson, 1985; Catchings, 1992). That planar faulting generates the largest earthquakes within the province has been found from geodetic and seismic studies (*e.g.*, Barrientos and Stein, 1987; Doser, 1986; 1988). Listric faults in the Basin and Range province have also been detected by seismic reflection profiles, *e.g.*, profiles of the Goshute and Mary's River valleys in Nevada indicate that basins formed through listric faulting (Anderson *et al.*, 1983). The third type of faulting, low-angle detachment faulting, appears to occur beneath the Sevier Desert in Utah. A sub-horizontal seismic reflector underlies the basin at 2-4 km depth (Anderson *et al.*, 1983). The fault dips at 15° to 25° west and extends to depths of 15 km. It has been suggested that the fault extends 150 km westward and that the displacement in the down-dip sense may be up to 60 km (Smith *et al.*, 1989). Low-angle detachment faults have been found in Arizona and southeast California. None of these faults are seismically active but they may creep aseismically (Thompson *et al.*, 1989).

The three modes of faulting may be a result of different lateral offsets of the basin axis and zones of localized deep-crustal extension (Thompson *et al.*, 1989). The idea that extension may be restricted to narrow zones within the deep crust arises from the trend of seismicity in Holocene and Quaternary times. A continuous zone of faulting no more than 6 km wide and 60 km long was created by the 1915, **M**6.7, Pleasant Valley earthquake in northern Nevada. The segments of the fault which were activated crossed the trends of four separate, fault-bounded, range blocks (Wallace, 1984). In 1954 the Fairview Peak-Dixie Valley sequence involved rupture on a band of faults 30 km wide and 120 km long. Basins such as Dixie Valley have formed through displacement on single, steep, planar faults and may be a result of deep-crustal extension in a narrow zone beneath the basin axis at 14-20 km depth (Stewart, 1971). The broad width of the tilted ramps associated with Goshute and Mary's River Valleys indicates that the listric faults which bound them

must penetrate to deep levels. The zone of extension could then be placed at some distance laterally from the basin axis (Anderson *et al.*, 1983). The low-angle detachment fault below the Sevier Desert separates a highly fractured upper crust from a stratigraphically older crust. These basins may represent surface deformation in the upper 5 km of the brittle crust due to extension in the deep crust at great distances, several tens of kms, away from the basin.

1.3.4 Crustal structure

The extensional episode over the past 17 Ma has resulted in a crust which is thin, hot, and uplifted. Heat flow is up to twice that of stable continental regions and mantle P-wave speeds are relatively low. The entire region is uplifted to 1.5-2 km above sea level and the Bouguer gravity anomaly is at the -150 to -200 mGal level. There is widespread seismic activity. Three seismic surveys in northern Nevada, the COCORP reflection survey (Allmendinger *et al.*, 1987), the PASSCAL refraction survey (Catchings and Mooney, 1991) and the FALLON-EUREKA refraction survey (Thompson *et al.*, 1989) (Figure 1.4) provide independent data sets from which compatible seismic velocity models of the Nevada crust have been formed.

The crustal model of the northern Basin and Range province formed by Catchings and Mooney (1991) consists of 9 different velocity layers which form the uppermost 36 km of the crust and upper mantle. The upper crust is defined by four layers (Figure 1.4) with velocities of 2.5 to 6 km/s. The material in layer 1 is basin fill while layer 2, which is 2 to 3 km thick, represents the rock of the ranges. A relatively high-velocity layer (layer 4) underlies the ranges while thick, lower-velocity material (layer 3) underlies the basins. The transition from a brittle deforming zone to a ductile deforming zone occurs in the middle crust and is marked by a change from non-reflective to reflective material and an increase in seismic velocity. The middle crust is defined by two layers with velocities of 6.15 and 6.3 km/s and varies in depth from 11 to 20 km across the profile. The lower crust is also defined by two layers (layers 7 and 8) with velocities of 6.6 and 7.4 km/sec respectively. The ninth layer, with a velocity of 8 km/s, is considered to be the upper mantle and is separated from the crustal layers by the Moho. Depth to the Moho varies from 30 to 36 km along the east-west profile. The FALLON-EUREKA seismic reflection profile (Figure 1.4) was used to form a seismic velocity model of Dixie Valley (Thompson *et al.*, 1989). The data, however, are sparse compared to those of the COCORP and PASSCAL surveys. A 6-8 km/s layer was detected at depths of 16.5 to 21.5 km along the line and a 7.5 km/s layer was detected between 24 and 30 km depth.

The modal heat flow in the province is 85 mWm⁻². Northern Nevada is an area of anomalously high heat flow (103 mWm⁻²) called the Battle Mountain High while regions

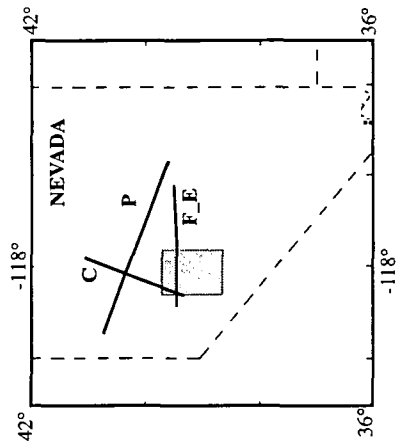
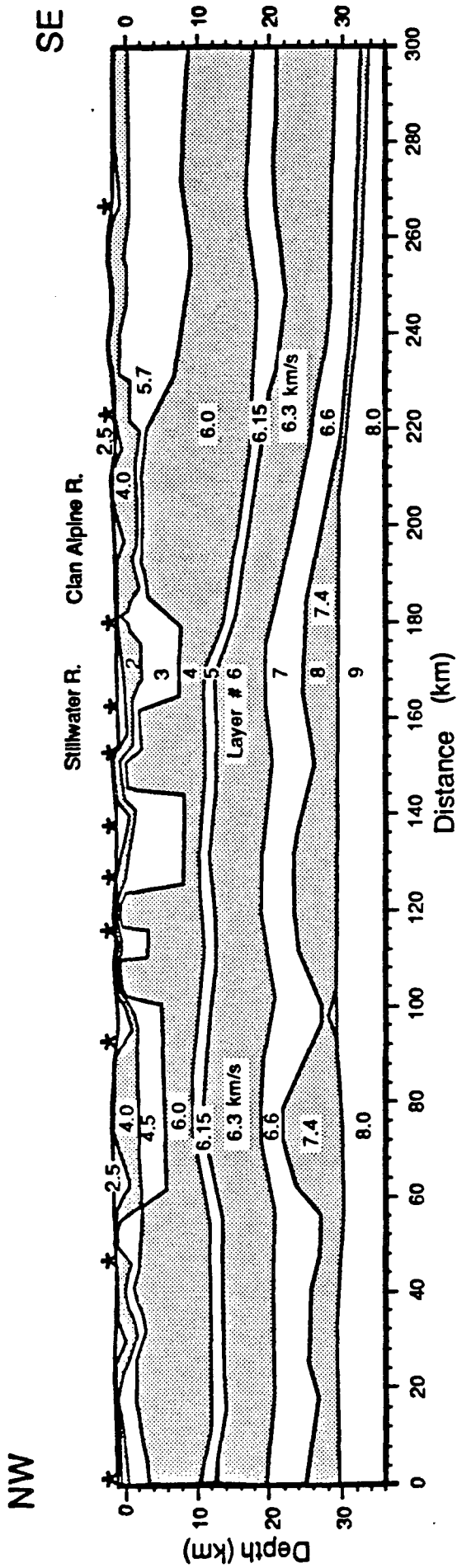


Figure 1.4 The seismic model of the northern Basin and Range province derived from the PASSCAL seismic refraction data. Stars show shot locations. Inset shows location of the PASSCAL (P), COCORP (C) and FALLON_EUREKA (F E) seismic transects, from Catchings and Mooney, (1991).

to the south and west have lower heat flow (Lachenbruch and Sass, 1978). The Curie isotherm, the temperature at which ferromagnetic components in rocks lose their magnetism, varies in depth from 30 km in eastern Nevada to 10 km in the Dixie Valley-Fairview Peak area (Blakely, 1988). The Curie isotherm may be used as a guide to the depth of the brittle-ductile transition zone. Heat-flow values recorded in western Nevada and strain rates of $1 \times 10^{-15} \text{ s}^{-1}$ indicate that the depth to the transition zone is 8 to 12 km beneath western Nevada (Catching, 1992). In regions east of this the depth of the Curie isotherm is 12 to 18 km.

1.3.5 Seismicity

Some of the largest earthquakes to have been recorded geodetically and seismically in the western United States have occurred in the Basin and Range province. The three largest are the 1959, **M7.3**, Hebgen Lake, Montana earthquake, the 1983, **M7.3**, Borah Peak, Idaho earthquake and the 1954, **M7.2**, Fairview Peak earthquake in Nevada. This century seismic activity has been concentrated in three seismic belts along the western margin of the province: the Walker Lane Seismic Zone, the Eastern California Shear Zone and the Central Nevada Seismic Zone (Figure 1.5). The Walker Lane seismic zone is a northwest-trending shear zone of right-lateral faults which extends from southeast to western Nevada. The Eastern Californian shear zone trends $N35^\circ W$ from the eastern end of the Big Bend in the San Andreas fault across the Mojave Desert to northern Owens Valley (Savage *et al.*, 1990). The Central Nevada Seismic Zone is a band of seismicity which trends north-northeast through central Nevada and has historically been the most active seismic region in the province. Earthquakes in this zone display significant components of right-lateral displacement. These events include the 1932, **M6.7**, Cedar Mountain, Nevada event and the Fairview Peak and Pleasant Valley earthquakes (Doser, 1988; Slemmons, 1957). The Hebgen Lake and Borah Peak events, which occurred in the north-west corner of the province, did not display such right-lateral components. The seismogenic zone in the Basin and Range province is 12 to 15 km deep (Doser, 1986; 1988). The change in seismicity levels at 12 to 15 km depth is coincident with a change in seismic reflectivity, velocity and the Curie isotherm.

1.3.6 The Rainbow Mountain - Fairview Peak - Dixie Valley area

1.3.6.1 Tectonic setting

Dixie Valley lies 40 km east of Fallon, Nevada, and within the Central Nevada Seismic Zone. It is a northeast-trending valley, 80 km long and up to 24 km wide (Figure 1.6). It is bordered on the west by the Stillwater Range and to the east by the Clan Alpine Range. The mountains rise over one km above the valley floor. To the south, is the 2,539 m high Fairview Peak and 30 km west of Dixie Valley, are the Rainbow Mountains. The region

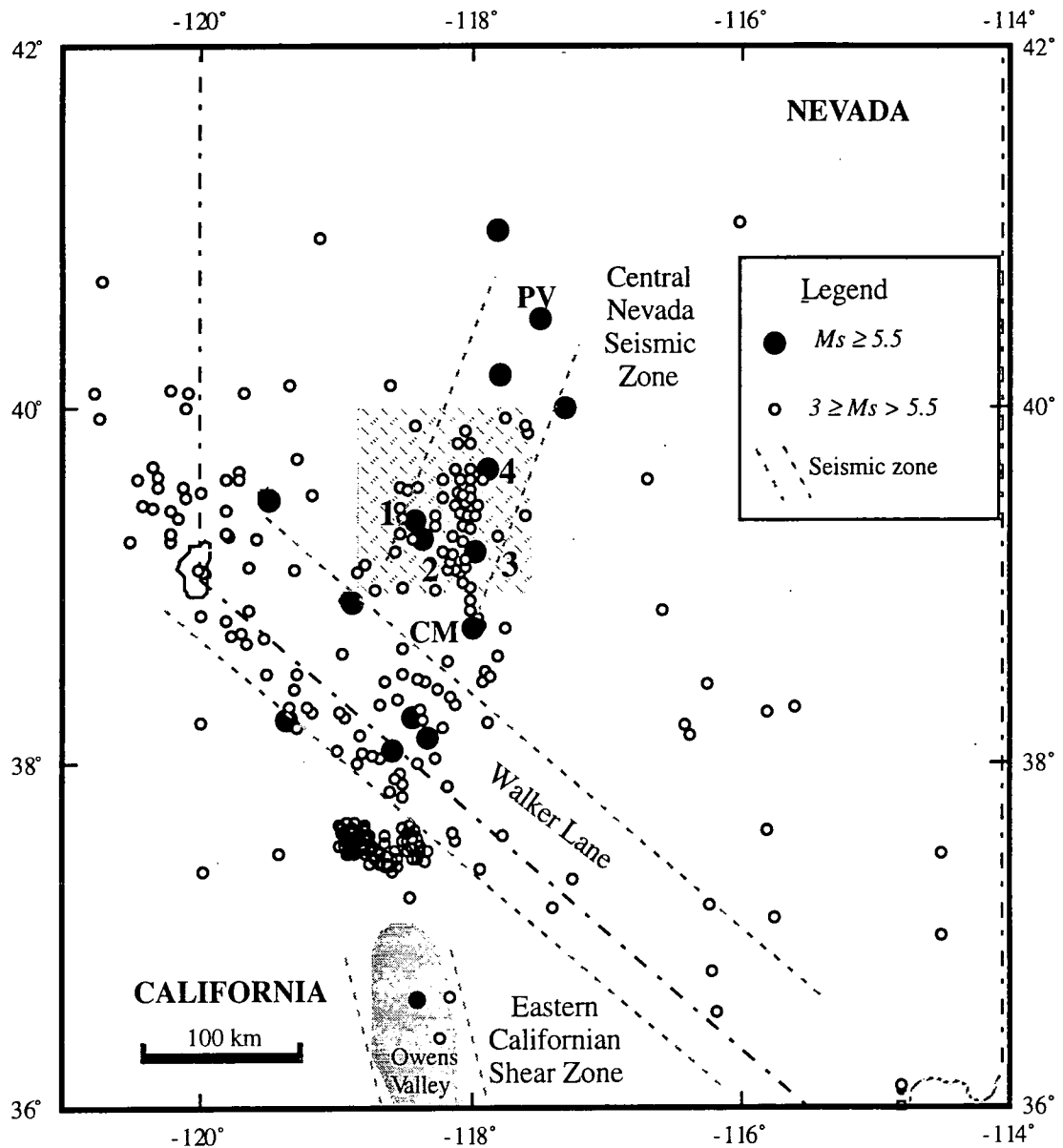


Figure 1.5 Seismic zones in western Nevada. Shaded area is Owens Valley. Earthquakes along the western margin of the Basin and Range province since 1857 ($M_s > 3$) are shown as open circles. Earthquakes of $M_s > 5.5$ are shown as black dots (information from the University of Reno Earthquake Catalogue). Locations of the Cedar Mountain (CM) and Pleasant Valley (PV) earthquakes are shown. The earthquakes in the 1954 Rainbow Mountain-Fairview Peak-Dixie Valley sequence are numbered 1 to 4 in the order in which they occurred. The stippled area is the Dixie Valley area studied in this thesis.

was the scene of intense seismicity in 1954, the latest burst of seismicity in a 100-year period of increased activity within the zone (Wallace, 1984).

The oldest rocks in the Stillwater and Clan Alpine Mountain ranges are of Mesozoic age (Page, 1965; Willden and Speed, 1974; Bell and Katzer, 1987). Extrusive rocks in the ranges have been dated as upper Jurassic (140 Ma). Rocks of Cenozoic age cap both Fairview Peak marks the southern end of Dixie Valley. The eastward dipping Fairview

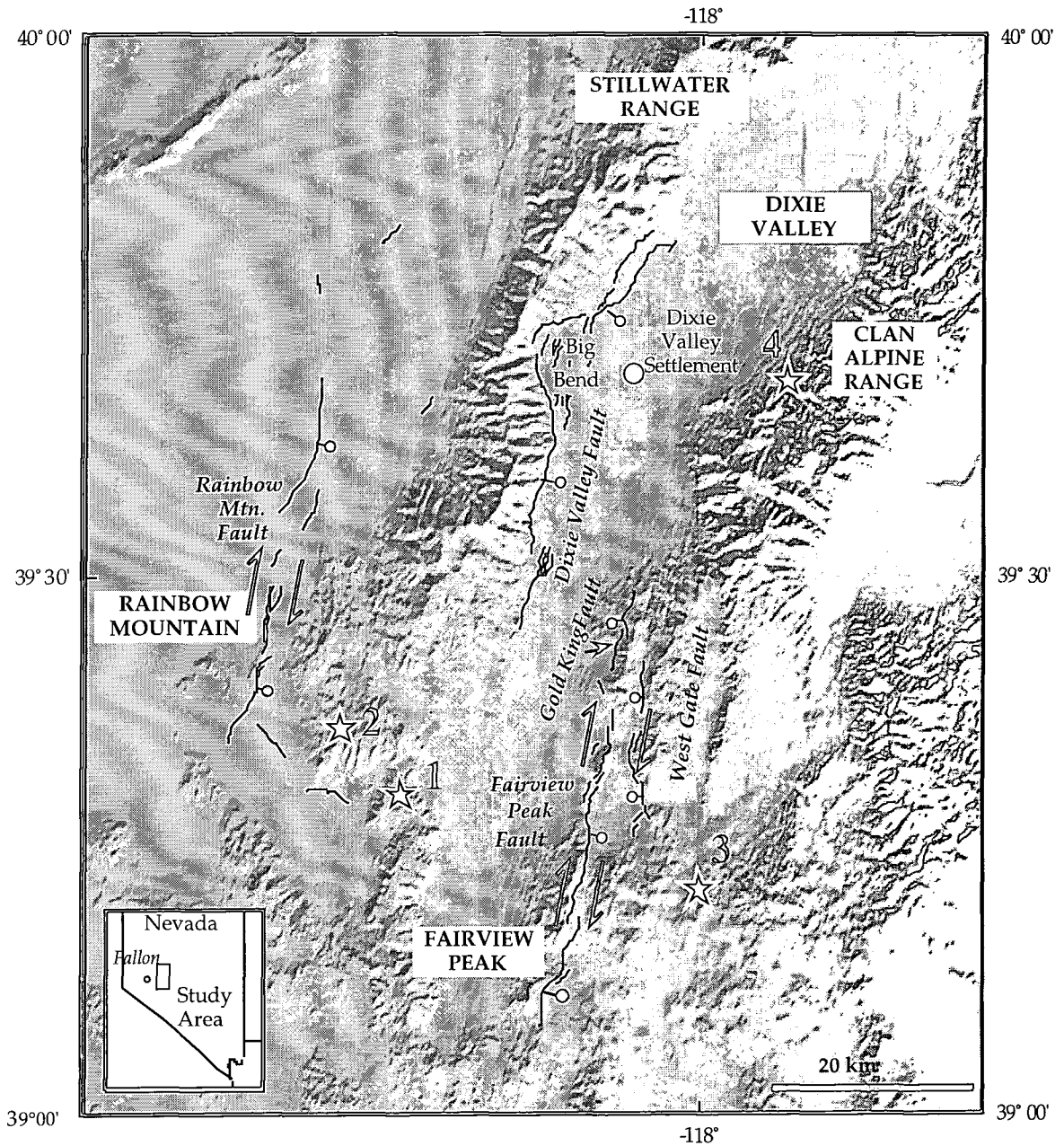


Figure 1.6 The Rainbow Mountain-Fairview Peak-Dixie Valley area, Nevada. Inset shows location of the study area. The 1954 fault scarps are shown as black lines. Dots show the direction of fault dip and arrows indicate the direction of horizontal slip. Epicenters of the 1954 earthquakes are shown as stars: 1) Rainbow Mountain, July 6, 2) Rainbow Mountain, August 24, 3) Fairview Peak, December 16, 4) Dixie Valley, December 16, (locations from Doser, 1986).

Peak fault lies to the east side of Fairview Peak where high-angle faults with 100s of metres of displacement are observed in the Tertiary rocks. Geodetic data, mapped surface offsets, and seismic recordings of the 1954 Fairview Peak earthquake suggest the fault is planar (Savage and Hastie, 1966; Doser 1986). Rainbow Mountain, 50 km west of Fairview Peak, is a tilted block of Tertiary sedimentary layers which dip westward at 35° to 50° . The Rainbow Mountain fault bounds the east side of the Rainbow Mountains.

Faulting is found everywhere in the alluvial apron along the base of the Mountain and in the valley floor to the east which consists of Lahontan deposits.

Structural models of Dixie Valley derived from seismic refraction and reflection profiles and gravity data depict it as an asymmetrical graben filled with up to 2 km of alluvial and lacustrine fill (Anderson *et al.*, 1983; Okaya and Thompson, 1985; Thompson and Burke, 1973). The deepest part of Dixie Valley is 2-3 km from the Stillwater Mountain Range. The seismic data indicate the west side of Dixie Valley is bounded by two sub-parallel, high-angle, planar faults. A range-front fault lies at the mountain range contact and a piedmont fault lies a few km east of it (Bell and Katzer, 1987). The faults are high-angle and planar to depths of 9 km and the Mesozoic basement of the range underlies the basin. Granitic and volcanic rocks in the Valley basement are offset from those in the Stillwater Range by 90 to 150 m on the downthrown side of the rangefront fault. East of the piedmont fault they are offset by 1,800 m. There is no one major fault on the opposite side of the valley but several parallel faults stepped. Gravity measurements made in the valley are consistent with models derived from seismic data (Schaefer, 1983). Measurements made at 300 stations on 9 east-west profiles indicate that Dixie Valley is filled with a maximum of 3,000 m of fill and the central depression of the valley is to the west. Intensive faulting along the Stillwater Range was indicated by high gravity gradients.

A sharp break in the slope of the Stillwater Mountain range in Dixie Valley, and faceted spurs 100s of metres high, provide geomorphic evidence of millions of years of activity on the Dixie Valley fault (Wallace and Whitney, 1984). Fault scarps, which in some places are 28 m high, are preserved above the highest level of the Pleistocene lake which filled Dixie Valley. These scarps are therefore older than 12,000 years but no older than late-to-early Miocene, as they are superimposed on Miocene basalts (Wallace and Whitney, 1984). The 1954 sequence occurred on the range-front fault and produced a new set of fault scarps on a fault which had not ruptured in the previous 10,000 years (Bell and Katzer, 1991) a characteristic of current faulting modes within the Central Nevada Seismic Zone. Late Quaternary deposits on the range-front fault record three large events in prehistoric time. The piedmont fault, however, ruptured between 1.5 and 6.8 Ka, a time when the main range front was quiescent (Bell and Katzer, 1991). Seismicity has therefore migrated between and along the fault segments over the past several Ma.

Lake shorelines were formed as 'bath tub ring' features of calcareous tufa on the mountain ranges. From the preservation of the shoreline and carbon dating of the calcareous tufa it can be concluded that the highest lake level was contemporaneous with Lake Lahontan's highest level at $11,560 \pm 180$ years ago (Thompson and Burke, 1973).

The spreading rate of Dixie Valley has been estimated to be 1 mm/yr over the last 12,000 years and 0.4 mm/yr over the last 15 Ma (Thompson and Burke, 1973). Pleistocene shoreline deposits which are 12,000 years old have been vertically offset by 9 m on both sides of the valley. The horizontal extension is ~10 m implying an average rate of extension of 1 mm/yr and an uplift rate of 0.5 mm/yr. Correlating the basalt which forms the base of the valley with the Tertiary volcanoclastic sequence exposed in the Stillwater Range allows a longer-term rate to be determined. The vertical offset is 2.2 km - 2.9 km and the Tertiary volcanoclastic sequence have been dated at 8 Ma yielding a spreading rate of 0.38 mm/yr (Okaya and Thompson, 1985). This extension rate is consistent with that obtained from seismic refraction measurements which show that 5 km of vertical uplift and 6 km of horizontal extension has occurred since Miocene-Pliocene times. The average extension rate from these dates is 0.4 mm/yr over the past 15 Ma (Thompson and Burke, 1973).

1.3.6.2 The Rainbow Mountain-Fairview Peak-Dixie Valley earthquakes

The Dixie Valley- Fairview Peak - Rainbow Mountain area (referred to as the Dixie Valley area) in west central Nevada, USA, was the scene of a sequence of normal faulting events unique in historic times. Four earthquakes of $M > 6.0$ occurred within 6 months and within a 30 km radius (Table 1.1). The earthquakes were felt over an area of 675,000 square km in Nevada, California, Utah, Idaho Oregon and Arizona and created ~120 km of surface ruptures (Tocher, 1956; Slemmons, 1957; Larson, 1957; Wallace and Whitney, 1984; Bell and Katzer, 1991; Caskey *et al.*, 1996). The series of earthquakes began with two events on the Rainbow Mountain fault, July 6, 1954 ($M6.2$) and August 24, 1954 ($M6.5$) (Figure 1.6). On December 16, 1954 a $M7.2$ earthquake occurred on the Fairview Peak fault. Rupture occurred simultaneously on the West Gate and Gold King faults (Doser, 1986). Four minutes and twenty seconds after the Fairview Peak event the Dixie Valley fault ruptured ($M6.7$). The events were recorded at 41 stations 150 km to 240 km away and at 35 stations at greater distances. The seismic recordings have been analyzed by many authors to locate the events and determine the source mechanisms (*e.g.*, Doser, 1986; Okaya and Thompson, 1985; Fara, 1964; Romney, 1957). The Rainbow Mountain, Fairview Peak, and Dixie Valley scarps dipped between 50° and 70° east at the surface while the West Gate and Gold King fault scarps dipped west (Table 1.2). First motion data, teleseismic body wave modelling and geodetic analyses indicate that the events occurred on planar faults and had significant components of right-lateral slip. All the scarps exhibited normal slip and all, with the exception of the Dixie Valley scarp, showed a right lateral sense of motion.

The epicenters of the events were located using a master event technique and focal depths and source mechanisms determined by body-wave modelling of teleseismic data from 7

worldwide stations (Doser, 1986). The Fairview Peak earthquake was used as the master event as it had been recorded by the largest number of stations. P arrivals were read from seismograms of western U.S. stations and focal depths fixed at 12 km. From this information Doser (1986) estimated the rupture lengths and moment magnitudes of the events (Table 1.1). Moment magnitudes (M) were calculated using,

$$\log M = \frac{2}{3} \log M_o^b - 10.7 \quad (4.1)$$

where M_o^b is the moment estimated from body-wave modelling.

Table 1.1 Location, magnitude of the 1954 events derived from body-wave modelling (Doser, 1986).

Earthquake	Rainbow Mtn (6 July)	Rainbow Mtn (24 August)	Fairview Peak	Dixie Valley
Date	6/6/54	24/8/54	16/12/54	16/12/54
Location	39.29 -118.36	39.35 -118.34	39.20 -118.00	39.67 -117.87
Mechanism (strike, dip, rake)	336, 80, -140	355, 50, -145	350, 60, -160	350, 50, -90
Focal Depth (km)	10±1	12±1	15±2	12±3
Magnitude (M)	6.2	6.5	7.2	6.7

The focal mechanism of the first Rainbow Mountain event (July 6, 1954, $M6.2$) indicated right-lateral oblique slip along a fault plane striking 20° - 30° west. The scarp, however, runs north-east along Rainbow Mountain with an average strike of $N15^\circ E$ (Table 1.2). It is notable that the strike of the 1954 faults tend to strike east of north while the focal mechanisms suggest the faults are orientated west of north. Body-wave modelling suggests this event had a focal depth of 10 ± 1 km. The earthquake consisted of two subevents and had a total seismic moment of 2.3×10^{18} Nm. The rupture began at the south end of the fault and propagated northwards creating 18 km of fault scarps. The west side of the fault was uplifted everywhere and the maximum vertical displacement measured was 0.30 m (Table 1.2).

The second event on the Rainbow Mountain fault (Aug. 24, 1954, $M6.5$) caused rupture on the northern part of the July fault scarp and created an additional 20 km of fault scarps (Tocher, 1956). The focal mechanism shows right lateral oblique slip along a fault plane striking $N05^\circ W$ and dipping at $50^\circ E$ (Doser, 1986; Fara, 1964). A focal depth of 12 ± 1 km and a rupture time of 30 s was estimated from body-wave modelling. The average strike of the scarp was $N20^\circ E$. Recent mapping of the Rainbow Mountain fault scarps indicates that there was an average of 0.9 m right-lateral offsets along the Rainbow Mountain fault (Caskey, personal communication, 1996), (Table 1.2). The August 24

Table 1.2 Geometry of the fault ruptures and associated slip as observed along the surface ruptures. The maximum displacements found at single points along the fault scarps are given and the average displacements, where available, are shown in parentheses. References are denoted by superscript; a, Caskey, personal communication (1996), b, Tocher (1956), c, Caskey *et al.*, (1996).

Fault	Displacement (m)		Dip	Strike
	Horizontal	Vertical		
Rainbow Mtn.	0.9 ^a	0.3 ^b	E	N15°E
Fairview Peak	2.9 (1.0) ^c	3.8 (1.2) ^c	55°-75°E	N12°E
West Gate	1.2 (0.6) ^c	1.2 (0.4) ^c	W	N10°E
Gold King	0.0 ^c	1.0 (0.5) ^c	W	N10°E
Dixie Valley	0.0 ^c	2.8 (0.9) ^c	50°-70°E	N10°E

event was followed by two aftershocks. The first, on August 31, 1954, occurred at the north end of the Rainbow Mountain fault and the second, on September 1, occurred close to the July 6 epicentre.

The Fairview Peak earthquake (Dec. 16, 1107 UT, M7.2) ruptured bilaterally along the fault (Romney, 1957). Fault plane solutions indicate a fault striking N11°W and dipping at 62°E. A right-lateral component of slip almost twice as large as the normal component is evident in the focal mechanism (Doser, 1986; Romney, 1957). The focal depth, estimated from P-pP arrivals, was 15±2 km. The total seismic moment was 5.3×10^{18} Nm (Doser, 1986). The scarp dipped east at 55° to 75° and trended N10°E (Slemmons, 1957). At points along the surface, right-lateral displacements were equal to the vertical offsets (Slemmons, 1957; Caskey *et al.*, 1996). Vertical and right-lateral offsets were greatest at Fairview Peak where they were 3.8 m and 2.9 m respectively (Caskey *et al.*, 1996). The fault plane solutions for the Fairview Peak event agrees with surface displacements with the exception of the fault strike.

The West Gate and Gold King faults ruptured with the Fairview Peak event. The West Gate fault scarp dips to the west and is 19 km long. The maximum vertical and right-lateral offsets were equal and about 1.2 m (Caskey *et al.*, 1996). At some points along the rupture the right-lateral motion was almost three times as large as the vertical. The westward-dipping Gold King fault scarp extends for 18 km as a discontinuous group of fractures (Figure 1.6). Vertical displacements were a maximum of 1 m at the north end of the fault. Right-lateral displacements of a few 10s of cm were observed in places by Slemmons (1957) but none were observed by Caskey *et al.*, (1996). There are no focal mechanisms available for these events as they occurred at the same time as the Fairview Peak event (Doser, 1986).

The Dixie Valley event, (Dec. 16, 1111 UT, M6.8), occurred 4 minutes after the Fairview Peak event. The focal depth of the Dixie Valley event estimated from body-wave modelling, was 12 ± 3 km (Doser, 1986). It was not possible to obtain a focal mechanism from the first motion data for this event as it was mixed with the coda of the Fairview Peak earthquake, but the best fit to the waveforms was for normal slip on a fault striking at $350^\circ\pm 20^\circ$ and dipping at 50° E (Doser, 1986). The earthquake created 50 km of surface faulting. The scarp dips at 50° to 70° to the east and follows the contour of the Stillwater Range (Bell and Katzer, 1991). The maximum vertical offset observed was about 2.8 m. Between 0.25 and 1 m of slip was observed on a piedmont fault to the east of the Dixie Valley fault (Caskey *et al.*, 1996). No right-lateral offsets were observed along the fault, a left-lateral offset of 2.1 m was observed in one place and is considered anomalous (Slemmons, 1957).

1.4 TURKEY

1.4.1 Tectonic setting

The Anatolian plate, which includes all of Asian Turkey, forms the western part of the tectonic escape system caused by the convergence of the African, Eurasian and Arabian plates (Figure 1.7). It is bounded in the west by the Aegean Sea, to the north by the North Anatolian fault (NAF), to the east by the East Anatolian fault (EAF), and to the south by the Hellenic Arc and Florence Rise subduction zones. The kinematics of the region are governed by the interaction of the surrounding plates. The African plate is moving northwards with respect to the Eurasian plate at a rate of 9.5 mm/yr (DeMets *et al.*, 1994; 1990). Motion between the African and Arabian plates is accommodated by slip along the Dead Sea fault at a rate of 12 mm/yr (DeMets *et al.*, 1994; 1990). In comparison to this, slip rates along the EAF, which accommodates motion between the Arabian and Anatolian plates, are much lower at ~ 5 mm/yr (Oral, 1995a). The rates of subduction along the Hellenic Arc vary from 10 mm/yr in the west of the arc to 15 mm/yr in the east (Le Pichon and Angelier, 1979). GPS measurements across the NAF indicate that right-lateral slip occurs at a rate of 25 ± 9 mm/yr (Oral, 1993). Geological estimates of the slip rate range from 5 to 30 mm/yr while seismological estimates tend to agree with those observed by GPS and are in the range of 25 to 30 mm/yr (Jackson and McKenzie, 1988). The result of plate interactions in the eastern Mediterranean is that a compressional regime exists in eastern Turkey which forces the Anatolian plate westward. Superimposed on this westward motion is a north-south extensional field thought to be created by the southward migration of the Hellenic Arc and the “peeling back” of the down-going slab. South Greece, the Aegean and southwest Turkey are all part of the resulting, broad back-arc extensional province. The area is among the most seismically active in the world and

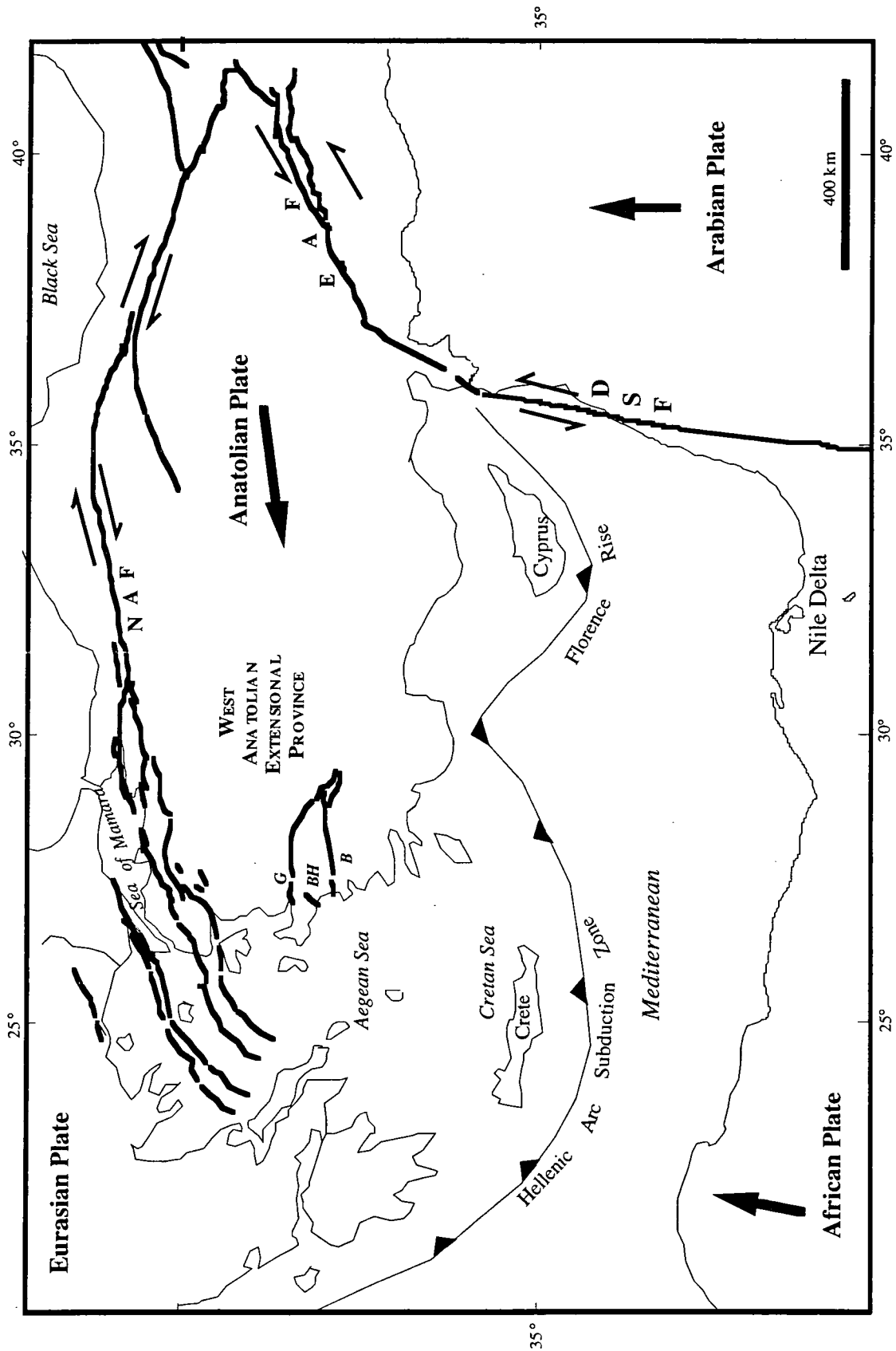


Figure 1.7 The tectonic units of the eastern Mediterranean. The black arrows show the plate motions with respect to the Eurasian plate. Thick black lines indicate major faults. NAF, North Anatolian fault; EAF, East Anatolian fault; DSF, Dead Sea fault; BH, the Bozdag Horst; G, the Gediz graben; B, the Buyuk Menderes Graben.

is one where continental extension through normal faulting and aseismic deformation in the continental crust can be studied.

The Anatolian plate may be divided into four major provinces. The east Anatolian province is a continent-continent collision zone and one of north-south shortening accommodated by thrusting and strike-slip faulting. The northern Turkish province is shortening in the east-west direction and is bounded to the north by the NAF, a major right-lateral strike-slip fault. Large earthquakes have occurred along the NAF at about 10-year intervals. Central Turkey is relatively quiet seismically. It is characterised by large extensional basins which connect to the grabens of western Turkey. Western Turkey is dominated by extensional features and deformation is accommodated by movement on a system of normal faults which trend east-west across the region (Sengor *et al.*, 1985).

Estimates of extension rates in western Turkey and the Aegean, based on seismological data, range from 30 to 50 mm/yr (Jackson and McKenzie, 1988). Satellite Laser Ranging (SLR) measurements made in the region since 1986, and GPS measurements made in the region since 1989, indicate that western Turkey is being extruded at rates of ~36 mm/yr and is rotating at a rate of 0.3°/Ma with respect to a pole in the Nile delta (Noomen, 1993; Oral, 1995a,b). Thus, for the westward motion of the western Anatolian plate, estimates based on seismicity this century give results comparable to those measured geodetically over a much shorter time period and are in the order of 30 to 40 mm/yr.

1.4.2 Tectonic evolution of the Aegean and the Anatolian plate

The westward escape of Turkey, the curvature of the Hellenic arc and the initiation of slip on the NAF began between 14 and 10 Ma when the Arabian plate collided with the Eurasian plate (Sengor *et al.*, 1985). This collision caused crustal thickening and an extensive compressional stress regime over the eastern Anatolian plate (Sengor *et al.*, 1985; Barka and Hancock, 1984). Paleomagnetic data suggest that clockwise rotation in the opposite sense began to occur in the western and eastern extremities of the arc in the middle Miocene (Kissel *et al.*, 1988). At this time the NAF began to form as a broad shear zone to accommodate the beginning westward motion of the Anatolian plate. The sea of Marmara developed as a broad furrow and marked the western termination of the shear zone (Sengor *et al.*, 1985).

By the late Miocene the tectonic regime which governs the tectonics of Anatolia today was well established. The broad shear zone which had accommodated the right-lateral motion of the Anatolian plate had formed into the narrow fault zone of the NAF. The Tortonian (12 Ma) marked the initiation of the prominent east-west grabens in western Turkey. The uplands which once characterized the region had subsided locally beneath sea level as a result of extension forces at the Hellenic subduction zone. The topography of western

Turkey was fractured by fault systems as the plate moved westward and the region was disrupted internally by the bending of the Hellenic arc. Block rotations of up to 48° clockwise have been detected in western Greece and up to 30° counter-clockwise in SW Turkey (Kissel *et al.*, 1988).

1.4.3 Crustal structure

Seismic refraction surveys indicate that the crustal thickness in relatively unstretched parts of Greece and Turkey is almost double that in the Aegean Sea (Makris, 1978). The crust thins eastward from inland Greece where it is 46 km thick and locally has up to 10 km of sedimentary cover, to 20 km with ~3 km of sedimentary cover in Neogene basins (Makris, 1976; 1978). The crust then thickens again eastward between the Cretan Sea and Turkey. Strong P_mP reflections indicate a highly reflective layer defining the boundary between the upper and lower crust. The thickness of the crust is ~32 to 35 km in western Turkey (Ezen, 1991). Thickening of the continental crust from the mid Aegean to Turkey is also indicated by gravity data. Negative Bouguer anomalies with maximum values of -30 mGals in western Greece become positive westward reaching +80 mGals in the Aegean and then steadily decrease towards the east and in Turkey (Makris, 1976). The trend in gravity anomalies also varies across the Aegean, from NNW-SSE in the Greek mainland to ENE-WNW in the mid Aegean. Fault plane solutions and micro earthquake studies in the area show the seismogenic layer is 10 to 15 km thick (Jackson and White, 1989; Jackson *et al.*, 1982; Hatzfeld *et al.*, 1987).

1.4.4 Southwest Turkey

1.4.4.1 Tectonics

The geomorphology of SW Turkey is dominated by two east-west trending 150-km long grabens, the Buyuk Menderes and Gediz grabens (Figure 1.8). The grabens form the northern and southern boundaries of the Bozdag Horst. North of the Bozdag Horst major faults tend to dip north and south of the Horst they tend to dip south. The Buyuk Menderes graben, the southern boundary of the Bozdag Horst, is bounded by low-angle, large-displacement normal faults on its north side and by several smaller-displacement faults on the south side. One of the largest recent events in western Turkey, the 1899 M6.5 Buyuk Menderes event, occurred on the northern fault (Ambraseys, 1988). These observations suggest that the northern fault is the main active fault of the graben, the smaller faults on the southern wall being formed in response to large displacements on this fault. The Gediz graben is the northern boundary of the Bozdag Horst and is almost a mirror image of the Buyuk Menderes graben. The north-dipping fault which defines the southern edge of this graben ruptured last in the 1969, M6.9, Alasehir earthquake. Body-wave modelling of the seismograms of this event has allowed the subsurface fault structure to be inferred (Eyidogan and Jackson, 1985). The 1969 event consisted of 4



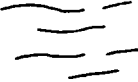



-  Strike lines of Cimmeride & Alpidic structures of the Sakarya Continent
-  Trend of mineral stretching & fold axis lineations & strike lines of prominent schistosities in the core of the Menderes Massif
-  Schist & marble envelope of the Menderes Massif
-  Karakaya Complex

Figure 1.8 The Gediz and Buyuk Menderes grabens of SW Turkey (from Sengor *et al.*, 1985).

discrete subevents. The first two subevents caused the surface rupture and occurred on a fault dipping at 32° to the NNE and at depths of 6 km. The third and fourth subevents were at depths of 6 to 10 km. These later events were best modelled as motion on subhorizontal faults. It therefore appears that the 1969 Alasehir earthquake occurred on a fault which was planar to depths of at least 6 km and which then flattened at a maximum depth of 10 km (Eyidogan and Jackson, 1985). Bouguer gravity and magnetic data from the Gediz graben indicate that the basement of the graben is at 1.2 to 1.5 km depth.

The grabens become narrower towards the east suggesting the greatest stretching is towards the west. There is discontinuous surface faulting along the entire length of the grabens. Surface breaks are 10 to 20 km long suggesting the grabens rupture in sections in earthquakes of magnitude 6 to 7 (Paton, 1992). Sengor (1985) suggested the Buyuk Menderes and Gediz faults may be listric in nature and underlie most of SW Turkey. Evidence for listricity comes from geological data and body-wave modelling of the teleseisms of the 1969 earthquake. Some of the normal faults in Pliocene and Pleistocene sediments have dips of 20° (Paton, 1992). The wide distribution of aftershocks following large earthquakes on the graben faults are also cited as evidence. Based on seismic analysis of the 1969 Alasehir earthquake Eyidogan and Jackson (1985) concluded that during the earthquake the brittle upper crust ruptured through its entire thickness, which in SW Turkey is thought to be 6 to 15 km based on the maximum depth of seismicity.

1.4.4.2 Extension rates in western Turkey

Eyidogan (1988) determined the rates of crustal deformation within the Bozdag Horst region from seismic moments of earthquakes to be 10-13.5 mm/yr in the north-south direction and 3.6 mm/yr in the east-west direction. The extension rate measured using GPS is 11.7 ± 5 mm/yr in the north-south direction (Oral, 1995a). The geological estimate of total extension across the Gediz graben is 6 km (Paton, 1992). If the graben began to form at about 12 Ma then the extension rate across the graben is 0.5 mm/yr or 1 mm/yr total across both the Gediz and Buyuk Menderes grabens.

The amount of extension in a region can be estimated by assuming a simple domino-type model (Jackson and McKenzie, 1983). The crustal extension β is given by:

$$\beta = \frac{\sin \theta_o}{\sin \theta_f}$$

where θ_o and θ_f are the initial and final dips of the faults. The extension rate determined from seismic moment tensors in the Aegean area by Jackson and McKenzie (1988) yield a β of 1.84, *i.e.*, extension of the crust is about 84%. A much lower β value is found for southwest Turkey. From the tilting of sediments along the Buyuk Menderes and Gediz

grabens Paton (1992) determined that the initial dips of the faults were greater than 50° while the active faults today dip between 35° and 50° yielding a β of 1.1 to 1.3.

1.5 SUMMARY

The brittle crust in Iceland is about 10 km thick under the rift zones and the entire island is underlain by a shallow, anomalous mantle. The crust is hot, the temperature gradient being about 100°C/km. Estimates of the viscosity of the lower layers of the Icelandic crust derived from GPS and tiltmeter measurements range from 0.8-1.1x10¹⁸ Pa s. Crustal extension in Iceland is accommodated through discrete rifting events that involve the injection of near-vertical dykes along the rift zones, perpendicular to the direction of extension. Modelling of post-rifting GPS measurements in north Iceland predicts that a rifting event, which creates several metres of horizontal extension near a new dyke, is followed by a rapid redistribution of stress in the crust. Horizontal extension is predicted to cease relatively quickly with respect to the recurrence interval of rifting events. Continuous spreading motion does not appear to occur within 250 km of the spreading plate boundary. The extensional process in this oceanic crust is therefore highly episodic. The Hengill triple junction lies at the southern tip of a dying rift zone and at the western end the SISZ.

The crust in the Basin and Range province is thin, hot and uplifted. The seismogenic layer is 10 to 15 km thick and the Moho lies between 25 and 35 km depth. Heat flow is high in the province, up to twice that in other continental regions, and the Curie isotherm lies at 10 to 30 km depth. Extension in the province is accommodated primarily through normal faulting earthquakes. This century seismicity has been concentrated in the west of the province and many of the events have exhibited significant components of right-lateral slip. Extension in the province may be as much as 100%. The 1954 Rainbow Mountain-Fairview Peak-Dixie Valley earthquake sequence created 120 km of surface rupture on high-angle planar faults. The sequence was the latest burst of seismicity to have occurred within the Central Nevada Seismic Zone in a 100-year period of increased activity.

SW Turkey is part of a broad, back-arc extensional province which includes the Aegean Sea and south Greece. Seismic reflection and gravity data suggest the Moho lies at about 30 km in western Turkey. The seismogenic layer appears to be 10-15 km thick. As in the Basin and Range province, extension is accommodated through normal faulting. The amount of extension within the Aegean area ranges from 100% in the central Aegean to 10 to 30% in western Turkey. The focal mechanisms of well-recorded earthquakes in

western Turkey indicate pure normal slip. Extension rates within SW Turkey, measured using GPS, suggest aseismic north-south extension at 11.7 mm/yr over a region 100 km broad. Similar rates have been estimated from seismicity this century.

CHAPTER 2

PRINCIPLES OF GPS SURVEYING AND DATA PROCESSING

2.1 INTRODUCTION

The Global Positioning System (GPS) constellation has been developed and installed by NASA and the US Department of Defense to provide a network of radio beacons in space for highly precise navigation. It is an important system for monitoring crustal deformation because it has the potential to give the positions of points in 3-dimensional space at low cost and to a very high precision over regional distances. Surveying using GPS offers considerable advantages and few disadvantages over conventional terrestrial surveying. It is a global, all-weather, continuous positioning tool which is free to an unlimited number of users because of its passive nature. Line of sight between points is not required and therefore network design need not be constrained by topography. The accuracies for regional networks are superior to those achieved using terrestrial methods. Complex data post-processing is necessary though. Under field conditions submillimetre repeatabilities in the horizontal and 1-2 cm repeatability in the vertical components can be expected. Such a high accuracy allows monitoring of deformation in areas such as Iceland, Turkey and the western United States where GPS is being used to estimate seismic risk along active fault or volcanic zones (Lisowski *et al.*, 1991; Heki *et al.*, 1993).

The GPS system consists of three segments: the space, control and user segments. Signals are transmitted by space vehicles (SVS), the space segment. The orbits, health and broadcast signals of the SVS are monitored and maintained by the control segment on Earth. Signals broadcast by the SVS are received at a GPS antenna, which may be positioned over a ground control point, and are recorded by a GPS receiver. This comprises the ground segment. Measurements of the time of arrival of coded signals transmitted by the SVS, combined with knowledge of the SV positions, enables the distances to the SVS to be determined. If measurements are made of signals from several SVS simultaneously, the receiver point position may be calculated. The history and

development of GPS hardware, processing techniques and descriptions of the geodetic applications of GPS are documented by many authors (*e.g.* Blewitt, 1993; Dixon, 1991; Hager *et al.*, 1991; Bilham, 1991; Larson and Agnew, 1991; Rothacher *et al.*, 1990; Beutler *et al.*, 1987a; Blewitt, 1989; Dong and Bock, 1989).

2.2 THE GLOBAL POSITIONING SYSTEM

2.2.1 The space segment.

The space segment consists of approximately 21 SVS distributed in 6 orbital planes around the Earth oriented at 55° to each other. They follow elliptical paths around the Earth at a height of about 26,000 km and have orbital periods of approximately 12 hours. Each SV has one or more atomic clocks for accurate timing. The high altitudes of the SVS allow several to be viewed simultaneously at any time from any point on the Earth's surface. The SVS transmit messages on two frequencies, L1 (1575.42 MHz) and L2 (1227.6 MHz) to enable the ionospheric delay to be calculated. Two codes, the Precise (P) and Coarse-Acquisition (CA) codes, and SV information, are broadcast to Earth on the L1 and L2 frequencies. The SV information contains details about the ephemerides, age of the data, clock stability and health of all the SVS. The ephemerides describe hour-long segments of the SV orbit in terms of Keplerian parameters.

2.2.2 The control segment

To use GPS as a point positioning system the SV orbits and drift of the SV clocks from GPS time must be known to the user. Any error in the position of the SV or timing of the signal transmitted will propagate into the position of the point. The control segment consists of several stations around the world that continuously monitor SV orbits and clock drift. The data are sent to the Master Control Station in Colorado, USA. This station determines the corrections which must be applied to the SV clocks. It also models and forward extrapolates the SV orbits over several days. The modelled orbits, called the broadcast ephemerides, predict where the SV will be for hourly segments expressed as Keplerian elements. This information is broadcast up to the SVS for transmission to the user.

2.2.3 The user segment

The GPS receiving equipment is the ground segment. Most receivers have quartz crystal clocks and the ability to replicate the codes transmitted from the SVS. Geodetic field measurements are conducted by erecting surveying tripods over ground control points. A GPS receiver antenna is mounted on each tripod and several hours of data recorded at each site. To find the position of one point with respect to another, receivers must be

deployed simultaneously and record data from common SVS. The data are subsequently processed interferometrically and, knowing the absolute position of one point, the three-dimensional vectors connecting this point to the others may be calculated.

GPS survey points is typically a brass bolt cemented into bedrock with central dots over which the antenna is positioned. If the antenna is to be mounted on a tripod a plumb is used to centre and level the tripod. The height of the antenna above the point must be measured since GPS data processing yields the position of the antenna phase centre which must be corrected to obtain the position of the ground marker. Receivers can only record the signals from SVS which are above the horizon. The process of picking up the signal takes up to a few minutes. Modern receivers can record data from up to 12 SVS simultaneously.

2.3 GPS DATA TYPES

2.3.1 Pseudorange code data

Each SV transmits two known pseudo-random noise (PRN) codes, the Precision code (the P code) and the Coarse Acquisition code (the C/A code). These are binary codes that resemble random sequences of +1's and -1's. Both L1 and L2 are modulated with the P code which has a bit rate of 10.23MHz. L1 only, is modulated with the C/A code which has a bit rate of 1.023 MHz. The whole P code is divided into 38 different, week-long segments. Each SV is assigned a one week segment that will uniquely identify it. This allows several SVS to be tracked simultaneously without confusion. Because of its higher bit rate and thus shorter "wavelength", the P code enables higher precision point location and is the code required for surveying. The C/A code is used for locking on to SVS and for coarse positioning. The codes modulate the carriers by shifting the phase by 180° if the binary code is -1 or by leaving it unchanged if the code value is +1 (Figure 2.1).

Geodetic receivers record pseudorange data, which are calculated distances to the SVS. The receiver generates replicas of the incoming PRN codes. By cross-correlating the replica with the signal received, the receiver can measure the arrival time of each bit of the incoming code. From the time broadcast by the SV, the receiver can calculate the travel time of the signal. The arrival time of the code can be measured to an accuracy of 1% of a bit. Multiplying by the velocity of light yields the distance, or range, to the SV.

When 4 SVS have been detected, 4 receiver-SV distances may be determined and with information on the SV positions from the satellite message the receiver can calculate the

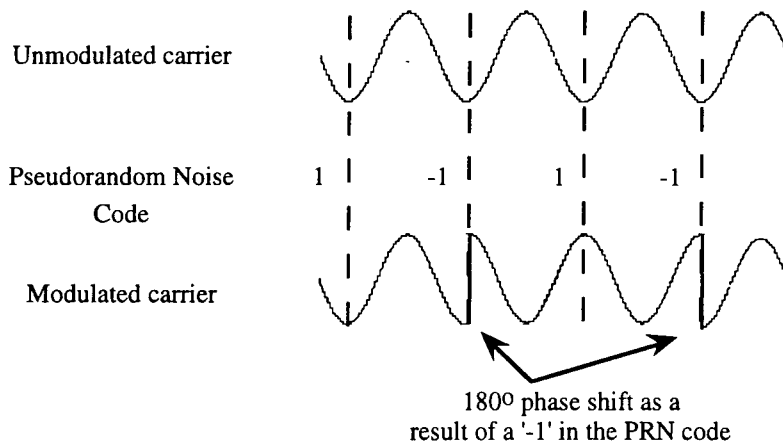


Figure 2.1 Modulation of the carrier by PRN codes.

four unknowns which are the position of the antenna phase centre and its own clock offset. The receiver resets its clock accordingly. These distances are called pseudoranges because they are inaccurate due to the substantial receiver clock errors that remain. The pseudorange r between SV p and receiver k can be written as:

$$r = c \cdot d\tau = \rho_k^p + c(dt - dT) + d_{ion} + d_{trop} \quad (2.1)$$

where ρ_k^p is the true distance between the SV and receiver, dt is the SV clock error, dT is the receiver clock error and the delays due to the ionosphere and troposphere are d_{ion} and d_{trop} (Figure 2.2).

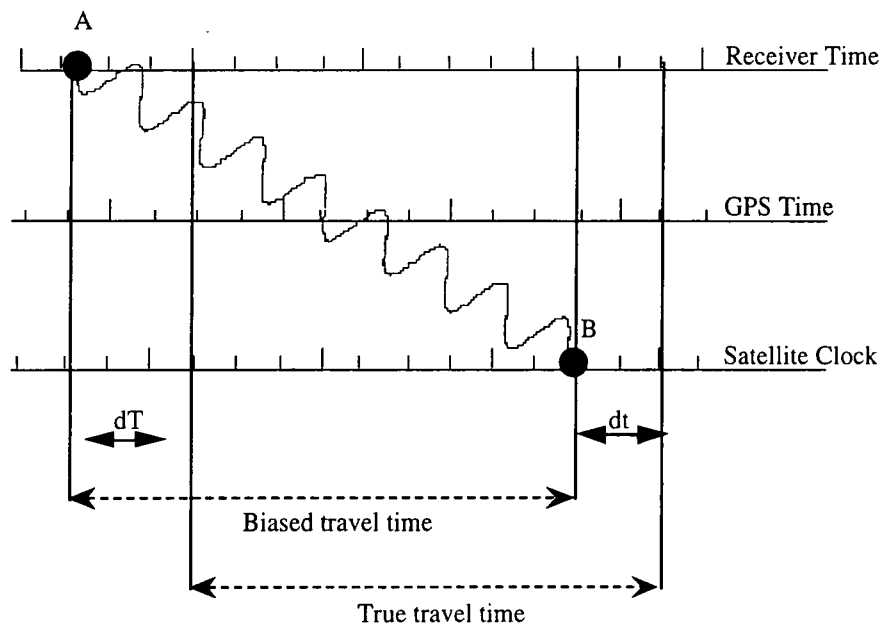


Figure 2.2 A signal transmitted at time A in the SV clock time frame is received at time B in the receiver clock time frame (adapted from Wells *et al.* (1987)). The offset between the SV clock and GPS time is dt , and the offset of the receiver clock is dT . The true travel time is $(B-A+dt-dT)$.

2.3.2 Carrier phase data

In addition to replicating the codes, geodetic receivers also generate replicas of the carriers. The carrier phase measurement is the difference in phase between the incoming carrier signal and that generated by the receiver. The phase shift required initially to align the two signals is always a fraction of a full wavelength. The measured phase $\varphi_{measured}$ can then be written as:

$$\varphi_{measured} = Fr(\varphi_o) + Int(t_o, t)$$

where $Fr(\varphi_o)$ is the required phase shift and $Int(t_o, t)$ is the number of wavelengths that pass from time t_o , when the receiver begins recording the signal, to time t . This is a biased range measurement because it does not contain the number of full cycles N_o between the SV and the receiver at time t_o . This unknown is called the cycle ambiguity. There is only one ambiguity per SV-receiver pair unless the receiver loses count on the integer number of incoming wavelengths. In that case a step discontinuity occurs in the stream of phase measurements called a cycle slip.

The carrier phase measurement between SV p , and receiver k , φ_k^p , is expressed as:

$$\varphi_k^p = -\frac{f}{c}\rho_k^p - f(dt - dT) - \frac{f}{c}(d_{trop} - d_{ion}) + N_k^p \quad (2.2)$$

where ρ_k^p is the true distance between SV and receiver, $f(dt - dT)$ represents the clock errors and, N_k^p is the cycle ambiguity. The distance, r , from the SV to receiver at time t is found by multiplying the carrier phase measurement by the wavelength, $\lambda = c/f$,

$$r = -\lambda\varphi_k^p = \rho_k^p + c(dt - dT) + (d_{trop} - d_{ion}) + \lambda N_k^p \quad (2.3)$$

The ionospheric and tropospheric effects are contained in $(d_{trop} - d_{ion})$. The only differences between the equations for the pseudorange measurement and the carrier phase measurement are the sign of the ionospheric effect, d_{ion} (see section 2.4.2) and the integer ambiguity term.

2.4 GPS DATA PROCESSING THEORY

2.4.1 Relative and absolute point positioning

Pseudoranges are used for absolute point positioning. An absolute point position is found by using four pseudoranges to solve for the x , y , and z co-ordinates of the point and the receiver clock offset. The main GPS geodetic surveying technique used is relative point positioning. At least two receivers are operated simultaneously at different points for a

measurement session that may last several hours. The vector between the two antenna phase centres is then obtained by post-processing the suite of code and phase range measurements recorded. Errors that degrade the absolute positions obtainable may be made to largely cancel out if the data are appropriately combined, giving 3 to 4 orders of magnitude greater accuracy for relative positioning than for single point positioning. Phase measurements are necessary for relative point positioning though pseudorange facilitate data processing.

The receiver can correlate the phase to within 1% of the wavelength. For the L1 and L2 frequencies this corresponds to $\sim 10^{-11}$ s. When multiplied by the speed of light the error introduced is approximately 2 mm. An equivalent calculation for the code pseudorange would give an accuracy of 30 cm for the P-code and 3 m for the C/A code. The accuracy obtained with the pseudorange measurement is 10-20 m if the P code is used and less if the C/A code is used.

2.4.2 Modelling the ionospheric effect

The ionosphere is an electron cloud which surrounds the Earth between heights of 100 and 1000 km. The GPS signals are electromagnetic waves and are refracted by the ionosphere. This causes a time delay, called the ionospheric time delay, which must be corrected for to obtain the true distance between the SV and receiver. The ionospheric delay, in metres, can be expressed as:

$$d_{ion} = \pm \frac{aN_T}{f^2} \quad (2.4)$$

where a is a constant, N_T represents the total electron content between the SV and receiver and f is the frequency of the carrier signal (Wells *et al.*, 1987; Rocken, 1988). The delay is positive for pseudorange measurements and negative for carrier phase measurements, a result of the dependence of the delay on the refractive index of the signals. The change in path length due to the ionospheric effect is $d_{ion} = \int (n - 1) ds$ where n is the refraction index and the integration is done along the path. The GPS code signals are dependent on the group refractive index which is proportional to $+1/f^2$ while the carrier phase measurements are dependent on the phase refractive index which is proportional to $-1/f^2$ (Wells *et al.*, 1987). Hence, the ionospheric group delay of the GPS code is positive while the ionospheric phase delay of the carrier is positive. The electron content varies from about 10^{16} to 10^{18} e/m³ and the ionospheric delay thus varies from about 15 to 150 m of range.

Any difference between the L1 and L2 phase measurements is a result of ionospheric delay and is dependent on the frequency. To difference the two measurements they must be expressed in the same units, in this case units of L1 cycles. The signal phase is defined as $\varphi = tf$ where t is the time and f is the frequency. Hence the L2 phase measurement, φ_{L2} , may be converted to units of L1 cycles, φ_{L1} , through:

$$\begin{aligned}\varphi_{L2} &= tf_2 \\ &= tf_2 \frac{f_1}{f_1} = \varphi_{L1} \frac{f_2}{f_1}\end{aligned}$$

where f_1 is the frequency of L1 and f_2 the frequency of L2. The difference in the two phase measurements in units of L1 cycles is:

$$\varphi_{ion} = \varphi_{L1} - \frac{f_1}{f_2} \varphi_{L2} \quad (2.5)$$

Substituting equations 2.2 and 2.4 for the φ_{L1} and φ_{L2} measurements this becomes:

$$\varphi_{ion} = N_{L1} - \frac{f_1}{f_2} N_{L2} - \frac{aN_T}{f_1} \left(\frac{f_2^2 - f_1^2}{f_2^2} \right) \quad (2.6)$$

If the difference between the integer ambiguities are known the parameter a can be determined and the ionospheric delay corrected for.

2.4.3 Single-, double- and triple-differenced data

Relative point coordinates are estimated by forming linear combinations of single and double differences of the carrier phase measurement between the SVS and receivers. Differenced data are used almost universally in GPS post processing since in this way many of the most serious errors cancel out.

Single Differenced Data. Single-differenced data are formed by differencing the carrier phase measurements recorded by two receivers which have simultaneously tracked the same SV. If two receivers, k and m , track SV p the single-difference equation is:

$$\Delta_{km}^p = \varphi_k^p(t) - \varphi_m^p(t) \quad (2.7)$$

where $\varphi_k^p(t)$ represents the phase measurement at receiver k at time t and $\varphi_m^p(t)$ the measurement at receiver m . Δ denotes between-receiver differences. Combining equations 2.2 and 2.7 the single-difference equation becomes:

$$\Delta_{km}^p = -\frac{f}{c}[\rho_k^p(t) - \rho_m^p(t)] - f[dt_p - dT_k - dt_p + dT_m] + N_{km}^p + \frac{f}{c}(d_{trop,km}^p - d_{ion,km}^p) \quad (2.8)$$

where $N_{km}^p = N_k^p - N_m^p$. The difference in the receiver clock offsets is $dT_k - dT_m$, and the difference in the ionospheric delay by $d_{ion,km}^p$. Equation 2.8 can be simplified to:

$$\Delta_{km}^p = -\frac{f}{c}\Delta\rho - f\Delta dT + \Delta N + \Delta d_{ion} - \Delta d_{trop} \quad (2.9)$$

Any error in the SV clock cancels by between receiver-differencing of the carrier phase measurements as the SV clock error, dt_p , is common to both observations. Orbital errors are also greatly reduced as these tend to cancel

Double Differenced Data. Double differenced data are differenced single-difference data and can be calculated when two receivers, k and m , observe two SVS, p and q , simultaneously (Figure 2.3). The double difference equation is:

$$\begin{aligned} \nabla\Delta_{km}^{pq} &= \Delta_{km}^p - \Delta_{km}^q \\ &= (\varphi_k^p(t) - \varphi_m^p(t)) - (\varphi_k^q(t) - \varphi_m^q(t)) \end{aligned} \quad (2.10)$$

The symbol ∇ indicates between-SV differences. The error due to the clock offsets of the receivers dT_k and dT_m cancels, and combining equations 2.3 and 2.10, the double difference observation equation becomes:

$$\nabla\Delta_{km}^{pq} = -\frac{f}{c}\nabla\Delta\rho + \nabla\Delta N + \nabla\Delta d_{ion} - \nabla\Delta d_{trop} \quad (2.11)$$

Triple Differenced Data. Triple differenced data are calculated by differencing two double-differenced data between two epochs:

$$\partial\nabla\Delta_{km}^{pq} = (\Delta_{km}^p - \Delta_{km}^q)_{t_1} - (\Delta_{km}^p - \Delta_{km}^q)_{t_2} \quad (2.12)$$

where t_2 and t_1 indicate different epochs and ∂ is used to indicate between-epoch differences. The triple difference observation equation is:

$$\partial\nabla\Delta_{km}^{pq} = -\frac{1}{\lambda}\partial\nabla\Delta\rho + \partial\nabla\Delta d_{ion} - \partial\nabla\Delta d_{trop} \quad (2.13)$$

The integer ambiguity term $\nabla\Delta N$ cancels in triple differenced data since, in the absence of cycle slips, the integer ambiguities remain constant with time.

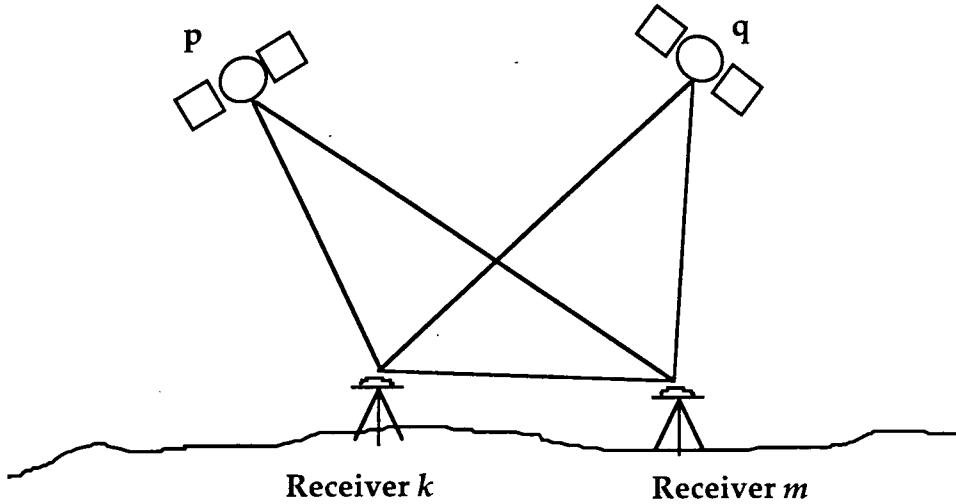


Figure 2.3 Two receivers observe two SVS simultaneously. The double difference data are calculated by differencing the two single difference data.

2.4.4 Linear combinations of differenced observations

Using linear combinations of the single and double differences of the carrier phase data the L1 and L2 integer ambiguities, ionospheric effect, and final coordinates can be determined. The combinations used in the Bernese V3.2 software are here called the L3, L4 and L5 (widelane) combinations.

The L3 Linear Combination. The L3 combination is known as the ionosphere-free combination as it cancels out the effect of the ionosphere (Rothacher *et al.*, 1990). It is defined in units of metres as:

$$L3 = \left(\frac{f_1^2}{f_1^2 - f_2^2} \right) L1 - \left(\frac{f_2^2}{f_1^2 - f_2^2} \right) L2 \quad (2.14)$$

Substituting equation 2.11 into equation 2.14, the L3 double difference combination is calculated, in metres as:

$$\nabla \Delta L3 = \left(\frac{f_1^2}{f_1^2 - f_2^2} \right) (\nabla \Delta \rho + \lambda_1 \nabla \Delta N_1) - \left(\frac{f_2^2}{f_1^2 - f_2^2} \right) (\nabla \Delta \rho + \lambda_2 \nabla \Delta N_2) \quad (2.15)$$

The ionospheric term in equation 2.11 cancels since $d_{ion} = \frac{aN_T}{f^2}$, and

$$\left(\frac{f_1^2}{f_1^2 - f_2^2} \right) d_{ion,1} = \left(\frac{f_2^2}{f_1^2 - f_2^2} \right) d_{ion,2} \quad (2.16)$$

The L4 Linear Combination. The L4 linear combination is equivalent to the difference between the L1 and L2 double differenced phase measurements in units of length:

$$L4 = L1 - \frac{f_1}{f_2} L2 \quad (2.17)$$

Substituting equation 2.11 this becomes:

$$\nabla \Delta_{km}^{pq} L4 = \lambda_1 \nabla \Delta N_1 - \lambda_2 \nabla \Delta N_2 - \nabla \Delta d_{ion,1} + \nabla \Delta d_{ion,2} \quad (2.18)$$

The true range factor cancels since it is the same for both L1 and L2 measurements. L4 is known as the “geometry free combination” as it is independent of the receiver and SV positions. It is used to derive ionospheric corrections.

The L5 Linear Combination. The L5 combination is a linear combination of the L1 and L2 double difference observations in units of numbers of cycles:

$$L5 = \frac{f_1}{f_5} L1 - \frac{f_2}{f_5} L2 \quad (2.19)$$

where

$$L5 = \frac{\rho_5 f_5}{c} = \frac{\rho_2 f_1}{c} - \frac{\rho_2 f_2}{c}$$

Substituting equation 2.11 into equation 2.19 we get:

$$\begin{aligned} \nabla \Delta L5 &= \frac{f_1}{f_5} (\nabla \Delta \rho + \nabla \Delta d_{ion,1} + \lambda_1 \nabla \Delta N_1) \\ &\quad - \frac{f_2}{f_5} (\nabla \Delta \rho + \nabla \Delta d_{ion,2} + \lambda_2 \nabla \Delta N_2) \end{aligned} \quad (2.20)$$

The ambiguity terms in equation 2.20 can be expressed as:

$$\frac{f_1}{f_5} \lambda_1 \nabla \Delta N_1 - \frac{f_2}{f_5} \lambda_2 \nabla \Delta N_2 = \lambda_5 (\nabla \Delta N_1 - \nabla \Delta N_2) \approx 86.2 \nabla \Delta N_5$$

where $\nabla \Delta N_5$ is known as the L5 ambiguity and the L5 combination becomes:

$$\nabla \Delta L5 = \frac{f_1}{f_5} (\nabla \Delta \rho + \nabla \Delta d_{ion,1}) - \frac{f_2}{f_5} (\nabla \Delta \rho + \nabla \Delta d_{ion,2}) + 86.2 \nabla \Delta N_5 \quad (2.21)$$

The L5 linear combination is a valuable aid to data processing as $\nabla \Delta N_5$, the difference between the L1 and L2 ambiguities, is easily resolved on account of the long apparent wavelength.

2.5 GPS DATA PROCESSING USING THE BERNESE V3.2 SOFTWARE

2.5.1 Introduction

The Bernese V3.2 software (Rothacher *et al.*, 1990) is a widely used program for precise geodetic GPS data processing. It is installed at the University of Durham on a Sun4 computer using a menu-style interface written by K. Heki. The processing procedure involves many steps but can be divided into 5 parts (Figure 2.4):

- data transfer
- orbit modelling
- outlier removal, cycle slip detection and clock corrections
- ionosphere modelling
- parameter estimation.

The data recorded by the receiver are converted to the Bernese V3.2 format. The SV orbits are then determined as continuous functions in time. Cycle slips must be removed from carrier phase measurements and the ionospheric effect may be modelled if required. GPSEST, the parameter estimation program, is used to estimate the station co-ordinates and other parameters if required, *e.g.*, improved SV orbit model.

2.5.2 Data transfer

Different GPS receivers record data in different formats. The Bernese software includes many programs which convert receiver data to Bernese format, *e.g.*, RXNBV3 and RXNOBS. The navigation messages are converted to broadcast ephemeris format by program RXNBV3. The pseudorange and carrier phase data are extracted by program RXOBS and written into Bernese prange (pseudorange) and phase format respectively (Figure 2.5a and b).

2.5.3 Orbit modelling

The broadcast ephemerides, which give the orbits of the SVS in hourly segments, may be used to derive “standard orbits”. Standard orbits describe the position of the SVS as a continuous function of time for periods up to a few days long. Broadcast ephemeris files can be obtained from the International GPS Service (IGS) if the navigation messages recorded in the field are of poor quality. Precise orbits are also available from IGS. Precise orbits are orbits which have been computed using phase data from the SVS, recorded at permanent GPS and VLBI stations of known locations. These are more accurate than the broadcast ephemeris orbits as they are formed post-priori using observations rather than by forward extrapolation.

Three programs, BRDTST, BRDTAB and DEFSTD are used as follows. Outlier detection in the navigation and SV clock messages is performed BRDTST. Outliers

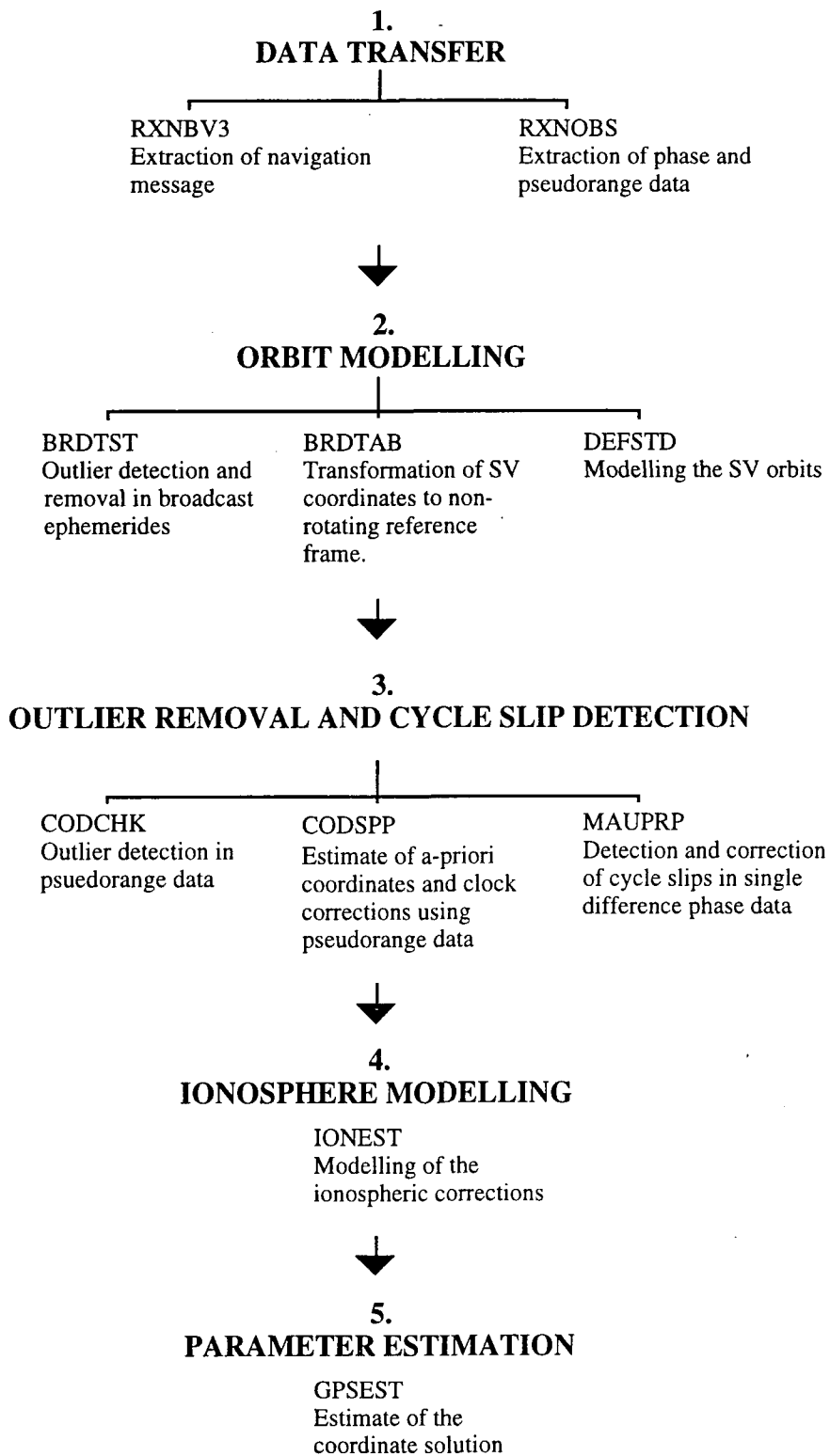


Figure 2.4 A flowchart of GPS processing steps using the Bernese V3.2 software.

obs	time	f #s	code (m)	ffs sa	code (m)	ffs sa	date	fract.(s)	clock (s)
1	6:30:00	2	27903589.546	0 14	27897024.686	0 12	91-08-22	0.0170	-0.017937641
2	6:30:30	2	27918376.511	0 14	27918046.440	0 12	91-08-22	0.0170	-0.017949941
3	6:31:00	2	29847012.443	0 14	25910883.168	0 20	91-08-22	0.0170	-0.017962243
4	6:31:30	2	29837229.920	0 14	25907604.638	0 20	91-08-22	0.0170	-0.017974551
5	6:32:00	2	29827542.729	0 14	25904431.927	0 20	91-08-22	0.0170	-0.017986850
6	6:32:30	2	29817928.671	0 14	25901359.362	0 20	91-08-22	0.0170	-0.017999149
7	6:33:00	2	29808417.468	0 14	25898388.414	0 20	91-08-22	0.0180	-0.018011452
8	6:33:30	2	29798957.513	0 14	25895527.503	0 20	91-08-22	0.0180	-0.018023746
9	6:34:00	2	29789605.191	0 14	25892769.112	0 20	91-08-22	0.0180	-0.018036035

Figure 2.5a Example of a prange data file. The first field is the observation number and the second is time. The third column is the number of SVS observed and the following six correspond to the pseudorange (code), the noise (ffs) and the SV number (sa) for two satellites. Each record ends with the date, fraction of second and the clock time. In this example only the L1 signal is recorded, *i.e.*, there is just one line of data for each time (epoch).

obs	time	f #s	phase (m)	ffs sa	phase (m)	ffs sa	date	fract.(s)	clock (s)
1	23:00:00	2	114767.255	4 17	2638963.978	9 16	91-08-23	0.006	-0.00696966
			114766.948	6 17	2638959.807	9 16			
2	23:00:30	2	130977.678	3 17	2641781.788	9 16	91-08-23	0.006	-0.006982907
			130977.322	6 17	2641777.608	9 16			
3	23:01:00	2	147139.768	3 17	2644505.947	9 16	91-08-23	0.006	-0.00699616
			147139.396	6 17	2644501.762	9 16			
4	23:02:00	2	179311.638	4 17	2649666.910	9 16	91-08-23	0.007	-0.007022659
			179311.247	6 17	2649662.710	9 16			
5	23:02:30	2	195322.160	5 17	1834159.432	6 19	91-08-23	0.007	-0.00703592
			195321.747	6 17	1834156.388	7 19			
6	23:03:00	2	211279.895	5 17	1830252.395	6 19	91-08-23	0.007	-0.00704917
			211279.453	5 17	2654443.027	9 16			

Figure 2.5b Example of a phase data file. The fields are as for Figure 2.5a except the measurement is the carrier phase. There are two lines of observation data for each epoch, the L1 and L2 observations.

found are flagged and not used in further processing. Program BRDTAB is then used to transform the SV positions into a non-rotating coordinate frame so that orbits can be modelled using the equations of motion. Program DEFSTD models a continuous orbit using this information, called the standard orbit. The program solves for the six

unknowns which describe the SV orbit, the inclination of the SV at a certain time, the semi-major axis of the orbit, the eccentricity, the inclination of the orbital plane with the equator, the perigee and the right ascension of the ascending node. The ascending node is the intersection of the orbital plane and the equatorial plane as the SV passes from the southern hemisphere into the northern hemisphere. The program models the orbit, applying a correction for the non-sphericity of the Earth's gravitational potential and estimates the effect of solar radiation. DEFSTD extrapolates to produce an orbit which spans a time period specified by the user. The orbit can be improved later by program GPSEST if the station coordinates are well determined.

2.5.4 Outlier removal, cycle-slip detection and clock corrections

The pseudorange data are checked for outliers by program CODCHK using the assumption that the pseudorange varies smoothly with time. Outliers found are flagged and not used by subsequent programs. Cycle slips in the phase data are found and corrected in the single difference phase data by program MAUPRP. The program uses the triple differenced data to identify discontinuities in the double differenced data and time intervals in which no slips occur are isolated. The program then finds the best integer values for the L1 and L2 slips where discontinuities do occur. The triple differenced data are free from SV and receiver clock errors and initial integer ambiguities. Receiver clock corrections and a-priori point coordinates are calculated using program CODSPP. The receiver clock correction can be modelled either as a polynomial, the degree of which is specified by the user, or as one clock offset per epoch. The clock corrections are then written to the phase file. This program uses single point positioning to determine a-priori point coordinates. Coordinates determined in this way are accurate to a few 10s of metres which is sufficient for subsequent processing steps.

2.5.5 Ionosphere modelling

Program IONEST uses the difference between the L1 and L2 phase measurements (equation 2.6), *i.e.*, the L4 linear combination, to determine an ionospheric model for a single session (Beutler *et al.*, 1987b). The ionospheric component N_T varies both spatially and numerically throughout one recording session so its effect must be modelled as a function of time, possibly with a different model for different stations. The integer ambiguities are constant throughout the session and are estimated by IONEST. The parameter N_T , the total electron content (Equation 2.4), is the only unknown and is modelled as a two dimensional polynomial the degree and order of which are specified by the user. IONEST assumes a single layer model where the ionosphere is an infinitesimally thin shell around the Earth.

2.5.6 Parameter estimation

Program GPSEST uses an iterative weighted least squares technique to estimate various parameters including the final station coordinates, improved orbits and ionosphere models. Linear combinations of the double differences are used to reduce the SV and receiver clock errors. An ionospheric model created by IONEST may be used. GPSEST can estimate standard SV orbits, solar radiation coefficients, coordinates and tropospheric parameters. Several program runs are usually required, progressively determining parameters such as ambiguities and unresolved cycle-slips before the final coordinates are obtained. The goal is to resolve all integer ambiguities and to solve for the point coordinates using equation 2.3. The process usually comprises four stages;

1. The ionosphere-free ambiguity-free solution. This solution provides accurate, preliminary coordinates of the stations, resolves the ambiguities to real (floating point) numbers and enables any remaining cycle slips to be detected manually by visually inspecting the postfit residuals for discontinuities. The L3 linear combination is used, thus the ionospheric effect is removed and no ionospheric model is required. The coordinates of one point are held fixed and the positions of the other stations found with respect to it. New cycle slips are detected by visually inspecting the L3 residual files, and manually flagged in the single difference files. The ionosphere-free ambiguity-free solution is calculated repeatedly, until inspection of the residuals shows the data are free of slips. Program GPSEST calculates new coordinates each time along with the covariance matrix of standard errors for all the unknowns.

2. Determining the L5 integer ambiguities. The second processing step determines the L5 integer ambiguities using equation 2.21. The coordinates calculated in the ionosphere-free ambiguity-free solution are used as *a-priori* and held fixed along with the ionosphere model and the standard orbit. The L5 ambiguities are then the only unknowns. L5 has a “wavelength” of 86 cm and the ambiguities are thus the easiest to resolve correctly. If they are known then the number of ambiguities to be resolved in later program runs is halved since the L5 ambiguity is the difference between the L1 and L2 ambiguities. Cycle slip editing is done at this stage too, again by inspecting the residual files. Slips which occurred in L1 and L2 simultaneously and are of equal size are undetectable in the previous stage but are visible in the L5 residuals.

3. Determining the L1 and L2 integer ambiguities. The ambiguities in the individual carriers are sought using the L5 ambiguities. The station coordinates and SV orbits are held fixed and the ionosphere model calculated using IONEST is used. The L4 combination is formed and the L5 ambiguities used to solve for the L1 ambiguities, *i.e.*, equation 2.18 becomes:

$$\nabla\Delta L4 = (\lambda_1 - \lambda_2)\nabla\Delta N_1 - \lambda_2\nabla\Delta N_5 - \nabla\Delta d_{ion,1} + \nabla\Delta d_{trop,1} \quad (2.22)$$

The only unknown is the L1 ambiguity which can now be estimated.

4. *The ionosphere-free ambiguity-fixed solution.* In the final GPSEST program run any remaining unsolved L1 and L2 ambiguities are calculated along with the final solution for the station coordinates. The L3 combination is used again. Unlike the ionosphere-free, ambiguity-free run, most of the ambiguities are known and held fixed at this stage.

2.6 NETWORK ADJUSTMENT

In most GPS surveys, each point is measured twice or more, and so multiple results are available for each coordinate. Program GPSEST produces a set of point coordinates along with covariance matrices for each recording session. The formal errors, or standard deviations, of the coordinates are the square roots of the diagonal elements of the coordinate covariance matrix. They are a measure of the scatter of the measured phase data throughout one observation session. These errors express the precision of the results. Network adjustment is the process by which all the results are combined to form a single set of point coordinates. Program NETADJ (Heki, 1992) was used in this work. This program calculates a final set of coordinates that minimises the weighted root mean square (WRMS) difference between the individual sessions. It calculates the repeatability (the WRMS) of the results and the normalized root mean square (NRMS) for the network and individual points. The repeatability associated with a point location is the WRMS of the differences between the coordinates from the individual sessions and the network solution and is expressed as:

$$WRMS = \left(\frac{\frac{n}{n-1} \sum_{i=1}^n \frac{(y_i - \langle y \rangle)^2}{\sigma_i^2}}{\sum_{i=1}^n \frac{1}{\sigma_i^2}} \right) \quad (2.23)$$

where n is the number of coordinates, y_i is each individual result, $\langle y \rangle$ is the weighted mean estimate of the coordinate and σ_i is the formal error. The repeatability can, within one survey, give an idea though not a precise evaluation of the accuracy of that survey, *i.e.*, how close the results are to the truth. The NRMS is the ratio of the network repeatability to the formal errors for each point and is expressed as:

$$NRMS = \frac{1}{N-1} \sqrt{\frac{(y_i - \langle y \rangle)^2}{\sigma_i^2}} \quad (2.24)$$

The NRMS expresses the amount by which the formal error underestimates the measurement repeatability. The WRMS is useful both for blunder detection and for assessing the effect of errors that vary from session to session but not during a single session. The formal errors are a conservative estimate of the true error as they do not assess systematic errors in the data, *e.g.*, tripod setup errors. A better estimate of the true error is the scaled formal error (*SFE*):

$$SFE = \sigma_i NRMS \quad (2.26)$$

Program STAAVE scales the formal errors in the individual point determinations using the NRMS of the whole network. In the absence of a more accurate, independent check on the coordinates of the points, *e.g.*, from another geodetic technique, these scaled formal errors, are the best estimates of the accuracy of the results available.

2.7 BIASES AND ERRORS

In GPS terminology, the accuracy of a measurement is how close it is to the truth while the precision is a measure of the scatter of the data (Larson and Agnew, 1991). The error, e , in the measurement of a line of length L using GPS has been found by various workers to be well described by the equation $e^2 = a^2 + b^2L$, where a and b are constants. This reflects a length dependency of the error. In controlled experiments repeatabilities of $17+13 \times 10^{-8}L$ mm, $3.4+1.2 \times 10^{-8}L$ mm and $5.2+2.8 \times 10^{-8}L$ mm, for the north, east and vertical components respectively have been reported (Larson and Agnew, 1991). In field experiments the accuracy of the results is limited by the number of independent measurement sessions at a point. Only with several sessions can random errors such as incorrect tripod setups be reduced by averaging and the true repeatability of the survey found.

The accuracy of GPS results is influenced by the geometric strength of the SV constellation observed, errors in the actual observations, and in modelled errors at the data processing stage. The last, modelled errors, are called *biases* in GPS geodesy and include clock offsets, orbit uncertainties, phase ambiguities and ionospheric and tropospheric delays. Cycle slips, multipath, antenna movement and operational blunders are known as *errors*. Errors map proportionally into baseline lengths and must preferably be completely removed from the data. Biases must be modelled or made to cancel out.

Most biases can be removed by differencing the observed ranges between common receivers and SVS as in relative point positioning, *e.g.*, the receiver and SV clock offset. Table 2.1 summarizes the effect of common errors and biases on the range measurement.

Table 2.1 Summary of errors and biases (Wells, 1987; Hager *et al.*, 1991; Bilham, 1991).

Bias or Error	Typical effect on range measurement	Correction Obtainable
SV and receiver clocks	300, 000 m	<ul style="list-style-type: none"> The error can be eliminated by differencing between receiver and SV observations (Section 2.4.3).
Orbit uncertainty	80 m to 10 m depends on orbit data used.	<ul style="list-style-type: none"> By differencing the carrier phase measurements orbital errors can be reduced to 1 ppm of line length. Reduced by using high quality orbit data.
Ionospheric delay	10 cm to 10s of metres	<ul style="list-style-type: none"> Can be modelled and removed by linearly combining the L1 and L2 measurements (Section 2.4.2). Residual effect is at the centimeter level.
Tropospheric delay	2 - 3 m for atmospheric pressure of 1013 bars	<ul style="list-style-type: none"> Using standard tropospheric models such as the Saastamoinen reduces the effect by 95%.
Carrier phase ambiguity of 1 cycle	19 cm for L1 24 cm for L2	<ul style="list-style-type: none"> Can be estimated as an unknown parameter along with station coordinates (Section 2.5.6). If estimated correctly a precision of 1 to 3 mm is obtainable.
Slip of one cycle in phase data series	19 cm for L1 24 cm for L2	<ul style="list-style-type: none"> May be completely removed using cycle slip editing software.

2.8 SUMMARY

The Global Positioning system consists of 24 SVS which orbit the Earth providing a continuous all-weather positioning tool. The SVS transmit data on two frequencies, L1 and L2, which give information on the SV identity, orbit, health, and the clocks. The SV signals can be detected by a GPS antenna on Earth and recorded by a GPS receiver. The position of the antenna may be found using the pseudo-random noise code which modulates the transmitted signal, or by determining the change in phase of the recorded

signal. The former gives the pseudorange measurement while the latter yields the carrier phase measurement.

The highest degree of accuracy in determining coordinates is achieved through relative point positioning, where the position of one point with respect to another is calculated. Using this method, and appropriately combining the data recorded on the L1 and L2 frequencies, many of the effects which can degrade the accuracy of GPS surveying will tend to cancel out. For example, single, double and triple differencing the L1 and L2 data cancels out SV and receiver clock errors. Linear combinations of the double differenced observations, the L3, L4 and L5, allow the ionospheric effect to be modelled, the initial integer ambiguities associated with the carrier phase measurement to be found, and the final point coordinates to be determined.

Before coordinates can be estimated the data must be post processed. The SV orbits must be modelled, outliers and cycle slips removed and the ionospheric effect calculated. These processes, and the final coordinate estimation, can be accomplished using the Bernese V3.2 software. The final coordinates are estimated through progressively solving for the L5, L2 and L1 integer ambiguities. A weighted least squares algorithm is used to produce the coordinate results. The best solution for a single set of point coordinates, given they have been observed more than once is then found through a network adjustment. Network adjustment combines all the measurements to form a final set of coordinates and calculate the repeatability of the results.

Accuracies obtainable today using GPS surveying are sub-centimeter when common errors and biases such as cycle-slips and the ionospheric effect have been removed or modelled. The high degree of accuracy obtainable in relative point positioning has made it a valuable tool to the scientific community in monitoring crustal deformation.

CHAPTER 3

A FIRST EPOCH GPS SURVEY OF THE HENGILL TRIPLE JUNCTION AND THE EFFECT OF OCEAN TIDES

3.1 INTRODUCTION

The current interaction of the tectonic units that meet at the Hengill triple junction and deformation within the area are not well understood and little data on crustal movements are available. The area therefore provides a prime target for study using GPS geodesy. In 1991 a 23 point, 30 x 25 km GPS geodetic network was established in the Hengill ridge-ridge-transform triple junction by the University of Durham. The project was run by Kathleen Hodgkinson and Dr. G.R. Foulger and the data were processed by Kathleen Hodgkinson. The network was tied to regional points up to 75 km distant to the west and east (Figure 3.1). Over 16 days 28 points were measured at least twice in six- to eight-hour observing sessions. Measurements were made by day and night and one central point was measured each session. The data were processed using the Bernese V3.2 Software.

Ocean tides cause periodic deformation of the Earth's surface due to the redistribution of water on the sea floor. Modelling deformation due to ocean loading has been shown to reduce the errors in VLBI data by a significant amount (Schuh, 1989). Predictions of the effect of ocean loading in Iceland suggest the diurnal variation in the vertical and horizontal components may be several millimetres. In the 1991 Hengill GPS experiment four lines of 60 to 75 km in length were observed for 24 hours. The variation in relative position of these points through out the survey was calculated and compared to the theoretical predictions of the variation.

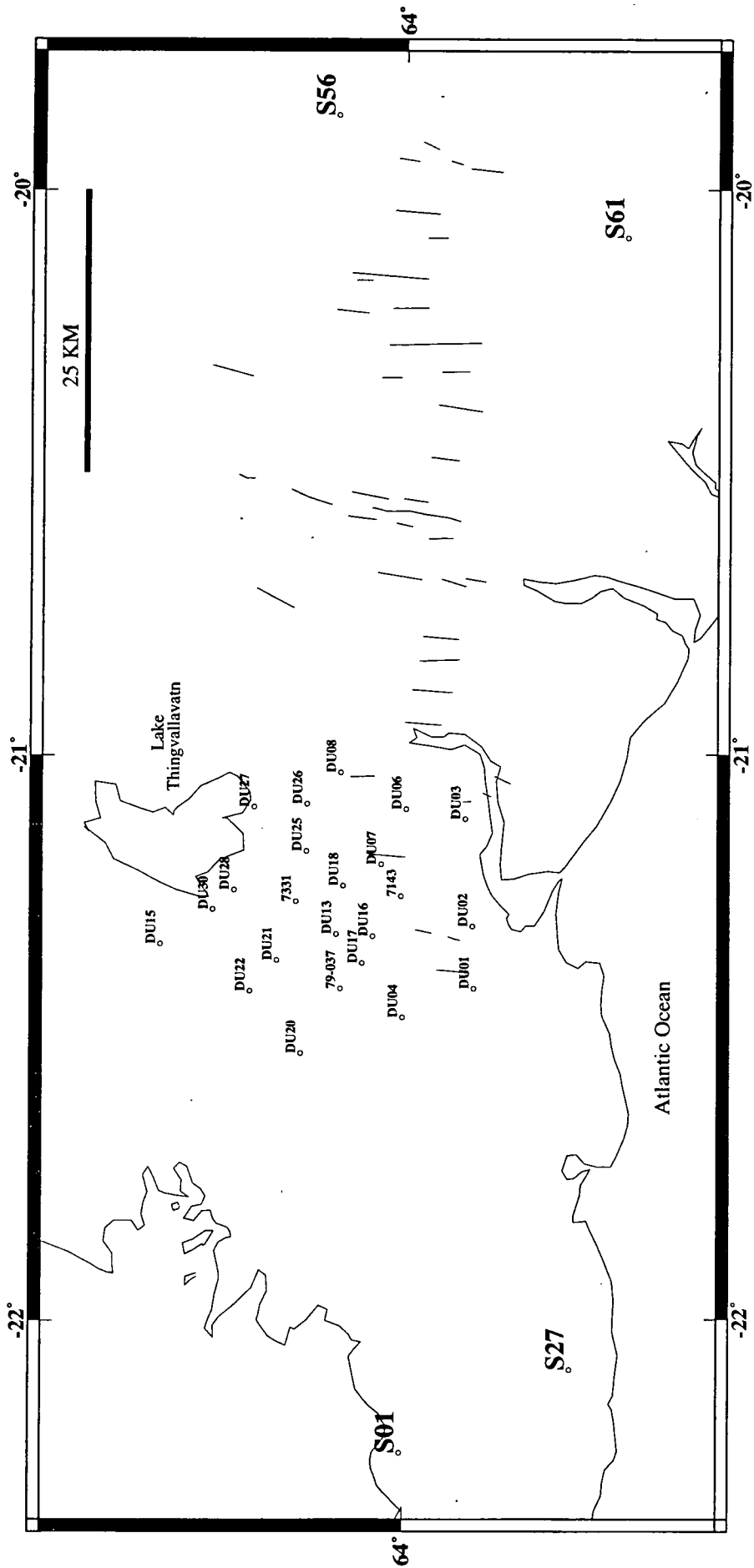


Figure 3.1 Locations of points of the Hengill GPS network. Point 7143 (Nupafjall) was occupied each day. Lines indicate faults of the SISZ.

3.2 DESIGN AND MEASUREMENT OF THE NETWORK

3.2.1 Network design

The Hengill GPS network was established in an area 750 km² in and around the Hengill triple junction. The point positions were selected to achieve fairly uniform coverage of the Hengill triple junction including all three volcanic systems and the transform branch in Ölfus. Twenty of the points were newly installed. One point was a pre-existing GPS point, OS-1985-7143, and two were old triangulation points, NE-79-037 and OS-1985-7331 (Table 3.1, Figure 3.2). Newly installed GPS points consisted of 3 inch long brass pegs with heads 1.5 cm in diameter. The letters OS-DU and a serial number which uniquely identifies the point are stamped on the points. The points were cemented into stable bedrock to avoid movements due to nontectonic deformation such as groundwater withdrawal between surveys. Points were installed where multipath was a minimum. Descriptions and maps of access to each point are given in Appendix I. Four regional pre-existing GPS points (OS-7139-S01, OS-7478-S27, OS-7481-S56 and OS-7480-S61) were measured to tie the new network to the rest of the Iceland GPS network and to neighbouring crustal blocks. The two western points were on the Reykjanes Peninsula and the two easternmost points within the South Iceland Seismic Zone. The survey spanned the Western Volcanic Zone. Within the Hengill network directly-measured lines ranged from 6 to 33 km. The four regional points were located up to 75 km away.

3.2.2 Fieldwork

The network was measured using three C/A-code Ashtech dual frequency receivers powered by 12-volt batteries. For military reasons the P-code was not transmitted during the Hengill 1991 survey and only the C/A code on L1 was observable. The receivers recorded the squared incoming carrier signal which removed the classified Y code. Recorded data consisted of the C/A code and phase measurements on L1, and squared phase measurements on L2. The receivers had 2 Mbyte internal memories. Data were recorded at 15 or 30 second intervals. The lengths of the observing sessions were limited by the size of the Ashtech's internal memory. About 1.4 Megabytes of data were collected during each session. After recording, the data were downloaded from the receivers to an IBM laptop computer at the survey headquarters at Kirkjuferja, Ölfus (near point DU03) and archived on floppy discs. Nupafjall was selected as the fixed point because it was central to the network and had been occupied in an earlier GPS survey (Hackman, 1991). The drive time to Nupafjall was 20 minutes from the survey headquarters. The antenna and tripod at Nupafjall were sandbagged down and held in place with rocks on the tripod feet. The stability of the tripod was checked and its height remeasured each session but it was not dismantled over the course of the survey. The antenna height did not change by more than 1 mm in this time.

Table 3.1 Point occupation schedule for the Hengill survey, 10-27 August 1991.

Point	Observation Date, August 1991															
	10	11	13	14	15	16	18	20	21	22	23	24	25	26	27	
(Nupafjall) OS-7143	*	*	*	*	*	*	*	*	*	*	*	*	*	*	*	
DU01		*											*			
DU02			*													
DU03	*												*			
DU04			*													
DU06		*												*		
DU07	*															
DU08											*					
DU13				*												
DU15						*										
DU16									*							
DU17														*		
DU18								*								
DU20					*											
DU21							*									
DU22					*											
DU25											*					
DU26								*								
DU27											*					
DU28											*					
DU30						*										
NE-79-037							*									
OS-1985-7331									*							
S027										*						
S001										*						
S061												*				
S056												*				

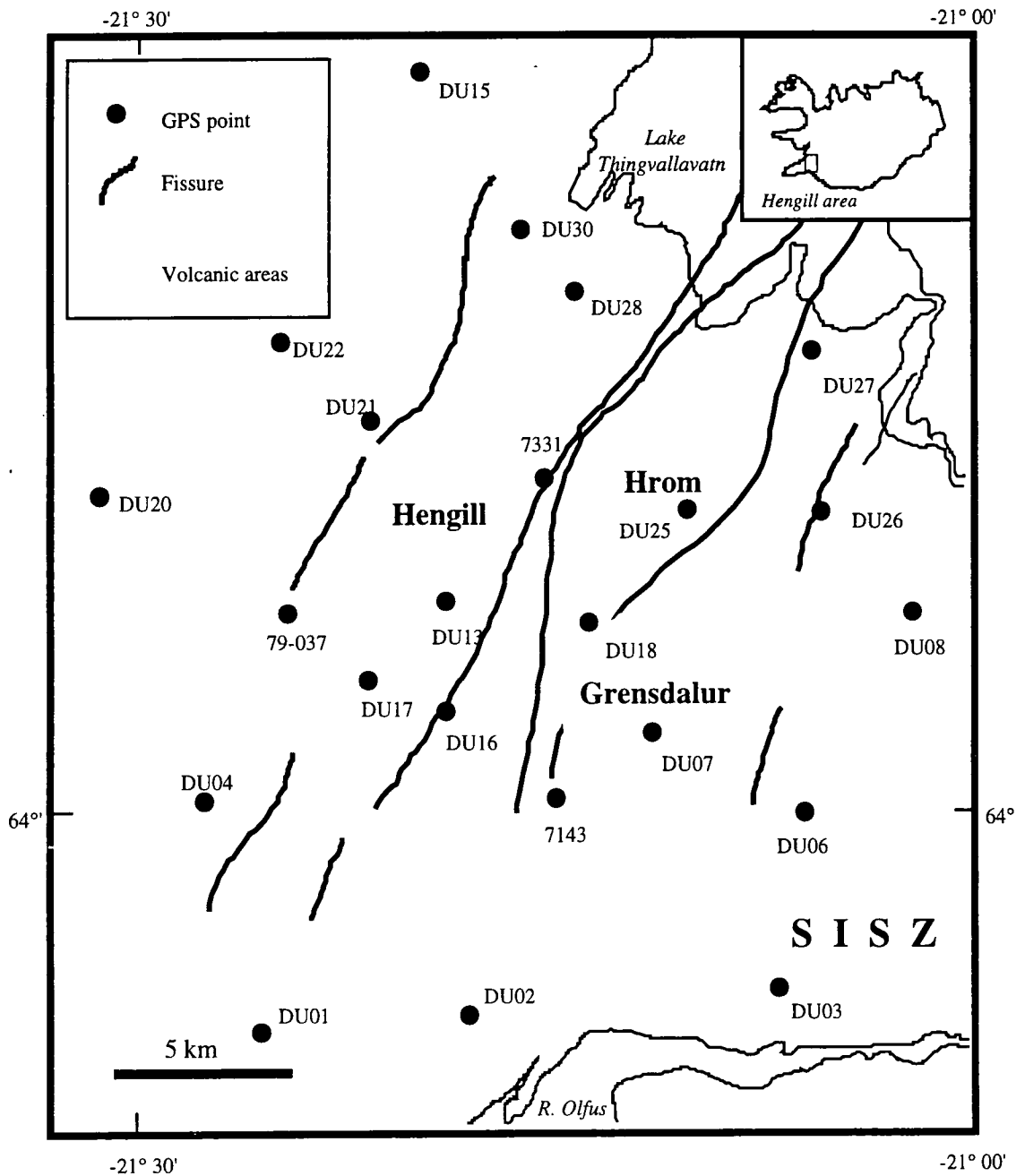


Figure 3.2 Schematic tectonic map of the Hengill triple junction showing the Hengill, Hromundartindur (Hrom) and Grensdalur systems and GPS points. Inset shows the regional setting.

Recording was conducted when the SV configuration was optimal, *i.e.*, when four or more SVS were visible for several hours. A six-hour recording interval is estimated to be the time interval necessary to acquire sufficient accuracy for lines of moderate length (Blewitt, 1989; Dong and Bock, 1989). At the time of the survey there were two periods per day of about 9 hours during which at least four SVS were always visible. These were from 9:40 to 18:40 GMT and from 22:30 to 8:30 GMT (Figure 3.3).

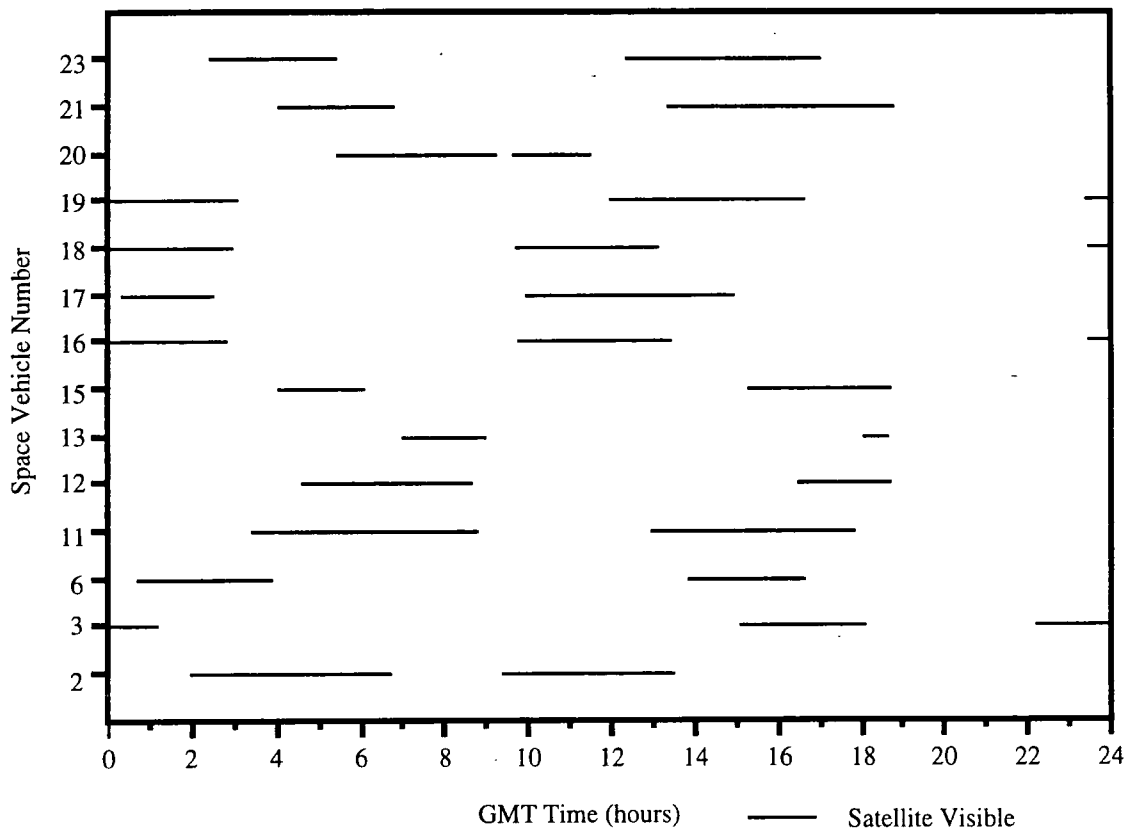


Figure 3.3 SV visibility over the Hengill area, August 1st, 1991

For the network in the Hengill area, data were recorded for a single long session daily which averaged about eight hours. The session covered the period 9:40 to 20:30 GMT and regressed by four minutes each day. A 15-second recording interval was used for these sessions. The regional points were measured in sessions that lasted about 24 hours and data were recorded at 30 second intervals. These sessions spanned both observation windows.

The GPS station setup routine was standard. On arrival at the point the tripod was set up, levelled using an optical plumb and fixed in place using rocks. The antenna was placed on the tripod, aligned with magnetic north and the slant height of the antenna above the point was measured at three azimuths. GPS data processing yields the position of the antenna phase center and the slant height is used to obtain the position of the ground marker. The receiver was then turned on and information such as the site name, date and antenna height was entered. The appropriate recording interval and SV elevation required were programmed in and the equipment left. On return, the antenna height was remeasured, and the coordinates of the point read off the receiver display. The receiver was then turned off and the equipment dismantled.

3.3 DATA PROCESSING

3.3.1 Introduction

The University of Durham implementation of the Bernese V3.2 Software was used to process the data (Rothacher *et al.*, 1990). Point coordinates were calculated relative to the point at Nupafjall. The data recorded in the field were downloaded to a SUN4 computer at the University of Durham and converted from RINEX to the Bernese format.

The broadcast ephemerides recorded in the field often did not contain the required information for all the SVS observed, so broadcast orbits obtained from the Scripps Orbit and Permanent Array Center were used to form the orbit files. A-priori coordinates are required for GPS processing. Ideally these should be previous geodetic measurements but in most cases such coordinates were not available and those read off the receiver at the end of a session were used. The *a-priori* coordinates of Nupafjall were 64.00230006N, -21.24908591W, 366.3615 m and were held fixed throughout the processing.

Since the sessions were often over 8 hours long they were split into two and processed separately. A different ionospheric model was used for each half. A cut-off elevation angle of 15° was used, *i.e.*, data recorded from SVS below this elevation angle were not used.

3.3.2 Processing procedure

1. *Orbit modelling.* The broadcast orbit files were processed using programs BRDTST, BRDTAB, and DEFSTD (Chapter 2, section 2.4). Two-day satellite orbits were calculated using program DEFSTD. Two iterations of the program were used and the Earth's potential modelled as an eight-degree polynomial.

2. *Outlier removal and cycle-slip detection.* The pseudorange data were scanned in automatic mode using program CODCHK. Satellite clock corrections were calculated and the *a-priori* point coordinates improved using the C/A-code data and program CODSPP. Since the coordinates output by CODSPP are not as accurate as GPS results calculated using phase data, prior GPS coordinates were used for points where available. The coordinates of other points were updated from the field readings to those output by CODSPP. The differences in position between the field readings and the locations calculated by CODSPP were as much as 60 metres. One clock offset per epoch was estimated for the SV clock corrections, which were stored in the phase files.

For each daily measuring session, between-point phase single difference files were formed and cycle slip editing performed using program MAUPRP. Slips greater than 5

cycles and different in L1 and L2 were sought. If a slip smaller than this was sought, the program tended to pick out outliers as cycle slips. The data were scanned for half-cycle slips since squared phase measurements were recorded on L2. Most slips were detected using MAUPRP which usually left, at most, three to four slips undetected.

3. Ionosphere modelling. An ionosphere model for each session was derived using the phase data and program IONEST. The ionosphere was described by a polynomial of degree 2 for the hour angle, and degree 1 for the range in latitude. The troposphere was not modelled since it may be considered to be uniform over such a small network within the Hengill area. Instead, a standard tropospheric model (the Saastamoinen) was used.

4. Parameter estimation. Point coordinates were calculated using the L3, ionosphere-free phase combination and the program GPSEST and solving for the phase integer ambiguities as floating point numbers. The L3 phase residuals were browsed to detect slips smaller than 5 cycles not detected by program MAUPRP. These were added manually to the single difference files. The slip-free single-difference files were then used to calculate the L5 ambiguities using the L5 phase combination, the ionosphere model obtained with program IONEST and program GPSEST. The point coordinates were fixed to the values calculated in the earlier GPSEST run. In the final stage, the coordinates of the points and the size of the L1 and L2 ambiguities were calculated, using the L3, ionosphere-free phase combination and the L5 ambiguities obtained earlier. In addition to coordinates, the formal errors associated with the results were calculated.

5. Network Adjustment. The final coordinates were calculated by performing a network adjustment using the program NETADJ (Heki, 1992). Point Nupafjall was held fixed so the errors calculated correspond to the positions of each point relative to Nupafjall. The formal errors in the individual point determinations were scaled by the normalized RMS from the network adjustment to determine the scaled formal error associated with each point coordinate.

3.4 RESULTS

3.4.1 Ionospheric modelling

The electron content varied smoothly throughout each session. The ionospheric model produced by IONEST is used by program GPSEST to calculate the L5 ambiguities. Since all L5 ambiguities were resolved for the short lines and most for the longer lines it can be assumed that the ionospheric models were fairly good. Ionospheric noise in the data was

most problematic at sunrise and sunset. Ionospheric scintillations at the 30-second time scale resulted in outliers which can be mistaken as cycle-slips.

3.4.2 Ambiguity resolution

Data collected during the short Icelandic summer night were more difficult to process because of ionospheric fluctuations at sunrise and sunset. However, except for the long lines connecting Nupafjall and the regional points, all the L5 ambiguities in the data were resolved. The L5 ambiguity has a half wavelength of about 43 cm, and is therefore the easiest ambiguity to resolve. Resolving this ambiguity does not in itself improve the result but it is an important test of quality and a necessary prerequisite to calculating the L1 and L2 ambiguities. Resolution of the L1 and L2 ambiguities is not very important where observation windows are several hours long since the ambiguity-free and ambiguity-fixed solutions then approach one another. Which solution is superior then must be determined by examining repeatability where lines were measured multiple times. All the L1 and L2 ambiguities were calculable for the short lines and 60% for the long lines that involve the regional points.

3.4.3 Comparison of ambiguity-free and ambiguity-fixed solutions.

Network adjustments were performed on the ambiguity-fixed and the ambiguity-free results for (i) the Hengill network only, and (ii) the entire network. The Hengill network involves only lines less than 33 km in length. The entire network includes the regional points. The ambiguity-free solution is the solution found after the first run of GPSEST (the ambiguity-free ionosphere-free solution). The ambiguity-fixed solution is that found after the final run of GPSEST where the coordinates are estimated using the L1 and L2 ambiguities determined in previous runs.

The repeatabilities are the same for the Hengill-only and entire-network solutions. The ambiguity-fixed results were better in all components than the ambiguity-free solution (Figure 3.4). The best repeatabilities occur in the horizontal components. Repeatabilities in the north-south component fall below 10 mm for 74% of the ambiguity-free results and 100% of the ambiguity-fixed results. In the east-west component 73% of the ambiguity-free results and 100% of the ambiguity-fixed have repeatabilities of less than 10 mm. The repeatabilities in the vertical component are greatly improved in the ambiguity-fixed solutions where 87% of the repeatabilities fall below 10 mm compared to 39% of the ambiguity-free solutions. There is no correlation between repeatability and line length, probably because of the shortness of the lines. For both the entire network and the Hengill only network the scaled formal errors, which are the best estimate of the accuracy, are smallest for the ambiguity-fixed solutions (Figure 3.5a and b).

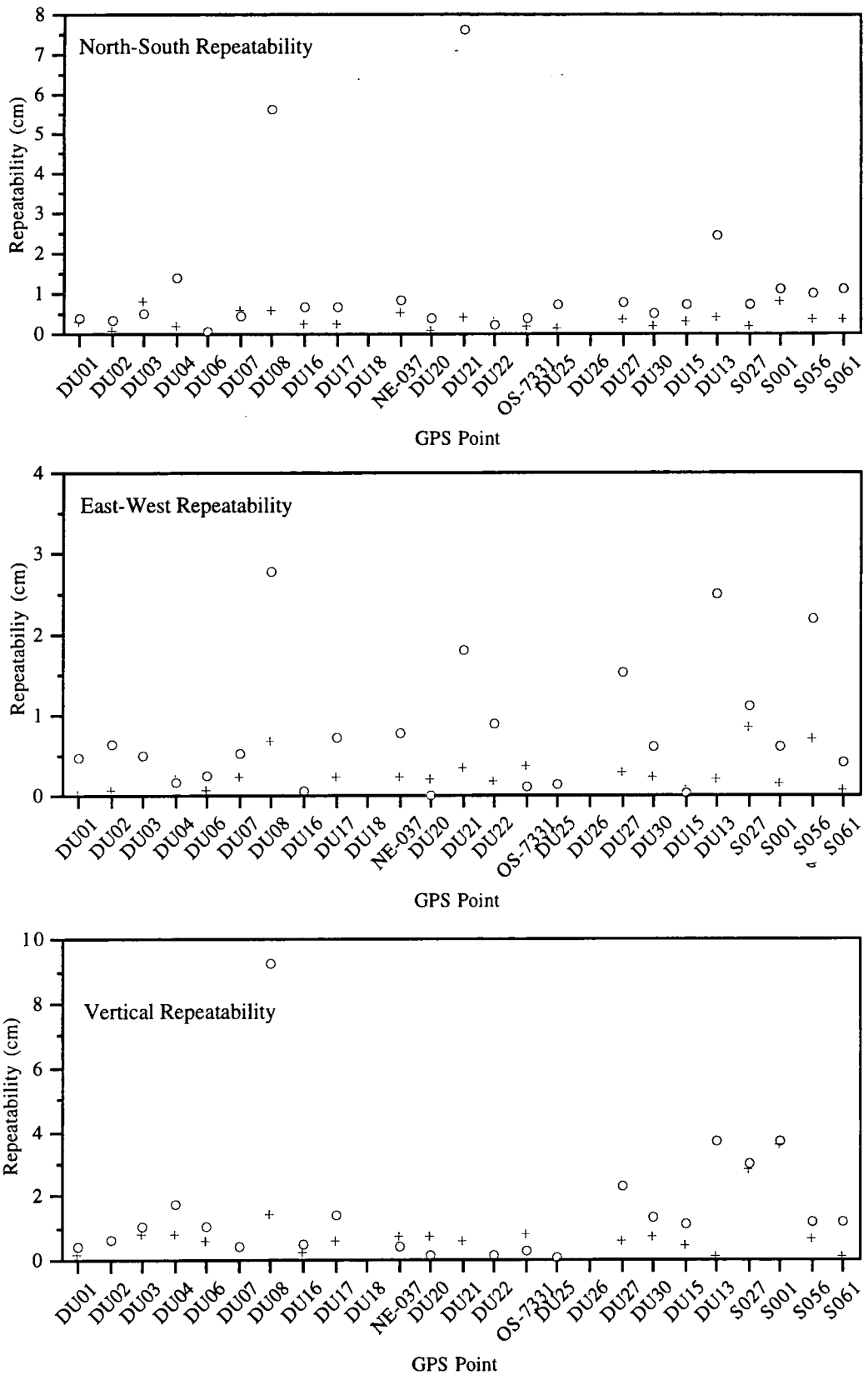


Figure 3.4 Repeatabilities of the horizontal and vertical components of the ambiguity-free and ambiguity-fixed solutions for the entire network. Circles denote ambiguity-free, ionosphere-free solution and crosses denote the ambiguity-fixed, ionosphere-free solution.

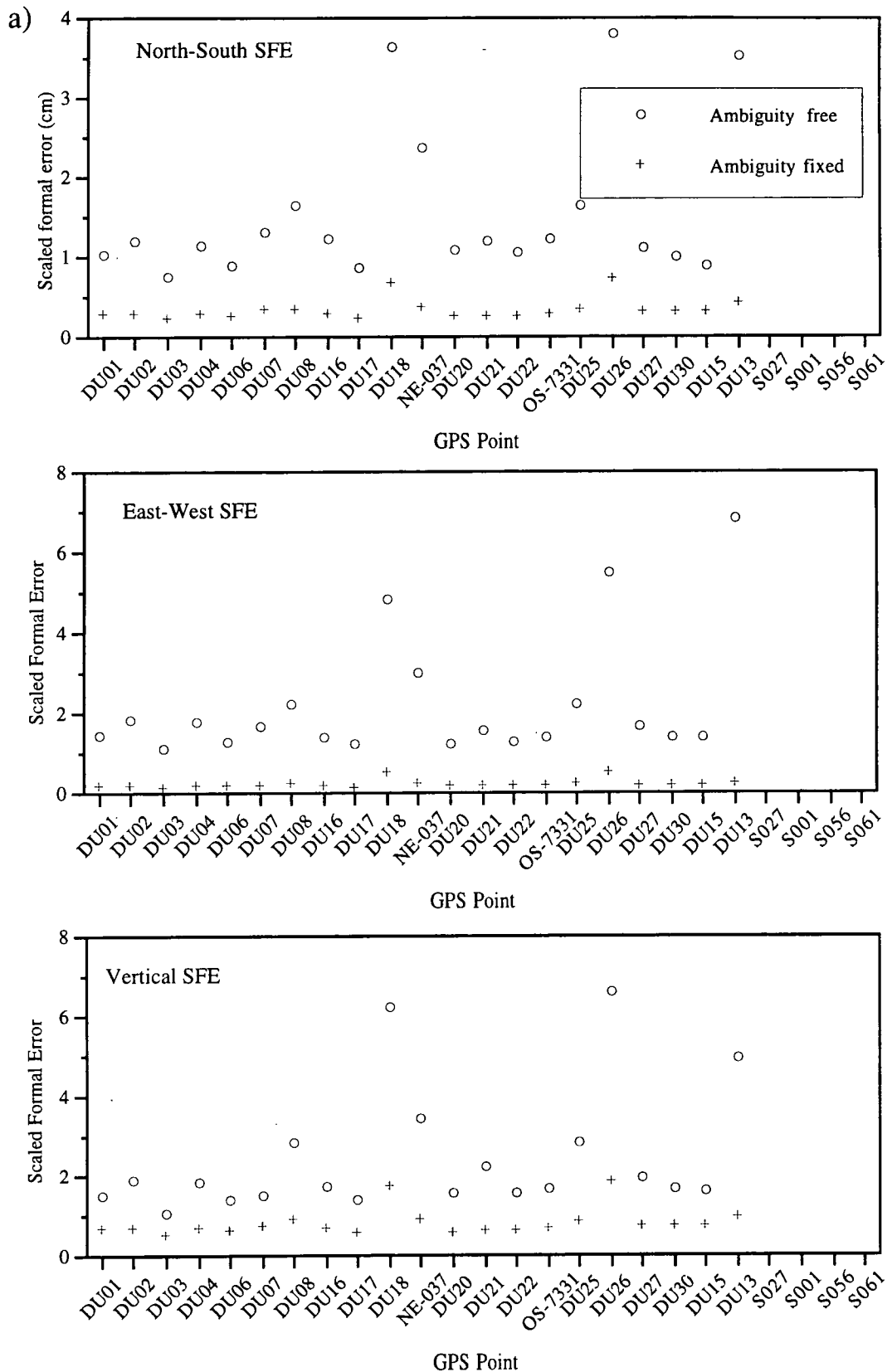


Figure 3.5a) Scaled formal errors of each point for the Hengill-only network. Circles denotes the ambiguity-free, ionosphere-free solution, crosses denote ambiguity-fixed, ionosphere-free solution.

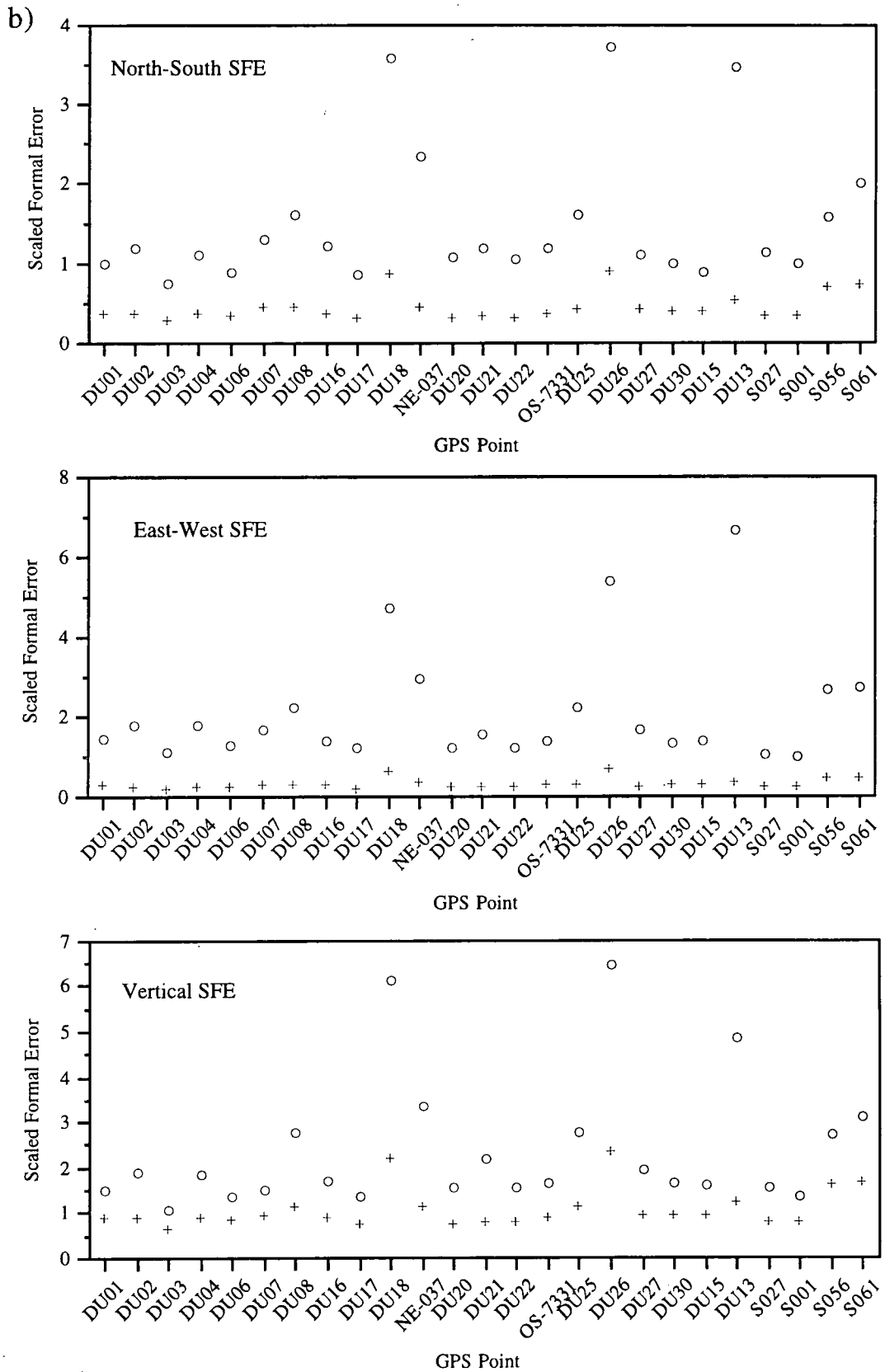


Figure 3.5b) Scaled formal errors of each point for the entire survey. Circles denotes the ambiguity-free, ionosphere-free solution, crosses denote ambiguity-fixed, ionosphere-free solution.

The scaled formal errors (SFEs) for the ambiguity-fixed solutions of the Hengill network and the entire network are fairly homogeneous and sub-centimetre at 1σ for the northern and eastern components (Figure 3.6). For both ambiguity-fixed solutions, 90% of the points of the Hengill network had 1σ errors less than 0.5 mm in the north and east components. The errors in the vertical component are larger than those in the horizontal components in both solutions. They are smaller in the Hengill-only solution with 90% being less than 10 mm compared to 68% when the regional points are included. In the case of the ambiguity-free solutions, the SFEs are between 1 and 7 cm for both the Hengill-only and entire-network solutions.

The horizontal scaled formal errors are relatively large for points DU18 and DU26 because these points were measured once only. (The scaled formal error is a product of $1/\sqrt{n}$ where n is the number of measurements.) The larger errors associated with the regional points are a consequence of the lengths of the lines being up to 12 times those of lines within the Hengill network. The geographic coordinates determined from the ambiguity-fixed solution are shown in Table 3.2 and the corresponding point repeatabilities (weighted RMS) and scaled formal errors (SFE) are shown in Table 3.3.

3.5 EARTH TIDES AND OCEAN LOADING

3.5.1 Effect of ocean loading on GPS measurements

The Earth deforms in response to the varying gravitational attraction of the Sun and Moon and the centrifugal force of the rotating Earth. The result is a periodic variation of ground elevation in the range of a few tens of cms on the Earth's surface. The deformation caused by Earth tides has been recognized in the field of GPS and is modelled and removed from observations. Superimposed on the Earth tides is deformation resulting from ocean tides, a secondary effect of the gravitational attraction of the Sun and Moon. Ocean tides cause changes in the gravitational potential on land by loading and deformation of the sea floor due to the redistribution of water, and results in deformation of the Earth's surface. The amount of displacement at a point is a function of the ocean tide height and the viscosity of the Earth's asthenosphere. In coastal areas the deformation due to ocean loading will exceed the effect of the Earth tides. A transcontinental gravity profile across the United States found that the diurnal variation in gravity decreased logarithmically with distance from the oceans (Kuo *et al.*, 1970).

Deformation as a result of ocean tidal loading causes periodic variations in the relative positions of points on the Earth's surface by a few centimetres vertically and a few millimetres horizontally. Line lengths may therefore vary on a diurnal basis and this

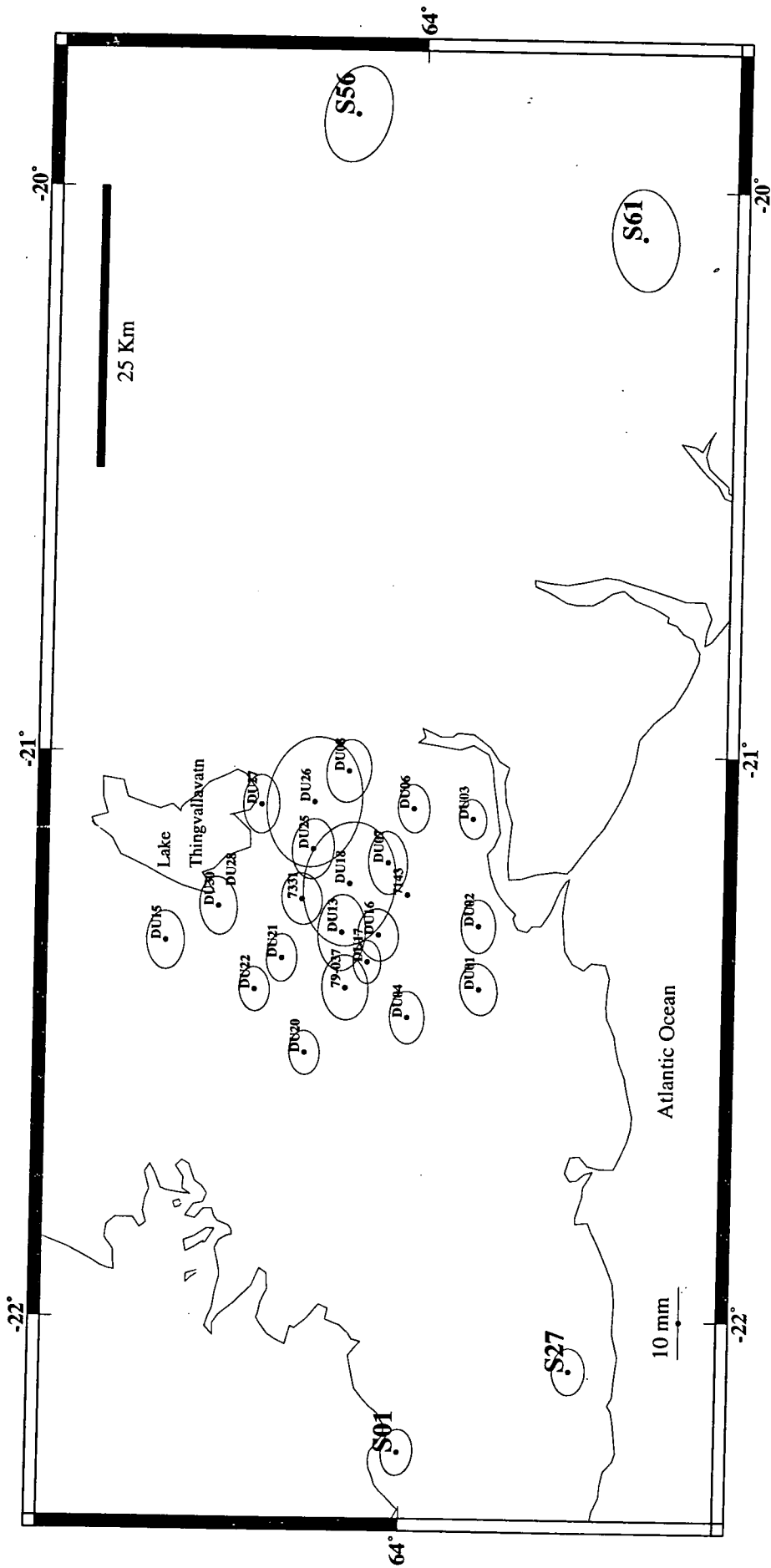


Figure 3.6 Map showing the 1-sigma horizontal scaled formal error ellipsoids for points of the entire network for the best solution, i.e., the ambiguity-fixed solution. Bar at lower left shows scale of error ellipsoids.

Table 3.2 Geographic coordinates (WGS84) of the Hengill network.

Station Name	Latitude (dd mm ss)	Longitude (dd mm ss)	Height (m)
OS-1991-DU01	63 56 40.49423	- 21 24 44.40134	271.7216
OS-1991-DU02	63 56 44.58384	- 21 18 8.82330	120.1459
OS-1991-DU03	63 57 5.26229	- 21 6 48.75422	96.2102
OS-1991-DU04	64 0 3.53244	- 21 27 48.55569	332.2630
OS-1985-7143	64 0 8.28023	- 21 14 56.70929	366.3615
OS-1991-DU06	63 59 54.38762	- 21 5 46.08682	186.1067
OS-1991-DU07	64 1 5.01431	- 21 11 34.37060	155.2210
OS-1991-DU08	64 3 0.61830	- 21 1 52.17382	150.7004
OS-1991-DU16	64 1 28.80668	- 21 19 9.79672	421.3068
OS-1991-DU17	64 1 58.98691	- 21 21 59.67748	453.8217
OS-1991-DU18	64 2 52.74540	- 21 13 49.09403	404.9480
NE-79-037	64 3 0.33801	- 21 24 43.08643	320.4233
OS-1991-DU20	64 4 52.46116	- 21 31 38.19653	268.9246
OS-1991-DU21	64 6 0.57516	- 21 21 40.41269	362.0458
OS-1991-DU22	64 7 16.39566	- 21 24 57.74706	392.5382
OS-1985-7331	64 5 6.43368	- 21 15 28.44684	371.9878
OS-1991-DU25	64 4 37.60983	- 21 10 10.79321	419.1513
OS-1991-DU26	64 4 35.65922	- 21 5 12.13848	271.5341
OS-1991-DU27	64 7 5.59767	- 21 5 30.04733	193.5484
OS-1991-DU30	64 9 1.11680	- 21 16 19.32871	303.4313
OS-1991-DU15	64 11 28.56085	- 21 19 56.84233	324.7847
OS-1991-DU33	64 3 12.52597	- 21 18 57.20400	516.4650
OS-7478 S27	63 52 2.74703	- 22 5 22.47219	194.1446
OS-7139 S01	64 0 8.10654	- 22 14 5.60426	123.9823
OS-7481 S56	64 3 14.41115	- 19 51 56.86488	242.7522
OS-7480 S61	63 49 24.75341	- 20 5 5.38733	163.7189

Table 3.3 Repeatabilities (WRMS) and scaled formal errors (SFE) in the north (dn), east (de) and vertical (du) components for all points measured. Results are from the ambiguity-fixed Hengill-only network solution unless indicated by a star, and those results are determined from the ambiguity-fixed solution for the entire network.

Station Name	N	WRMS			SFE		
		(cm)			(cm)		
		dn	de	du	dn	de	du
OS-1991-DU01	2	0.29	0.01	0.13	0.28	0.2	0.70
OS-1991-DU02	2	0.04	0.05	0.65	0.29	0.2	0.71
OS-1991-DU03	4	0.79	0.47	0.78	0.22	0.15	0.5
OS-1991-DU04	2	0.15	0.19	0.78	0.28	0.19	0.7
OS-1985-7143	23	0.00	0.00	0.00	0.00	0.00	0.00
OS-1991-DU06	2	0.01	0.06	0.54	0.26	0.18	0.66
OS-1991-DU07	2	0.54	0.24	0.41	0.34	0.22	0.73
OS-1991-DU08	2	0.56	0.68	1.37	0.34	0.25	0.89
OS-1991-DU16	2	0.22	0.04	0.23	0.28	0.22	0.71
OS-1991-DU17	4	0.23	0.22	0.53	0.23	0.16	0.58
OS-1991-DU18	1	0.00	0.00	0.00	0.67	0.51	1.74
NE-79-037	2	0.48	0.24	0.67	0.35	0.25	0.90
OS-1991-DU20	2	0.08	0.19	0.67	0.24	0.17	0.59
OS-1991-DU21	4	0.39	0.33	0.59	0.25	0.17	0.61
OS-1991-DU22	2	0.30	0.18	0.13	0.24	0.17	0.61
OS-1985-7331	2	0.19	0.36	0.80	0.28	0.22	0.71
OS-1991-DU25	2	0.12	0.13	0.04	0.33	0.23	0.88
OS-1991-DU26	1	0.00	0.00	0.00	0.71	0.53	1.85
OS-1991-DU27	2	0.32	0.29	0.54	0.32	0.2	0.75
OS-1991-DU30	2	0.18	0.24	0.71	0.31	0.21	0.73
OS-1991-DU15	2	0.29	0.06	0.40	0.31	0.21	0.74
OS-1991-DU33	2	0.42	0.21	0.06	0.41	0.26	0.96
OS-7478 S27 *	2	0.17	0.37	2.50	0.32	0.23	0.79
OS-7139 S01 *	2	0.15	0.10	4.03	0.31	0.22	0.76
OS-7481 S56 *	2	0.35	0.69	0.63	0.67	0.47	1.59
OS-7480 S61 *	2	0.36	0.06	0.08	0.70	0.47	1.67

represents an additional error source in GPS surveying hitherto generally ignored. Including the ocean loading effect has been found to reduce the error in VLBI observations, which shows that this is a source of error which cannot be ignored with the current improvement in space geodesy (Schuh, 1989). The amplitude of the vertical component of deformation due to ocean loading has been estimated from such data with formal uncertainties ranging from 0.4 to 1.6 mm (Sovers, 1994).

The magnitude of the loading is difficult to estimate as tides in the open ocean are poorly known and often can only be inferred from data at coastal stations. The vertical and horizontal movements of the surface of the Earth resulting from ocean loading may be computed by convolving Schwiderski's tidal model with Farrel's Greens function (Schwiderski, 1980; Farrel, 1972). Schwiderski's model divides the open oceans into 1 x 1 degree squares. For each square there are 11 different partial wave functions which describe the ocean tides. There are four diurnal tides with periods close to 24 hours, K_1 , P_1 , O_1 , and Q_1 and four semi-diurnal tides with periods close to 12 hours, K_2 , S_2 , M_2 , and N_2 . The three other longer period tides are M_f , M_m and S_{sa} which have periods of 14 days, one month and 6 months respectively. The largest tide is M_2 , the Principal Lunar Semi-Diurnal Tide.

The displacements d at a point in the vertical, east-west or north-south component at a time t are described by sine and cosine terms and can be computed by summing the displacements due to each of the 11 tides:

$$d(t) = \sum_{j=1}^{N=11} \left\{ A_{Cj} \cos(\omega_j t + V_j(t) - \varphi_j) + A_{Sj} \sin(\omega_j t + V_j(t) - \varphi_j) \right\} \quad (3.1)$$

where ω_j is the frequency of the tidal constituents, V_j is an astronomical argument and φ_j phase lags. The deformation constants A_C and A_S are the amplitudes of the cosine and sine components. Schwiderski's model yields 66 deformation constants for each node on the grid. These are six deformation constants for each of the 11 partial tide functions as there are two amplitude constants representing deformation in the each of the north, east, and up components. By summing these, theoretical vertical and horizontal deformations at a point may be calculated. Figure 3.7 shows the maximum vertical displacements over Iceland with respect to reference stations at Akureyri, Burfell, Borgarfjörður and Reykjavik. The deformation gradient across Iceland is roughly constant with distance. Relative differences are up to 50 mm and are predicted for lines which span the island, *e.g.*, Reykjavik to Borgarfjörður. Relative displacements between stations in the interior and on the coast are smaller.

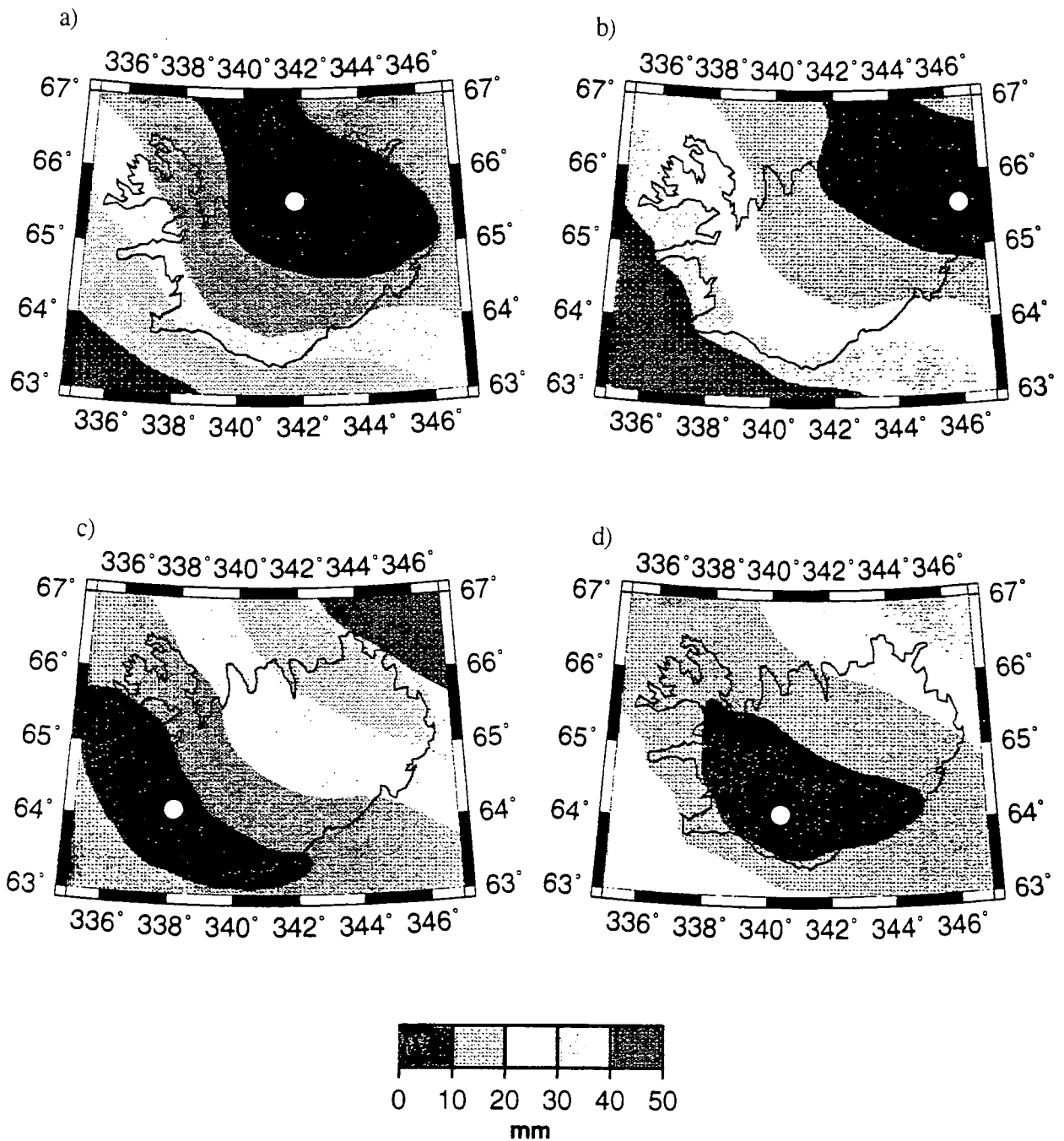


Figure 3.7 The effect of ocean loading in Iceland, computed using the method of Wu-Ling and Morgan (unpublished computer program). Shading shows maximum vertical difference with respect to stations at (a) Akureyri, (b) Burfell, (c) Reykjavik, and (d) Borgarfjörður.

3.5.2 Processing of the Hengill GPS data to determine the ocean loading effect

The effects of ocean loading are appreciable only in the case of the long lines connecting point Nupafjall to the regional points. For these lines, variations in the horizontal components of up to 2 mm and in the vertical of up to 6 mm are predicted. The horizontal deviation is only 10 to 50% of that in the vertical. This suggests that the deformation, though not zero in the horizontal component, may only be significant in the vertical, and therefore variations in this component only were studied for those lines. The recording sessions of the four regional points yielded about 18 hours of good data after periods of high ionospheric activity had been removed. Ambiguity-free, ionosphere-free solutions were used to study the effects of ocean loading because of the difficulty of fixing the L5 ambiguities in the long lines. This was a consequence of the long line lengths (~ 75 km) and high ionospheric noise during sunset and sunrise, which those sessions covered. A-priori point coordinates were obtained by processing two 6-hour windows from the full 18-hour sessions that were of high enough quality to fix the L5, L1 and L2 ambiguities. The longer the session processed, the more averaged is the effect of the ocean-loading. Ideally, 'snapshots' of the position of the point throughout the day are required. However, the shorter the session used to determine the coordinates the lower the accuracy of the results. Two-hour discrete intervals throughout the session were therefore processed separately to determine the variation in the vertical component. Because of the shortness of the sessions, the L1 and L2 ambiguities could not be fixed and ambiguity-free, ionosphere-free solutions were used.

3.5.3 Results

The formal 1σ errors associated with each position determination were generally a few mm, apart from some outliers. The calculated vertical components of those lines typically varied by about ± 50 -60 mm throughout the 18-hour measurement windows (Figure 3.8). The predicted effects of ocean loading were up to ± 6 mm. The calculated variations are thus a full order of magnitude greater than those predicted, and there is no correlation between the predicted and measured values. From this it may be concluded that factors other than ocean loading, and with larger effects, cause the variations in calculated height differences. The results for each pair of lines measured on the same day are highly correlated (compare Figures 3.8 (a) & (b) and Figure 3.8 (c) & (d)) whereas there is little correlation between the two days. This suggests that the variations are caused by site-independent, day-dependent factors. Possible candidate factors are errors from unmodelled ionospheric or tropospheric variations, noise in the data measured at point Nupafjall and variations in orbit quality. In particular, the SV geometries of the two-hour time windows varied considerably. The shortness of the sessions and lack of fixed ambiguities are probably largely responsible for the scatter in the results. The relative

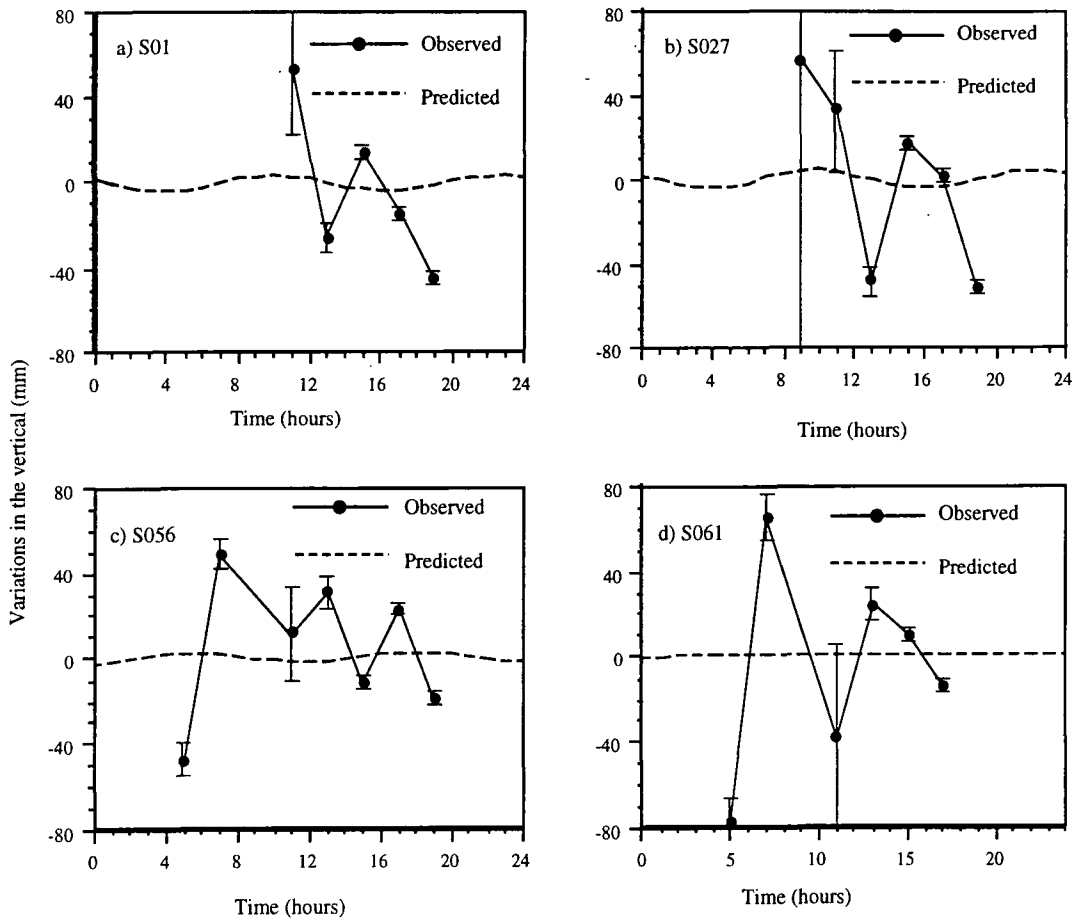


Figure 3.8 Predicted and observed variations in vertical point positions relative to point Nupafjall for regional points in the SISZ and on the Reykjanes Peninsula. The calculated results (observed) are from ionosphere-free, ambiguity-free solutions for two-hour discrete data windows. Error bars shown are 1σ scaled formal errors.

variation in calculated height difference when compared with the scaled formal errors further illustrates how that measure underestimates the true errors.

3.6 SUMMARY

A 30 x 25 km network of 23 ground control points was established in the Hengill area in 1991 and surveyed using GPS. Point repeatabilities after network adjustment were sub-centimetre in the horizontal and approximately one centimetre in the vertical. The best solution was an ambiguity-fixed solution, which, after network adjustment, yielded scaled formal errors of less than 1 cm in the horizontal and about 1 cm in the vertical for the majority of the points. The best estimates for the accuracies of the points of the local Hengill network are the scaled formal errors derived from the Hengill network measurements alone. This is because the scaled formal error can degrade the overall accuracy of the adjusted survey results if one measurement is bad. The longer line measurements suffer from error sources which are not so important in the local network

and therefore degrade the accuracy of the whole survey if they are included. The variation in the vertical component throughout the day is much larger than indicated by the scaled formal errors which ranged from 1.5 cm to 3 cm in the ambiguity-free solutions and from 0.8 cm to 1.7 cm in the ambiguity-fixed solutions.

Theoretical predictions of the effect of ocean loading in south Iceland suggest that diurnal variations of up to 6 mm in the vertical and 2 mm in the horizontal components are to be expected for lines up to about 75 km long. Diurnal variations in the calculated vectors of 70 km baselines were generally 50-60 mm in the vertical indicating that the effects of other error sources exceeded those of ocean loading in the case of this survey. Ocean loading effects on relative coordinates for lines up to 75 km long in South Iceland are thus an order of magnitude smaller than those of other error sources for typical GPS surveys such as this. The effect of ocean loading therefore does not need to be modelled for surveys of the size and type conducted in Hengill in 1991, although the importance of this effect will increase with line length and for surveys of higher accuracy conducted using better receivers.

CHAPTER 4

THE TRIANGULATION AND LEVELLING DATA CONSTRAINING THE 1954 RAINBOW MOUNTAIN - FAIRVIEW PEAK - DIXIE VALLEY EARTHQUAKE SEQUENCE.

4.1 INTRODUCTION

Both horizontal and vertical measurements that constrain the coseismic deformation caused by the 1954 Rainbow Mountain - Fairview Peak - Dixie Valley earthquakes are available since dense triangulation and levelling networks existed in Dixie Valley before 1954 and were remeasured almost immediately after it. The triangulation network spans Rainbow Mountain, Fairview Peak and the Stillwater Range covering an area 100 km by 80 km (Figure 4.1). The network was measured 8 months before the 1954 sequence and 5 months after it. Levelling routes in the area consist of 3 lines which lie both perpendicular and parallel to the faults activated in the 1954 sequence. The majority of the levelling lines were measured 20 years before the sequence and all were measured 6 months after it.

Previous analysis of the levelling data from the Dixie Valley area highlighted inconsistencies in the measured deformation (Savage and Church, 1974). In particular, an almost linear increase in elevation change with distance between 1955 and 1967 along an east-west levelling route perpendicular to the Fairview Peak fault. This deformation then reversed, and tilting occurred in the opposite direction after 1967. Using additional leveling data from that levelling route, and from two other levelling routes in the area not previously analysed, this apparent deformation is found to be a result of two factors, improperly miscalibrated levelling rods and subsidence due to groundwater withdrawal in the Fallon area.

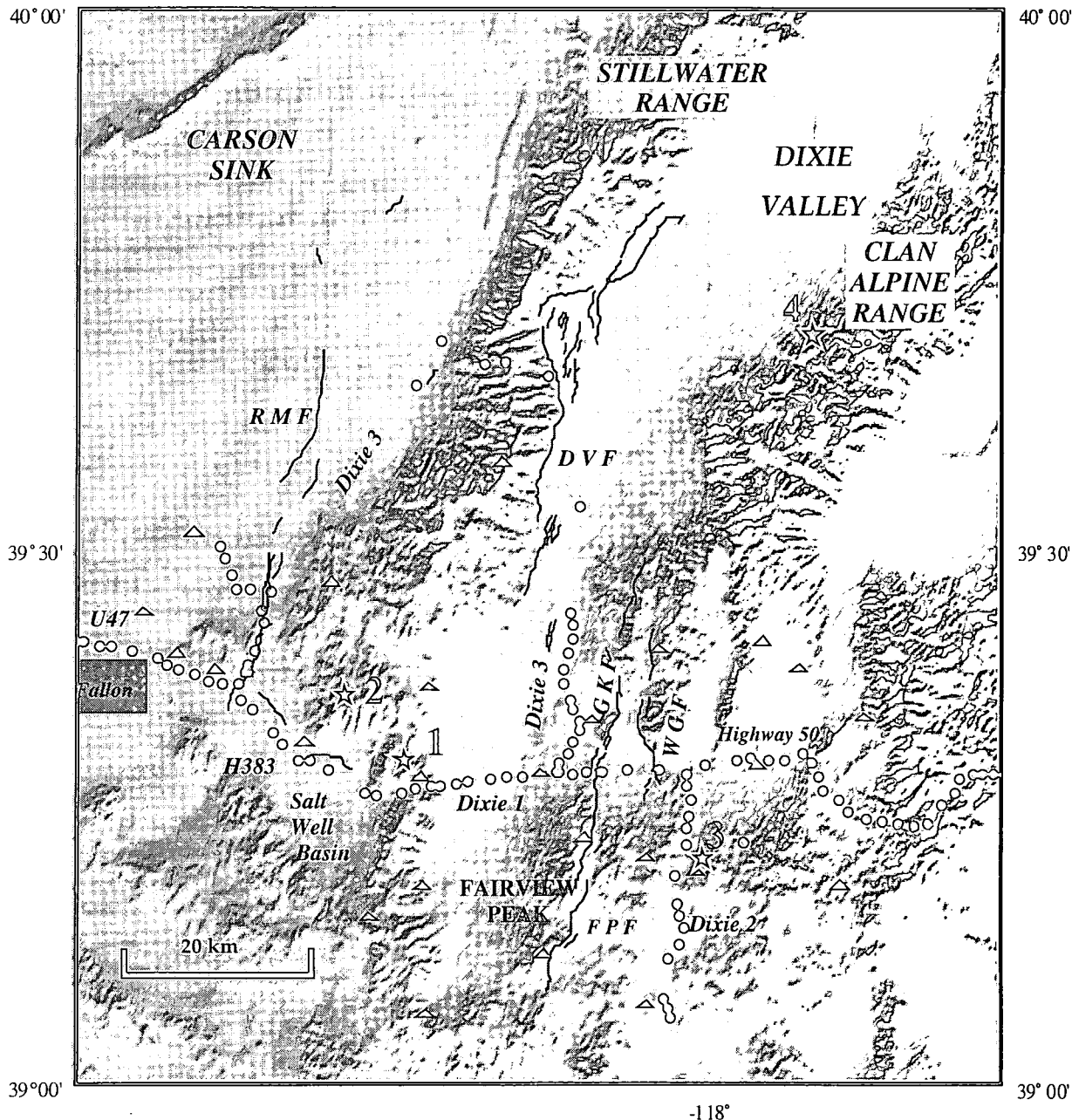


Figure 4.1 The Dixie 1, Dixie2 and Dixie 3 levelling lines. Dots denote levelling benchmarks and triangles denote triangulation stations. The mapped fault ruptures are shown as black lines, DVF: Dixie Valley fault, RMF: Rainbow Mountain fault, FPF: Fairview Peak Fault, WGF: West Gate fault, Gold King fault. Stars show epicentres of the 1954 earthquakes. Earthquakes are numbered in the order which they occurred, 1: Rainbow Mountain, July 6, $M=6.2$, 2: Rainbow Mountain, August 24, $M=6.5$, 3: Fairview Peak, December 16, $M=7.2$, 4: Dixie Valley, December 16, $M=6.7$.

Measured coseismic surface deformation can be used to calculate the amount of coseismic slip and infer the subsurface geometry of the faults that ruptured. Geodetic data are, however, affected by random and systematic errors and by blunders. They may also contain non-tectonic signals, *e.g.*, movements due to groundwater withdrawal or benchmark subsidence. Random errors are found by checking for consistency of the measurements within a survey while systematic errors can only be found by comparison of different surveys. Blunders, such as misreading an instrument, can be uncovered by

checking field records. In order to construct reliable source models for the earthquakes, the data quality must be assessed, systematic errors must be corrected and non-tectonic signals removed. The standard error assigned to each measured height difference and angle change must realistically reflect the true error.

4.2 THE DATA

4.2.1 Levelling

4.2.1.1 The levelling procedure

Levelling measures the relative height differences between points along a horizontal line of sight. The measurements are made with a pair of graduated rods and an optical spirit level. The relative height difference between two points is determined by setting up the level between the two rods which are positioned over benchmarks (Figure 4.2). Rod A is sighted first through the level telescope and the height of the telescope with respect to the point h_a is noted. This is the backsight measurement. The height of the telescope with respect to the point beneath rod B, h_b , is then measured. This is the foresight measurement. The height difference h_i between the two points is $h_i = h_a - h_b$. One pair of levelling measurements is called a setup and several setups may be required to measure the height difference between two widely-spaced permanent benchmarks. In this case rods are 'leapfrogged' over each other from one point to another, *i.e.*, the foresight rod is turned on its point and becomes the backsight rod for the next measurement pair while the backsight rod is moved to become the new foresight rod (Figure 4.2).

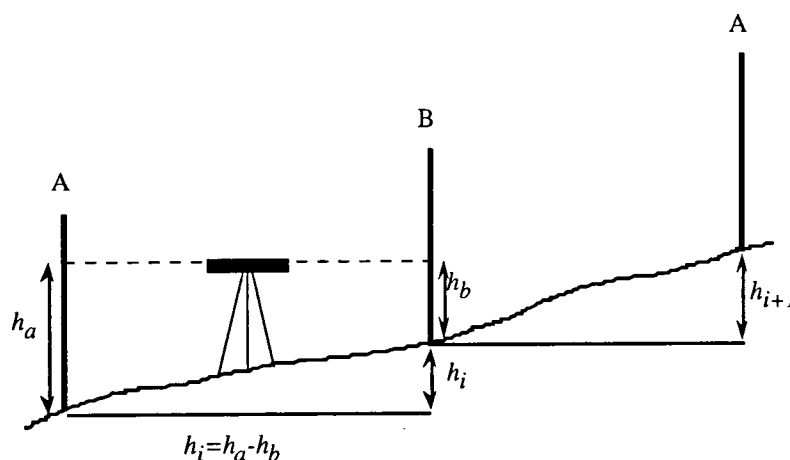


Figure 4.2 The levelling procedure.

The height difference between the two permanent benchmarks is the sum of the height differences measured at each setup, $H = \sum h_i$. The line between the two permanent benchmarks is called a section and the intermediate points measured are called turning

points. Before the 1970's most United States Coast & Geodetic Survey (USCGS) surveys were "double run". Each section was levelled first in a forward, and then in a backward direction. If the results determined from these two independent runs did not agree to within a prescribed tolerance (β) the section was remeasured.

4.2.1.2 Accuracy of levelling

Standards for levelling in the USA are set by the National Geodetic Survey (NGS) and fall into three orders: first, second and third. The most precise levelling is first-order. Each order has two subdivisions class I and class II, class I being of higher precision than class II. Procedures, equipment details and minimum precisions are defined for each order and class, *e.g.*, the accuracy of the calibration on the measuring rods and the maximum allowable setup length. The random error allowed to accumulate along a levelling line is expressed as $\alpha\sqrt{L}$ where L is the length of the line in kilometres and α is a value related to the precision of the survey. The value of α is usually the standard deviation computed from several double-run sections. Three methods are used here to assess the accuracy of the levelling surveys used in this thesis: (1) loop misclosures, (2) the difference between forward and backward runs, and (3) comparison with other surveys made under similar standards. For each of the levelling surveys one of these methods was used to assess the accuracy of the measurements and to calculate a value for α . The appropriate weighting could then be ascribed to each relevelled section.

(1) *Loop misclosures.* One way to assess the accuracy of a levelling survey is to continue the line back to the starting point or to a benchmark of known elevation. The levelling loop is then said to be 'closed'. The accuracy of the survey can be determined from the misclosure (Bomford, 1971; Marshall *et al.*, 1991). If the misclosure is greater than $\alpha\sqrt{L}$ then excess errors have accumulated. In that case the error is distributed around the loop and a new α value calculated using:

$$E = \alpha\sqrt{L} \quad (4.1)$$

where E is the misclosure of the loop in millimetres.

(2) *The difference between forward and backward runs.* When a loop is not closed the accuracy of the survey can be determined from the difference between the forward and backward measurements along the line if the line, was double-run (Section 4.2.1.1). If there are no errors then the sum of the forward observations should be equal and opposite to the sum of the backward observations. Along the entire line the cumulative sum of the forward and backward measurements for each section should be zero. If e_i is the

difference between the forward and backward measurements for section i , then α is calculated from the average misclosure of all the sections along the line, *i.e.*,

$$\alpha^2 = \frac{1}{4n} \sum_{i=1}^n \frac{e_i^2}{l_i} \quad (4.2)$$

where n is the total number of sections (Bomford, 1971). This value of α is used if the misclosure of the line is greater than the allowable error.

(3) *Comparison with similar surveys.* For a levelling survey which was not double run and did not close a loop, α can be calculated by comparing that survey with another made under similar conditions and standards and for which α is known. If the two surveys are of similar quality then it is assumed that the α/β ratios are equal where β is the tolerance for section closure (Marshall *et al.*, 1991).

The uncertainty in elevation change at a benchmark between the pre- and postseismic surveys is given by α_i where:

$$\alpha_i^2 = \alpha_{pre}^2 + \alpha_{post}^2. \quad (4.3)$$

and α_{pre} and α_{post} are the α values associated with the preseismic and postseismic measurements respectively. The associated uncertainty in the relative elevation change between two benchmarks i and $i+1$, l_i km apart is:

$$\sigma_i = \left[\left(\frac{\alpha_i + \alpha_{i+1}}{2} \right)^2 l_i \right]^{\frac{1}{2}} \quad (4.4)$$

where α_i and α_{i+1} are the uncertainties in the elevation changes at points i and $i+1$ (Marshall *et al.*, 1991).

4.2.1.3 Sources of systematic errors in levelling

In order to measure height differences accurately the line of sight must be horizontal and the rods must be vertical, stable and accurately calibrated. Practices specified by the NGS and corrections applied to the raw data ensure that these conditions hold. Three main sources of systematic errors which have traditionally contaminated levelling are: miscalibration of the rods; non-horizontal line of sight due to refraction; and, settlement of the rods and instrument.

Rod miscalibration. Rod miscalibration errors have been uncovered in levelling data in southern California (Stein, 1981). Inaccurately-calibrated rods cause a systematic error in levelling data which accumulates with distance and when that survey is differenced with another, apparent elevation changes mimic the topography (Stein, 1981). If the rod is miscalibrated by a factor of c along the rod, and the measured height difference is H_m , then:

$$H_t = H_m + cH_m \quad (4.5)$$

where H_t is the true height difference. When a measurement is made between two points a rod correction should be applied to remove any rod miscalibration. If the measured height difference between two points is expressed as:

$$H_m = H_t + eH_t \quad (4.6)$$

where e quantifies the rod miscalibration then differencing two surveys to obtain the elevation change between two points gives:

$$dH_m = dH_t + (e_{i+1} - e_i)H_t \quad (4.7)$$

The subscript i refers to the number of the survey, dH_m is the measured height difference between the two surveys and dH_t is the true section height change. The measured elevation change dH_m therefore contains a component which is proportional to the height difference between the two points.

Refraction. Refraction errors arise when the line of sight is no longer horizontal because of refraction caused by a vertical temperature gradient. The error will accumulate if the sight lengths at setups are too long and if there are a different number of setups in the forward and backward measurements (Holdahl, 1982; Stein *et al.*, 1986). The refraction of the line of sight is described by a parabola and the error is proportional to the sight length squared. Thus levelling over low-gradient terrain tends to suffer from this effect more than levelling over steep topography where the sight lengths are limited by the height of the rods. A different number of setups used in the forward and backward measurements will result in a discrepancy between the two measurements since the measurement made with fewer setups will have used longer sight lengths and therefore contain more refraction error (Stein, 1986). The refraction corrections applied to the raw data are calculated using the refraction equation described by Holdahl (1981):

$$ref_{correction} = -10^{-5} \gamma \left(\frac{s}{100n} \right)^2 \delta DW \quad (4.8)$$

where $\gamma=70$, s is the section length, n the number of setups, δ the temperature difference along the rod, D the observed height difference and W a weather factor (0.5, 1.0, or 1.5 depending on the cloud cover) (Holdahl, 1981).

Rod and Instrument settlement. The sinking of rods and the instrument during each setup causes an error to accumulate with the number of turning points (Craymer and Vaniceck, 1986). The result is that the topography appears to be steeper than it really is. The amount of settlement, S , is equal to:

$$S = n_{TP} e_{TP} \quad (4.9)$$

where n_{TP} is the number of turning points and e_{TP} is the average settlement per setup. Following specified levelling procedures, settlement effects can be reduced. However, its effect on the data can be determined by summing the forward and backward measurements of each section. Since the error is the same regardless of the direction of the levelling the effect tends to cancel in averaging the forward and backward measurements but accumulates when summed. If f is the forward measurement, b the backward measurement and e the associated errors then the sum of the two measurements E is:

$$E = \left(\frac{(f + e) + (b + e)}{2} \right). \quad (4.10)$$

If no other errors are present in the measurements then the forward and backward measurements are equal and opposite and cancel. Thus, the sum of the measurements equals e . This error, e , is equal to the amount of settlement, S . If settlement has occurred then the accumulated error will be proportional to the number of turning points in the measurement of that section.

4.2.2 Triangulation

4.2.2.1 Triangulation surveying

A triangulation survey determines the horizontal positions of points as coordinates in a plane coordinate system by measuring angles and azimuths between ground control points. The method is based on the principle that, knowing the length of one side and the sizes of three angles of a triangle, the lengths of the other sides can be computed. Combining the measurements with information about the length of at least one baseline and the coordinates of a single point, the coordinates of all the network points can be computed. The procedure used for triangulation surveys in the 1950s involved setting up

a theodolite at one station and sighting a staff erected at another (Gosset, 1952). So-called “directional angles”, the angles between lines joining pairs of points with respect to an arbitrary azimuth, were measured in the Dixie Valley surveys. Measurements were made in a clockwise direction, sighting at several stations and finishing at the first station. Each time a new point was sighted the angle between that point and the arbitrary azimuth was recorded (Figure 4.3). Distances between the stations were all less than 100 km.

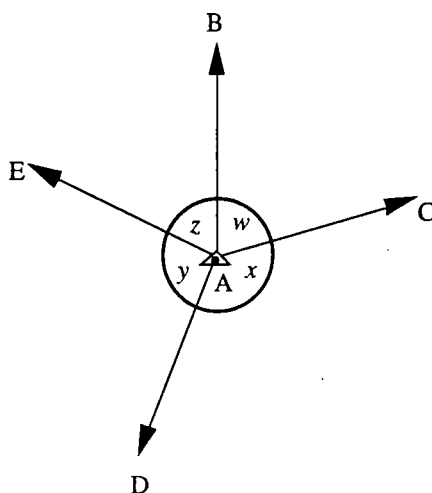


Figure 4.3 Directional angles measured.

The procedure is illustrated in Figure 4.3. Angles BAC, BAD, and BAE are measured and angles CAD and DAE calculated. Thus each angle w , x , y , z in the circle of points is known. For the highest-accuracy surveying each circle of observations was made once in a clockwise and once in the anticlockwise direction, and for 16 different settings of the theodolite. Each angle was therefore measured 32 times. Measurements were corrected for known systematic errors, screened for outliers and the mean subsequently calculated. Angles that differed from the means by the specified tolerance were remeasured. Baselines between certain stations within the network were measured with a geodimeter to compute the lengths of the other lines in the net.

Before final station positions are calculated errors in the field measurements must be removed or distributed throughout the network. In any adjustment procedure five conditions must be met. (1) The sum of three angles within one triangle must be 180° . Any discrepancy is known as the triangle misclosure. (2) In a quadrilateral the length of an unknown side must be the same when computed using two different sets of triangles. (3) The measured baseline lengths, (4) the azimuths of fixed lines and (5) the positions of known points, must agree with those computed from the angle measurements (Moffit and Bouchard, 1987).

4.2.2.2 Accuracy of triangulation surveying

There are three orders of accuracy of triangulation surveying, first, second and third order. As in levelling, each order has defined minimum tolerances and measurement procedures to be followed. First-order surveying is the highest order of accuracy and is required for measuring the US primary network. Second-order surveying is required for networks that densify the primary, and third-order surveying is used for small scale networks such as building developments. Each order is divided into two groups, class I and class II. Class I has higher accuracy requirements than class II. Making the measurements under the specified conditions and procedures reduces systematic and instrumental errors. The accuracy of a triangulation survey can only be estimated by comparing different measurements of the same quantity and by analysing misclosures. Measuring the same quantity several times within a short span of time allows blunders to be detected and the magnitude of random errors be estimated. The group of measurements is referred to as a sample and can be treated statistically assuming differences to be random.

Errors which remain after corrections for known systematic errors have been applied to the data are divided into types: internal and external errors. An internal error is the discrepancy between a set of measurements within one sample, *e.g.*, the repeated measurements of one angle, and is the standard deviation of the computed mean of all the measurements. An external error is one which is constant for all measurements within one sample but varies randomly when the quantity, such as an angle, is measured under different conditions. Since these errors introduce a constant bias into all the measurements in a sample their magnitude and presence is only uncovered after repeated measurements of the angle under different conditions or through the misclosure of triangles throughout the network. The standard error σ calculated for the measured angles is the square root of the sum of the squared internal and external errors in the survey.

After calculating the standard error, misclosures within the triangles of the pre- and postseismic surveys were used to reassess the quality of the data. For first-order surveying the triangulation misclosure may not be greater than 3 arcseconds for one triangle and 1 arcsecond on average. For second order surveying the specifications are 5 and 1.5 arcseconds (Gosset, 1952). If the misclosure was larger than the sum of the standard error of the three angle measurements, the misclosure was distributed equally among the three measurements and assigned as the error associated with that observation as described by Moffit and Bouchard (1987). The angle changes calculated by differencing pre- and postseismic surveys are attributed to be the coseismic angle changes. The error σ_c in the coseismic angle change is then calculated as:

$$\sigma_c = \left(\sigma_{pre}^2 + \sigma_{post}^2 \right)^{\frac{1}{2}} \quad (4.12)$$

where σ_{pre} and σ_{post} are the standard errors of the pre- and postseismic surveys respectively.

4.3 ASSESSMENT OF DATA QUALITY

4.3.1 The levelling data

There are three levelling routes in the Dixie Valley area (Figure 4.1). The main levelling route in the area is a 130 km east-west line along Highway 50 (US50) and shall be referred to as line Dixie 1. The line runs almost perpendicular to the 1954 fault scarps, crossing the Fairview Peak fault scarp at its northern end. The line was installed in 1934 by the USCGS and resurveyed in 1955 by the National Geodetic Survey (NGS). Portions of the Dixie 1 line have been resurveyed 4 times since 1955 (Table 4.1). The second line, referred to as line Dixie 2, is 22 km long and runs from US50 north-south along the eastern side of Fairview Peak parallel to the fault scarp. It was measured in 1934 and 1955 as part of the same survey that measured the Dixie 1 line. It also has been surveyed 4 times since 1955. The third line, Dixie 3, forms a closed loop with the Dixie 1 line. It begins 5 km west of Fairview Peak and runs north into Dixie Valley parallel to the Dixie Valley fault scarp. It crosses the Stillwater Range and continues south through Carson Sink parallel to the Rainbow Mountain fault scarp. The line was surveyed in 1950 and 1955 and three times since then. The levelling data from line Dixie 1 have been analysed in previous work. The inclusion of data from the Dixie 2 and Dixie 3 lines in this study is new, and not only allows systematic errors to be determined but allows the fault-parallel vertical displacements be studied.

Table 4.1 Dates and line numbers (LN) of levelling and triangulation surveys made in the Dixie Valley area.

DIXIE 1		DIXIE 2		DIXIE 3		TRIANGULATION
Year	LN	Year	LN	Year	LN	Year
1934	L1960	1934	L5797	1908	USGS08	1935
1955	L15586	1955	L15588	1950	USGS50	Dec. 1953-Jan. 1954
1967	L21083	1967	L21080	1955	L15607	July-Aug. 1954
1973	USGS73	1973	USGS73	1958	L16693	April-June 1955
1976	USGS76	1978	USGS78	1967	L21086	
1986	L24985	1985	L24887	1967	L21089	

4.3.2 Non-tectonic errors and signals

4.3.2.1 Water withdrawal in the Fallon area

Subsidence due to water withdrawal occurs when the water table is lowered and the effective pressure in the underlying sediments decreased. Six criteria must be satisfied before it may be concluded that deformation results from water withdrawal: 1) subsidence must be detected at least four benchmarks, 2) the subsidence must exceed the allowable random error, 3) there must be consistent temporal and spatial behaviour between repeated surveys, 4) there must be no tectonic deformation, such as coseismic offsets, that could explain the deformation, 5) there must be no systematic errors in the data, and 6) correlation between water withdrawal and subsidence must occur (Chi and Reilinger, 1984). Elevation changes between 1934, 1955, 1967 and 1986 along line Dixie 1 show subsidence common to all three postseismic surveys between 20 and 60 km along the line (Figure 4.4). The trend is not obvious in the 1955 to 1934 elevation changes as these are dominated by the effects of the earthquake sequence. Hence, they are not used in the analysis of water withdrawal. The signal spans 30 benchmarks along Dixie 1, nine of which were measured in 1955 and 1934.

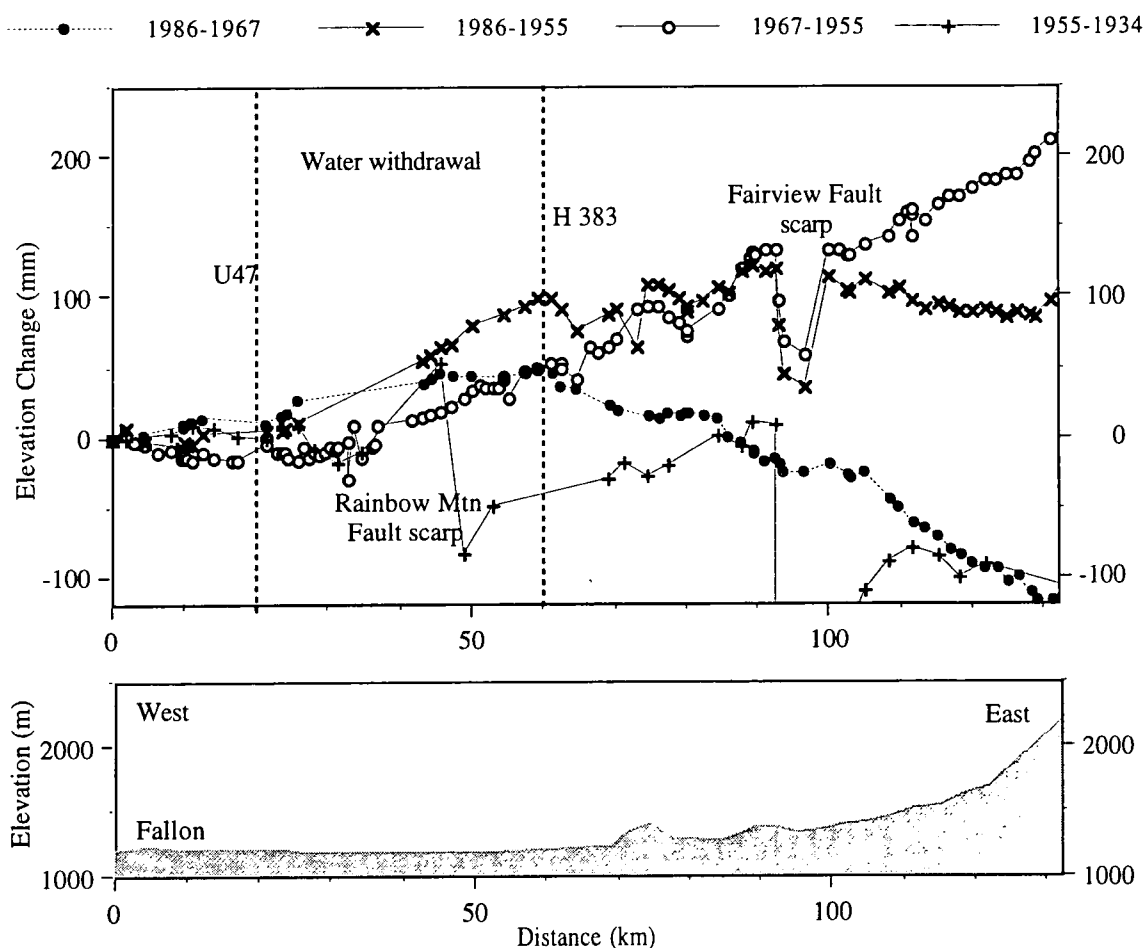


Figure 4.4 Elevation changes along line Dixie 1 between years 1934, 1955, 1967, 1986. The locations of benchmarks H383 and U47 are shown in Figure 4.1. Lower figure shows the topography.

For each of the postseismic surveys the elevation changes exceed the allowable random error of 26 mm (Section 4.3.2.4). There is consistent spatial and temporal behaviour between the postseismic surveys. The subsidence begins and ends at the same points along the line, H383 and U47. The difference in subsidence rates of benchmarks H383 and U47 are 2 mm/yr for 1967 to 1986, 3 mm/yr 1955-1986 and 4.5 mm/yr for the period 1955 to 1967 with an average rate of 3.17 mm/yr. Although the area was the scene of an earthquake it is unlikely this signal is postseismic deformation. Vertical postseismic deformation would be centered over the fault trace, which is approximately 50 km along the line, whereas this subsidence is almost uniform along the line. There are systematic errors in the 1967 data (Section 4.3.2.3), however, the influence of these errors over such flat topography is negligible.

Water flow into the Fallon area has been controlled since the completion of the Lahontan Dam in 1915 and the Carson River Dam in 1906. The Lahontan reservoir, 40 km west of Fallon, stores water from the Sierra Mountain Range and the Carson River which flows through Fallon and into Carson Lake (Figure 4.5). The main water use in the area has been crop irrigation. The delivery of water from the reservoir and the blocking of the Sierra run-off water and Carson River has altered water levels in Fallon. Although the depth to water in some wells in Fallon has risen because of the irrigation, water levels close to Carson Lake have dropped. A study of water levels in Fallon reports that in 1904 the depth to water along the Carson River was less than 1.5 metres. In 1992 the depth to water in the Fallon area was 1.5 to 3 metres (Seiler and Allander, 1993). In that period Carson Lake, which the levelling line borders, had almost dried up. The average drop of the water table was 60 mm/yr in thirteen wells that lie close to the levelling line (Figure 4.5). Most of these wells have been monitored since 1976. Since the subsidence is detected in all surveys made in the area and a water level drop has been recorded in Fallon, the two are probably related. Bedinger *et al.* (1984) mapped the Salt Well Basin (Figure 4.1) through which this section of the levelling line runs as an area of ground water withdrawal. The Stillwater Range to the east acts as a ground water flow barrier between Dixie Valley and the Carson Sink. Water withdrawal of similar magnitude has also been detected in Bunker Hill and Los Angeles, California (Table 4.2).

Table 4.2. Areas where subsidence due to water withdrawal has been recorded geodetically (from Chi and Reilinger, 1984). The results of this study of the Fallon area are shown in bold.

Location	Period	Water-level decline	Max. surface subsidence
Bunker Hill, Calif.	1900-1904	14.6 m	76.2 mm
Los Angeles, Calif.	1941-1956	9.1 m	150 mm
Fallon, Nevada	1955-1986	2 m	100 mm

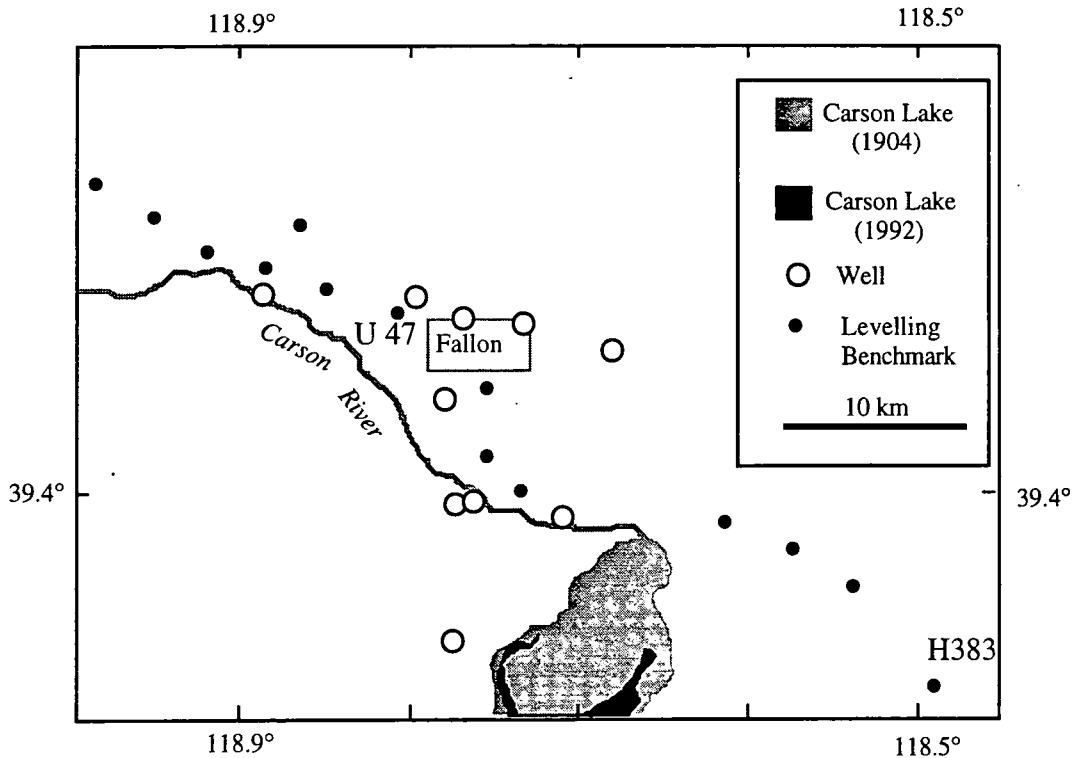


Figure 4.5 Wells where water level drops have been recorded are shown as open circles. Benchmarks are shown as solid black circles (from Seiler and Allander, 1993).

A correction proportional to the distance between two benchmarks and the time interval between the two surveys being differenced was applied to the elevation changes. The correction was calculated as:

$$corr = 0.08(LdT) \quad (4.13)$$

where L is the distance between two benchmarks and dT is the number of years between the surveys. The factor 0.08 is the average subsidence rate per unit distance. The correction was added to the elevation change detected at the 9 benchmarks which were observed before and after the earthquake sequence (Figure 4.6).

4.3.2.2 Systematic errors in the postseismic data

The postseismic levelling data along Dixie 1 are not self consistent. Savage and Church (1974) studied the 1934, 1955, 1967 and 1973 levelling data along the line Dixie 1 and concluded that either the 1955 or 1967 survey contained systematic errors. Since the 1955 data are used to constrain the coseismic deformation it is necessary to identify and correct for these errors. Using data from two additional surveys of the Dixie 1 line and the surveys of the lines Dixie 2 and 3 it is possible to do this. Comparison of the postseismic survey data shows that the surveys made in 1967 of the Dixie 1, Dixie 2 and Dixie 3 lines give elevation changes that are anomalous compared to all other survey pairs.

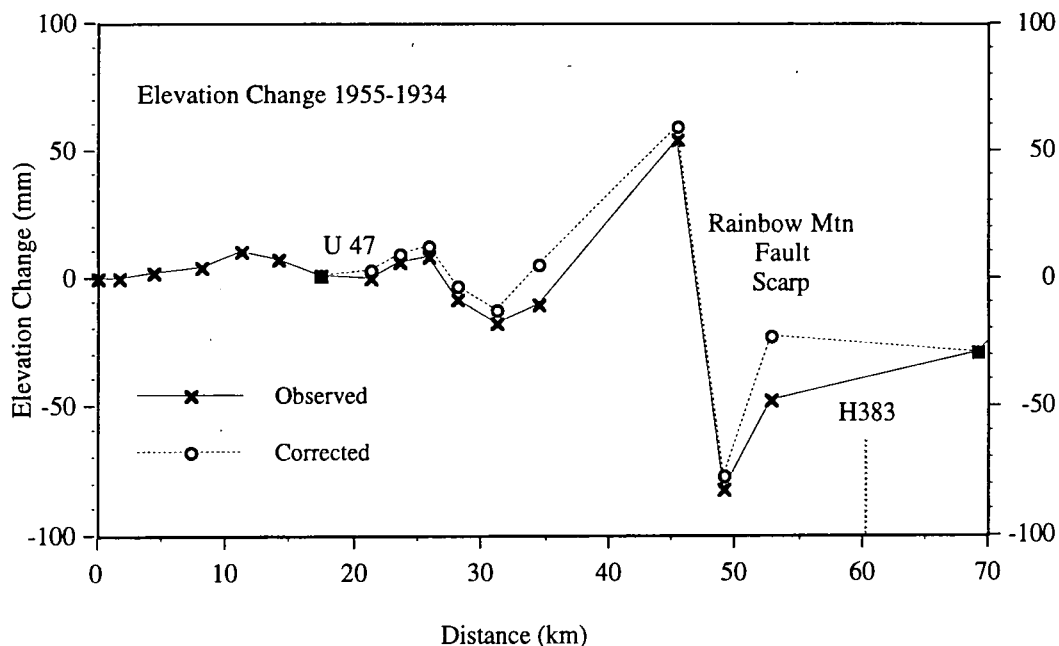


Figure 4.6 Elevation changes between 1955 and 1934 along line Dixie 1. The corrected data are those to which a correction for water withdrawal has been applied. The benchmark H383 was not measured in 1934, its position is shown by a dashed line.

Elevation changes increase almost proportionally with distance when the 1967 measurements along line Dixie 1 are differenced with any other survey of that line (Figure 4.7a). The trend is equal and opposite when the 1967 survey is differenced with surveys made earlier and later. There is no such trend when the other surveys, made in 1955, 1973, 1978 and 1986 are differenced (Figure 4.7b). Along line Dixie 2 there is also an equal and opposite trend of calculated elevation changes when the 1967 measurements are differenced with the 1985 and 1955 surveys (Figure 4.8). The deformation detected by the 1985 and 1955 data alone, are however, less than the allowed random error. The entire Dixie 3 line was measured in 1908 and 1955. Only the first and last 20 km of this line were surveyed in 1967 and only six benchmarks were measured in 1950. Figure 4.9 shows the 1967 to 1955 elevation changes compared with other survey pairs. Along the first twenty kilometres the elevation changes between 1955 and 1967 mimic the topography (Figure 4.9a). Along the last 20 km the measured height differences between the 1950 and 1967 surveys and between the 1950 and 1955 surveys record similar deformation (Figure 4.9c). The elevation changes measured between the 1908 and 1967 surveys and the 1908 and 1955 surveys are also similar. The surveys of the Dixie 3 line appear to be thus consistent along the last 20 km

Because the surveys made in 1967 along lines Dixie 1, Dixie 2 and Dixie 3 give elevation changes that are anomalous compared with those calculated using other surveys it is proposed that the 1967 surveys contain a systematic error. It is unlikely that the trends measured are tectonic effects. Along line Dixie 1 the elevation differences indicated that

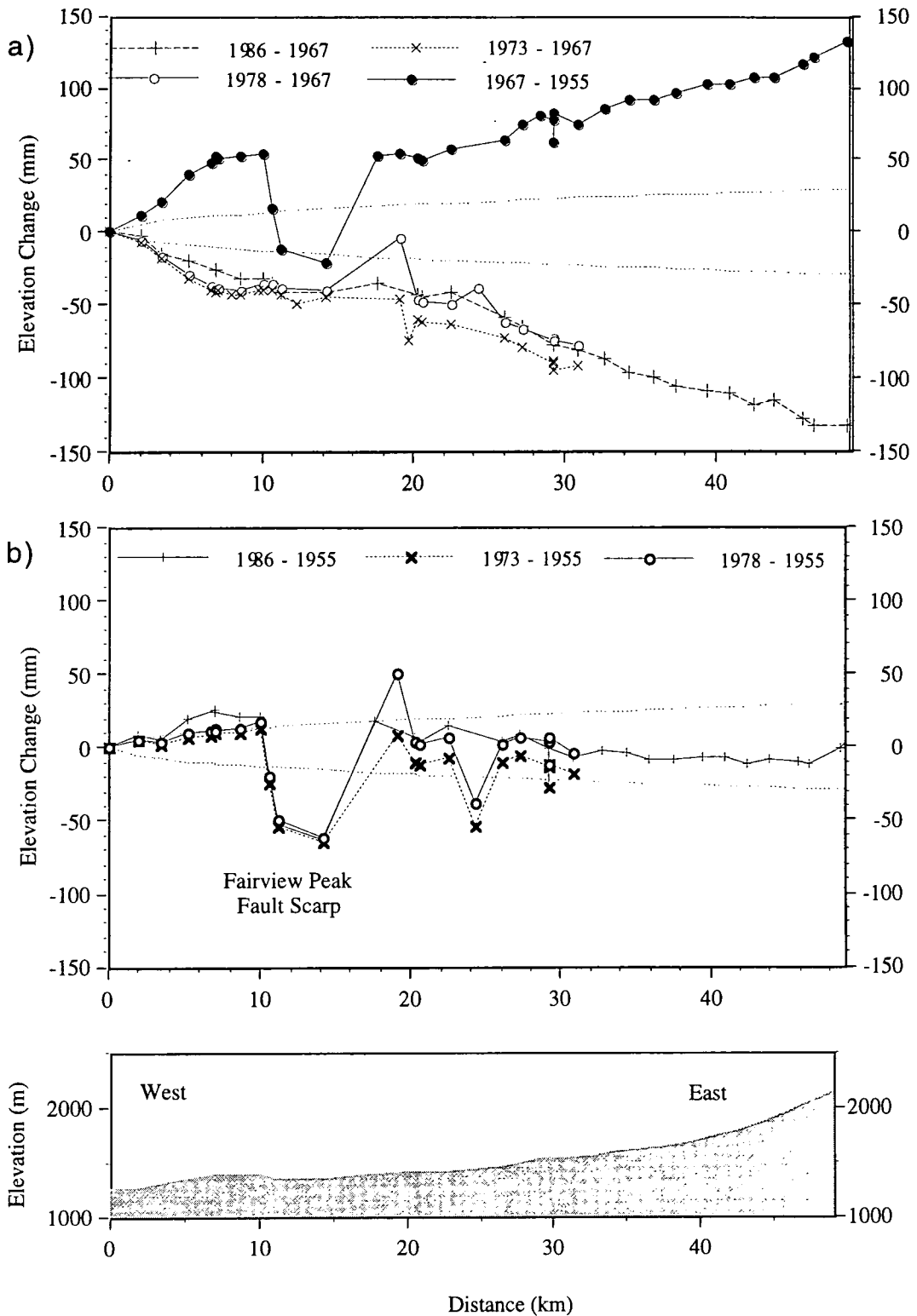


Figure 4.7 The elevation changes along line Dixie 1, calculated from the 1955, 1967, 1973, 1978 and 1986 surveys. The dotted line indicates the allowable accumulation of random errors.

the line tilted down to the west before 1967 and down to the east afterwards. Such a reversal is unlikely to be attributable to postseismic effects, and deformation caused by postseismic relaxation following an earthquake sequence would be centered in the

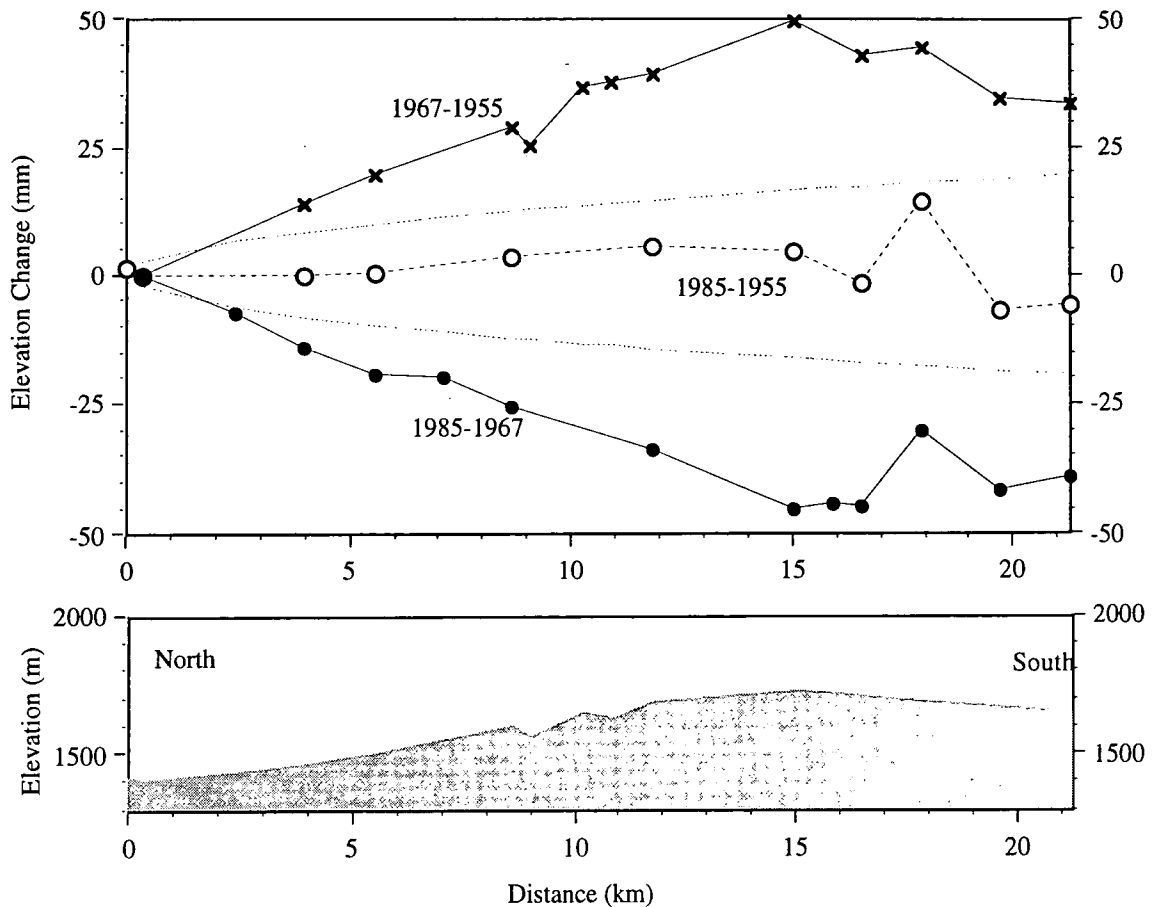


Figure 4.8 Elevation changes along line Dixie 2 levelling.

epicentral area. The tilt seen is also independent of the direction of the levelling. Elevation change accumulates with distance for both north-south and east-west lines. The three 1967 surveys were made by the same field personnel with the same instruments and immediately adjacent to one another. The error, if procedural or due to faulty equipment, is common to all three surveys. The main effects that contribute to systematic errors in levelling data are rod miscalibration, refraction and instrument settlement.

4.3.2.3 Error source of the 1967 levelling data

The correlation of topography and elevation changes suggests that the 1967 surveys were made with measuring rods which were incorrectly calibrated. Using the method of Stein (1981) the elevation change per unit distance for each section was regressed against the gradient of the topography. Equation 4.7 is normalised by dividing across by distance between benchmarks dx :

$$\frac{dH_m}{dx} = (e_{i+1} - e_i) \frac{H_i}{dx} + \frac{dH_i}{dx} \quad (4.14)$$

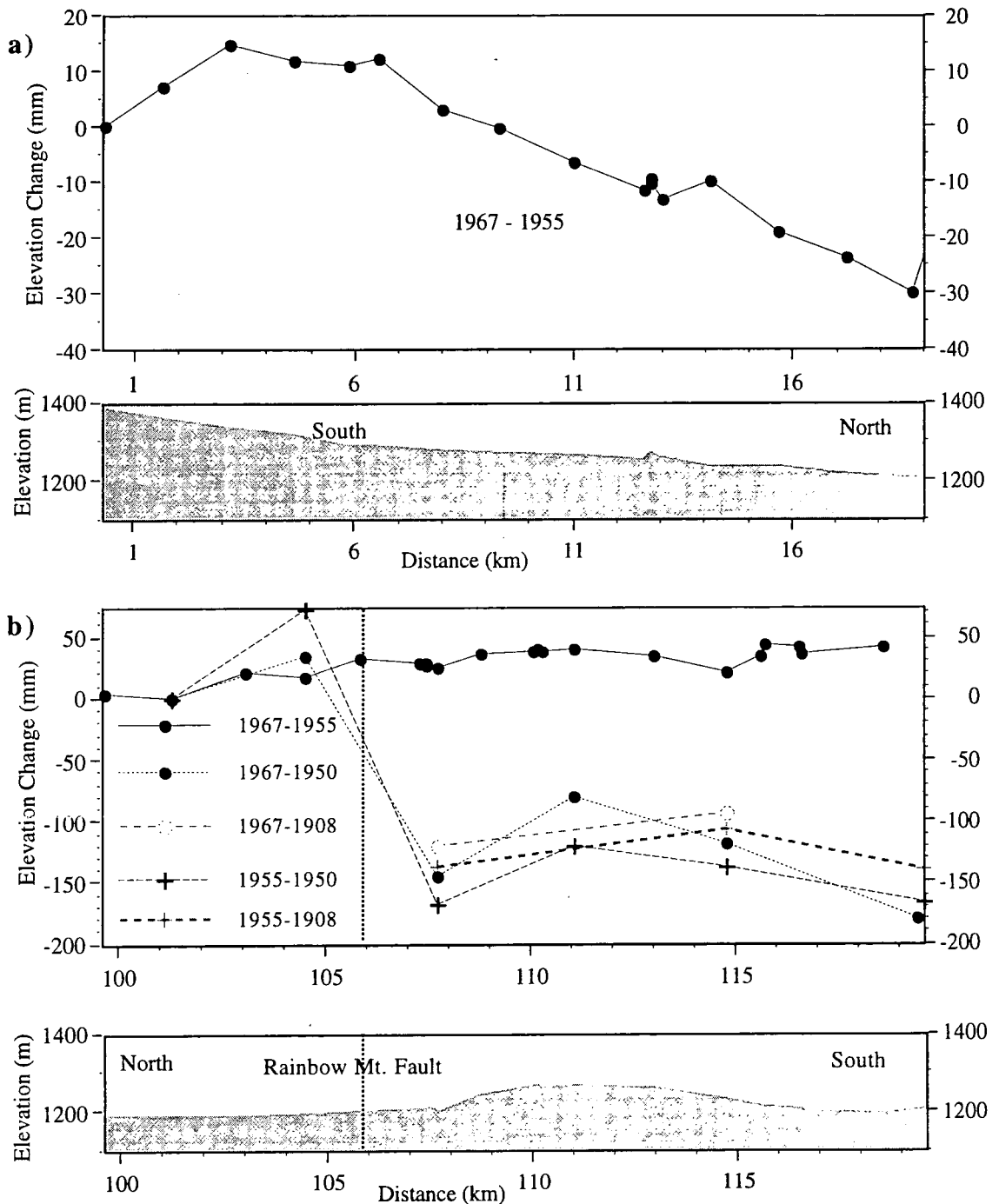


Figure 4.9 Elevation changes along the first and last 20 km of the line Dixie 3.

The term H_i/dx represents the topographic gradient of each section and dH_m/dx the elevation change per unit distance along the section (*i.e.*, the tilt). A linear least squares regression of tilt onto the topographic gradient will yield the value of $(e_{i+1} - e_i)$ the average miscalibration of the rods used in the two surveys.

The correlation of tilt and gradient was calculated for all elevation changes involving the 1967 surveys along all three levelling routes. Only elevation changes west of the water withdrawal region were used. Of the eight data sets formed, four had regression

coefficients that were significant at the 99% confidence level and two at the 98% confidence level (Table 4.3).

Table 4.3 Rod miscalibration coefficients determined from levelling surveys along lines Dixie 1, Dixie 2 and Dixie 3.

Route	Years	Number of Sections	Correlation Coefficient	Miscalib Coeff. (ppm)	Significance
Dixie 1	1967-1955	50	0.474	100±26	99%
Dixie 1	1978-1967	22	-0.809	-185±28	99%
Dixie 1	1986-1967	42	-0.458	-89±36	99%
Dixie 1	1973-1967	24	-0.859	-333±40	99%
Dixie 2	1985-1967	11	-0.752	-90±25	98%
Dixie 2	1967-1955	12	0.803	106±20	<95%
Dixie 3(i)	1967-1955	15	-0.247	-130±112	<95%
Dixie 3(ii)	1967-1955	17	0.303	192±140	<95%

The correlation of topography with elevation change for the two data sets from line Dixie 3 was not significant, probably because there is little topographic relief along this line. The weighted average of the miscalibration calculated is 150 ± 30 ppm. Two of the elevation change versus topography gradient plots 1967-1955 and 1986-1967, are shown in Figure 4.10. Measurements made with miscalibrated rods can be corrected when the miscalibration is known. Subtracting the average miscalibration of the rods multiplied by the gradient from the measured tilt gives corrected tilt. Applying a correction of 150 ppm to the 1967 surveys removes the anomalous signal when those surveys are differenced with others (Figure 4.11). The corrected elevation changes are within the allowable random error.

A miscalibration of ± 30 ppm is typical for rods of this period. The rods (numbered 312-347 and 312-383) used in the 1967 surveys were calibrated in 1965 to an accuracy of 0.05 mm. The calibration was made under tension to simulate the forces on the invar strip under working conditions. The rod corrections applied to the 1967 levelling data were consistent with the 1965 calibration of 36 ppm for the rod pair. No further calibrations were made after 1965 and in 1969 the rods were discarded. There is evidence from other surveys that rods 312-347 and 312-383 were miscalibrated. Between 1965 and 1969 the rods were used in 14 surveys in New Mexico, Arizona and Nevada. With the exception of the Dixie Valley survey and a survey at Gila Bend, Arizona, the rods were used for only one day of each survey and usually to cover spurs (Table 4.4). At Gila Bend, Line L21029 was measured in 1967 and 1992. Sixty-two km were measured

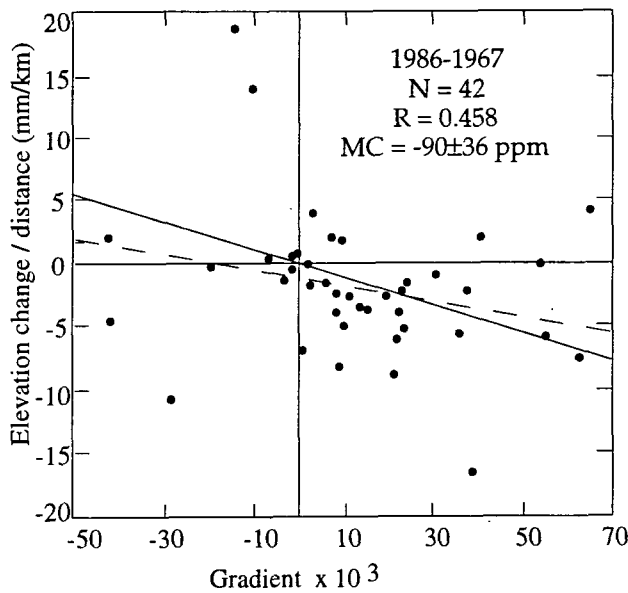
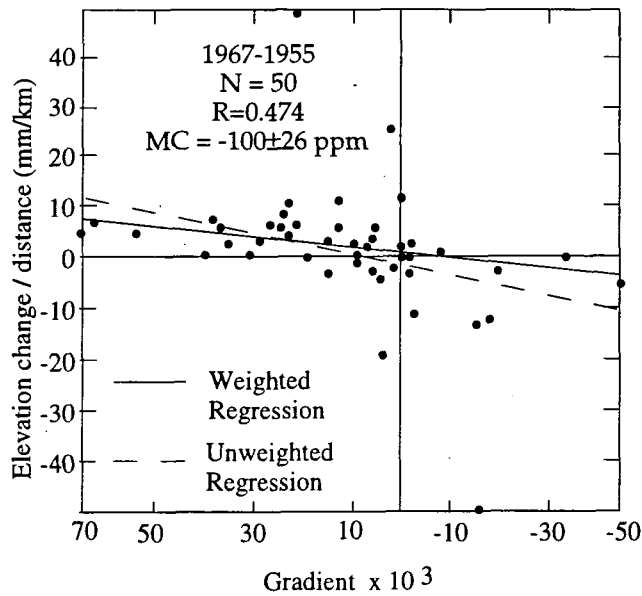


Figure 4.10 The elevation change per unit distance versus topographic gradient for elevation changes 1967-1955 and 1986-1967. N is the number of leveling sections analyzed, R, the regression coefficient and MC is the rod miscalibration. Removal of the two outliers in the 1967-1955 plot does not greatly affect the correlation. These correlations should be equal in magnitude and opposite in sign if they were caused by miscalibration of the 1967 rod errors.

using rods 312-347 and 312-383, but the route covered a region that was subsiding due to water withdrawal at a rate of 100 mm/yr.

Thirty eight sections unaffected by water withdrawal were isolated and a rod miscalibration of -571 ± 234 ppm determined (Table 4.4). Because the rods were used so infrequently after the Dixie Valley surveys, the data from the other surveys are insufficient to quantify the rod miscalibration. Except for the surveys made in San Antonio, Texas, however, there is a relationship between the elevation changes and slope confirming the rods involved were probably miscalibrated.

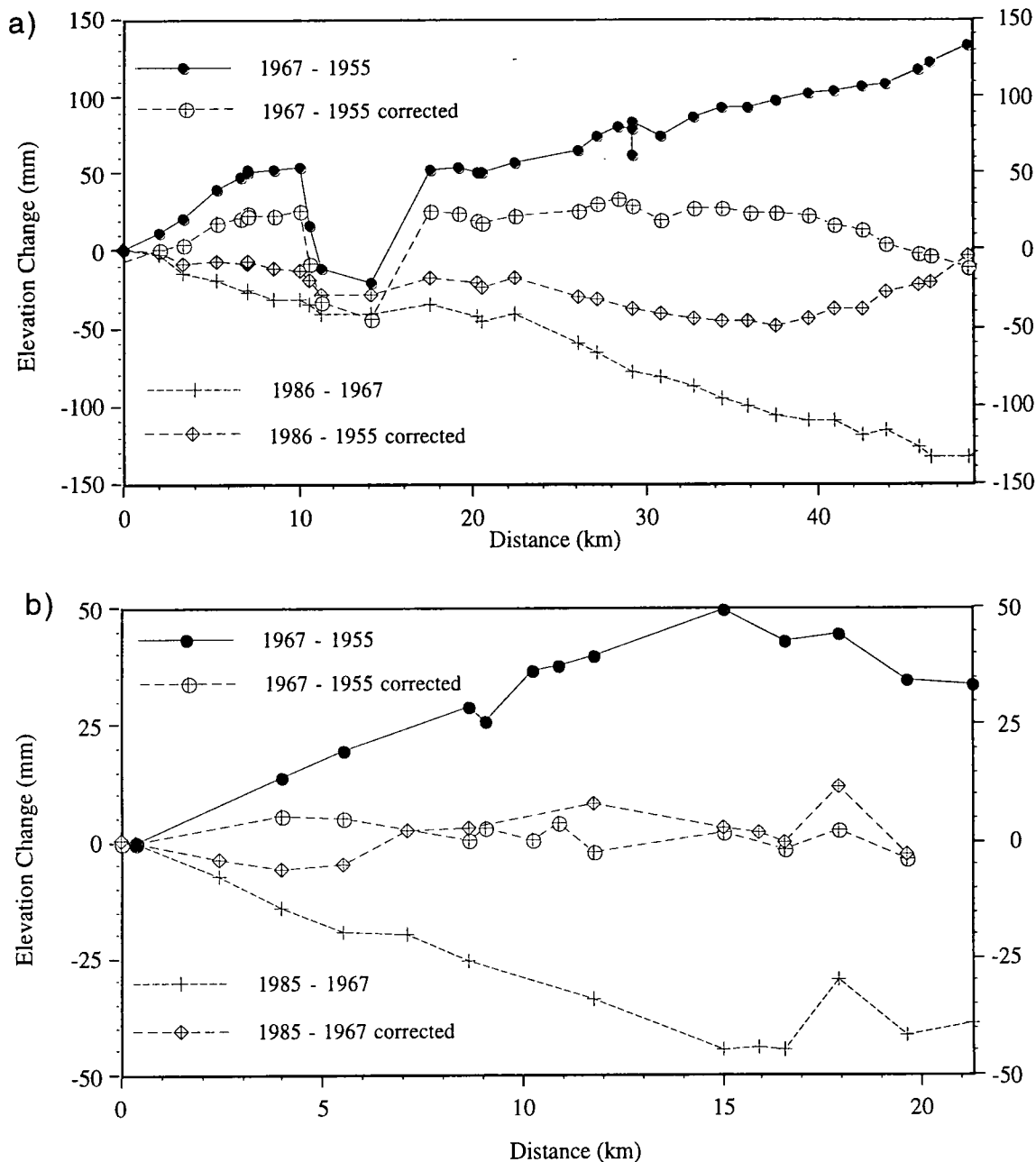


Figure 4.11 a) The elevation changes along line Dixie 1, calculated from the 1955, 1986 and corrected 1967 surveys. b) The elevation changes along line Dixie 2, calculated from the 1955, 1986 and corrected 1967 surveys.

Table 4.4 Other surveys made using rods 312-347 and 312-383.

Area	Year	Levelling Lines	N	MC (R)
San Antonio, Texas	1967	L20946, L20943	5	325±651 ppm (0.242)
Anthony, New Mexico	1967	L20952, L20955	6	540±16 ppm (0.998)
Gila Bend, Arizona	1967	L21089, L21029	38	-571±234 ppm (0.506)
Carrizo, New Mexico	1969	L21908	4	161±.3 ppm (1)

A refraction error could cause a systematic tilt such as is determined when the 1967 data are used. However, the two conditions that result in refraction errors, a different number of forward and backward measurements of each setup and long setup lengths, did not occur in the case of the 1967 levelling. The average sight length in the 1967 survey along line Dixie 1 was 38 m which is less than the maximum allowed length of 50 m (Holdahl, 1982). Of 187 sections measured, only ten had a different number of setups in the forward and backward runs, so no errors would arise due a difference in sight lengths for the two measurements. Refraction corrections calculated using equation 4.8 were examined. Since there is little or no cloud cover in Nevada from May to August it was assumed that the weather factor was 1.5. Knowing the refraction correction it is possible to calculate the temperature difference along the rod, δ . The temperature differences varied from 0.5 to 0.2° which are acceptable (Holdahl, 1982). The 1967 data are thus free from the two effects which result in an accumulation in error due to refraction. The systematic tilt indicated by the 1967 data is thus probably not due to refraction error.

The procedure under which the 1967 surveys were made was designed to reduce the effect of settlement. Measurements were made first of the backsight rod, which was assumed to have settled totally since it would have been in place a few minutes and then the foresight rod was measured very quickly before it began to sink. Since the number of turning points is proportional to the error accumulated through settlement (equation 4.9) the number of turning points in each section was regressed against the sum of the forward and backward measurements of the 1967 Dixie 1 line. The number of sections measured was 165. The correlation coefficient of turning points to each section error is 0.03, which indicates that the two variables are uncorrelated and suggests that settlement errors cannot account for the systematic errors.

4.3.2.4 Assignment of errors

The random errors in the 1955 surveys, as measured by misclosure, are larger than expected. The misclosure around the 157 km loop is +47 mm, almost three times the expected 17 mm misclosure (for $\alpha = 1.4 \text{ mm/km}^{1/2}$). The surveys were double-run and no large blunders are obvious in the data. The 1955 misclosure was therefore distributed around the loop and an α value of $3.5 \text{ mm/km}^{1/2}$ ascribed to this line (equation 4.1). The 1967 survey of line Dixie 1 (L21086) (Table 4.5) has a misclosure of 110 mm and the 1934 line (L1960) a misclosure of 100 mm when the forward and backward differences are summed. The misclosures of these surveys are larger than the allowable random error and equation 4.4 was used to calculate the relevant alpha values. The α value for L5797, a single run survey made in 1934 along line Dixie 2, was calculated by comparison with another 1934 survey, L1960. The α value for line USGS08 was determined from the

calculations given in the field notebooks (book A7903). For the more recent post-1980 lines values calculated by the NGS were used (Table 4.5).

Table 4.5 α and β tolerances for each of the Dixie Valley levelling surveys. Method by which α is calculated is denoted by a superscript: [†] taken from USCGS field notebooks, [§] calculated using equation 4.1, [¶] calculated from misclosure of the 1955 loop, [¥] calculated by comparing values from line L1960. ⁺ Supplied by the NGS.

Line	Year	Route	Class	α (mm)	β (mm)
USGS08	1908	Dixie 3	III	3.50 [†]	9
L1960	1934	Dixie 1	I/II	1.07 [§]	4
L5797	1934	Dixie 1	II	2.54 [¥]	8.4
L15586	1955	Dixie 1	I/II	4.00 [¶]	4
L15607	1955	Dixie 3	I/II	4.00 [¶]	4
L15588	1955	Dixie 2	I/II	4.00 [¶]	4
L21083	1967	Dixie 1	I/II	1.26 [§]	4
L21086	1967	Dixie 3	I/II	0.94 [§]	4
L21089	1967	Dixie 3	I/II	0.94 [§]	4
L21080	1967	Dixie 2	I/II	1.00 [§]	4
L24887	1985	Dixie 2	I/II	1.24 ⁺	4
L24985	1986	Dixie 1	I/II	1.24 ⁺	4

4.3.3 Triangulation data

Three triangulation surveys made before the 1954 earthquake sequence and a survey made one year after the sequence were used to calculate the coseismic angle changes. The observations include angles from the U.S. primary network, a large-scale triangulation network which covers the United States, and a second order network which densifies the primary. The data set consists of directional angle measurements. Eight points within the Dixie Valley network were surveyed in 1935 as part of a survey of the primary net. All the points lay west of the Stillwater Range (Figure 4.12). From December 1953, to January 1954, an extension of the primary net was surveyed. This survey spanned the Rainbow Mountains and the Clan Alpine Range (Figure 4.1). Coverage in Dixie Valley was sparse, only one point being measured in the Stillwater Range and Dixie Valley (point Horse). Twenty-nine points were measured and seven of the 1935 points were reoccupied. A second survey in 1954 began 2 days after the July 6, event in the Rainbow Mountains and continued until August 24, the date of the next event in that mountain range. This survey extended the network east of Fairview Peak. Twelve points measured earlier that year were remeasured. One baseline was measured by a geodimeter, North Shosone to Dee. All the stations observed in 1954 were re-surveyed in 1955 and two baselines, Twin to Alpine and Wonder to Grant were measured by geodimeter.

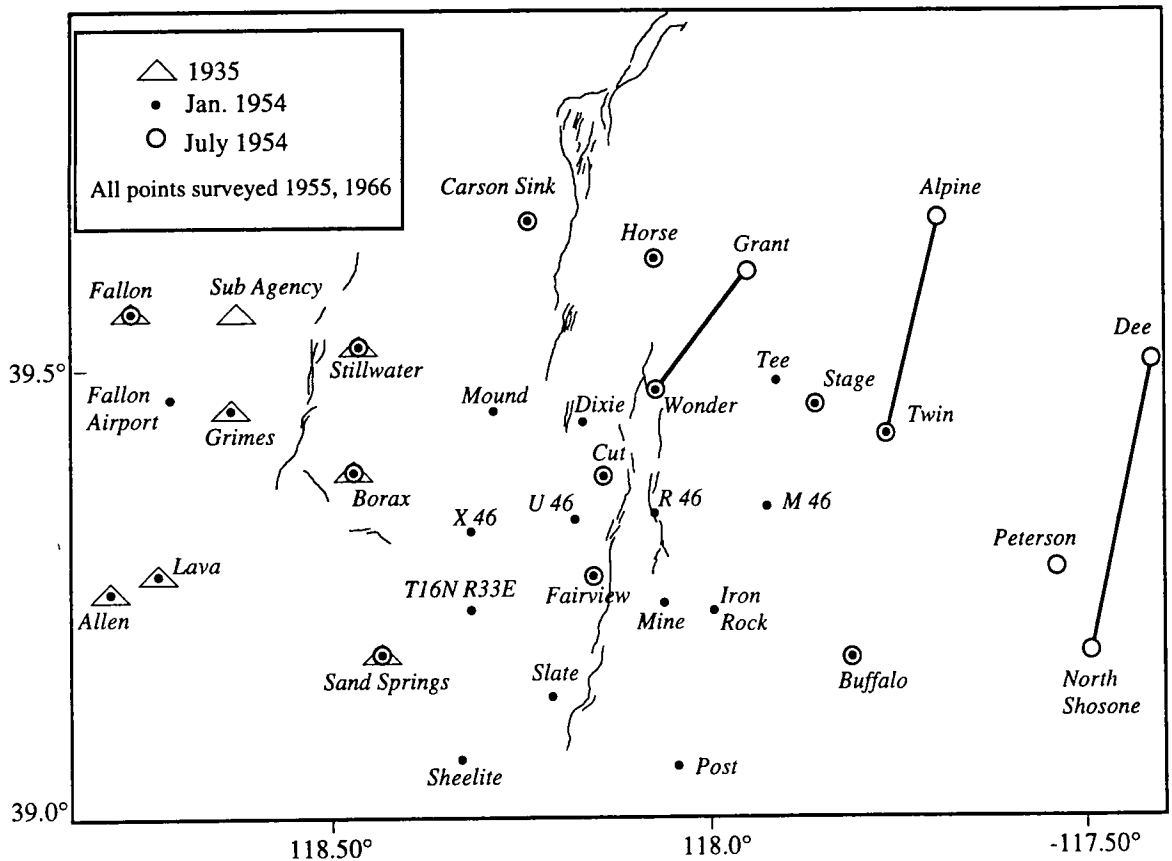


Figure 4.12 Map showing triangulation network and the years each point was occupied. See Figure 4.1 for regional location of this map. All points were resurveyed in 1955. Distances measured by geodimeter are shown as solid black lines.

In total there are 119 observations at 33 triangulation stations which constrain the horizontal coseismic deformation. The entire network was remeasured in 1966. The surveys made in 1935 and 1954 provide pre-seismic data. Including the 1935 survey allowed greater coverage of the Rainbow Mountain fault. The measurements made west of longitude 118.4°W in the second 1954 survey were not used to form the pre-seismic data set, since they are contaminated by deformation associated with the July and August Rainbow Mountain events. The 1955 survey constrains the coseismic deformation.

4.3.4 Data quality

4.3.4.1 Misclosures in the data set

The 1935 survey was a first-order survey of the primary network. The 1954 and 1955 surveys were carried out under first-order specifications for the primary network measurements and second-order class I specifications for the densification network. The surveys met the standard of first-order class II surveying for the primary network and second-order class I for the secondary network (Miller, 1967). Using a least squares adjustment by the method of variation of geographic coordinates Miller (1967) calculated the average misclosure, maximum correction to the measured angles and the probable

error of a single observation for the 1935, 1954 and 1955 surveys independently (Table 4.6). The triangulation data are of high quality and appear to be free of systematic errors. This is indicated by the misclosure of the triangles being within specified tolerances.

Table 4.6 Average misclosures and probable error of the 1935, 1954, 1955 and 1966 surveys from a least squares adjustment of the surveys.

Survey Year	Triangle Misclosure (seconds)		Maximum Correction (s)	Probable Error (s)
	Average	Maximum		
1935	0.91	2.33	1.37	0.35
1954	1.14	4.66	2.49	0.60
1955	1.36	4.24	2.00	0.50

4.3.4.2 Assignment of errors

In this study, angle changes at triangulation stations are modelled rather than derived quantities such as the displacement or strain fields which were used by Savage and Hastie (1969) and Snay *et al.* (1985) respectively. Coseismic angle changes are direct observations and no point needs to be fixed or minimally constrained during the coseismic period to calculate the coseismic angle changes. Thus, errors caused by rotation or dilation of the network are avoided. Although the triangulation data set used in this analysis is similar to that of Savage and Hastie (1969) and Snay *et al.* (1985) the observations modelled are different and formed directly from the measured data.

The standard error normally assumed for first order triangulation is 0.7 arcseconds and 1.4 arcseconds for second order. Rather than assume the specified errors for each order of surveying, the standard error for each angle measurement was used. In this way less weighting was given to data with larger uncertainties. The misclosures of the pre- and postseismic survey triangles were calculated. If a misclosure was larger than the specified tolerance (3 arcseconds for first-order surveying) then the error was distributed amongst the three measured angles. This was required for fourteen of the observations and of these, the largest error assigned was 1.23 arcseconds. If an angle was measured several times the weighted average of the measurement was used and the standard deviation of the errors associated with each measurement calculated. The mean standard deviations for the pre- and post-seismic surveys were 0.86 and 1.05 seconds respectively.

4.4 THE MEASURED COSEISMIC AND POSTSEISMIC DEFORMATION

4.4.1 Data constraining coseismic movements

The levelling data constraining the coseismic deformation were obtained by: (1) differencing the 1955 and 1934 surveys of line Dixie 1; (2) differencing the 1955 and 1935 surveys along line Dixie 2; and (3) differencing the 1955, 1950 and 1908 surveys of line Dixie 3. The errors assigned reflect the water withdrawal effects in the Fallon area and the loop misclosure of the 1955 levelling surveys (Table 4.5). The isolation of the 1967 surveys as those surveys which contained the systematic rod calibration error results in a data set from which the coseismic deformation can be extracted with confidence.

Differencing the 1955 and 1934 surveys along line Dixie 1 yields the vertical coseismic displacements parallel to the Rainbow Mountain and Fairview Peak faults (Figure 4.13a). The Rainbow Mountain fault offsets lie at 48 km along the line and the Fairview Peak fault offsets at 95 km. The data show that the east side of each fault was downthrown with respect to the west side. The measured coseismic offsets on the Rainbow Mountain fault are 14 cm. The offset measured across the Fairview Peak fault is up to 3 metres. The benchmark with the greatest vertical displacement on the downthrown side of the fault is not shown in Figure 4.13a but is used in modelling the deformation. Differencing the 1955 and 1934 surveys along line Dixie 2 yields the coseismic deformation along a line perpendicular to the Fairview Peak fault (Figure 4.13b). The deformation is that of subsidence to the north and uplift to the south of the fault. This signal is as would be expected for right-lateral faulting where the region to the north-east of the fault experiences extension and therefore subsidence occurs and the region to the south-east experiences compression and therefore uplift. Differencing the 1955, 1950 and 1908 surveys along the line Dixie 3 yields the coseismic deformation across the Fairview Peak and Dixie Valley faults (Figure 4.13c). The maximum measured coseismic offset across the Dixie Valley fault is 2.1 metres. Where line Dixie 3 crosses the Rainbow Mountain fault the maximum measured offset is 18 cm.

The triangulation data constraining the coseismic deformation were obtained by differencing the 1955, 1954 and 1935 survey measurements. Figure 4.14 shows the coseismic deformation computed by Miller (1967). The displacement vectors shown in Figure 4.14 were calculated by holding one station (Sand Springs) and one azimuth (Sand Springs to Carson Sink) fixed. In the modelling method used in this study angle changes rather than displacement vectors are modelled. Displacement vectors, however, illustrate the coseismic deformation better than angle changes. The coseismic displacement vectors show that the coseismic deformation contained a significant

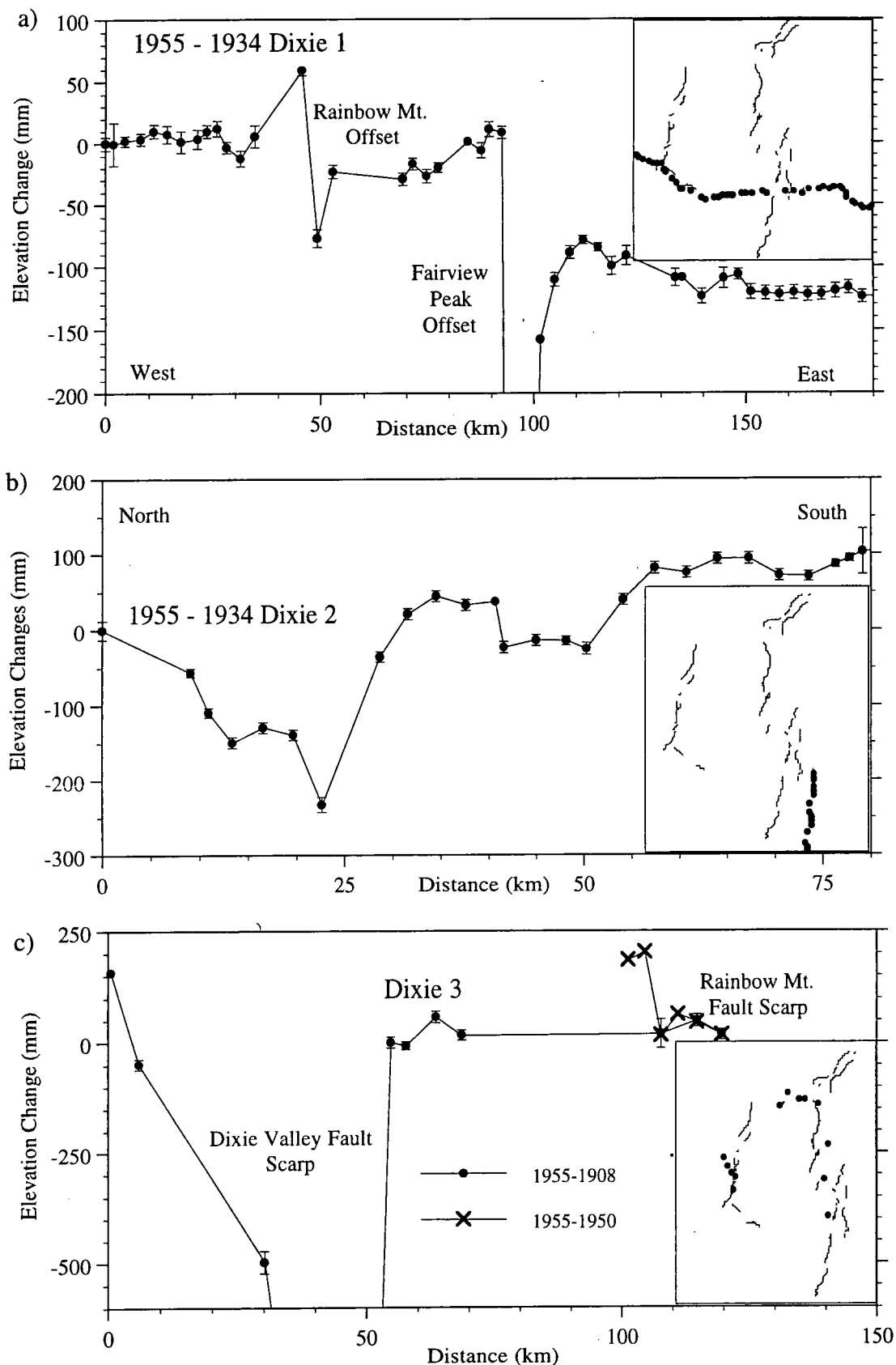


Figure 4.13 a) Coseismic deformation measured along line Dixie 1. 1σ errors are shown. Inset shows location of the line (c.f. Figure 4.1). b) Coseismic deformation measured along line Dixie 2. c) Coseismic deformation measured along line Dixie 3.

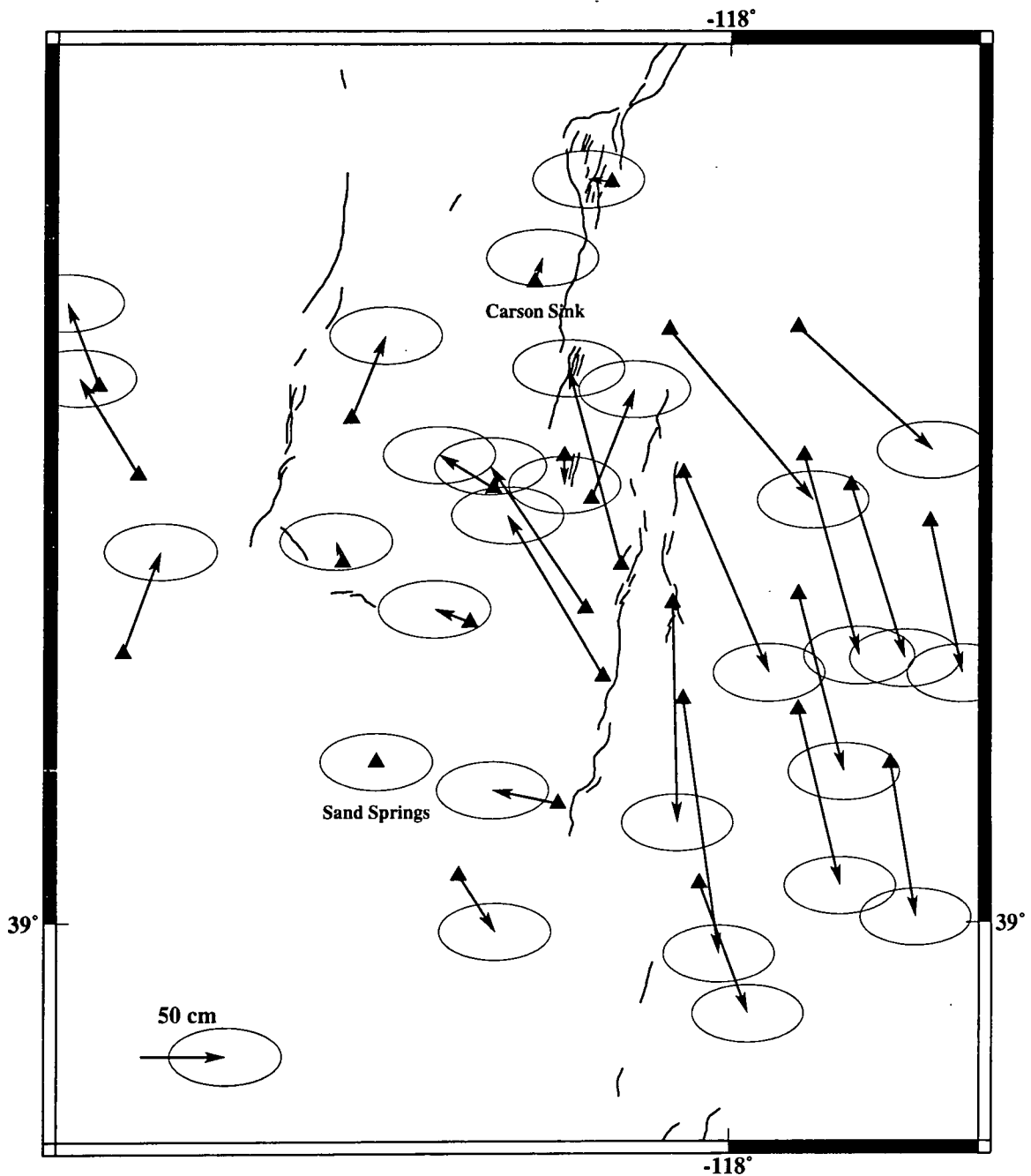


Figure 4.14 Coseismic displacement vectors calculated by Miller (1967). One sigma errors are shown.

component of right-lateral motion. Displacements relative to Sand Springs are largest around the Fairview Peak fault where they are up to 1.59 m in the north-south direction and 0.86 m in the east-west. The overall form pattern of deformation is north-northwest to south-southeast extension.

4.4.2 Data constraining postseismic movements

The postseismic deformation along line Dixie 1 is shown in Figure 4.15. Elevation changes are calculated between benchmarks which are common to the 1986, 1978, 1973 and 1955 surveys. Uplift in the vicinity of the Fairview Peak fault occurred after the 1954 earthquake and a subsidence feature of up to 80 mm formed between the Fairview Peak and West Gate faults between 1955 and 1973. Since the 1967 survey contains rod miscalibration errors it is not used in the analysis of the small postseismic deformation signal.

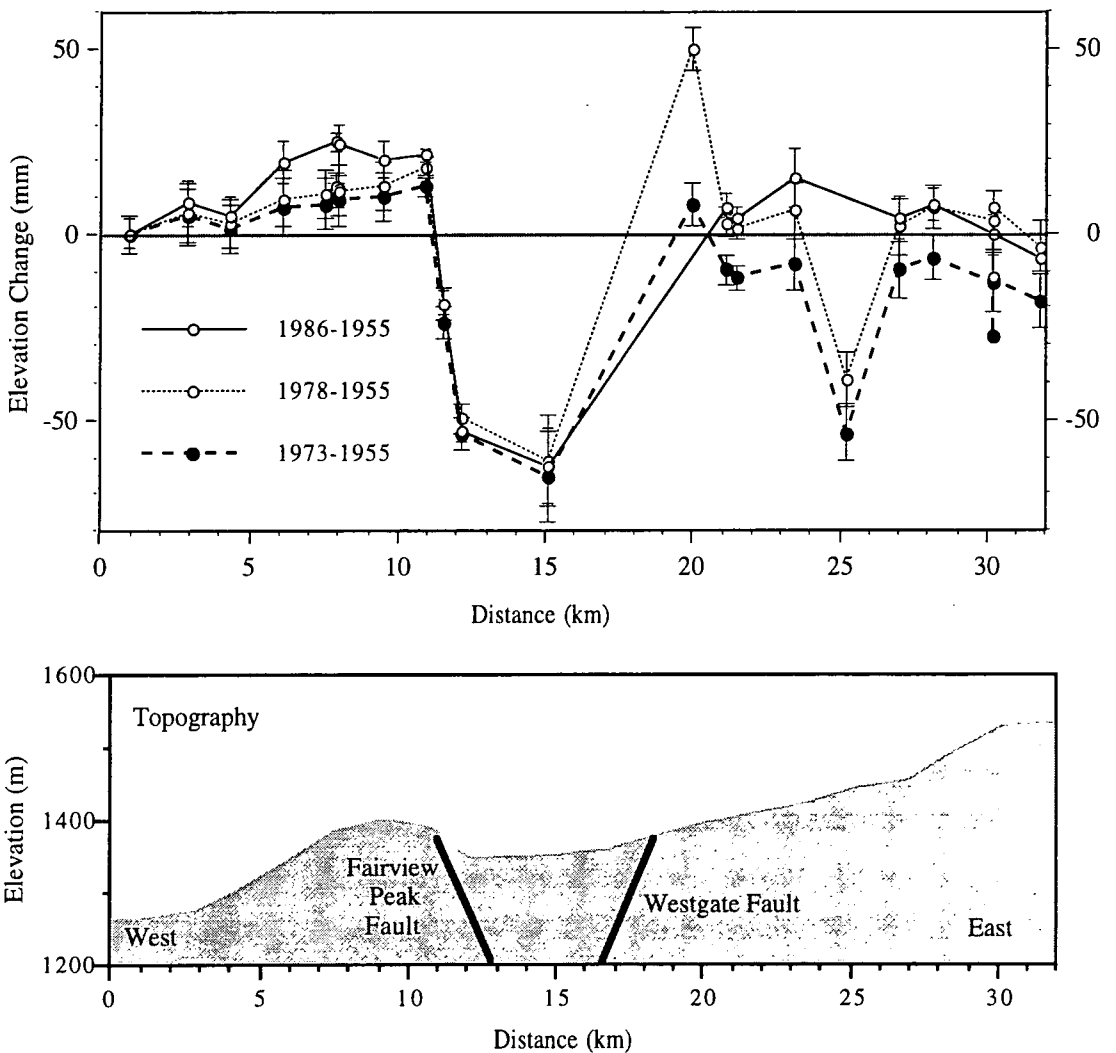


Figure 4.15 Postseismic deformation measured at benchmarks common to the 1986, 1978, 1973 and 1955 surveys along line Dixie 1.

4.5 SUMMARY

The geodetic data set that constrains deformation associated with the 1954 earthquake sequence consists of levelling and triangulation data. The levelling data are affected by non-tectonic deformation due to water withdrawal. This is confined to the Fallon area, spans about 40 km and is 30 km from the Fairview Peak fault rupture. Using water level records between 1977 and 1992, and observed trends between 1904 and 1992, it is possible to quantify the effect of subsidence due to water withdrawal and remove it from the data. Using levelling data which had not previously been analysed systematic errors were quantified and corrected. A large error of 150 ± 30 ppm in the 1967 surveys was traced to a miscalibration of the levelling rods used. The accuracy of the levelling data was reassessed from the misclosure of levelling loops and forward and backward runs of the lines. The triangulation data are of high quality and appear to be free of systematic errors. Errors associated with each angle measurement were calculated from the standard deviation of the measurements of each angle and the misclosure of triangles. Combining the levelling and triangulation data the co- and postseismic deformation fields of the Fairview Peak-Dixie Valley sequence of earthquakes are constrained.

CHAPTER 5

MODELLING OF THE COSEISMIC DEFORMATION FIELD OF THE 1954 RAINBOW MOUNTAIN - FAIRVIEW PEAK - DIXIE VALLEY, NEVADA EARTHQUAKE SEQUENCE

5.1 INTRODUCTION

Measurements of surface deformation caused by an earthquake can be used to determine subsurface fault geometry and the amount of coseismic slip. The observations of coseismic deformation associated with the 1954 earthquake sequence in Dixie Valley, Nevada, are used here to infer the fault geometries and slip associated with the events. The fault geometries are found by determining the fault parameters that best fit the levelling and triangulation data in the least squares sense and by simultaneously inverting both data types for the amount of strike-slip and dip-slip motion. The optimum fault model, *i.e.*, the model that minimises the difference between observed and computed motions, is determined using a gradient search of parameter space. The data are then inverted using the single value decomposition method since this can produce the 'inverse' of a singular matrix and can be used as a tool to examine how well the slip values can be resolved given the data resolution.

This study differs from previous analyses of the Dixie Valley coseismic geodetic data set in that the levelling data have been properly corrected and that both levelling and triangulation data are inverted simultaneously to find the fault geometries. The coseismic observations consist of angle changes between triangulation stations and relative height changes between levelling benchmarks. Angle changes are modelled as they are direct observations rather than a derived quantity, such as the displacement field, and appropriate weighting can be applied to each observation. Also, unlike the displacement field, angle changes can be modelled without arbitrarily fixing any position. Relative

height changes between levelling benchmarks are modelled rather than absolute benchmark height changes because these are free of datum offsets between surveys.

The signal to noise (S/N) ratio of the data may be calculated using:

$$S/N = \left[\frac{1}{N} \sum_i \left(\frac{y_i}{\sigma_i} \right)^2 \right]^{\frac{1}{2}} \quad (5.1)$$

where y_i are the observations, σ_i the associated uncertainties and N is the total number of observations. The S/N ratios of the levelling and triangulation data are 33 and 12 respectively. The combined data set has an S/N ratio of 22. The large S/N ratio of the levelling data results from some sections crossing the fault having large elevation changes.

5.2 FAULT GEOMETRIES AND SLIP ESTIMATES FROM PREVIOUS GEODETIC ANALYSES

Several authors have forward-modelled or inverted the coseismic levelling and triangulation data to obtain the fault geometries and/or the coseismic slip vectors. All previous work has modelled either the levelling or triangulation data separately. This study involves a simultaneous inversion of triangulation and levelling data for slip during all the major earthquakes in the sequence. Table 5.1 presents the data, method used, and number of earthquakes examined in previous studies. In all the studies where fault geometries or coseismic-slip estimates were derived, uniform slip on planar surfaces embedded in an elastic half space were assumed.

Savage and Hastie (1969) inverted triangulation and levelling data separately to determine the coseismic slip and fault geometry of the Fairview Peak fault. The results were similar to those of earlier modelling of the levelling data (Savage and Hastie, 1966). The triangulation data consisted of the horizontal displacement vectors of several triangulation stations measured between 1953 and 1958 and computed by Whitten (1957). The vectors were produced by comparing pre- and postseismic surveys and assuming there was no motion between stations at the extremities of the network. Both data sets indicated a fault which had a width of 8 ± 2 km and a strike of N9°E (Table 5.2). The strike of the model fault was consistent with the orientation of scarps, which trended a few degrees east of north, but it was not consistent with the focal mechanism of the Fairview Peak earthquake which gave a strike of N10°W (Romney, 1957; Doser, 1986).

The triangulation data were fitted best by 2.9 ± 0.4 m of right-lateral strike-slip motion, 2.3 ± 0.4 m of dip-slip motion and a fault length of 50 km. The levelling data were best fit by 2.8 ± 0.1 m of dip-slip motion. The fault length could not be determined from the levelling data and so was assumed to be 50 km according to the result found by modelling the triangulation data. The difference in the vertical slip estimates resulted because strike-slip motion was not modelled using the levelling data.

Table 5.1 Previous studies which have derived displacement vectors, fault geometries or coseismic slip values from geodetic data. The data column indicates whether triangulation, T, or levelling, L data were used. The leftmost column gives which parameters were obtained. FP: Fairview Peak; RM: Rainbow Mountain; WG: West Gate; GK: Gold King; DV: Dixie Valley; -: no particular event was investigated, but calculations were made for the entire geodetic network.

Author	Data	Method	Earthquake investigated	Estimates
Whitten, 1957	T	Calculated displacement at triangulation stations	-	Coseismic slip vectors
Savage and Hastie, 1966	L	Forward modelling of data	FP	Fault geometry, Coseismic slip
Miller, 1967	T	Calculated displacement at triangulation stations	-	Coseismic slip vectors
Savage and Hastie, 1969	L T	Inversion of data (Data inverted separately)	FP	Fault geometry, Coseismic slip
Savage and Church, 1974	L	Analyses of data quality, forward modelling of postseismic data	FP	Postseismic slip
Snay et al., 1985	T	Forward modelling	RM, FP, WG, GK, DV	Fault geometry, Coseismic slip
This study	L T	Simultaneous inversion of both data sets.	RM, FP, WG, GK, DV	Fault geometry, Coseismic slip

Table 5.2 Fault parameters derived by Savage and Hastie (1969) and Snay *et al.* (1985). * The parameter was constrained to this value.

Fault	Displacement (m)		Length (km)	Strike	Dip	Width (km)
	Horizontal	Vertical				
Savage and Hastie, 1969						
Fairview Peak	2.9±0.4	2.3±0.4	50	N9°E	57±6°E	8±2
Snay <i>et al.</i> 1985						
Fairview Peak (Shallow fault)	3.6±0.4	2.3±0.5	34±4	N12±3°E	63±10°E	5±1.5
Fairview Peak (Deep fault)	0.8±0.4	1.6±0.7	58±40	N13±7°W	59±17°E	20±2
West Gate-Gold King	1.3±0.5	0.5±1.0	23±16	N7±3°E	70±23°W	5*
Dixie Valley	-0.3±1.1	2.4±1.6	42*	N6±17°E	60°E*	15*
Rainbow Mountain (Five fault model)	0.6±.6	5.5±3.0	112*	N7±7°E	68±5°E	7±3
Rainbow Mountain (Six fault model)	0.6±0.4	0.4±0.5	35±28	N13±30°E	35±50°E	20*

Snay *et al.* (1985) simultaneously estimated fault geometry and coseismic slip for all the major earthquakes in the sequence by forward modelling the triangulation data. The data consisted of displacement vectors at each triangulation point. To compute these vectors, motion at stations at the extremity of the network was minimally constrained in network adjustments between the two surveys. The displacement vectors were then translated into shear strains and used as para-observations to determine fault parameters and coseismic slip. Each fault parameter was varied systematically until strains comparable to those observed were modelled. Two sets of fault parameters were produced, one where five planar surfaces represented the major faults (the five fault model) and a second where a hypothetical fault between Rainbow Mountain and the Stillwater Mountain Range was included additionally (the six fault model).

In both models the deformation around Fairview Peak was best fitted by assuming a two-fault structure. A shallow fault with lower depth of 5 km overlay a deeper fault with an upper depth of 2 to 4 km and a lower depth which was constrained to be 20 km. While the strike of the upper fault is similar to that of the surface scarp, the lower fault has a strike of 1° to 13° west of north. The upper depth calculated for the deep Fairview Peak fault varied from 2.2±2 km to 3.9±1.5 km while the lower depth was 20±50 km. The



Rainbow Mountain fault in the five fault model dips at $68^\circ \pm 5^\circ \text{E}$ and has a lower depth of 6.7 ± 3 km. The length of the fault was constrained to be 112.4 km and would have been greater if not fixed at this value. This length resulted in an unrealistic seismic moment of 1.45×10^{20} N m. To reduce this large moment a sixth, hypothetical fault was introduced. The vertical motion required on this fault, however, was 1.8 m, and is not observed in the coseismic levelling data which crosses it. The dips of the Rainbow Mountain fault and the hypothetical fault were then $35^\circ \pm 5^\circ \text{E}$ and $42^\circ \pm 16^\circ \text{W}$. The position, depth and the amount of slip on the Dixie Valley fault were the only parameters determined for that fault. The lower fault depth was suggested to be 5.4 ± 4.5 km. Vertical slip on this fault was much greater than lateral slip. The West Gate and Gold King faults were modelled as one fault. The depth was constrained to 5 km in both solutions. The combined fault dipped steeply to the west at $70^\circ \pm 23^\circ$ to $80^\circ \pm 13^\circ$. Strike-slip motion was greater than vertical motion on this fault.

5.3 METHOD

5.3.1 Calculating coseismic displacement fields

The displacement fields caused by uniform slip on a rectangular fault embedded in an elastic half-space can be computed numerically using closed analytical expressions. Steketee (1958) showed that the displacement field, u_i , produced by a dislocation Δu_j across a surface Σ in a uniform elastic half-space is given by the Volterra formula:

$$u_i = \frac{1}{F} \iint_{\Sigma} \Delta u_j \left[\delta_{jk} \lambda \frac{\partial u_i^j}{\partial \xi_k} + \mu \left(\frac{\partial u_i^j}{\partial \xi_k} - \frac{\partial u_i^k}{\partial \xi_j} \right) \right] \nu_k d\Sigma \quad (5.2)$$

where λ and μ are Lamé constants, ν_k is the direction cosine of the normal to the surface element $d\Sigma$, δ_{jk} is the Kronecker delta function, and u_i^j is the i th component of displacement caused by the point force F at (ξ_1, ξ_k, ξ_j) acting in the j th direction. The point force displacements are given in Press (1965). Equations describing the displacement field due to uniform slip on a vertical finite fault are given by Chinnery (1961) and for inclined faults by Savage and Hastie (1966) and Manshina and Smylie (1971). Expressions for displacements, strains and tilts for strike-slip, dip-slip and tensile faults were presented by Okada (1992).

The displacement field is a non-linear function of the dip, depth, length and strike of the fault and will vary with these parameters. However, the displacement at a point due to slip on a rectangular finite fault is proportional to the amount of slip on the fault surface.

If $\vec{m}(\gamma)$ is the slip vector at the point γ on a fault surface Σ then equation 5.2 can be expressed as:

$$u(i) = \iint [G(i, \Sigma) \vec{m}(\gamma)] d\Sigma \quad (5.3)$$

where $u(i)$ is the displacement at a point p on the Earth's surface and G is a matrix of functions that describes the fault geometry and elastic properties of the Earth. If uniform slip across a finite planar, fault surface is assumed then equation 5.3 can be linearised and written as $u(i) = Gm$. Because of the linearity of the equation, if there is slip on more than one fault, the total displacement at a point is the sum of the displacements due to each event. The total displacement u at point i due to slip on M faults is expressed as:

$$u_i = \sum_{j=1}^M G_{ij} m_j \quad (5.4)$$

The vertical coseismic deformation field following a normal faulting event is one of uplift on the footwall of the fault and subsidence on the hanging wall (Figure 5.1a). The ratio of uplift to subsidence is dependent on the fault dip. For a vertical fault the offsets are about equal, the amount of uplift however decreases with decreasing dip. The vertical deformation tends to zero at about 2.5 fault widths when the fault reaches the surface. The uplift becomes broader and the sharp discontinuities over the fault trace disappear when the fault is buried below the surface (Figure 5.1b).

The horizontal deformation field in the direction perpendicular to the fault is much broader than the vertical deformation field (Figure 5.2a) and does not tend to zero until about 5 fault widths from the fault. The horizontal deformation field for a fault which reaches the surface is characterised by a sharp discontinuity over the fault trace and a local minimum over the lower edge of the fault on the downthrown side. There is little difference in the width of the horizontal deformation field for faults which are buried (Figure 5.2b) and faults which reaches the surface. The sharp discontinuity disappears and the magnitude of the extension decreases for a buried fault.

5.3.2 The optimum fault model

Fault geometries were found in this study by determining the fault parameters which best fit the levelling and triangulation data in the least squares sense, simultaneously inverting for the magnitude of strike-slip and dip-slip motion. The goodness of fit was assessed by calculating the reduced chi-squared statistic:

$$\chi_v^2 = \frac{1}{v} \sum_{i=1}^n \left\{ \frac{1}{\sigma_i^2} (y_i - c_i)^2 \right\} \quad (5.5)$$

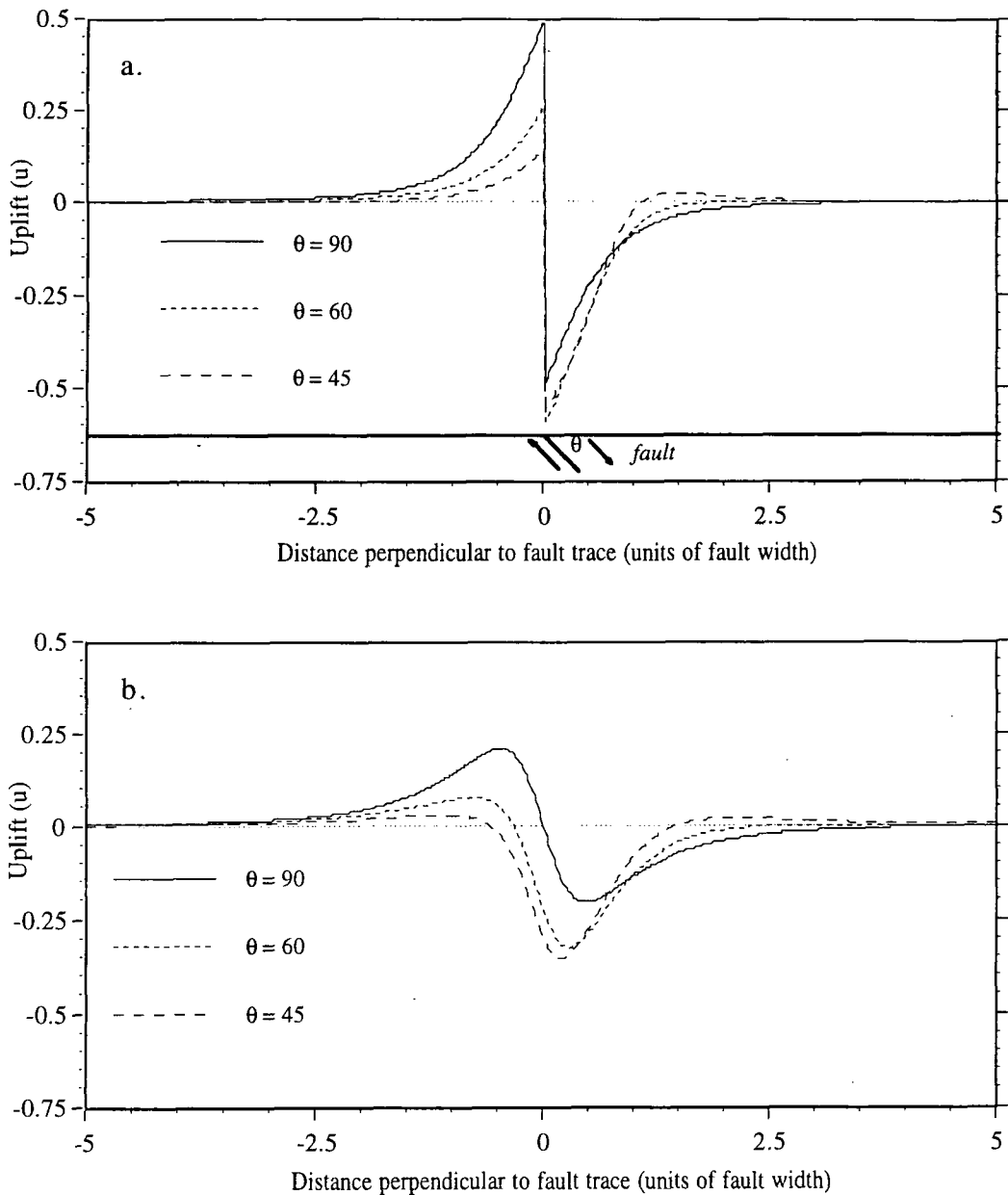


Figure 5.1 Surface displacement due to slip (u) on a fault of length L and width $L/2$ for fault dips of 90° , 60° and 45° . a) Vertical displacement, upper fault depth = 0. b) vertical displacement, upper fault depth = $L/4$.

where y_i is the observed value, c_i is the computed, ν is the number of degrees of freedom, and σ_i is the associated uncertainty. The variance of each data point is normalised by its standard deviation, which gives more weight to data with smaller uncertainties and allows simultaneous inversion of parameters in different dimensions, *e.g.*, arcseconds and mm. The optimum model is that which gives the lowest residuals for the observations.

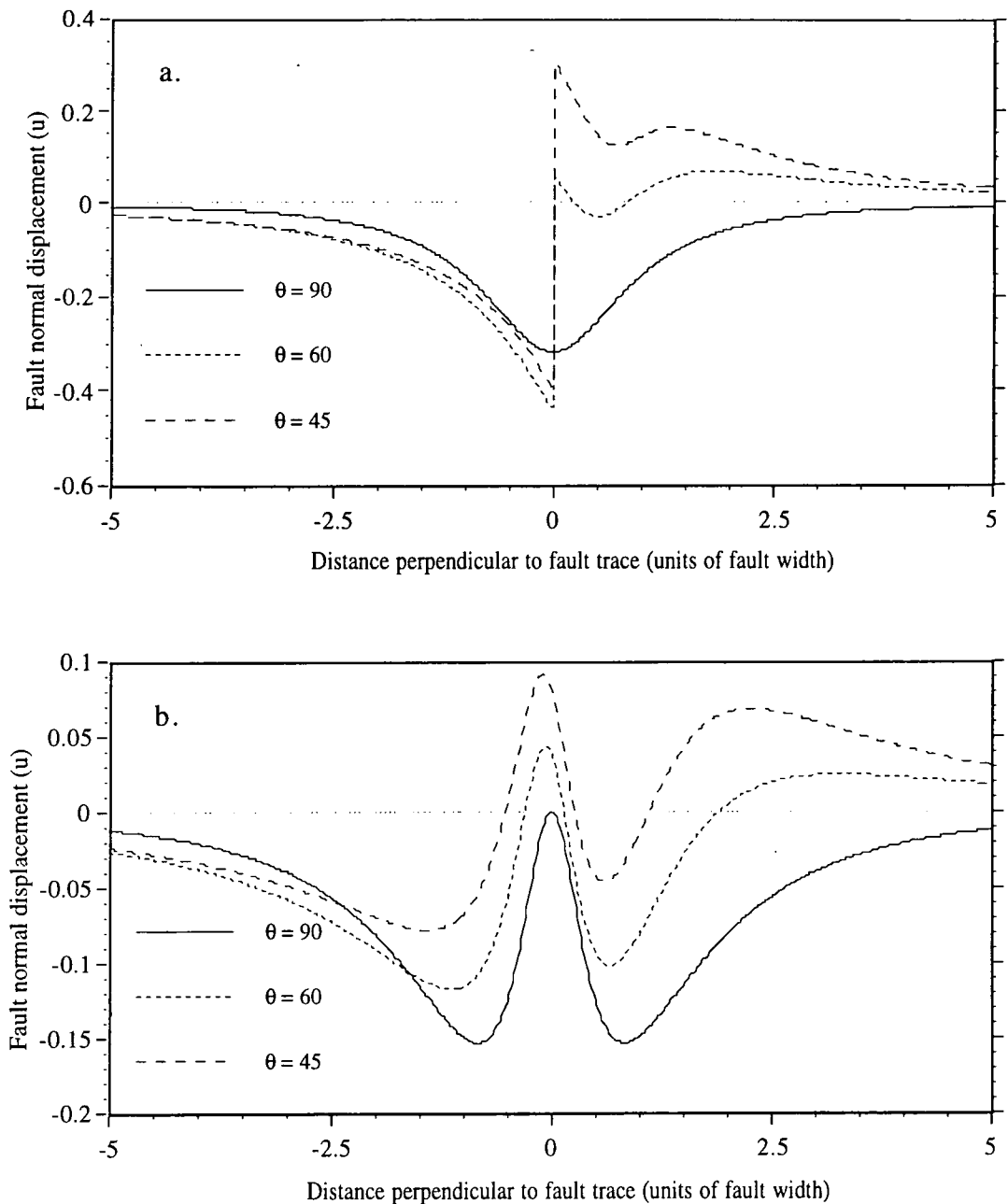


Figure 5.2 Surface displacement due to slip (u) on a fault of length L and width $L/2$ for fault dips of 90° , 60° and 45° . a) Horizontal displacement, upper fault depth = 0, b) horizontal displacement, upper fault depth = $L/4$.

The coseismic displacement field is a non-linear function of the fault parameters. A non-linear function is one which cannot be expressed as a sum of terms with parameters appearing only as coefficients of terms. This non-linearity results in local minima in the value of χ^2 as the parameters vary. The most rigorous way to find the optimal fault geometry is to conduct a grid search through parameter space. This deals with the problem of the existence of local minima. However, the large number of free parameters in this problem, seven on each of five faults, makes a grid search computationally impractical. A gradient search of the parameter space was made. This method finds the minimum value of χ^2 by varying all the parameters simultaneously and adjusting the

relative magnitudes of the variations so the direction of searching is along the direction of maximum change in χ^2 . The method used was that of Bevington (1969).

The observations can be represented by:

$$y(obs) = a_0 + \sum_{j=1}^n a_j X_j \quad (5.6)$$

where X_j are functions of the strike, dip depth and length and a_j are the fault parameters. The gradient $\nabla\chi^2$ is expressed as:

$$\nabla\chi^2 = \sum_{j=1}^n \left[\frac{\delta\chi^2}{\delta a_j} \hat{a}_j \right] \quad (5.7)$$

where \hat{a}_j is a unit vector in the direction of the a parameter axis. Each parameter is incremented independently and the first derivative calculated numerically using:

$$(\nabla\chi^2)_j = \frac{\partial\chi^2}{\partial a_j} \approx \frac{\chi^2(a_j + f\Delta a_j) - \chi^2(a_j)}{f\Delta a_j} \quad (5.8)$$

where Δa_j is the step size increment of each parameter. To calculate the partial derivatives the parameters are incremented by only a fraction of the step size f . The size of the increment should be about 10% of the step size for a detailed examination of the parameter space. Because the parameters have different dimensions each parameter is divided by its step size and the dimensionless parameter b_j , where:

$$b_j = \frac{a_j}{\Delta a_j} \quad (5.9)$$

The partial derivative with respect to b_j is calculated as:

$$\frac{\partial\chi^2}{\partial b_j} \approx \frac{\chi^2(a_j + f\Delta a_j) - \chi^2(a_j)}{f} \quad (5.10)$$

A dimensionless gradient γ_j of unit magnitude can then be defined as:

$$\gamma_j = \frac{\delta\chi^2}{\delta b_j} \cdot \left(\sum_{j=1}^n \left(\frac{\delta\chi^2}{\delta b_j} \right)^2 \right)^{-1/2} \quad (5.11)$$

Using a dimensionless gradient allows parameters of different dimensions to be increased simultaneously by the same relative magnitude δa_j , given by $\delta a_j = -\gamma_j \Delta a_j$. To begin with the search the value of χ^2 is calculated for the starting parameters. The variation of χ^2 in the neighbourhood of the starting point is then calculated using equation 5.10 and the dimensionless gradient γ_j for each parameter determined. Each parameter is then incremented by δa_j . The χ^2 value is calculated at the new point. If χ^2 is larger at $a + \delta a$ than at a then the step size Δa_j is reduced, the gradient components γ_j are recomputed and the process repeated. If it is smaller, then searching continues along this gradient. When the minimum has been straddled then the search terminates.

The gradient search deals with the non-linearity of the problem but its disadvantage is that it is dependent on the starting model. Because the number of dimensions of the problem are so large there are many minima in parameter space and if the starting point is far from the global minimum the latter may not be found. However, using χ^2 as a measure of the goodness of fit enables the model fit to be quantitatively assessed.

5.3.3 Inversion of a mixed-determined matrix

5.3.3.1 Single value decomposition

Single Value Decomposition (SVD) (Lanczos, 1961) was used to invert the data as this method finds the inverse of a mixed-determined matrix and determines how well slip can be resolved from the data distribution. SVD was first used to invert geophysical data by Backus and Gilbert (1968) and its power as a tool to study the resolution of the model parameters is described by Jackson (1972) and Thatcher (1979).

Using equation 5.4 the displacement at N points caused by slip on M faults is written as:

$$u = Gm \quad (5.12)$$

where u is a matrix of dimension Nx1 and G an NxM partial derivative matrix. The matrix m of slip values associated with each fault is one of dimension Mx1. The column vector u represents the data space S(d), and m the model parameter space S(m). Each value in m represents the amount of slip on each fault. To solve for m both sides of equation 5.12 are multiplied by a matrix G^{-s} such that:

$$\hat{m} = G^{-s}u = G^{-s}Gm \quad (5.13)$$

where \hat{m} is the solution matrix. G^{-s} , the 'inverse' of G , is considered a good inverse if GG^{-s} equals an NxN identity matrix, $G^{-s}G$ equals an MxM identity matrix and the

uncertainties in \hat{m} are not too large (Jackson, 1972). $G^{-s}G$ is a measure of the uniqueness of the solution while GG^{-s} is a measure of how well the model fits the data.

The problem is often mixed-determined. A problem is overdetermined if a unique solution cannot be found because the number of data is greater than the number of model parameters. If the problem is overdetermined some of the solutions to Gm will not span the entire data space $S(d)$ but only a portion $S_p(d)$ of it. Data lying outside the space $S_p(d)$ will not influence the final solution. An underdetermined problem occurs when there are insufficient data to solve the problem. The data can then only yield information on some of the model parameters. In this case the data are unable to resolve slip on some of the faults. These model parameters are said to fall into the null space of $S(m)$ while the others fall into resolvable space, $S_p(m)$. A mixed-determined problem occurs when some of the model parameters are overdetermined and others underdetermined. If a matrix is mixed-determined then it will be singular. Because equation 5.12 is mixed determined and SVD allows an inverse of a singular matrix to be determined, this method is used to determine an 'inverse' for the G matrix.

Any $N \times M$ matrix can be decomposed into:

$$G = UAV^T \quad (5.14)$$

where U represents an $N \times J$ set of eigenvectors which span the data space, V represents a $J \times M$ matrix of eigenvectors which spans the model parameter space and A represents a square diagonal matrix of eigenvalues (Lanczos, 1961; Menke, 1984). The eigenvalues are usually written in order of decreasing absolute value and the eigenvectors in U and V^T ordered accordingly. Equation 5.14 can be re-written as:

$$G = U \begin{bmatrix} \Lambda_p & 0 \\ 0 & 0 \end{bmatrix} V^T \quad (5.15)$$

where Λ_p forms the diagonal matrix of non-zero eigenvalues. It is the zero eigenvalues which cause the matrix to be singular. Any information not in the first p columns of U and first p rows of V^T are not 'seen' by the model or are insensitive to the model. The inverse of G is then found by determining G^{-s} :

$$G^{-s} = (U_p \Lambda_p V_p)^{-1} = V_p \Lambda_p^{-1} U_p^T \quad (5.16)$$

where V_p and U_p^T are the eigenvectors corresponding to the non-zero eigenvalues. The solution to $u = Gm$ is then:

$$\hat{m} = V_p \Lambda_p^{-1} U_p^T u \quad . \quad (5.17)$$

$V_p \Lambda_p^{-1} U_p^T$ is called the natural generalised inverse of G . The natural generalised inverse always exists since the zero eigenvalues are not used.

If all the eigenvalues are used, *i.e.*, if p equals the number of model parameters M , then the solution of $u = Gm$ reduces to that of a weighted least squares inversion. The least squares procedure may be described as finding the solution vector \hat{m} which minimises the residual vector ε , *i.e.*,

$$|\varepsilon|^2 = |Gm - u|^2$$

or,

$$|\varepsilon|^2 = (Gm - u)^T (Gm - u) \quad . \quad (5.18)$$

Differentiating with respect to m^T and setting the result equal to zero yields, $G^T Gm = G^T u$ and the solution vector \hat{m} is:

$$\hat{m} = [G^T G]^{-1} G^T u \quad . \quad (5.19)$$

Substituting equation 5.14 into equation 5.19, \hat{m} is expressed as:

$$\hat{m} = [V \Lambda^2 V^T]^{-1} V \Lambda U^T u \quad . \quad (5.20)$$

This simplifies to $\hat{m} = V_p \Lambda_p^{-1} U_p^T u$. Therefore, as long as all the eigenvalues are used and the G matrix is non singular, the inversion process becomes that of a weighted least squares inversion.

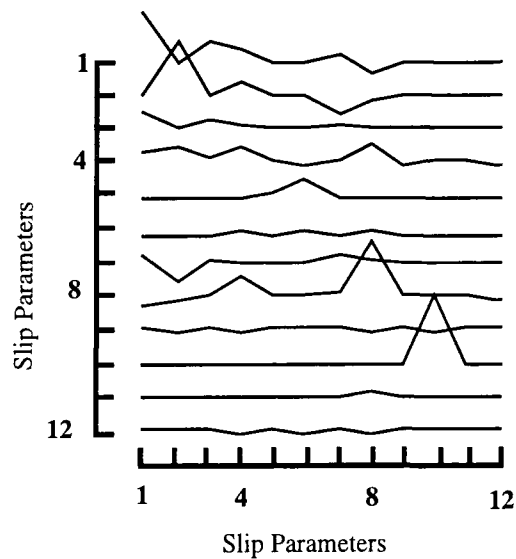
The information density matrix $S = GG^{-s}$ defines the independence of the data or how well the model fits the data. It is defined as $S = U_p U_p^T$. The model resolution matrix $R = G^{-s} G$ is defined as:

$$G^{-s} G = \{V_p \Lambda_p^{-1} U_p^T\} \{U_p \Lambda_p V_p^T\} = V_p V_p^T \quad (5.21)$$

The resolution matrix R maps the set of true parameters m onto the solution vector \hat{m} . If the model parameters are uniquely determined, or perfectly resolved, then $R = V_p V_p^T = I$. If R is not the identity matrix then each element in \hat{m} is a weighted sum of the columns of R with the weighting factors given values in m for any solution of $u = Gm$. Each column represent the resolvability of one model parameter from the rest. For example, the entry r_{ij} represents the resolvability of slip parameter i from parameter j .

Figure 5.3a is a graphic illustration of a resolution matrix. The numbers in each row of the matrix are represented as a line. A sharp peak represents a value of 1 in the resolution matrix. In Figure 5.3a the first, second, eighth and tenth parameters are resolved (on lines 1, 2, 8, and 10). Each row of R is the best fit to the corresponding row in the identity matrix. A solution which does not use all the eigenvalues is non-unique and dependent on the starting slip values. To get a unique solution, estimates for unresolvable parameters must be found from another source and then excluded from the inversion process. The full eigenvalue solution is then found and the result is independent of the starting values.

a.



b.

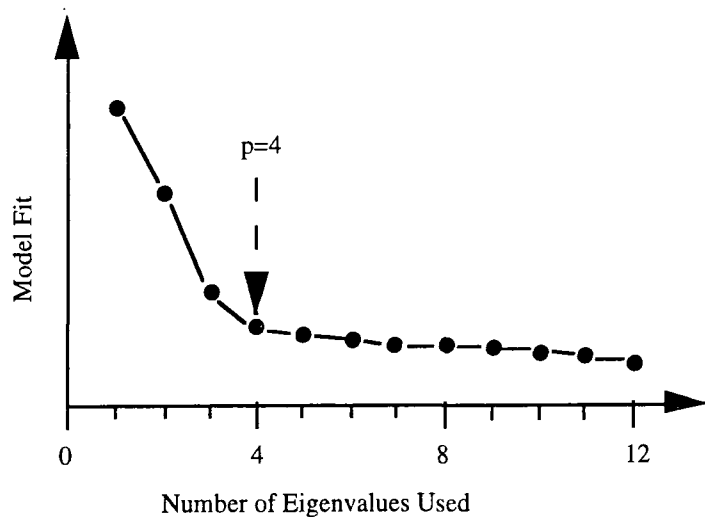


Figure 5.3 a) A graphic illustration of a resolution matrix. The matrix represented is of dimension 12×12 . The maximum value is represented as 1 and occurs on lines 1, 2, 8 and 10. b) The model fit versus number of eigenvalues used in calculating the solution of $u = Gm$. The cut-off eigenvalue is at $p=4$.

5.3.3.2 Determining coseismic slip

SVD is an algorithm which is designed to find the generalised inverse of any matrix, singular or non-singular. Even if it is unresolvable from the data distribution, the method will determine an amount of slip. By examining the resolution matrix $V_p V_p^T$ a process is formalised through which parameter resolution can be determined and the number of eigenvalues which should be used to calculate the natural generalised inverse found. Typically, the model fit decreases with increasing number of eigenvalues and, after a certain number of eigenvalues, it is not improved by the addition of more. The problem is said to be over-parameterised or the model is too complex. The number of eigenvalues which significantly reduce the model fit is p . An F-test is used to establish how many parameters add to the complexity of the model without making a significant decrease in the misfit of observed and computed values. The significance of the improvement in model fit (χ^2) between the k th eigenvalue solution and the $(k+i)$ th eigenvalue solution was computed using:

$$\left(\frac{\chi_k^2 - \chi_{k+i}^2}{(N-k)(M-k) - (N-k-i)(M-k-i)} \right) \left(\frac{(N-k-i)(M-k-i)}{\chi_{k+i}^2} \right) \quad (5.22)$$

An eigenvalue is retained if the reduction in misfit in going from the k -eigenvalue solution to the $(k+1)$ solution had a probability of 1% or less being due to random noise (Jacobson and Shaw, 1991). Using the resolution matrices formed using the chosen number of eigenvalues it can then be found which parameters are resolved.

As an example, if the model consists of 6 faults there are $M=12$ model parameters, a component of dip-slip and strike-slip motion for each fault. In the example shown in Figure 5.3b, a plot of the model fit against the number of eigenvalues, from largest to smallest eigenvalue, used in the solution, shows an inflection at the fourth eigenvalue, *i.e.*, $p=4$. Using equation 5.22 it is found that using more than four parameters in the solution does not significantly improve the fit. To get a unique solution for the parameters which are resolvable, *a-priori* estimates for the unresolvable parameters must be made and those parameters excluded from the inversion process. In the example shown in Figure 5.3a, only the slip parameters 1, 2, 8, and 10 may be inverted for. The other values must be held fixed. The complete eigenvalue solution can then be used and the SVD algorithm then becomes a weighted least squares inversion of the data. The solution is unique and independent of the starting slip values used.

5.3.4 Frank's method of calculating shear strain

The shear strain across the Fairview Peak and Dixie Valley faults can be estimated from the triangulation data using Frank's method (Frank, 1966). The shear strain is calculated

from measured angle changes between stations. The method is independent of the fault geometry and does not require any assumptions about slip on the faults. The shear components γ_1 and γ_2 are defined as:

$$\gamma_1 = e_{11} - e_{22} \quad (5.23)$$

$$\gamma_2 = e_{12} + e_{21} \quad (5.24)$$

where e_{ij} is the tensor strain, γ_1 represents right-lateral shear on a northwest-southeast striking vertical plane, and γ_2 right-lateral shear on an east-west striking plane. The total shear strain γ is given by:

$$\gamma = (\gamma_1^2 + \gamma_2^2)^{\frac{1}{2}} \quad (5.25)$$

and the maximum axis of elongation is oriented at ψ from north where:

$$\tan 2\psi = \frac{\gamma_1}{\gamma_2} \quad (5.26)$$

Angle changes $\Delta\theta$ are assumed to be linear functions of γ_1 and γ_2 :

$$\Delta\theta = a\gamma_1 + b\gamma_2$$

where a and b are constants. If two or more angle changes are observed these values can be obtained by a least squares inversion (Savage and Burford, 1970). The strain found represents the average strain across the network.

5.4 RESULTS

5.4.1 Fault geometry

Trial and error was used as a preliminary first step to find approximate geometries using mapped fault offsets as a starting model (Table 1.2). This was important because there are many local minima in parameter space and a starting point very different from the true values might drive the solution towards a local rather than the absolute minimum. A gradient search of the parameter space was then made to reduce the misfit. The set of fault geometries which best fit the observations are given in Table 5.3 and shown in Figure 5.4. Five of the major faults were incorporated into the model: the Fairview Peak, West Gate, Gold King, Rainbow Mountain, and Dixie Valley faults. Another fault which is referred to as Fairview Peak South was required to fit the levelling data along line Dixie 2. The best fitting fault geometries resulted in a reduced chi-squared fit of 1.9.

Table 5.3. The best fitting fault geometries for the Rainbow Mountain, Fairview Peak, Fairview Peak South, Westgate, Gold King and Dixie Valley faults. Below each parameter, in italics, is the range it can span with less than a 5% degradation of the data fit. * indicates the lower bound of this parameter was constrained to this value.

PARAMETER	RAINBOW	FAIRVIEW PEAK	F.P. SOUTH	WEST GATE	GOLD KING	DIXIE
Dip	87°E <i>31°E ↔ 35°W</i>	69.0°E <i>64°E ↔ 75°E</i>	64.0°E <i>36°E ↔ 80°W</i>	59°W <i>49°W ↔ 73°W</i>	83°W <i>70°W ↔ 71°E</i>	49.0°E <i>39°E ↔ 57°E</i>
Lower Depth (km)	14.0 <i>4.0 ↔ 14.0*</i>	8.0 <i>6.5 ↔ 9.5</i>	8.0 <i>4 ↔ 12.0</i>	8.0 <i>5.0 ↔ 11.0</i>	5.0 <i>2.0 ↔ 6.0*</i>	5.5 <i>4.5 ↔ 6.5</i>
Upper Depth (km)	0.2 <i>0.0 ↔ 1.0</i>	0.0 <i>0.0 ↔ 0.5</i>	0.0 <i>0.0 ↔ 6.0</i>	0.4 <i>0.0 ↔ 1.0</i>	0.2 <i>0.0 ↔ 1.5</i>	0.0 <i>0.0 ↔ 1.0</i>
Strike	N25°E <i>N18°E ↔ N35°E</i>	N4°E <i>N2°W ↔ N10°E</i>	N4°W <i>N19°W ↔ N21°E</i>	N2°E <i>N13°W ↔ N3°E</i>	N3°E <i>N12°W ↔ N13°E</i>	N8°E <i>N4°E ↔ N11°E</i>
Length (km)	24.9 <i>24 ↔ 33</i>	24.2 <i>2 ↔ 30</i>	13.2 <i>1.5 ↔ 20.0</i>	14.8 <i>15 ↔ 22</i>	16.2 <i>16.0 ↔ 24.5</i>	24.3 <i>21 ↔ 28</i>
Latitude of north point	39.54°N <i>39.62 ↔ 39.52</i>	39.29°N <i>39.29 ↔ 39.28</i>	39.15°N <i>39.23 ↔ 39.05</i>	39.43°N <i>39.58 ↔ 39.41</i>	39.44°N <i>39.52 ↔ 39.37</i>	39.66°N <i>39.70 ↔ 39.66</i>
Longitude of north point	-118.48°W <i>-118.46 ↔ -118.52</i>	-118.13°W <i>-118.12 ↔ -118.14</i>	-118.12°W <i>-118.07 ↔ -118.16</i>	-118.06°W <i>-118.06 ↔ -118.14</i>	-118.11°W <i>-118.09 ↔ -118.15</i>	-118.19°W <i>-118.18 ↔ -118.20</i>
Latitude of south point	39.34°N <i>39.37 ↔ 39.33</i>	39.07°N <i>39.10 ↔ 39.02</i>	39.03°N <i>39.08 ↔ 39.98</i>	39.30°N <i>39.30 ↔ 39.29</i>	39.29°N <i>39.31 ↔ 39.28</i>	39.45°N <i>39.49 ↔ 39.40</i>
Longitude of south point	-118.61°W <i>-118.60 ↔ -118.67</i>	-118.15°W <i>-118.13 ↔ -118.18</i>	-118.11°W <i>-118.07 ↔ -118.12</i>	-118.07°W <i>-118.06 ↔ -118.07</i>	-118.12°W <i>-118.09 ↔ -118.15</i>	-118.23°W <i>-118.21 ↔ -118.24</i>

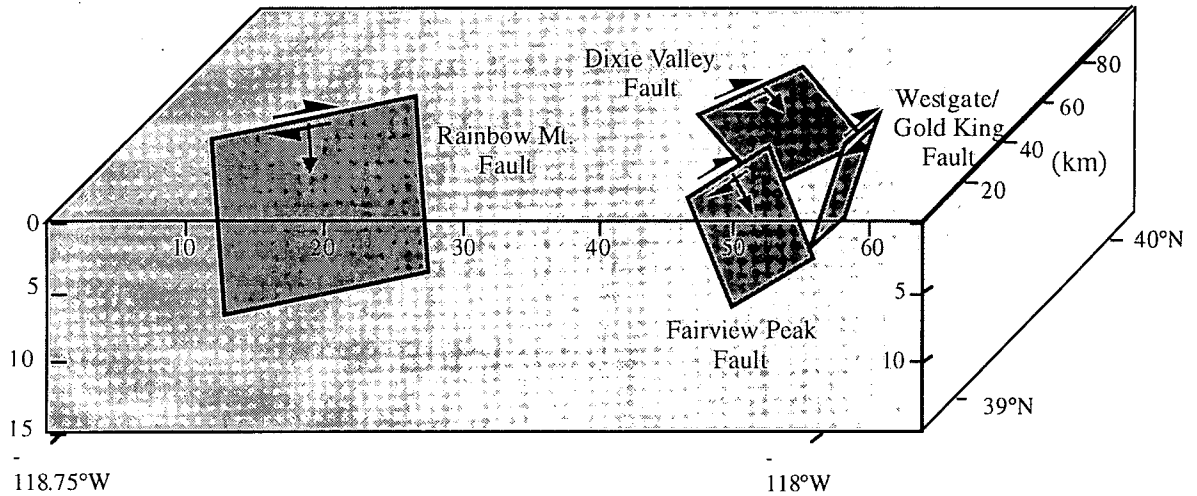


Figure 5.4 Best fitting fault geometry derived from the geodetic data.

The normalised residuals r_i are calculated as:

$$r_i = \left(\frac{y_i - c_i}{\sigma_i} \right) \quad (5.27)$$

where y_i is the observation, c_i is the computed deformation and σ_i is the associated error. Ninety percent of the data fall within the 3σ normalised residual level and seventy-one percent within the 2σ level (Figure 5.5).

For the triangulation points where several observations were made from one point the average residual fit is:

$$r_i = \frac{1}{T} \sum_{i=1}^T \left(\frac{y_i - c_i}{\sigma_i} \right) \quad (5.28)$$

where T is the number of observations made from that point. The influence of the levelling and triangulation data is about equal. If the triangulation data only are modelled χ_v^2 is 1.8. If the levelling data only are modelled χ_v^2 is 2.

To estimate the errors in the fault geometry each parameter was systematically varied about the best fitting value by stepping through positive and negative increments of the value while holding the others fixed, until the χ_v^2 value was degraded by 5%. This method does not account for the non-linearity of the problem, but gives some indication of how tightly each parameter is constrained. The best-fitting geometry (Table 5.3) was used as the basic model. The upper and lower parameters of the values determined by this method are given in Table 5.3.

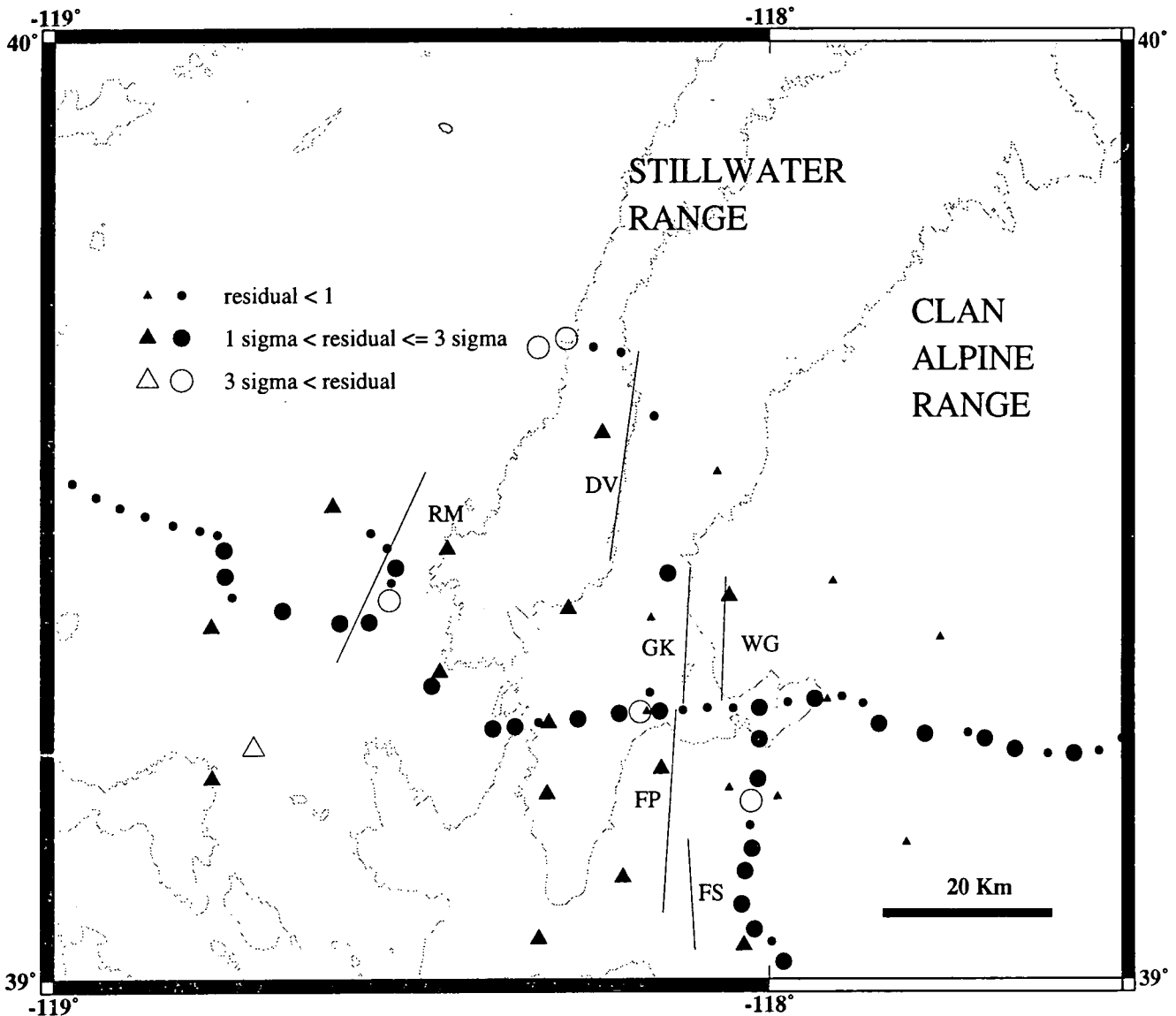


Figure 5.5 Normalised residuals from inversion of the geodetic data. Benchmarks are denoted by circles and triangulation stations by triangles. The solid black lines represent the modelled faults. FP: Fairview Peak, RM: Rainbow Mountain, WG: West Gate, GK: Gold King, :DV: Dixie Valley, FS: Fairview Peak South. The 1500 m contour is shown.

1. *The Rainbow Mountain fault:* Modelling the geodetic data places the Rainbow Mountain fault west of the mapped fault scarp. Its strike is N25°E and its position is determined by data from the levelling line which runs perpendicular to the scarp. Although many points lie close to the fault, the data constrain the dip poorly. The best fit was found with a dip of 87°E but the fit was decreased by 5% only outside the range 31°E to 35°W. Lower depths greater than 14 km do not reduce the data to model misfit, the data

being insensitive to its lower depth. The signal to noise ratio for the data around this fault is 6 and the misfit is 2.1. The fault is much shorter than 112 km determined by Snay *et al.*, (1985) (Table 5.2) and strikes in a more easterly direction while the dip and width are similar. The fault geometry obtained here is consistent with source parameters determined from body wave modelling (Doser, 1986).

2. *The Fairview Peak and Fairview Peak South faults:* The best fitting Fairview Peak fault dips at 64°E and has a lower depth of 8 km. The strike of the fault follows the surface rupture and can range from $\text{N}2^{\circ}\text{W}$ to $\text{N}10^{\circ}\text{E}$ without causing more than a 5% degradation of the data fit. The geometry is similar to that determined by forward modelling of the triangulation data by Savage and Hastie (1969). The only difference is in the length of the fault. Savage and Hastie (1969) suggest a length of 50 km whereas the present modelling yields a maximum of 30 km. This is a result of the inclusion of the West Gate and Gold King faults in the model calculated here, which were omitted in the study of Savage and Hastie (1969). The dip obtained is similar to that determined by Snay *et al.* (1985) using triangulation data only to model a deep Fairview Peak fault buried below a shallower one (Table 5.2). The dip of the Fairview Peak fault is consistent with the focal mechanism which suggests a strike of $\text{N}10^{\circ}\text{W}\pm 3^{\circ}$ and a focal depth of 15 ± 3 km (Doser, 1986). The lower depth of the fault is probably underestimated by modelling the geodetic data, a result of assuming uniform slip over a finite plane when the slip distribution probably tapers to zero at depth.

Without the Fairview Peak South fault the strike of the Fairview Peak fault is rotated to $\text{N}6^{\circ}\text{W}$. Although this strike agrees better with the focal mechanism the fit is degraded with triangulation residuals increasing to exceed 3σ at two stations south-east of Fairview Peak. The inclusion of the Fairview Peak South fault is also consistent with contemporary field reports of small surface ruptures to the southwest of the main Fairview Peak fault rupture (Slemmons, 1957). The paucity of data across this fault, however, make the dip and length, in particular, difficult to determine.

3. *The West Gate and Gold King faults:* The inferred geometries of the West Gate and Gold King faults are influenced by their proximity to one another. The West Gate fault strikes a few degrees west of north, dips at 59°W and has a lower depth of 8 km. The strike and position of the fault are constrained by the levelling sections that span it and its southerly extent is well constrained by the levelling data along line Dixie 2. The levelling and triangulation data around the fault, with the exception of one observation, lie within 2σ of the computed values. The Gold King fault dips steeply though the direction of the dip, east or west, is not well constrained ranging from 71°W to 70°E . The surface scarp dips to the west and seismic refraction results show that Dixie Valley is bounded in the

east by westward dipping faults (Okaya and Thompson, 1985). This would suggest that the Gold King fault dips westward like the West Gate fault and in contrast to the Fairview Peak fault which dips east. The upper limit for the depth to the bottom of the fault is 5 km and the fit was insensitive to depths greater than 6.0 km.

4. The Dixie Valley fault: Although associated with an earthquake of $M6.7$ this fault is least well constrained by the data, a result of the poor spatial coverage of the geodetic network. The best-fitting fault geometry dips at 49°E , has a maximum depth of 5.5 km and strikes at $\text{N}8^\circ\text{E}$. The lack of data north of the bend in the fault renders the northerly extent of the fault poorly constrained. Two levelling sections west of the Stillwater Mountains have residuals greater than 3σ . The deformation along these sections could have been caused by faulting on the west side of the Stillwater Mountains (Figure 5.5). The geometry derived is similar to that determined by Snay *et al.* (1985) except for fault length. The inferred fault geometry is consistent with the focal mechanism of the Dixie Valley event though the earthquake hypocentral depth was estimated to be 12 ± 3 km (Doser, 1986).

5.4.2 Coseismic slip

The plot of model fit versus number of eigenvalues for the weighted least squares inversion solution indicates that six slip values are resolvable (Figure 5.6). This was verified using equation 5.22. The dip-slip components of the Fairview Peak, Gold King, West Gate, Rainbow and Dixie Valley events and the strike-slip component of the Fairview Peak earthquake are well resolved. The triangulation data give little resolvability of the strike-slip motion of the other faults because the angle changes involved are small at distances greater than 10 km from the ruptures. Although slip on the Fairview Peak South fault is unresolvable, movement on this fault is required by the data as its omission significantly degrades the data fit. Removal of the fault degraded the model fit in a way that has a 0.2% probability of being due to random noise.

To solve for a unique set of slip values the problem must be reparameterised and *a-priori* information introduced. Since strike-slip motion on the West Gate and Gold King faults could not be distinguished they were combined and the best fitting position of the combined fault determined from the triangulation data. The model thus was reduced to 10 slip parameters. For this simpler model, dip-slip motion on the combined West Gate/Gold King fault and strike-slip motion on the Fairview Peak South and Dixie Valley faults only were unresolvable. To obtain a unique weighted least-squares solution, those slip values were held fixed and not inverted for. Vertical surface offsets of about 20 centimetres were observed by Slemmons (1957) along a small scarp to the southwest of the main Fairview Peak fault.

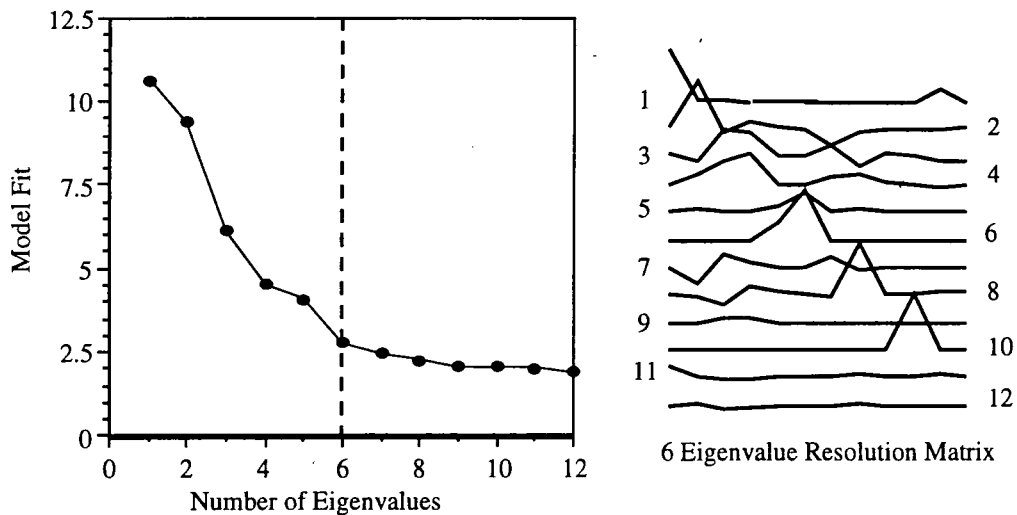


Figure 5.6 Model fit versus number of eigenvalues curve, and illustration of the resolution matrices for the 12-eigenvalue problem. The parameters represented by each eigenvalue are numbered one to twelve and the corresponding rows numbered on the resolution matrix: 1) Fairview Peak strike-slip, 2) Fairview Peak dip-slip, 3) West Gate strike-slip, 4) West Gate dip-slip, 5) Dixie Valley strike-slip, 6) Dixie Valley dip-slip, 7) Gold King strike-slip, 8) Gold King dip-slip, 9) Rainbow Mountain. strike-slip, 10) Rainbow Mountain dip-slip, 11) Fairview Peak South strike-slip, 12) Fairview Peak South dip-slip. The model fit is not significantly improved after the 6th eigenvalue solution.

The vertical motion was therefore fixed to 20 centimetres on the Fairview South fault. An estimate of the dip-slip motion on the combined West Gate/Gold King fault was obtained by summing the two dip-slip values determined from the weighted least squares solution for the separate West Gate and Gold King faults, since these values were resolvable. The mapped horizontal offset of zero along the Dixie Valley fault was used for that parameter.

The shear strain across the Fairview Peak, Fairview Peak South, West Gate/Gold King and Dixie Valley faults was calculated from the triangulation data using Frank's method and used to test the assumption of zero horizontal slip on the Dixie Valley fault. The shear strain across these four faults, calculated using Frank's method, was 38.7 ppm orientated at N14°W. Over a zone 59 km long this represents a total strike-slip motion of 2.22 m. The strike-slip motion found assuming pure normal motion on the Dixie Valley fault was 3.38 m on the Fairview Peak fault and 3.29 m on the combined West Gate/Gold King fault. The average slip per unit length of fault using these values is 1.7 which is 23% less than Frank's method suggests. The deficit is probably caused by underestimating the slip on the Dixie Valley fault since the slip on the Fairview Peak and West Gate faults are well resolved in the inversion process due to the density of the geodetic network in the vicinity of these faults. Calculating the horizontal slip from the 2.22 m of strike-slip motion determined using Frank's method results in 1.58 m of horizontal slip on the Dixie Valley fault. The final slip estimates calculated using this value are given in Table 5.4.

Table 5.4 Final coseismic displacements and seismic moments determined from weighted least squares inversion of the data. The geologic moment is derived from mapped fault offsets (Slemmons, 1957) and the seismic moments from body-wave modelling (Doser, 1986). The moments of the Fairview Peak, Fairview South and West Gate/Gold King are summed and denoted by the superscript †. Slip values which were fixed at a priori values are denoted by *.

Fault	Displacement (m)		Moment $\times 10^{18}$ Nm		
	Strike-slip	Dip-slip	Seismic	Geologic	Geodetic
Rainbow Mountain	0.91±0.68	0.21±0.08	9.9	6.4	9.8
Fairview Peak	3.37±0.03	1.82±0.02	53.0 [†]	55.0 [†]	46.3 [†]
Fairview South	1.15±0.05	0.20*			
WGate/GKing	3.35±0.06	1.60*			
Dixie Valley	1.58*	3.58±0.02	9.8	18.0	22.4

Holding the horizontal slip on the Dixie Valley fault at zero or 1.58 m makes no significant difference to the overall fit when the data are inverted. This is a result of the small number of observations made across the fault. Using Frank's method does not remedy the paucity of data but it does give an estimate of strike-slip motion from the triangulation data which is independent of fault geometries and assumed slip vectors.

The moments of the Dixie Valley - Rainbow Mountain - Fairview Peak sequence of events were calculated using the equation: $M_0 = \mu w L \bar{s}$ where μ is the shear modulus (3×10^{11} dyne cm^2), w is the width of the fault, L the length and \bar{s} the slip (Table 5.4). The moment calculated for the Fairview Peak event includes those of the West Gate/Gold King and Fairview Peak South events. The geologic and geodetic estimates for the Fairview Peak and Rainbow Mountain events are similar to magnitudes obtained from body-wave modelling (Doser, 1986). Both the geologic and geodetic moments of the Dixie Valley event are almost twice as large. There was difficulty in analyzing the seismic data associated with the Dixie Valley event since it was difficult to separate it from the Fairview Peak event.

Generally the modelled slip is greater than the maximum surface offset (Tables 1.2 and 5.4). The exceptions are the observed displacements on the Rainbow Mountain fault and vertical displacement on the Fairview Peak fault. An average 0.91 m of right-lateral offset has been observed along the Rainbow Mountain fault (Caskey, personal communication, 1996) and the mapped vertical offsets range from 0.2 to 0.3 m (Tocher, 1956). The geodetically determined slip values are thus close to that observed at the surface. Along the Fairview Peak fault the maximum vertical offset along the scarp (3.8 m) is almost twice that of the geodetically determined value.

On the Dixie Valley fault, the geodetically determined vertical slip is much larger than the observed surface vertical offset and 1.58 m of right-lateral slip is determined while none is observed along the fault rupture. The vertical slip determined geodetically on the combined West Gate and Gold King fault (1.6 m) is larger than that observed along either the Gold King or West Gate faults where the maximum vertical displacements were 1-1.2 m. The right-lateral offset determined geodetically along the fault is 3.3 m. No horizontal slip is observed at the surface along the Gold King fault while 1.2 m of right-lateral offset is measured in one place along the West Gate fault. The horizontal deformation field caused by the events is shown in Figure 5.7.

5.5 SUMMARY

The coseismic deformation field caused by an earthquake can be calculated by assuming uniform slip on rectangular faults embedded in an elastic half-space. Comparison of the calculated deformation to the measured deformation can be used to infer fault geometries and coseismic slip values. The deformation observed at the surface can be related to the coseismic slip through a matrix which describes the elastic properties of the Earth and the geometry of the fault or faults which failed. The data can then be inverted to obtain the coseismic slip and the fault geometry that yield the best model fit. Using the method of Single Value Decomposition for the matrix inversion process allows to be determined which slip parameters are resolvable by the data. This method of inversion is therefore superior to a least squares inversion.

The surface deformation created by the 1954 Rainbow Mountain - Fairview Peak - Dixie Valley earthquakes was measured by levelling and geodetic surveys made before and after the events. These data were inverted to obtain the fault geometry and coseismic slip. A reduced chi-squared fit of 1.9 was obtained. The best fitting fault geometries were planar faults and extended to depths of 8 to 14 km. The geometries are typical of other Basin and Range faults on which $M_s 6.5$ and greater earthquakes have occurred. The slip estimates found suggest an average 2.5-3 m of strike-slip motion over all the faults compared to an average 2.5 m of dip-slip motion. The geodetic moments calculated for these events are not inconsistent with those derived from seismic studies. The geodetically determined slip tends to be about equal to, or greater than that observed along the surface scarps. The geodetic data suggest that the Fairview Peak, West Gate, Gold King and Dixie Valley earthquakes had greater right-lateral slip at depth than was observed at the surface.

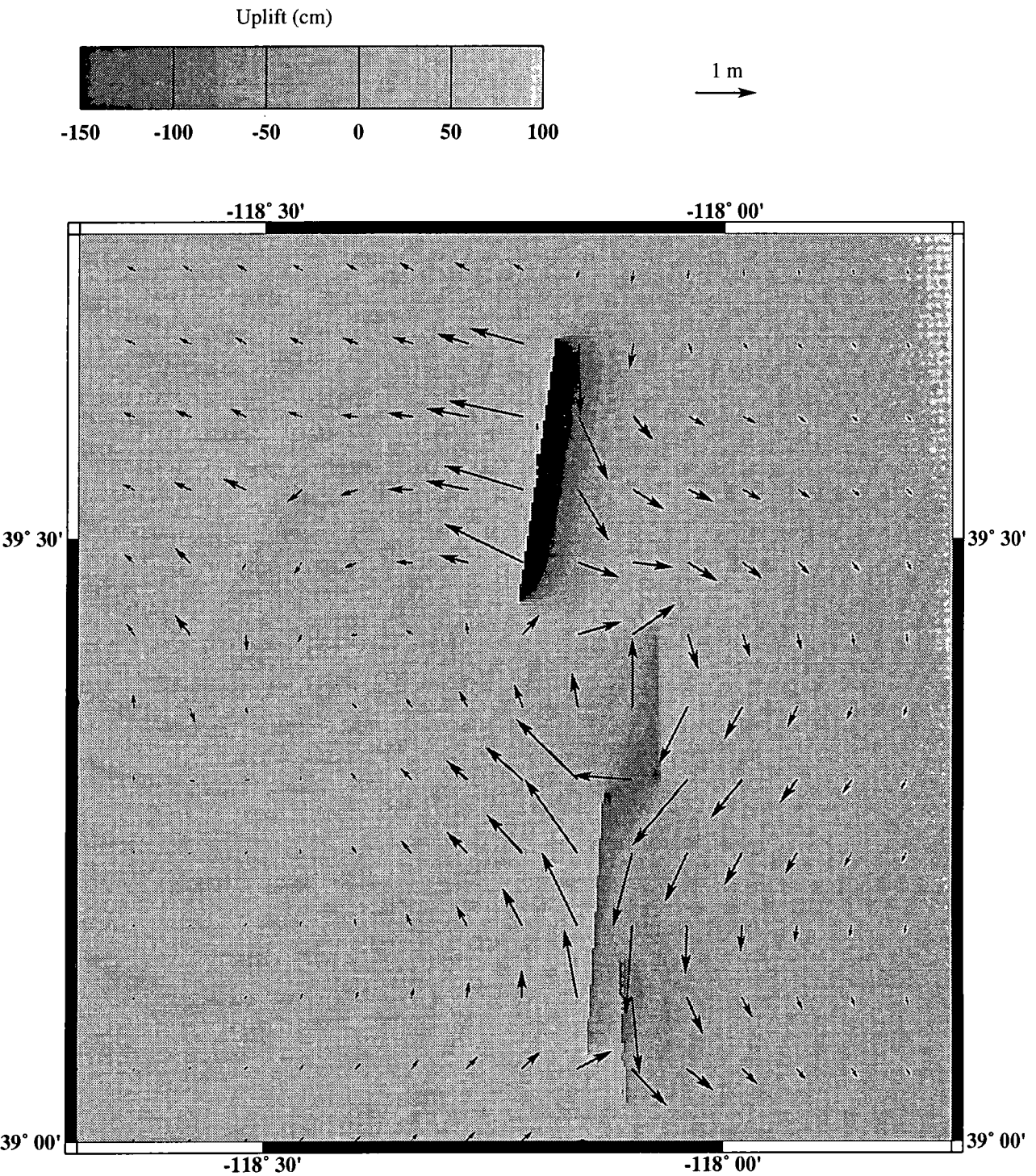


Figure 5.7 The coseismic deformation field calculated using the slip vectors determined from the data inversion. Arrows indicate the horizontal displacement field while gray shading shows the uplift.

CHAPTER 6

THE RAINBOW MOUNTAIN-FAIRVIEW PEAK-DIXIE VALLEY EARTHQUAKES: TRIGGERED SEISMICITY

6.1 INTRODUCTION

The Rainbow Mountain-Fairview Peak-Dixie Valley earthquake sequence provides an opportunity to study earthquake triggering and the encouragement of fault failure by increased static stresses. Unlike the M7.4 (1992) Landers and M7.3 (1989) Loma Prieta Californian earthquakes, where the static stress changes have been calculated and triggered earthquakes predicted for the future, the Rainbow Mountain-Fairview Peak-Dixie Valley sequence is probably complete. The sequence was an unusual one because four large earthquakes occurred within six months and in a 30 km radius. The Rainbow Mountain events occurred on July 6 and August 24, 1954, and were followed 3 months and 23 days later by the Fairview Peak earthquake. Four minutes and 20 seconds later the Dixie Valley event occurred. By modelling the static stress changes associated with each event in the sequence it is possible to determine whether the stress changes caused by each earthquake encouraged or discouraged the succeeding event.

Earthquakes release stress in the Earth's crust. When an earthquake occurs on a fault static stresses are immediately reduced on that fault and perturbed in regions away from it. This perturbation in the static stresses would be expected to change the seismicity in the surrounding region. Evidence to support this includes:

- The correlation of aftershock locations with regions of positive stress changes,
- The occurrence of moderate-sized events within such regions and,
- Periods of seismic quiescence in areas where static stresses have been reduced.

The correlation of aftershocks with positive static stress change may be studied as a result of the increase in quality of the location of small magnitude earthquakes and lowered location thresholds with the densification of seismic networks. Such a correlation has been reported following four well-recorded Californian events, the Homestead Valley (1979), Morgan Hill (1984), Loma Prieta (1989) and Landers (1992) events (Das and Scholz, 1983; Stein and Lisowski, 1983; Oppenheimer *et al.*, 1988; Simpson and Reasenber, 1994). Moderate-sized “triggered” events within regions of positive stress include the M5.5 earthquake at Big Bear (1992) which occurred 3.5 hours after, and within 100 km of, the M7.4 Landers event (King *et al.*, 1994). Four earthquakes in the 15 years preceding the Landers event caused a cumulative positive stress change of 1×10^5 Pa in the area of the future Landers rupture suggesting that it too was a triggered event (Stein *et al.*, 1992). The M7.1 Petrolia earthquake (1992) off the northern California coast may have been precipitated by the M6.8 Honeydew earthquake that occurred a year earlier and 25 km away.

Just as moderate-sized events have been triggered, and follow immediately after some earthquakes, periods of seismic quiescence have followed others. After the 1906 M8.25 San Francisco earthquake only one earthquake greater than M6 occurred on faults in the San Francisco bay area between 1906 and 1989. It is possible that the 70-year quiescent period was a result of the bay area faults receiving a negative static stress change from the 1906 earthquake (Simpson and Reasenber, 1994). A 19-year period of seismic quiescence that followed the 1857 M8 Ft. Tejon earthquake in southern California could also be explained the same way (Harris and Simpson, 1993). A similar scenario exists in south Iceland where a period of high seismicity in the early 1900's has been followed by an eighty-year period of low seismicity (Einarsson, 1991). On the Wasatch fault, in the eastern Basin and Range province, paleoseismology shows that repeated earthquakes occur along sections of the fault, yet no earthquakes \geq M5.5 have occurred since two M5.5 events in 1910 and 1914 (Schwartz and Coppersmith, 1984).

Understanding how an earthquake can load or relax stress on a nearby fault is important for assessing seismic hazard. For example, the loading effect of the 1992 Landers earthquake on the nearby San Andreas fault has been calculated, establishing that the Landers event enhanced the probability of failure on it by increasing static stresses in the region (Jaumé and Sykes, 1992; Stein *et al.*, 1992). What roles the regional stresses, friction, pore pressure and fault geometries play in the triggering process also bear on whether an earthquake rupture is limited to one fault segment a few 10s of km long or cascades into a much larger event, rupturing several segments, such as the M8 1939 Erzincan earthquake that ruptured 400 km of the North Anatolian fault in Turkey (Barka and Kadinsky-Cade, 1988).

6.2 FAULT FAILURE

6.2.1 Static stress changes

The static stress changes are the permanent stress changes associated with an earthquake and can be modelled by assuming slip on a planar surface embedded in an elastic half-space (*e.g.*, Chinnery, 1961; Okada, 1992). The dynamic stress changes are short-term and temporary, and are due to the propagation of seismic waves generated by the earthquake. The induced static stress changes are due to coseismic energy released. Two assumptions are made when studying earthquake triggering by static stress changes, (i) that earthquakes occur through a stick-slip mechanism with the fault locking after slipping, and (ii) that failure occurs when the shear and normal stresses on the fault satisfy the Navier-Coulomb failure criterion.

The stick-slip theory of faulting is based on observations in laboratory rock friction experiments (*e.g.*, Brace and Byerlee, 1966). A fault fails and an earthquake occurs when the stresses on a fault plane are great enough to overcome the static friction of the fault zone. Movement on the fault then occurs rapidly, during which time the energy released is dissipated as heat and seismic waves. Slip ceases when the loading stress drops below the dynamic friction of the fault. The next earthquake will not occur until the stress on it reaches the failure level again. There are other mechanisms through which fault zones can accommodate the forces acting on them, *e.g.*, aseismic creep, but no attempt is made here to model these processes.

6.2.2 The Navier-Coulomb failure criterion

Normal and shear stresses on a plane can be calculated in any coordinate system x' , y' inclined at an angle θ to the x axis (Figure 6.1). If the normal and shear stresses are σ_{xx} , σ_{yy} , σ_{xy} and σ_{yx} respectively then the normal stress in the x' , y' coordinate system parallel to the y' axis is written as:

$$\sigma_n = \sigma_{xx} \cos^2 \theta + \sigma_{yy} \sin^2 \theta + \sigma_{xy} \sin 2\theta \quad (6.1)$$

and the shear stress parallel to the x' axis is:

$$\sigma_\tau = \frac{1}{2}(\sigma_{yy} - \sigma_{xx}) \sin 2\theta + \sigma_{xy} \cos 2\theta \quad (6.2)$$

where σ_n is the normal stress and σ_τ is the shear stress (Turcotte and Schubert, 1982). If σ_{xx} and σ_{yy} are the principal stresses then σ_{xy} and σ_{yx} are zero and equations 6.1 and 6.2 simplify to:

$$\sigma_n = \frac{1}{2}(\sigma_{xx} + \sigma_{yy}) + \frac{1}{2}(\sigma_{xx} - \sigma_{yy}) \cos 2\theta \quad (6.3)$$

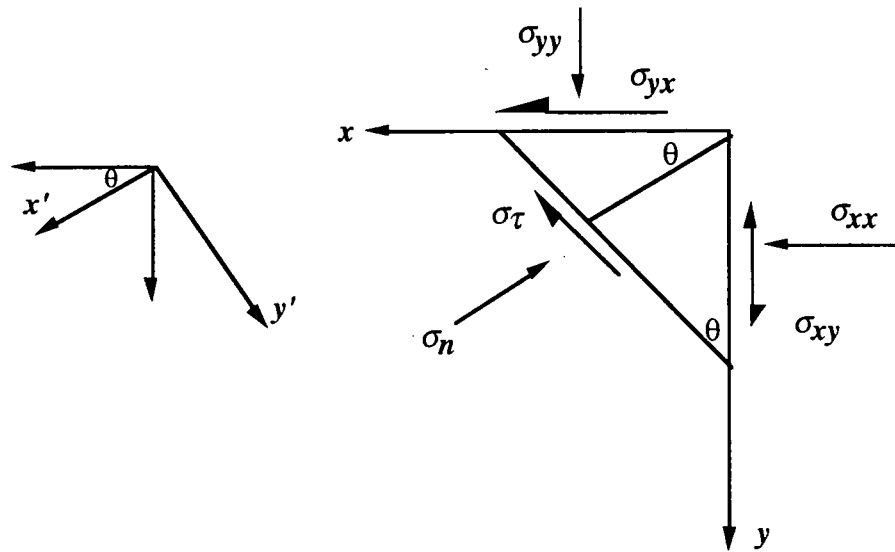


Figure 6.1 Shear and normal stresses in a coordinate system that has been rotated at θ to the x-axis.

$$\sigma_{\tau} = \frac{1}{2}(\sigma_{xx} - \sigma_{yy}) \sin 2\theta. \quad (6.4)$$

It can be shown that:

$$\left(\sigma_n - \left(\frac{\sigma_{xx} + \sigma_{yy}}{2} \right) \right)^2 + \sigma_{\tau}^2 = \left(\frac{\sigma_{xx} - \sigma_{yy}}{2} \right)^2$$

which is the equation of a circle. This is called the Mohr circle and may be used to graphically represent stress in two dimensions on fault planes (Figure 6.2). The circle has a radius $\left(\frac{\sigma_{xx} - \sigma_{yy}}{2} \right)$ and is centered on $\left(\frac{\sigma_{xx} + \sigma_{yy}}{2} \right)$.

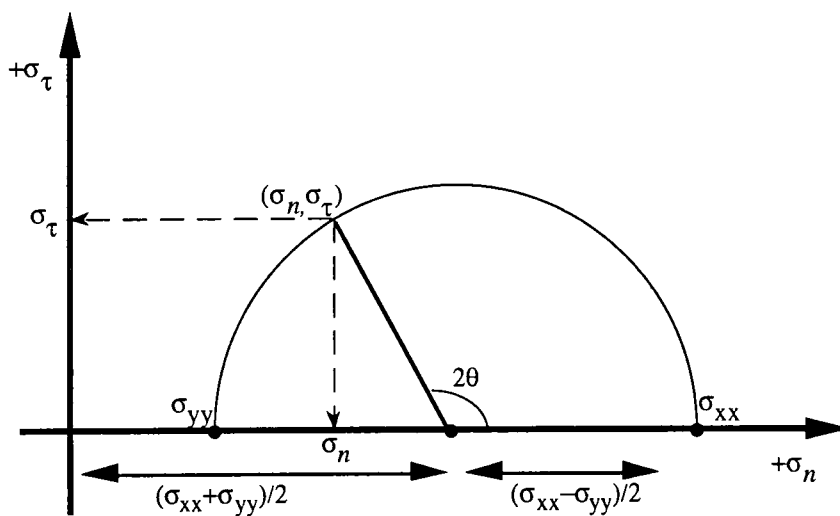


Figure 6.2 The Mohr diagram for stress in two dimensions. The circle shows how shear stress varies with normal stress for particular values of σ_{xx} and σ_{yy} . The plane has an inclination θ to the σ_{yy} axis.

Laboratory rock experiments have shown that if the axial load on a sample is increased while the confining pressure is kept constant a point is eventually reached where failure occurs. The fracture strength of the rock increases with increasing load. At confining pressures greater than about five times the tensile strength of the rock it increases fairly linearly with confining pressure (Brace, 1964). This is known as Coulomb behaviour.

The results may be illustrated by plotting σ_τ against σ_n for a range of confining pressures (Figure 6.3). The resulting curve is known as the failure envelope and is described by

$$\sigma_\tau = S_o + \mu\sigma_n \tag{6.5}$$

where μ is the coefficient of friction and S_o is the cohesion of the rock. Equation 6.5 is the Coulomb-Navier failure criterion. The failure envelope indicates the values of σ_n and σ_τ at which failure occurs, and a Mohr circle may be constructed to determine the angle θ of the failure plane.

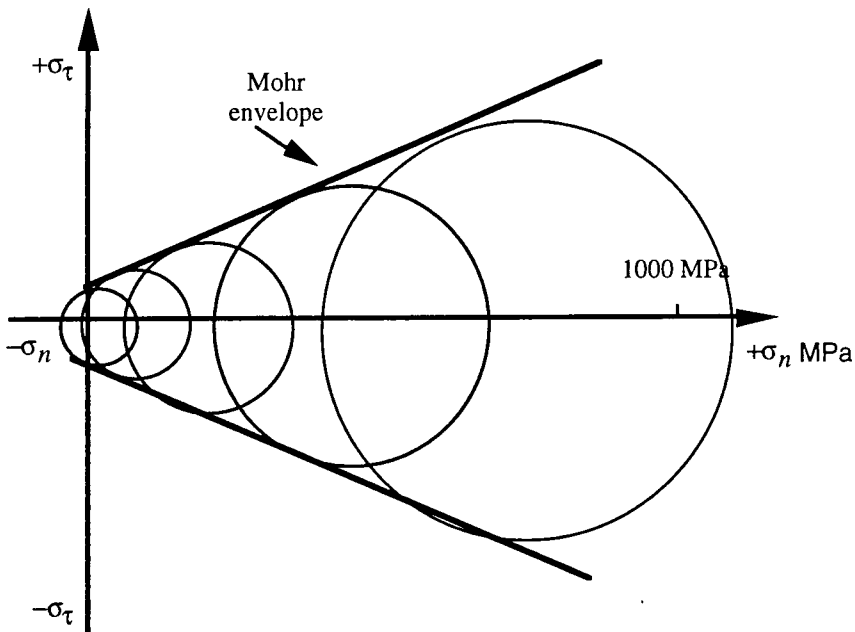


Figure 6.3 Mohr diagram showing how rock strength increases with mean stress. The locus of stress states that bound the field of stable stresses is called the Mohr envelope (Brace, 1964).

In the natural state all materials contain fluid. Porosities can vary from 80% for an unconsolidated sediment to 0.01% for a coarse-grained igneous rock. Fluid in a fault zone causes the material to act as though the normal stresses are reduced by an amount equal to the pressure of the fluid in the fault. The shear stresses are unaffected. If the fault contains a fluid with pressure P , called the pore pressure, then the *effective* normal stress is defined as:

$$\sigma_{eff} = \sigma_n - P \tag{6.6}$$

The physical properties of most solids will depend on the effective stress rather than on the tectonic stresses alone. For example, an increase in pore pressure will reduce the effective normal stress making it easier for a fault to slip. This is illustrated by a correlation between change in pore pressure and change in seismicity observed for reservoirs (Roeloffs, 1988). In terms of the Mohr diagram the Mohr circle is translated to the left while the failure envelope remains unchanged. The effect is a weaker fault. The Coulomb-Navier failure criterion then becomes:

$$\sigma_{\tau} = S_o + \mu(\sigma_n - P) \quad (6.7)$$

and failure will occur when,

$$\sigma_{\tau} - S_o - \mu(\sigma_n - P) > 0 . \quad (6.8)$$

The failure stress, σ_f , is defined:

$$\sigma_f = \sigma_t - S_o - \mu(\sigma_n - P) . \quad (6.9)$$

Using equations 6.3 and 6.4 this is written in full as:

$$\sigma_f = \frac{1}{2}(\sigma_{xx} - \sigma_{yy})(\sin 2\theta - \mu \cos 2\theta) - \frac{1}{2}\mu(\sigma_{xx} + \sigma_{yy}) + \mu P - S_o . \quad (6.10)$$

6.3 CALCULATION OF STATIC STRESS CHANGES

6.3.1 Method of calculation

The static stress changes caused by an earthquake can be modelled using dislocation theory and the Coulomb-Navier failure criterion. Stress changes are calculated assuming slip on rectangular faults embedded in an elastic half-space. The program GEN0.3 written by G.C.P. King was used to perform the calculations (King *et al.*, 1992). The difference in pre- and postseismic static stress is equal to the change in the state of stress. If $\sigma_{f_{PRE}}$ and $\sigma_{f_{POST}}$ represent the states of stress before and after the earthquake, then the change is:

$$\begin{aligned} \Delta\sigma_f &= \sigma_{f_{PRE}} - \sigma_{f_{POST}} \\ &= (\sigma_t - S_o - \mu(\sigma_n - P))_{PRE} - (\sigma_t - S_o - \mu(\sigma_n - P))_{POST} \end{aligned}$$

If it is assumed the coefficient of friction μ , and the cohesion of the rock S_o , remain constant then,

$$\Delta\sigma_f = \Delta\sigma_t - \mu(\Delta\sigma_n - \Delta P) \quad (6.11)$$

where $\Delta\sigma_t$ is the change in shear stress, $\Delta\sigma_n$ is the change in normal stress and ΔP is the change in pore pressure. The change in pore-pressure ΔP is defined in terms of Skempton's coefficient B , and mean normal stress:

$$\Delta P = -B \frac{\Delta\sigma_{kk}}{3} \quad (6.12)$$

where $\sigma_{kk} = \sigma_{11} + \sigma_{22} + \sigma_{33}$, and the value of B varies from 0 to 1 (Roeloffs, 1988). In a fault zone the normal stresses, σ_{11} , σ_{22} , and σ_{33} are approximately equal (Rice, 1992) and therefore the mean normal stress is equal to $\frac{\sigma_{kk}}{3}$. Thus, $\Delta P = -B\Delta\sigma_n$. Substituting this into equation 6.11,

$$\Delta\sigma_f = \Delta\sigma_t - \mu(\Delta\sigma_n + B\Delta\sigma_n) .$$

The change in stress can then be written as;

$$\Delta C = \Delta\sigma_t - \mu'(\Delta\sigma_n) \quad (6.13)$$

where $\mu' = \mu(1 - B)$ is the apparent coefficient of friction. The sign of $\Delta\sigma_t$ may be positive or negative in cases of right- or left-lateral slip respectively. A positive $\Delta\sigma_f$ indicates that the fault has experienced an increase in stress and is more likely to fail. A negative $\Delta\sigma_f$ indicates a stress decrease and a lowered likelihood of fault failure. The extent to which stress changes encourage or discourage fault failure can be determined by resolving them onto a particular fault or onto the fault plane along which $\Delta\sigma_f$ is maximized.

6.3.2 Stress changes on fault planes

6.3.2.1 Stress changes on a geodetically-inferred fault.

To find if the static stresses associated with an earthquake encourage or discourage failure on a known fault the stress changes must be resolved onto that particular fault plane. The change in stress is calculated using equation 6.13. An illustrative example is shown in Figure 6.4. Stress changes are induced by 1 m of slip on a 30 km "source fault" that is 10 km wide and positioned 5 km west of a "receiving fault". The cases of a vertical and a dipping fault source are shown. Coulomb stresses are resolved onto a 20 km vertical fault and four possible stress changes are calculated. These are the stress changes encouraging right-lateral and left-lateral strike-slip faulting and stress changes encouraging normal faulting and thrust faulting. In the example shown one metre of right-lateral slip on a vertical source fault encourages left-lateral and normal failure on the receiving fault whilst

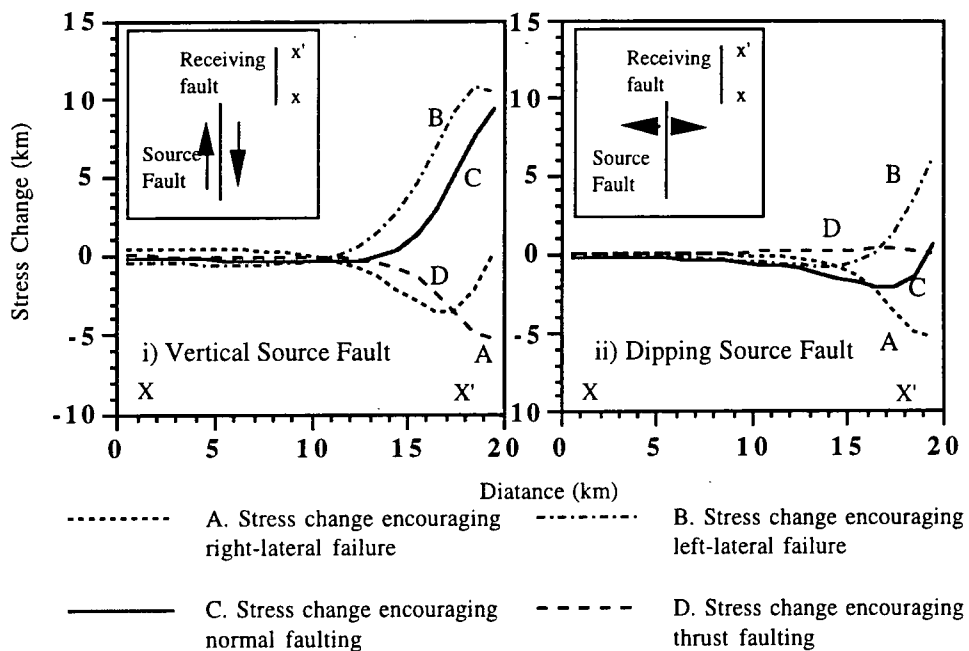


Figure 6.4 Stress changes caused by slip on a source fault resolved onto a receiving fault. The source fault is 30 km long and 10 km wide. The receiving fault is vertical, 20 km long and 10 km wide. i) Vertical source fault, ii) 70°E dipping source fault. Stresses are resolved at 5 km depth for $\mu' = 0.4$.

discouraging right-lateral and thrust failure. One metre of normal slip on a dipping source fault encourages the receiving fault to fail by left-lateral and thrust faulting but discourages right-lateral and normal failure. The calculated stress changes depend only on the apparent coefficient of friction and fault geometries.

6.3.2.2 Stress changes on optimally-orientated faults.

Calculating the stress changes on faults that are optimally-orientated for failure enables predictions to be made of the distribution of aftershocks where an area is fractured with faults with many orientations. Optimally-orientated planes represent fault orientations where the Coulomb stress change is a maximum. Two sets of calculations may be made: the Coulomb stress changes on optimally-orientated (i) vertical, and (ii) dipping faults. In the case of vertical faults planes are identified on which the stress changes encouraging right lateral and left lateral slip are maximised. For optimally-dipping faults, planes are identified where stress changes encouraging thrust and normal slip are maximised. The dip of optimally-dipping faults and the strike of optimally-striking vertical faults are dependent on both μ and the principal stresses.

The orientation of the principal stresses are calculated from the sum of the regional stresses and the coseismic stress change. The orientations of the axes of greatest and least compression are then given by,

$$\Psi = \frac{1}{2} \tan^{-1} \left(\frac{2\sigma'_{xy}}{\sigma'_{xx} - \sigma'_{yy}} \right) \quad (6.14)$$

and the normal to Ψ where σ' signifies the total stress, coseismic plus regional (King *et al.*, 1994; Turcotte and Schubert, 1982). The angle θ is the orientation of the fault at which the Coulomb stress change is greatest and is found by differentiating Equation 6.10 with respect to θ which yields:

$$\tan 2\theta = \pm \frac{l}{\mu} .$$

The stress change on such faults may then be calculated by substituting the corresponding calculated values for shear and normal stresses into equation 6.10. Optimally-dipping faults strike perpendicular to the axis of minimum principal stress and their dip is given by $\Psi \pm \theta$. The strike of the vertical faults most likely to fail is also given by $\Psi \pm \theta$. This method involves assumptions about the orientation of the regional stress field which may be poorly known in real cases.

Gradient plots are used here to illustrate graphically static stress changes on optimally-orientated faults. The static stress changes induced by 1 m of normal slip on a 30 km long, 10 km deep, 60°E dipping fault are illustrated in Figure 6.5. Calculations are made every 2 km on a grid and interpolated in between. A coefficient of friction of 0.4, a Skempton's coefficient of 0, and an east-west extensional regional stress of 10 MPa, are assumed. The Coulomb stress changes are calculated at depths of 5 km on optimally-orientated vertical faults (Figure 6.5a), and optimally-orientated dipping faults (Figure 6.5b). The two stress fields are similar, both optimally orientated strike-slip faults and dipping faults to the east and west of the slipped fault are relaxed. The orientation of optimally dipping normal faults is north-south, perpendicular to the direction of extension. The orientation of optimally orientated vertical faults is ~N34°E. Only at the end points of the fault are stresses increased. The maximum of either of these two fields gives the field of maximum stress change in the region (Figure 6.5c). This quantity shall be called the *maximum Coulomb stress change* and it shows where triggered aftershocks and triggered events are most likely to occur. The difference between the increase of stress encouraging normal slip and the increase encouraging right-lateral slip suggests which mechanism may dominate. This is illustrated in Figure 6.5d. The Coulomb stress changes shown in Figure 6.5 and Figures 6.8 to 6.13 were produced by contouring the stress change field produced by GEN0.3 using the software package Spyglass Transform.

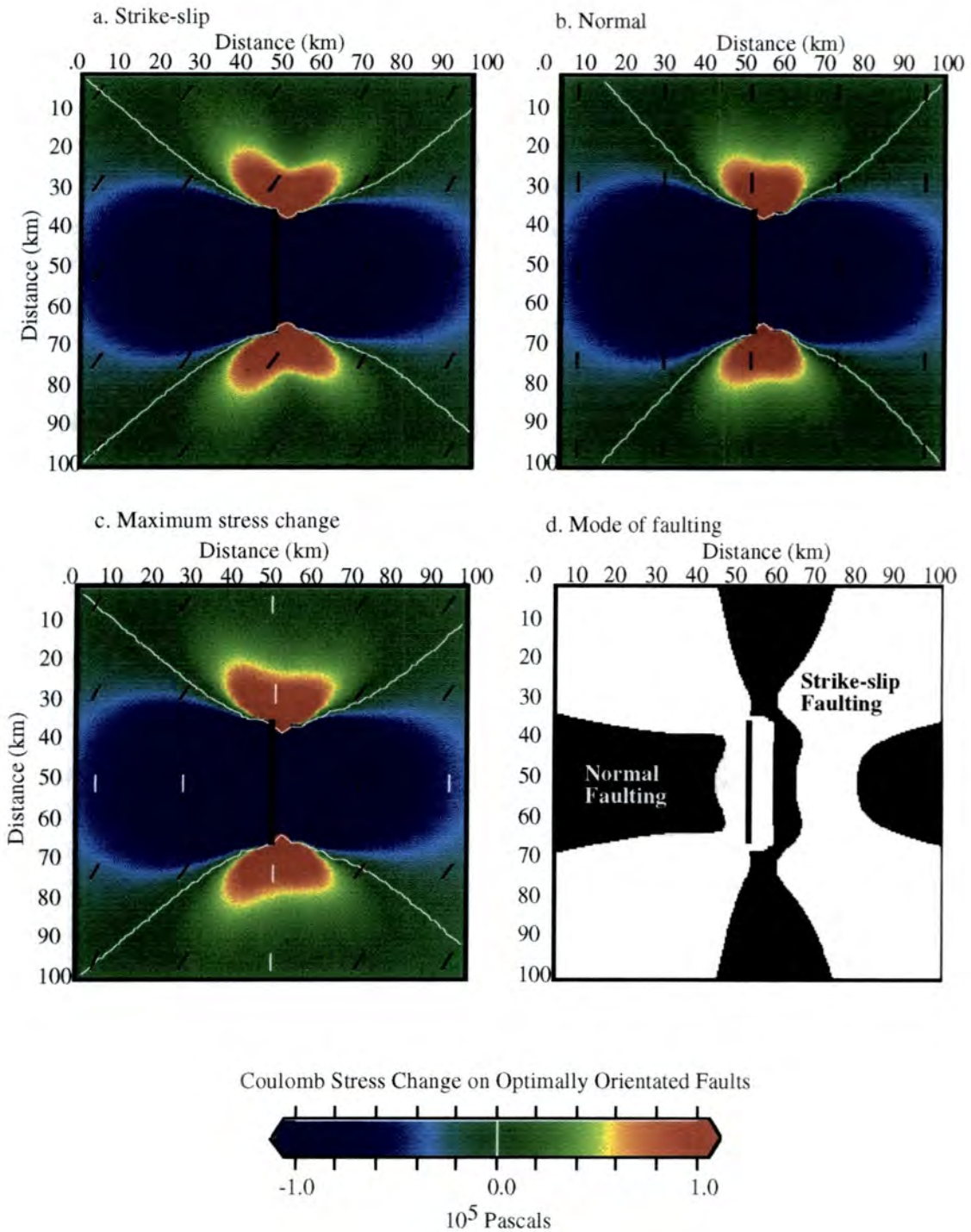


Figure 6.5 Coulomb stress changes associated with 1 m of normal slip on a 60°E dipping fault. The regional stresses are that of east-west extension. The panel shows the Coulomb stress change on optimally orientated faults. a) Stress changes encouraging strike-slip failure. The black lines indicate the orientation of planes which are most likely to fail through right-lateral slip. b) Stress changes encouraging normal failure, the orientation of optimally dipping faults is north-south. c) The maximum Coulomb stress-change field, the orientation of optimally orientated vertical faults are shown as black lines and optimally orientated dipping faults as white lines. d) Stress changes encouraging normal faulting (black) - and strike-slip faulting (white).

6.4 MODELLING THE 1954 EARTHQUAKE SEQUENCE

6.4.1 The method

To find if the Rainbow Mountain events could have triggered the Fairview Peak event and if these events in turn could have triggered or transferred stress to the West Gate/Gold King and Dixie Valley faults, the earthquake sequence was modelled in three stages: (1) Stress caused by the Rainbow Mountain event, (2) Stress caused the Rainbow Mountain, Fairview Peak and West Gate/Gold King faults events, (3) Stress changes caused by slip on all faults.

The fault geometry and slip estimates used to model stress transfer by the earthquakes are those determined from the geodetic data (Table 5.3). The West Gate and Gold King faults are represented as one combined fault. Figure 6.6 shows the spatial distribution of the faults at the surface. Coulomb stress changes are resolved on optimally orientated faults and on each of the faults that failed in the sequence. The parameters which define the stress change field on optimally orientated faults are the magnitude and orientation of the regional stress field, and the apparent coefficient of friction, μ' .

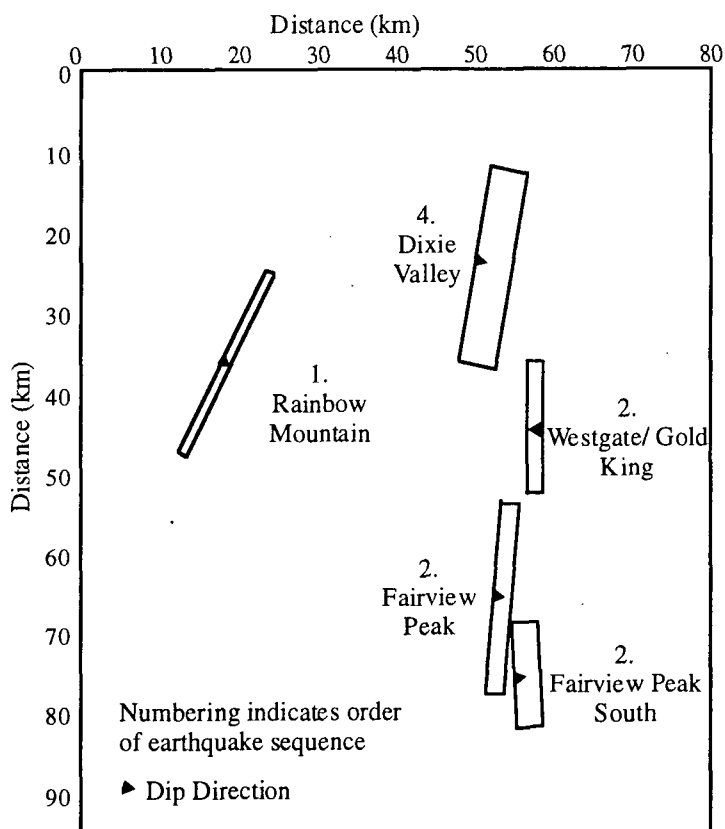


Figure 6.6 Spatial distribution of faults modelled. Stress changes caused by the Fairview Peak, Fairview Peak South and West Gate/Gold King earthquakes are calculated together.

6.4.2 The regional stress field

The combination of the regional stress field and the stress changes due to coseismic slip determine the orientation of faults most likely to slip (Equation 6.14). Stress changes are not very sensitive to the magnitude of the regional stress field but they are sensitive to its orientation (King *et al.*, 1994). For this reason care must be taken in assessing the orientation of the regional stress field. Information about the regional stress field can be obtained from earthquake focal mechanisms, fault slip data and geological data (*e.g.*, the alignment of young volcanic vents and hydraulic fracture orientations). The Basin and Range province is an extensional regime with the principal stresses orientated approximately in the vertical and horizontal planes. The axis of minimum compressive stress, σ_3 , varies from east-west along the Sierra Nevada boundary to N60°W in active interior parts of the province such as the Dixie Valley region. This was found by simultaneously inverting fault-slip data and focal mechanisms from the Central Nevada seismic zone (Zoback, 1989). Well-bore elongations from the Nevada Test Site confirmed these findings (Stock and Healy, 1988).

A regional extensional stress orientation of N56°W±10° was derived from geologic and geodetic data from Very Long Baseline Interferometry (VLBI) measurements (Minster and Jordan, 1987). If geologic data alone were used an orientation of N64±10°W was obtained, and using VLBI data alone, N48±17W. However, modelling VLBI data measured over an eight year period from 27 stations distributed throughout the USA and around the Pacific rim indicated an orientation of N34°W (Ward, 1990). If the geologic data are given less weighting then the axis of maximum extension is rotated to a more northerly direction. The two extreme estimates are N34°W and N60°W. The difference could be a result of a change in the stress field with time, as the geological data span the past 9-10 Ma while the recent geodetic data represents the last few years only. This is supported by fault-slip data from recent earthquakes such the Fairview Peak event that has a large strike-slip component whereas the topographic relief is one of east-west extension. In the modelling these two orientations are both used to cover the full range of possible stress field orientations.

The magnitude of the regional stress field can be estimated from hydraulic fracture measurements. The vertical stress is assumed to correspond to the overburden and the magnitude of the stresses perpendicular to this in the near-horizontal plane of the borehole can then be calculated. However, there are no hydraulic fracture measurements within the 7-15 km of the earthquake nucleation point so the magnitude of the stress field is nominally set to 10 MPa.

6.4.3 The coefficient of friction.

Laboratory-determined values of the coefficient of friction (μ) range from 0.6 to 0.9 and *in-situ* stress measurements in the upper 3 km of the Earth's crust have shown that these values are valid for brittle failure of rock. There is evidence, though, that slip is resisted by very low shear stresses in fault zones. Byerlee's Law predicts that strike-slip motion would occur at a depth of 15 km only under shear stresses of about 150×10^6 Pa, whereas heat-flow measurements show that slip occurs at stresses as low as 20 MPa. Crustal stress magnitudes may also be inferred from *in-situ* well measurements, well breakouts and heat flow measurements. The low stress drops associated with earthquakes and the lack of high heat flow suggests that below the upper few kilometres of the brittle crust the value of μ is much lower than expected. This may be due to the presence of fluids in the crust acting to reduce the normal stress on the fault (Rice, 1992).

Low coefficients of friction have also been found in faults around the San Francisco Bay area of California (Reasenber and Simpson, 1992). The best correlation of seismicity-rate changes south of the bay area following the Loma Prieta event were obtained using an apparent coefficient of friction of 0.2 (Reasenber and Simpson, 1992). Assuming a laboratory coefficient of friction of 0.75 and using $\mu' = \mu(1 - B)$, Skempton's coefficient would be ~ 0.73 . This suggests a large change in fluid pressure during earthquakes (equation 6.12). As the fluid pressure drops the shear stresses required for slip become larger and slip eventually ceases. A good agreement between locations of the Landers (M7.4, 1992) southern California aftershocks and the Coulomb stress increase was found using an apparent coefficient of friction of 0.4 (King *et al.*, 1994). Extreme values of 0.2 and 0.6 were used to calculate the loading effect of the Landers earthquake on the San Andreas fault (Jaumé and Sykes, 1992). It was suggested that if the value of μ lies near the laboratory values, and there was a stress drop of 5×10^5 Pa, then the apparent coefficient of friction was approximately 0.2 immediately after the event and later rose to 0.6 due to the diffusion of fluids. An apparent coefficient of 0.4 is used to model the static stress changes on optimally-orientated faults since this is a typical value. In all cases a Skempton's coefficient of 0 is assumed. The stress changes are calculated at depths of 7 km as this is near the base of the geodetically-inferred faults.

6.5 RESULTS

6.5.1 Stress changes preceding the Fairview Peak earthquake

6.5.1.1 Stress changes on the geodetically inferred faults

Static stress changes encouraging right-lateral slip on the Fairview Peak fault caused by the Rainbow Mountain events are at most 0.2×10^5 Pa, assuming $\mu' = 0.4$, and decrease

with increasing friction (Table 6.1; Figure 6.7a). The stress changes become negative at 5 km along the fault. Stress changes encouraging normal faulting are at most 4×10^3 Pa, and are approximately the same for all values of μ' . The stress changes on the West Gate/Gold King fault show that right-lateral strike slip faulting was encouraged on this fault by a stress change of up to 0.65×10^5 Pa for $\mu'=0.4$ and normal faulting was encouraged by a stress change of 0.7×10^5 Pa (Figure 6.7b). The Dixie Valley fault was brought closer to strike-slip failure along its southernmost 10 km and closer to normal faulting along most of its length for $\mu'=0.4$. Normal and right-lateral stresses resolved onto the Dixie Valley fault are about three times greater than those on the Fairview Peak fault (Figure 6.7c). The stress changes encouraging right-lateral and normal slip were 0.7×10^5 Pa and 0.1×10^5 Pa respectively (Table 6.1).

Table 6.1 Stress changes induced by the events in the 1954 earthquake sequence. RM: Rainbow Mountain, WG/GK: West Gate and Gold King, FP: Fairview Peak, DV: Dixie Valley.

Triggering Earthquakes	Triggered Earthquakes	Calculated Stress Change (10^5 Pa)*			
		RESOLVED		OPTIMALLY-ORIENTATED	
		Right-lateral	Normal	N60°W	N34°W
RM →	FP	0.2	0.04	0.1	0.2
	WG/GK	0.6	0.7	0.6	0.4
	DV	0.7	0.1	1.0	0.8
RM+FP+WG →	DV	3.0	0.4	1.0	0.4

* Assumed $\mu=0.4$, $B=0$. Maximum stress change at 7 km shown.

6.5.1.2 Stress changes on optimally-orientated faults

Planes that are optimally orientated for normal failure in the Dixie Valley-Fairview Peak region strike northeast-southwest, close to the orientations of the faults which failed (Figure 6.8). Stresses on favourably-orientated planes around the Fairview Peak fault are increased by $0.1-0.2 \times 10^5$ Pa at the north end of the fault but along most of the fault are decreased. There is little variation in stress change with depth (Figure 6.9). Increasing the apparent coefficient of friction decreases the calculated stress changes on optimally-orientated faults in the vicinity of the Fairview Peak fault. Values of $\mu'=0.2$ to $\mu'=0.8$, ($B=0$), resulted in stress changes on the fault varying from 0.3×10^5 Pa to 0.1×10^5 Pa respectively.

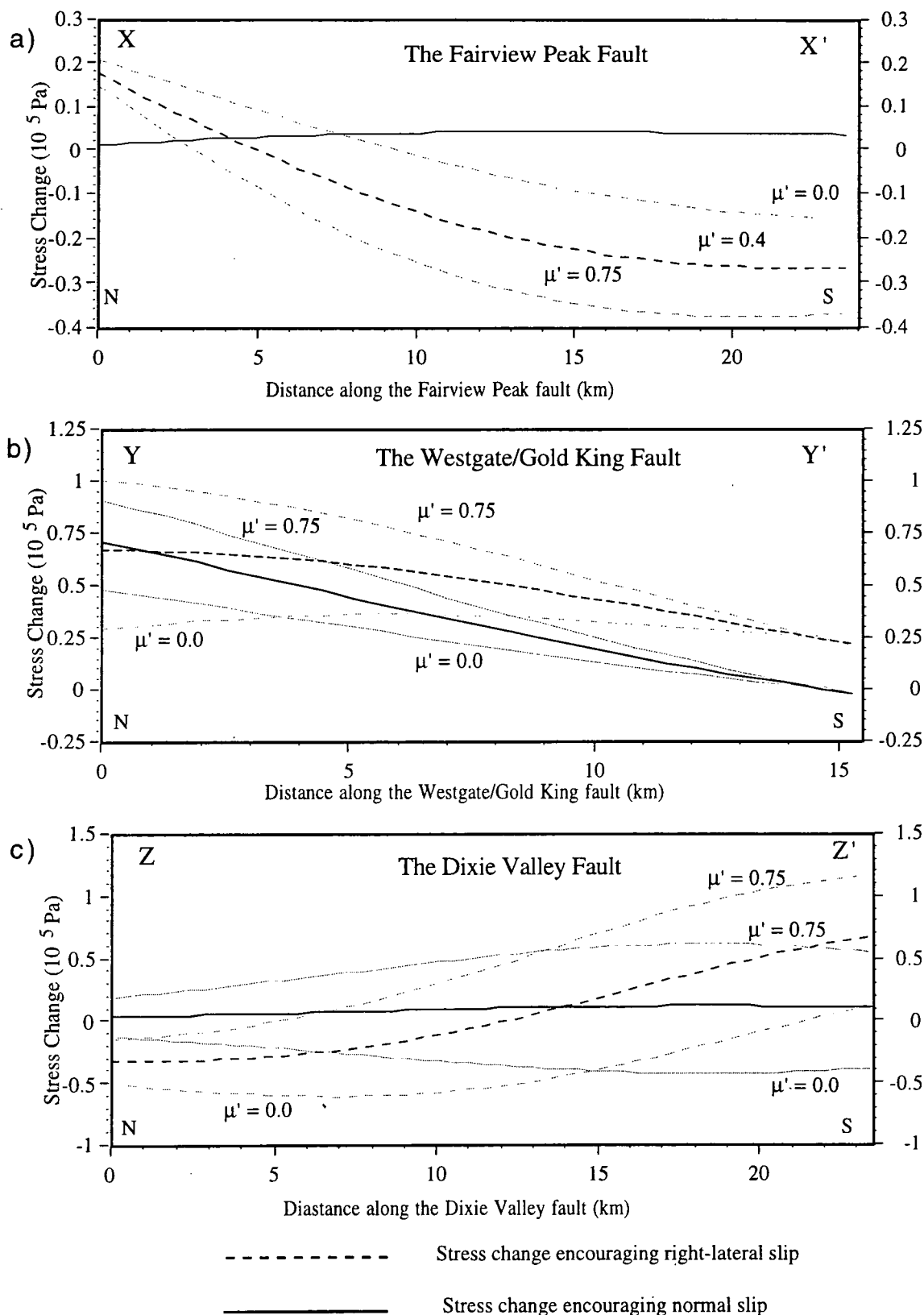


Figure 6.7 Stresses induced by the Rainbow Mountain event resolved onto a) the Fairview Peak fault, b) the West Gate/Gold King fault, and c) the Dixie Valley fault. Dashed lines represent stress changes encouraging right-lateral slip and solid lines represent stress changes encouraging normal slip. Calculations are made for $\mu' = 0.0, 0.4$ and 0.74 . The black lines represent calculations made with $\mu' = 0.4$ and the gray lines represent the upper and lower limits of these values calculated using $\mu' = 0.0$ and 0.75 . For positions XX', YY' and ZZ' see Figure 6.8a.

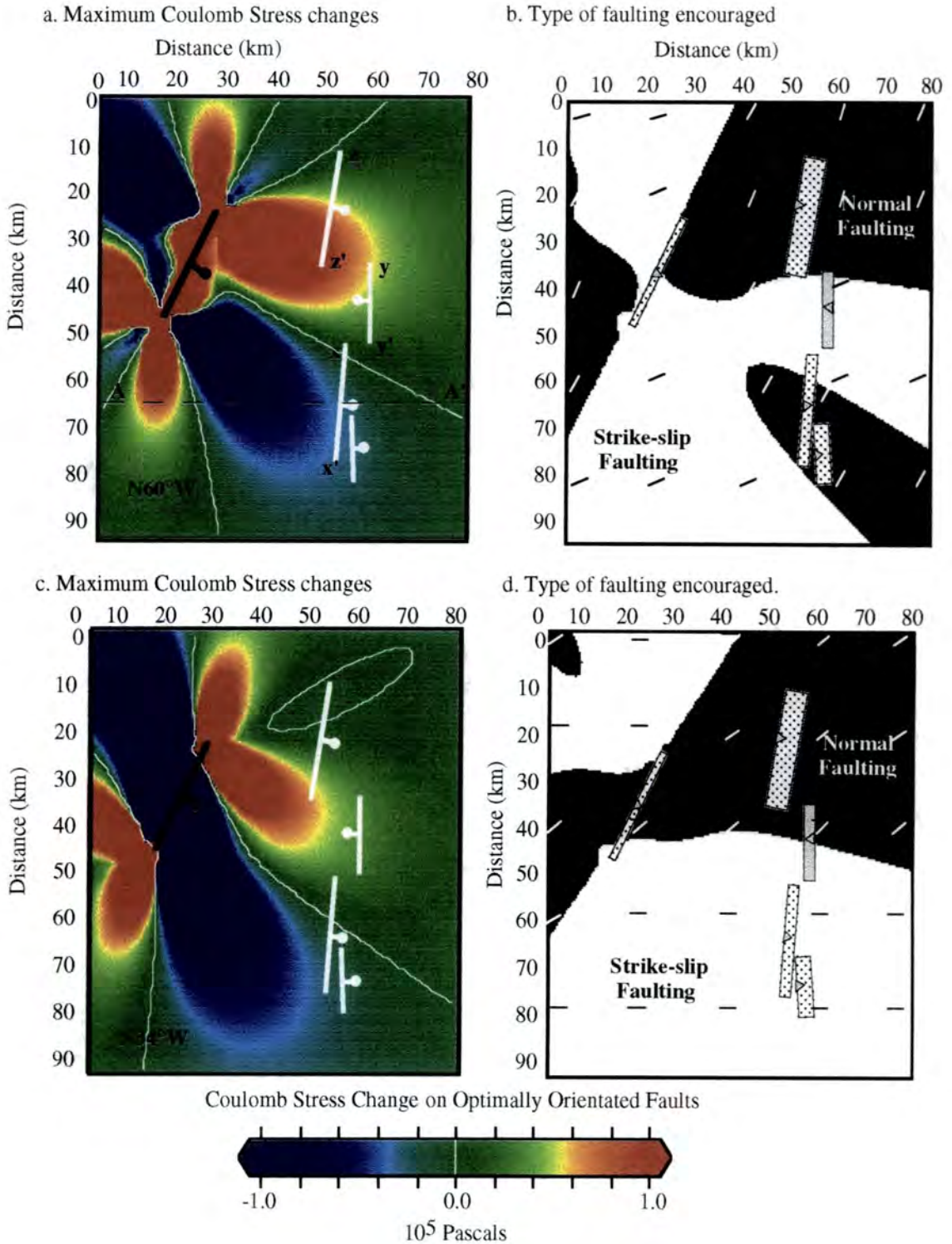


Figure 6.8 Coulomb stress change fields associated with slip on the Rainbow Mountain fault. Friction coefficient $\mu' = 0.4$. Depth = 7 km. Fault coloured black indicates the fault has slipped, while white indicates that the fault has yet to fail. a) and b) regional extensional stress orientated at N60°W, c) and d) regional extensional stress field orientated at N34°W. In b and d, black regions are areas where stress changes encouraging normal faulting are greater than those encouraging strike-slip faulting, in white areas stress changes encouraging strike-slip faulting. Planes most favourably orientated for failure are shown in 6b and 6d where black lines show the orientation of optimally orientated strike-slip faults and the white lines the orientation of optimally orientated dipping faults.

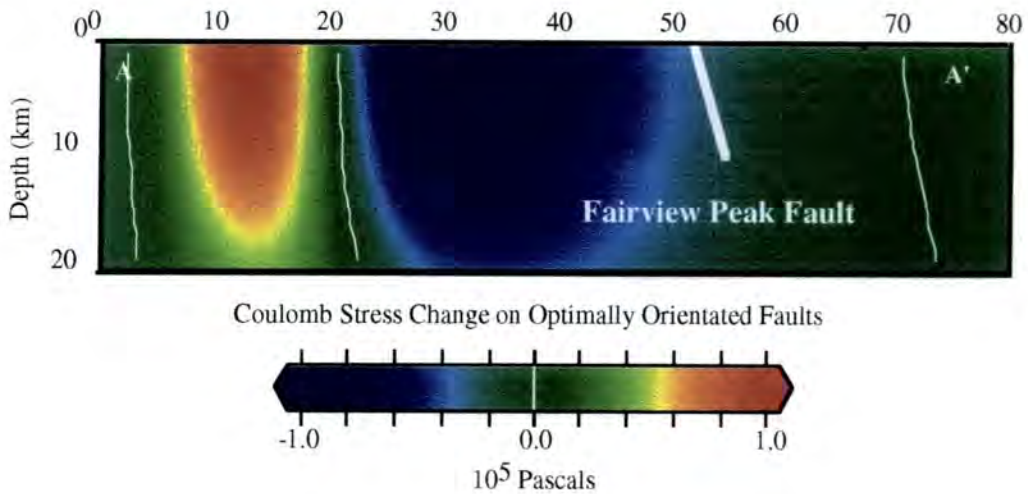


Figure 6.9 Coulomb stress changes across the Fairview Peak fault caused by slip on the Rainbow Mountain fault along profile AA' (shown in Figure 6.8a).

Optimally orientated faults in the West Gate and Gold King rupture area received a stress increase of 0.6×10^5 Pa (Table 6.1). The Dixie Valley fault region received a relatively large stress increase, about 1×10^5 Pa on optimally orientated faults. For a regional stress orientation of $N60^\circ W$, 50% of the fault received a positive stress increase. The Dixie Valley fault lies in a region where the stress changes encouraging normal faulting are greater than those encouraging right-lateral faulting regardless of the regional stress orientation (Figures 6.8b and 6.8d). The mode of faulting encouraged on the Fairview Peak fault however, changes from one of normal faulting for a regional stress of $N60^\circ W$ to one of right-lateral faulting for a regional stress of $N34^\circ W$.

6.5.2 Stress change preceding the Dixie Valley event

6.5.2.1 Stress changes on geodetically inferred faults

The combined stress changes resulting from the Rainbow Mountain Fairview Peak, West Gate and Gold King events encouraged normal faulting along the northern half of the fault where the Dixie Valley epicenter was located (Doser, 1986). The stress changes encouraging right-lateral faulting were large, up to 3×10^5 Pa for an apparent coefficient of friction of 0.4 (Figure 6.10) (Table 6.1). Stress changes encouraging normal faulting were small and varied from 0.4×10^5 Pa for $\mu' = 0.75$ to -4×10^5 Pa for $\mu' = 0.0$. For $\mu' = 0.4$ the fault received between 1×10^5 Pa and 0.4×10^5 Pa of stress increase encouraging normal failure. Towards the southern end of the fault, where rupture ceased, the stress changes discouraged failure.

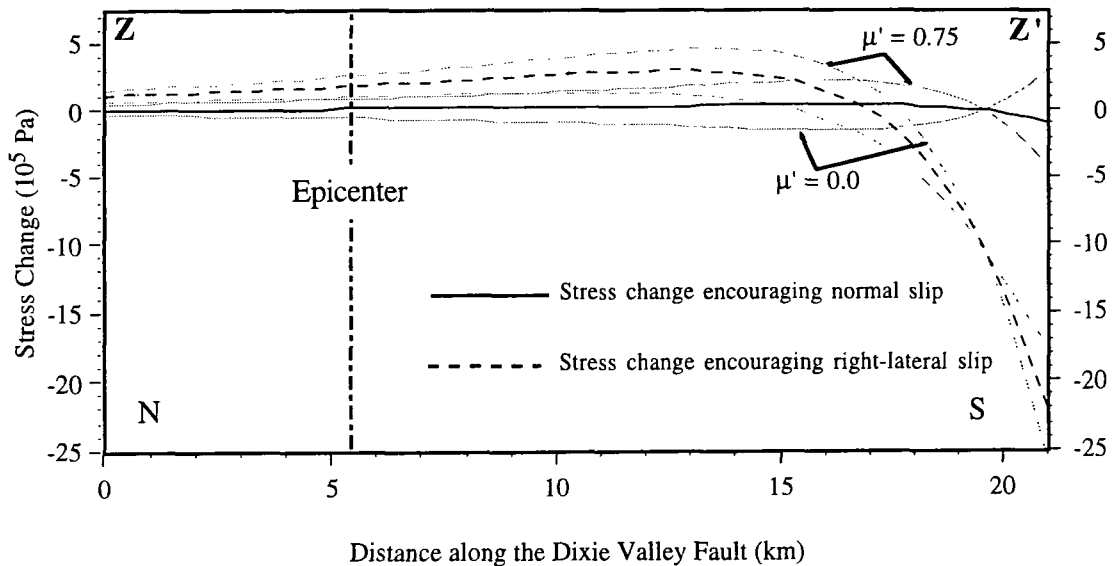


Figure 6.10 Stress resolved onto the Dixie Valley fault caused by the Rainbow Mountain, Fairview Peak and West Gate/Gold King events.

6.5.2.2 Stress changes on optimally-orientated faults

Slip on the Rainbow Mountain, Fairview Peak and West Gate/Gold King faults created a region of increased stress within Dixie Valley. The stress changes on optimally-orientated faults in the vicinity of the Dixie Valley fault were greater than 1×10^5 Pa along 70% of the fault for a regional stress orientation of $N60^\circ W$ (Figure 6.11a). The fault extends into areas of stress increase of 1×10^5 Pa or more at depths of 10 to 12 km (Figure 6.12). The regional stress field becomes important in distinguishing whether stress changes encouraging normal faulting or strike-slip faulting were greater on the Dixie Valley fault (Figure 6.11b and 6.11d). For regional extensional stress orientated at $N60^\circ W$ the Dixie Valley fault lies in a region where stress changes encouraging strike-slip faulting are greatest. For a stress field orientated at $N34^\circ W$ the upper part of the fault receives larger stress changes encouraging normal faulting but at depth stress changes encouraging strike-slip faulting were greatest.

6.5.3 Stress changes on optimally-orientated faults resulting from the 1954 earthquake sequence

There is a positive though imperfect correlation between areas of positive Coulomb stress change caused by the 1954 earthquake sequence and seismicity in the area between 1955 and 1990 (Figure 6.13). Red areas indicate regions that received a positive Coulomb stress change and regions where seismicity in following years would be expected to occur. Seismicity is concentrated in a north-south band along the Fairview Peak, West Gate and Dixie Valley ruptures as are the positive stress changes. The seismicity though is more diffuse than the 5 to 10 km wide band the positive stress changes would predict.

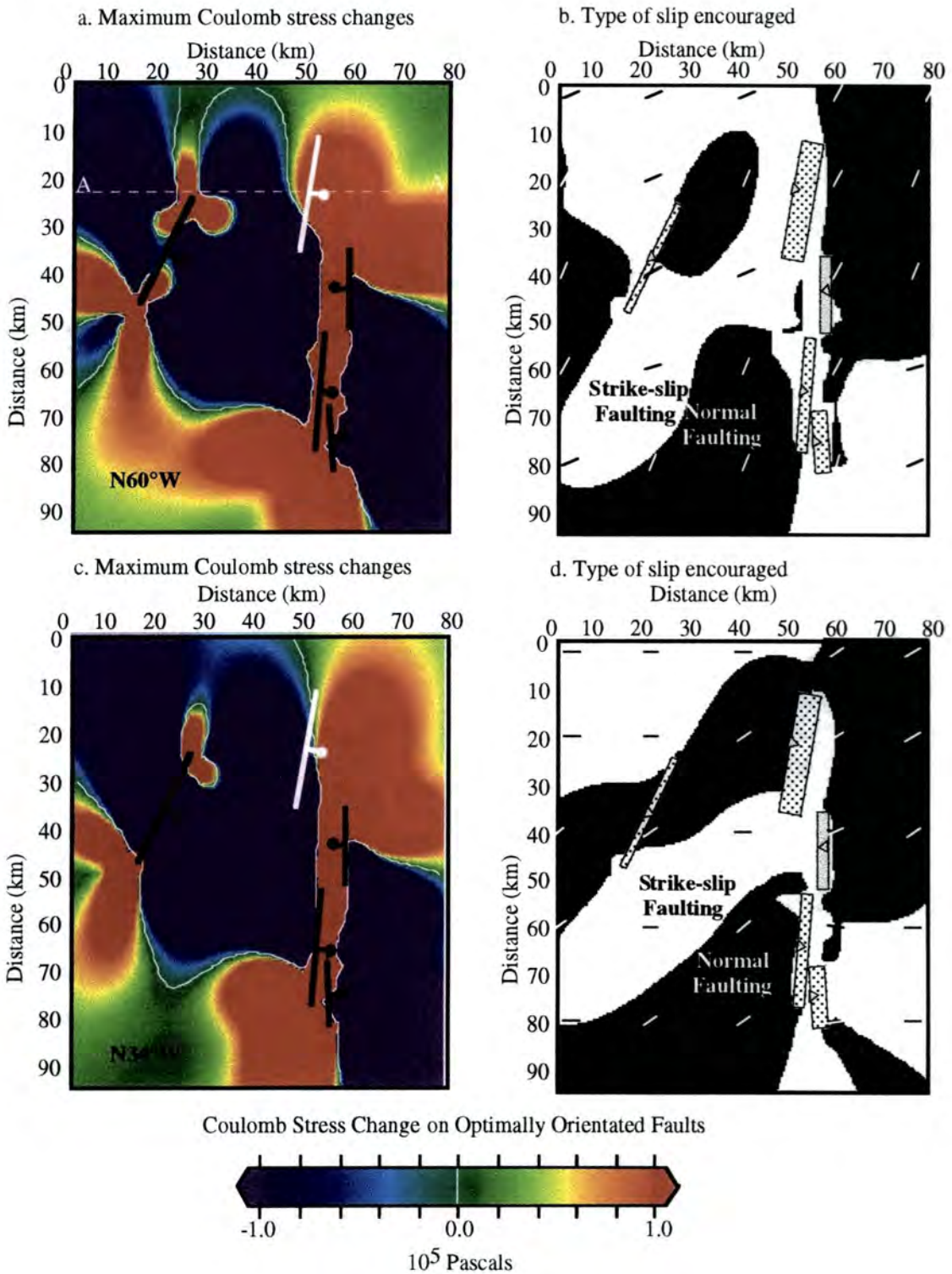


Figure 6.11 Coulomb stress-change fields associated with slip on the Rainbow Mountain, Fairview Peak and West Gate/Gold King faults. Faults coloured black have slipped, while white indicates the fault has yet to fail. a) and b) regional extensional stress orientated at N60°W, c) and d) regional extensional stress field orientated at N34°W. Planes most favourably orientated for failure are shown in b and d where black regions are areas likely to fail by normal faulting, white areas by strike-slip faulting.

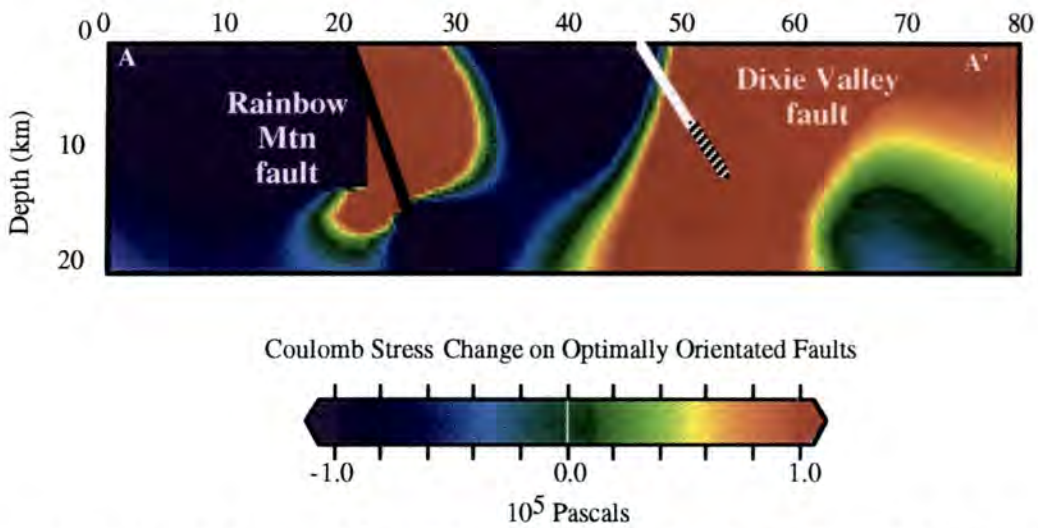


Figure 6.12 Variation in maximum Coulomb stress change with depth due to slip on all but the Dixie Valley fault along profile AA' (see Figure 6.12a). White fault line shows the geodetically-inferred Dixie valley fault, the hashed extension shows the extension to the focal depth calculated by Doser (1986).

There are few events to the west of the Rainbow Mountain fault where the Coulomb stress increases are negative, and the seismicity around the southwest of the Fairview Peak fault and to the east of the Dixie Valley fault lie with in the region of positive stress-change. Along the Rainbow Mountain fault however, there is a northeast trend of seismicity in an area where the static stresses where reduced. The stress-change field for a regional extension orientated at N34°W agrees slightly better with the seismicity, particularly to the north-east of the Dixie Valley fault. The mismatch between seismicity and regions of increased static stress changes may be a result of the poor epicentral location of some of the events which may have an error of 5 km.

6.6 SUMMARY

It has been proposed that increases in the static stress field can induce an increase in seismicity rates and trigger moderate to large earthquakes. By this theory, each earthquake releases stress on the fault that slipped but transfers it elsewhere. The rate of subsequent earthquakes is then higher where stress was raised. By calculating the static stress changes associated with each earthquake in the 1954 sequence, it is determined whether the stress changes caused by each event encouraged or discouraged the succeeding events. Stress changes are calculated both in the direction of slip on the faults and on optimally-oriented faults.

Each event in the 1954 sequence caused an increase in static stresses, encouraging right-lateral and/or normal faulting on some part of the faults which failed next. The magnitude

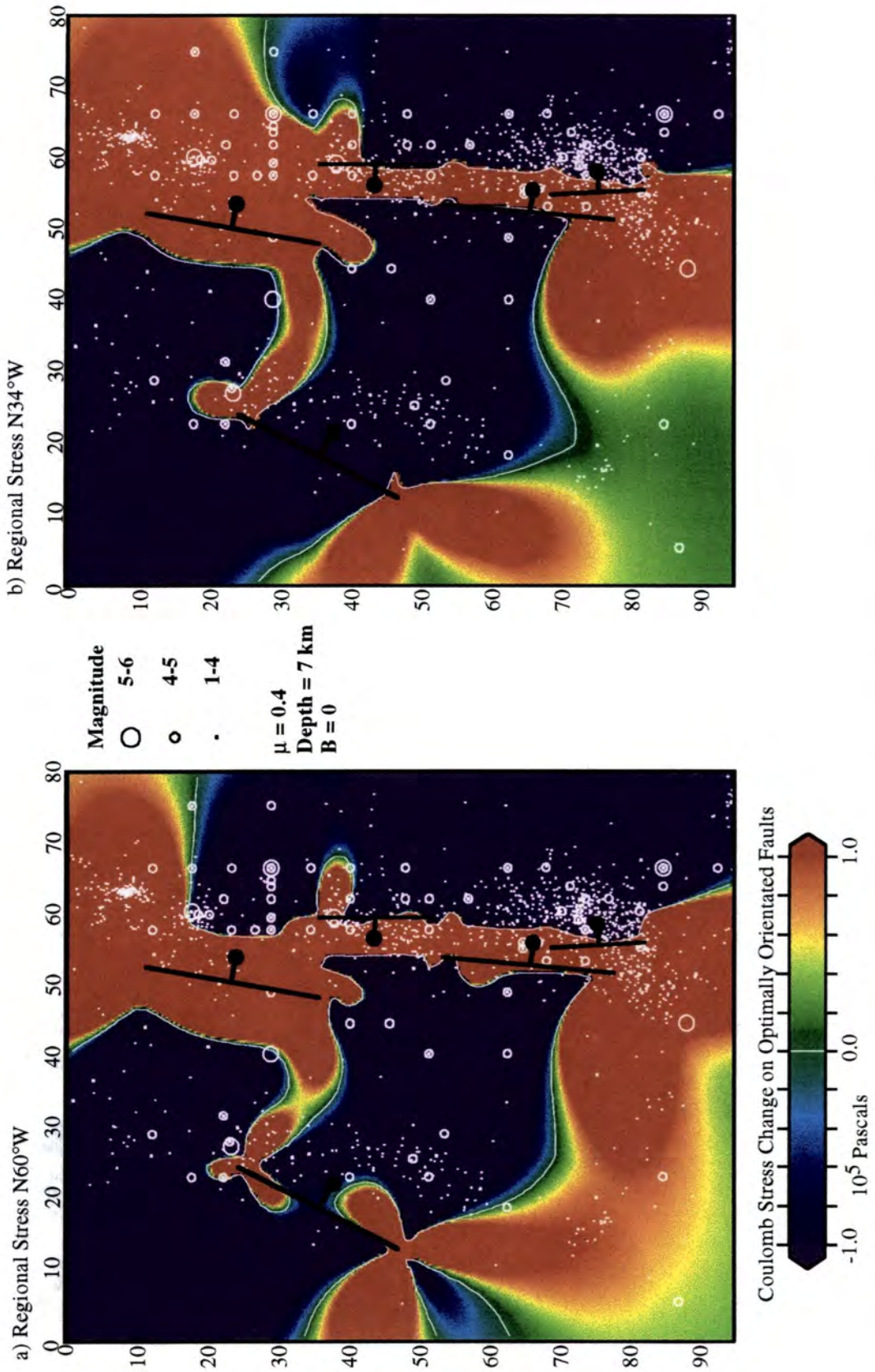


Figure 6.13 Regions of increased Coulomb stress caused by the 1954 sequence of earthquakes and aftershocks from 12/16/54 to 01/01/91.

of the stress increases ranged from 1×10^4 Pa to over 1×10^5 Pa. The Rainbow Mountain earthquakes transferred a positive but relatively low stress increase onto the Fairview Peak fault compared to that transferred to the Dixie Valley fault. The Rainbow Mountain events, although associated with the smallest amount of slip, play an important role in the triggering of the Dixie Valley earthquake. The Dixie Valley fault received a large stress increase from the Rainbow Mountain event because of the relative geometrical position of the faults, the orientation of the regional stress, and the right lateral motion which occurred on the Rainbow Mountain fault. This combination of factors caused a lobe of stress increase of 1×10^5 Pa to fall in the region of the Dixie Valley fault. The stress changes which preceded rupture on the Dixie Valley fault encouraged failure through normal and right-lateral slip and were greatest at the northern end of the fault where rupture began (Doser, 1986).

The orientation of the regional stress field does not greatly affect the magnitude of the maximum Coulomb stress on optimally-orientated faults but it does affect which stress changes dominate, those encouraging strike-slip or normal faulting. For an orientation of $N60^\circ W$ the stress changes encouraging normal slip are larger than those encouraging right-lateral slip preceding the Fairview Peak event and stress changes encouraging right-lateral slip are largest preceding the Dixie Valley event. For an orientation of $N34^\circ W$ however, the stress changes encouraging right-lateral slip are largest preceding the Fairview Peak event and stress changes encouraging normal slip are largest preceding the Dixie Valley event. It can be concluded that the Dixie Valley event was encouraged by the combined stress changes of the Rainbow Mountain and Fairview Peak events. The West Gate/Gold King events caused sufficient normal static stress changes to the north of the fault to push an already unstable fault to failure. The spatial distribution of aftershocks and later earthquakes do fall in regions of encouraged failure. The static stress changes do therefore predict regions of increased seismicity following the 1954 earthquake sequence.

CHAPTER 7

ANALYSIS OF THE POSTSEISMIC DEFORMATION THAT FOLLOWED THE FAIRVIEW PEAK EARTHQUAKE

7.1 INTRODUCTION

The earthquake cycle is envisaged as being divided into three stages: the preseismic, coseismic and postseismic stages. In the coseismic stage, strain in the Earth's crust is released through movement on faults. The postseismic stage which follows is the Earth's response to the sudden coseismic elastic release of stress. This stage may be divided into two epochs, the first being a period of relatively rapid postseismic deformation concentrated around the fault while the second, is characterized by slower, broader deformation. While modelling the coseismic deformation associated with an earthquake allows the fault geometry and coseismic slip to be estimated, modelling the postseismic deformation can yield information on the rheology of the Earth and the rates at which the stress released by the event is reaccumulated. Knowledge of the rates of postseismic deformation in turn allow estimates of earthquake recurrence intervals to be made.

There is controversy about the process that causes postseismic deformation, whether through deep, aseismic slip on a downward extension of the fault, or through ductile flow in viscoelastic layers below the brittle upper crust. The lack of high quality geodetic data spanning a sufficiently long time period after a large earthquake, combined with inherent ambiguity, has made it difficult to distinguish one model from the other. Geodetic data constraining the postseismic deformation associated with the Nankaido earthquake of 1946 in southwest Japan have been compared to the deformation predicted by both models (Savage, 1983; Thatcher and Rundle, 1984). It was found that while the deep-slip model explained best the short-term, postseismic deformation immediately following the earthquake, the long-term deformation was best modelled assuming a viscoelastic model. Neither model, however, could explain the permanent, cumulative deformation associated

with events in the subduction zone as recorded by uplifted Quaternary and Holocene marine terraces along the shoreline.

The 1954 Rainbow Mountain-Fairview Peak-Dixie Valley earthquake sequence provides geodetic measurements of the coseismic and postseismic stages of the earthquake cycle. Following the 1954 Fairview Peak earthquake four levelling surveys were made of the epicentral area. The first survey was made 6 months after the event and the fourth 32 years later. To investigate which model best fits the postseismic levelling observations around the Fairview Peak fault, the postseismic data are modelled using both the deep aseismic slip and the viscoelastic models. Using the former model, the data are inverted and the slip at depth found by assuming uniform slip on a rectangular dislocation embedded in an elastic half-space. Using the latter model the data are modelled assuming a rheologically-varied Earth's crust and using the finite element method. This numerical method has the advantage over analytical methods in that a crustal model consisting of several layers with different rheologies can be used. The relation between the postseismic vertical deformation and fault geometry, thickness of the brittle upper crust and viscosity are studied.

7.2 POSTSEISMIC DEFORMATION AND EARTH RHEOLOGY

7.2.1 Postseismic deformation

Elastic dislocation theory predicts that the horizontal and vertical deformation fields accompanying an earthquake have a limited spatial extent and are static. There is generally reasonable agreement between coseismic geodetic measurements and the displacement and strain fields calculated assuming uniform slip on dislocations embedded in an elastic half space. This shows that the coseismic deformation fields are usually adequately described by this theory (*e.g.*, Savage and Hastie, 1966; Reilinger, 1984; Stein and Barrientos, 1985; Murray, 1993).

There is geodetic evidence that postseismic stress and strain fields are time variant and not confined to distances of a few fault depths from the event. Twenty-four years after the 1959 $M_s7.3$ earthquake at Hebgen Lake, USA, 20 cm of additional vertical deformation was measured in the epicentral area (Reilinger, 1986). Trilateration measurements made in the area between 1973 and 1987 indicate a strain rate of $0.266 \mu\text{strain/yr}$ (Savage *et al.*, 1993). In Japan, 22 cm of vertical deformation were measured in the 20 years after the 1946 Nankaido earthquake (Thatcher *et al.*, 1980; Thatcher and Rundle, 1984). Within 6 months of the $M_s6.4$ San Fernando earthquake postseismic slip equal to 3% of the coseismic slip was observed on the San Fernando fault. Over a longer time period,

anelastic behaviour of the Earth is observed in postglacial rebound which is believed to be the viscous response of the Earth's asthenosphere to the melting of large glaciers (Haskell, 1935).

Elastic rebound theory fails to explain how the coseismic strain field, which is modelled well with dislocation theory and is confined to the vicinity of the fault, contributes to the relative motion between plates or accommodates extension over wide regions. Earthquakes on normal faults contribute to the extension of large portions of plates, *e.g.*, the Basin and Range province and western Turkey, and motion at the plate boundaries is influenced by slip on faults which are tens of kilometres away. At spreading plate boundaries, extension is effected by discrete rifting events along spreading segments. A decade after the 1975 to 1985 rifting event in the Krafla segment, Iceland, which caused an average extension of 3.5 m along the plate boundary, a spatially varying strain field was detected using GPS in north Iceland (Foulger *et al.*, 1992; Heki *et al.*, 1993).

Two hypotheses have been proposed to explain the time-dependent deformation observed after an earthquake. One hypothesis proposes that the Earth may be modelled as a sequence of rheologically-varying layers where there is at least one viscoelastic layer where flow occurs (Elsasser, 1969; Nur and Mavko, 1974). In the elastic-over-viscoelastic model the immediate elastic response to an earthquake is followed by slow deformation through viscous flow in a layer below the Earth's elastic upper crust. This flow allows relaxation of the deviatoric stresses around the ruptured fault and allows the strain to propagate out into the lithospheric plates. The second hypothesis states that while the portion of the fault which ruptured coseismically remains locked after the earthquake, slip occurs aseismically on its downward extension (Savage, 1990). The driving force behind the postseismic deformation in the latter model is then continued slip on the fault at depth. In the case of this model, the aseismic motion can be modelled as slip on a rectangular dislocation in an elastic half space.

Savage and Prescott (1978) suggested that surface measurements cannot be used to distinguish between the two models. Any deformation field caused by viscous flow could be reproduced by modelling a variable slip distribution at depth. This was illustrated by showing that geodetic measurements made along the San Andreas fault between 1973 and 1988 could be fitted by a variable slip distribution on a downward extension of the fault embedded in an elastic half space (Savage, 1990). Using this approach, the data suggested that the San Andreas fault was locked above 30 km and slipped at a rate of 36 mm/yr below this. The data could also be modelled as a 30 km brittle crust overlying a viscoelastic layer in an elastic-over-viscoelastic type model.

7.2.2 The rheology of the crust and upper mantle

There is an abundance of evidence which indicates the Earth's crust is made up of rheologically different layers. In the brittle upper crust rocks fail according to Byerlee's law which states:

$$\begin{aligned} \tau &= 50 + 0.6\sigma_n && \text{(for } \sigma_n > 200 \text{ MPa)} \\ \text{and,} & && \\ \tau &= 0.85\sigma_n && \text{(for } \sigma_n < 200 \text{ MPa)} \end{aligned} \tag{7.1}$$

where σ_n is the normal stress and τ is the shear stress. In-situ stress measurements of horizontal stresses in the upper 3 km of the crust in mines and laboratory experiments support equation 7.1 (Brace, 1980). These results imply that rock strength increases linearly with depth in the upper part of the crust and that the stress at which rocks fail in the brittle upper crust is independent of lithology. The term 'strength' is defined as the maximum stress difference which rocks can support at a specific temperature and pressure. The depth to which the brittle layer extends can be determined from the focal depths of earthquakes. Since earthquakes are associated with brittle failure it can be inferred that where they occur the rock is strong enough to fail according to Byerlee's law. The lower limit of seismicity in the brittle crust is generally 15 to 20 km in regions of strike-slip faulting and 12 to 15 km in regions of normal faulting (Chen and Molnar, 1983).

The presence of a rheologically weaker layer below the brittle crust beneath the Basin and Range province has been inferred from seismic reflection profiles as a change from non-reflective to reflective material accompanied by an increase in seismic velocity (Catching and Mooney, 1991). This interpretation is supported by the absence of seismicity below a certain depth. The explanation for the existence of this weaker layer comes from laboratory experiments. The brittle behaviour of crystalline materials gives way to ductile behaviour when the ductile strength equals the brittle strength, *i.e.*, when crystal dislocations can propagate as easily as cracks. The transition from brittle to ductile behaviour is dependent on the temperature, strain rate, pressure and lithology. For quartz the transition occurs at about 300°C while for feldspar the transition occurs at 450°-500°C (Scholz, 1990). At the high temperatures found in the lower crust, rocks are too weak to allow the stress levels needed for earthquakes to be reached and the strength of the rocks decreases rapidly with temperature (and depth) below this.

The Moho is the seismically-defined boundary between the lower crust and the upper mantle. There are many examples of intraplate earthquakes occurring at depths greater than 30 km and below the Moho. This indicates that in those areas the upper mantle is

strong enough to accumulate stress sufficient for brittle failure. Its greater strength is also verified by extrapolating laboratory values for the brittle and ductile strengths of materials at high temperatures. Whereas the lower crust is thought to be predominately comprised of pyroxenes and feldspars, the mantle is thought to be 80% olivine. The strength of olivine can be two orders of magnitude greater than that of pyroxenes or feldspars at temperatures between 300°C and 1000°C (Chen and Molnar, 1983). Thus the change of rock type causes increase in strength at this depth.

7.3 FINITE ELEMENT ANALYSIS

7.3.1 Overview of the method

Finite element analysis is used in this thesis to model the anelastic response of the Earth because it allows the assignment of different rheological properties to individual elements to create a rheologically-varying crustal model. The finite element program TECTON was used (Melosh and Raefsky, 1980). The program uses a two-dimensional plane-strain algorithm to calculate the static elastic and time-dependent viscoelastic response to an earthquake. It solves the static and time-dependent problem through the displacement-based finite element method. The analysis can be divided into four basic steps: (1) The region under study is divided into small areas called elements. (2) Joints, or nodes, which completely define the elements are identified. (3) The governing finite-element equations (force-balance equations) which express the node displacements when forces are applied to the grid are established. (4) When the nodal displacements are known the stresses within the element are calculated. Steps one and two involve the idealization of the problem and the finite element grid design. Steps three and four relate to calculating the displacements and stresses when the grid is subjected to a force.

Profiles of the strength of the Earth versus depth can be used to produce a shallow simplified model. The Earth is typically considered to comprise a brittle upper crust, a weaker ductile lower crust and a ductile but strong upper mantle (Figure 7.1).

7.3.2 The governing finite element equations

To calculate the distortion of the elements and the displacements of nodes in response to an applied force, equations called the governing finite element equations must be formed and solved. These equations relate the displacement of the nodes to the applied forces. The unknown nodal displacements, u , are related to the nodal point forces, F , by the stiffness matrix K . In the plain-strain algorithm each node normally has two degrees of freedom, i and j . The j -th column of the stiffness matrix is the vector of nodal forces applied to maintain static equilibrium when the j -th degree of freedom has unit

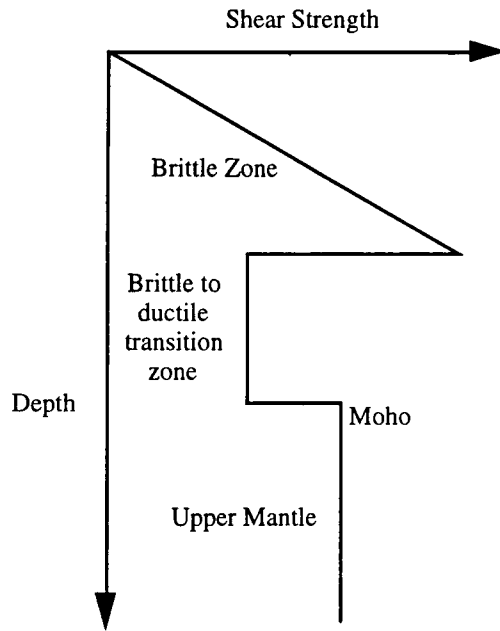


Figure 7.1 Idealised rheological strength of the Earth's crust and upper mantle versus depth.

displacement and the others have zero displacement. The deformation of the element is dependent on its material properties; Poisson's ratio, Young's modulus, and, in the case of a viscoelastic material, the viscosity.

The relation between stress and strain for elastic materials in two dimensions is given by:

$$\sigma = D\varepsilon - D\varepsilon_0 + \sigma_0 \quad (7.2)$$

where σ is the stress, ε the strain and σ_0 and ε_0 the initial stress and strain respectively. The material property matrix is represented by D , which for plane-strain is given by:

$$D = \frac{E}{(1-2\nu)(1+\nu)} \begin{bmatrix} 1-\nu & \nu & 0 \\ 0 & 1-\nu & 0 \\ 0 & 0 & \frac{1-2\nu}{2} \end{bmatrix} \quad (7.3)$$

where ν is Poisson's ratio and E is Young's modulus. For an elastic medium the strain is related to the displacement, u , of each node through,

$$\varepsilon = Bu \quad (7.4)$$

where B is the strain-displacement matrix. It can be shown that the potential energy, PE , of the finite element system can be expressed as:

$$PE = \frac{1}{2} u^T K u - u^T F \quad (7.5)$$

where K is the stiffness matrix and F represents the applied loads and initial stresses and strains (Bathe, 1982). The finite element system is stable when the potential energy of the system is a minimum, *i.e.*, when $\frac{\delta PE}{\delta u} = 0$, in which case,

$$F = K u \quad (7.6)$$

Once the stiffness matrix has been determined and the nodal point displacements have been found using equation 7.6, then the strains within each element can be calculated using equation 7.4 and the stress calculated using equation 7.2.

The time-dependent viscoelastic problem is solved by treating it as a series of static elastic steps. The driving forces at each step are derived from the viscoelastic strain calculated in the previous step (Cormeau, 1975; Hughes and Taylor, 1978). The inclusion of the viscoelastic materials requires modification of the basic elastic equations. In this study, viscoelasticity is modelled as Maxwellian. A Maxwell material behaves elastically over short periods and viscously over long time periods. If the viscoelastic flow is Newtonian, as is assumed here, the steady state strain rate $\dot{\epsilon}$ is linearly proportional to the applied stress, σ . The relation between the applied stress σ_{ij} and strain rate $\dot{\epsilon}_{ij}$ is:

$$\dot{\epsilon}_{ij} = \frac{1}{2\eta} \sigma_{ij} \quad (7.7)$$

where η is the Newtonian or linear viscosity and is a measure of the resistance to flow. Diffusion (Nabarro-Herring) creep and grain boundary (Cobel) creep are examples of Newtonian-type deformation processes. The Maxwell time t_m is the time required for the stress to relax to 1/e of its original value, and:

$$t_m = 2\eta / \mu \quad (7.8)$$

where μ is the rigidity of the material. A term defining the viscoelastic forces is included into equation 7.6 which becomes:

$$K u - \int_{\Omega} B^T D \epsilon^{vp} d\Omega - F = 0 \quad (7.9)$$

where ϵ^{vp} is the total viscoelastic strain at that time and Ω is the solution area. The program TECTON repeatedly solves this equation for u . The stresses at each time step are then calculated from the current viscoelastic strains and displacements using:

$$\sigma = DBu - D\varepsilon^{vp} - D\varepsilon_o + \sigma_o . \quad (7.10)$$

The basic rheological equation relating the stress and strain of a Maxwell viscoelastic material is:

$$\dot{\varepsilon}_{ij} = \frac{1}{2\eta} \sigma_{ij} + \frac{1}{E} \dot{\sigma}_{ij} . \quad (7.11)$$

The constitutive equations for Newtonian viscoelasticity used by TECTON are described by the following equations:

$$\begin{aligned} \dot{\varepsilon}_{xx} &= \frac{(1+\nu)}{E} [(1-\nu)\dot{\sigma}_{xx} - \nu\dot{\sigma}_{yy}] + \frac{1}{4\eta} [\sigma_{xx} - \sigma_{yy}] \\ \dot{\varepsilon}_{yy} &= \frac{(1+\nu)}{E} [(1-\nu)\dot{\sigma}_{yy} - \nu\dot{\sigma}_{xx}] + \frac{1}{4\eta} [\sigma_{xx} - \sigma_{yy}] \\ \dot{\varepsilon}_{xy} &= \frac{(1+\nu)}{E} \dot{\sigma}_{xy} + \frac{1}{4\eta} \sigma_{xy} \end{aligned} \quad (7.12)$$

where $\sigma = \sqrt{\left(\frac{\sigma_{xx} - \sigma_{yy}}{2}\right)^2 + \sigma_{xy}^2}$ (Melosh and Raefsky, 1980; 1983).

The program allows the use of either an explicit or implicit algorithm to solve these equations. In finite element analysis an explicit method of solution is stable for small time steps only but its advantage is that it does not use as much computer memory since the stiffness matrix is constant throughout the calculations. The implicit method is stable at all time steps but is expensive in terms of computer memory as the stiffness matrix is recalculated at each time step. In all the calculations presented here the implicit method is used to ensure numerical stability.

Slip on fault surfaces is modelled using uniquely identified nodes, called split nodes, which are assigned an extra degree of freedom (Melosh and Raefsky, 1981). A fault is defined by a single line of split nodes. Slip is imposed on the fault at a time t by specifying displacements on the nodes that define the fault. Before the displacement discontinuity is introduced, each node defining the fault is shared by two elements. For example, in Figure 7.2, node 9 is shared by elements 6 and 7. When slip occurs the nodes are "split" and displaced relative to each other. Node 9 becomes two separate nodes which act independently of one another. One 'half' of the node belongs to element 6 and the other to element 7. For a continuous offset across a fault equal and opposite displacements are specified on each split node. The advantages of the split node technique are that it does not require any more computer memory than an unfaulted grid as it does

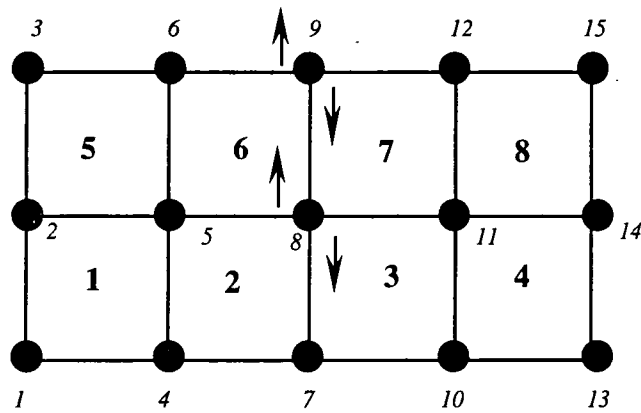


Figure 7.2 Split Nodes. Nodes 8 and 9 are split nodes and each will form two separate nodes after the displacement is imposed. Bold numbers indicate element numbers, node numbers are italicised.

not require any alteration of the stiffness matrix and does not compromise the stability of the computations.

7.4 RELATION BETWEEN FAULT GEOMETRY AND POSTSEISMIC DEFORMATION

7.4.1 Finite element calculations of the postseismic signal

Assuming deformation is caused by ductile flow, the size and rate of the postseismic deformation which follows an earthquake will depend on the rheological properties of the Earth's crust, the fault geometry and the crustal structure. In this section the relationship is examined between the amplitude of the postseismic deformation, viscosity, fault depth and thickness of the elastic layer. To facilitate this study the crustal model is kept as simple as possible. The generic crustal model used is that of an elastic layer overlying a viscoelastic layer overlying a viscoelastic layer which is rheologically stronger than the layer above (Figure 7.3a). A displacement is imposed on a fault surface, represented by a line of split nodes, and the postseismic deformation which follows is mostly a result of viscous flow in the lower crustal layer as the deviatoric stresses around the fault are relaxed.

A 1242-node grid with 1160 quadrilateral elements was used for the computations. When creating the grid three things must be considered; the size of the elements, the size of the grid and the computing resources available. The elements should be as small as possible to get good resolution and the grid must be large enough so that the boundary conditions do not interfere with the modelling. The resolution and size of the grid, however, must not be so large that memory requirements cannot be met. The grid used was 80 km deep and extended to 80 km on each side of the fault. The sides and bottom

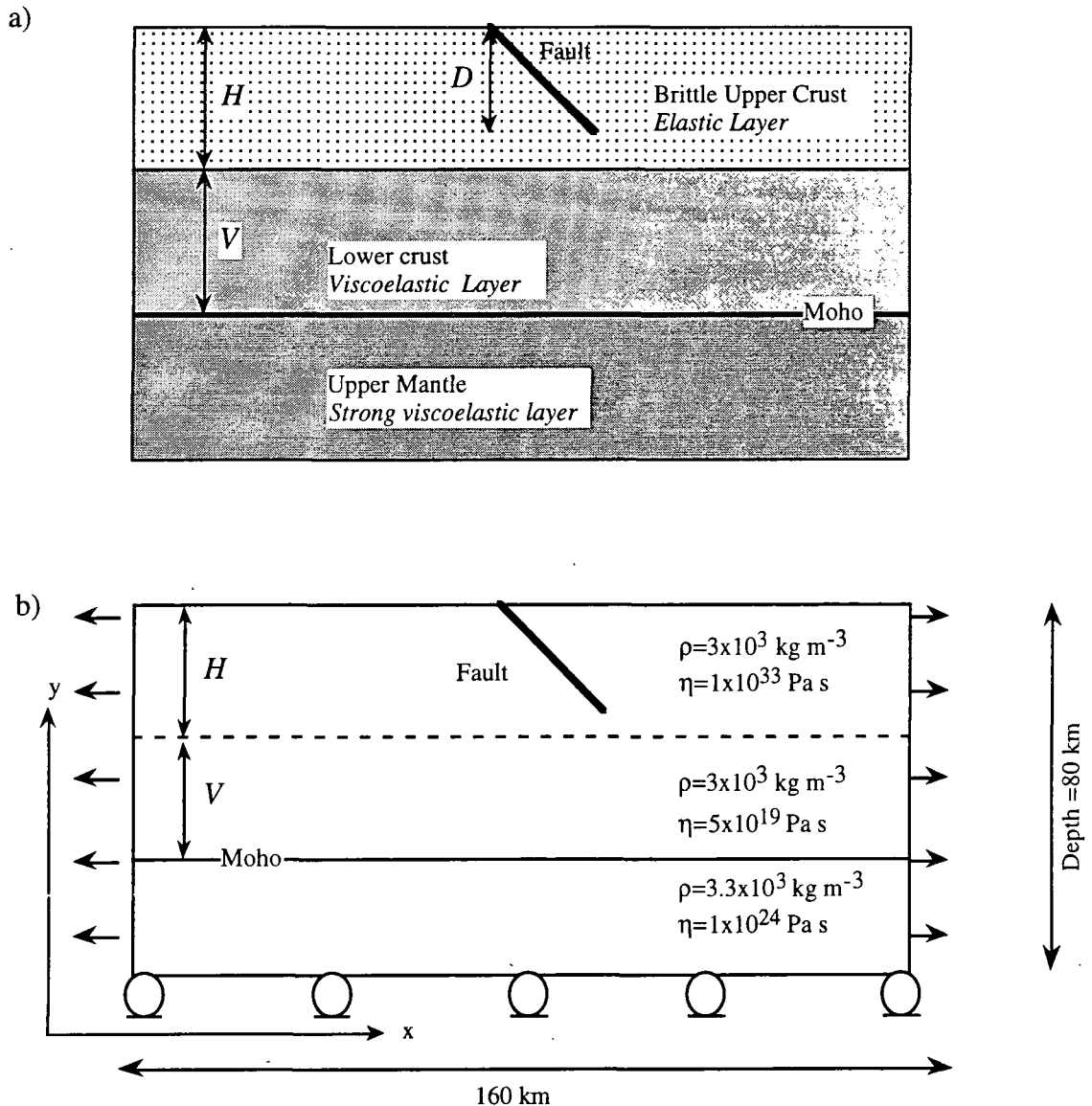


Figure 7.3 a) A simplified rheological model of the Earth's crust. An elastic layer over-lies a viscoelastic layer which overlies a rheologically-stronger viscoelastic layer, the upper mantle. The elastic layer is H km thick and the viscoelastic layer V km thick. The depth of the fault, which is represented by a solid black line, is D km deep. b) Finite element model of the Earth's crust and upper mantle. Rollers on the bottom of the grid represent zero constraints on movement in the x -direction. The density ρ and the viscosity η of each layer are shown.

of the grid were free to move in the horizontal direction but fixed in the vertical (Figure 7.3b). Poisson's ratio and Young's Modulus of 0.25 and 1.5×10^{11} Pa respectively were assumed for all three layers. The finite-element-calculated coseismic displacements agree well with the displacements calculated using the elastic dislocation analytical equations of Okada (1992) (Figure 7.4). One metre slip is imposed at $t = 0$ on a 70° E dipping fault. The viscosity of the brittle crust is 1×10^{33} Pa s and that of the upper mantle is 1×10^{24} Pa s. The viscosity of the lower crust is 5×10^{19} Pa s, which implies a Maxwell time of 26 years.

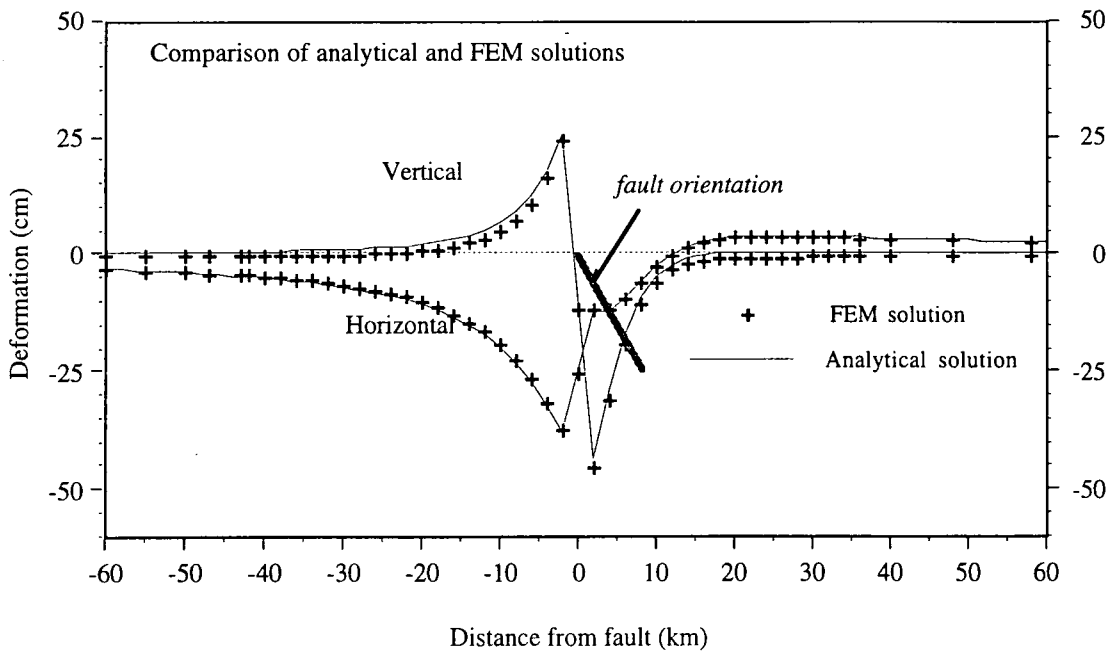


Figure 7.4 Comparison of coseismic offsets calculated using the finite element technique and the analytical equations of Okada (1992). Fault depth = 8 km, 1 m of slip applied.

The vertical and horizontal deformations are calculated at each time step. The peak-to-peak amplitude of the vertical postseismic signal is defined as the height difference between the maximum and minimum displacements and the width as the distance between them (Figure 7.5). The advantage of considering these quantities when examining the postseismic signal is that it is not necessary to define a reference point as fixed. The difference between the coseismic offset and the height of the postseismic uplift, v_t , are plotted for 10, 50 and 100 years after the event, *i.e.* $v_t = u_t - u_0$ where u_t is the coseismic plus postseismic uplift and u_0 the coseismic uplift (Figure 7.5). Positive deformation indicates uplift and negative deformation indicates subsidence. For the fault geometry used, uplift occurs over the fault trace and subsidence over the down-dip extension of the fault. Subsidence also occurs to a lesser extent on the upthrown side of the fault. The uplift and subsidence rates decrease with time, both being most rapid immediately after the earthquake. The horizontal postseismic deformation at time t is calculated analogously, *i.e.*, $h_t = x_t - x_0$ where h_t is the net horizontal deformation, x_t is the coseismic plus postseismic horizontal deformation and x_0 is the coseismic motion. Strains are large within one fault depth of the fault trace but tend to zero at larger distances (Figure 7.6). The most rapid deformation occurs immediately after the event. The horizontal velocities decay with time, though not as rapidly as the vertical motion (Section 8.3.3.2). The largest horizontal motion occurs over the downthrown side of the fault.

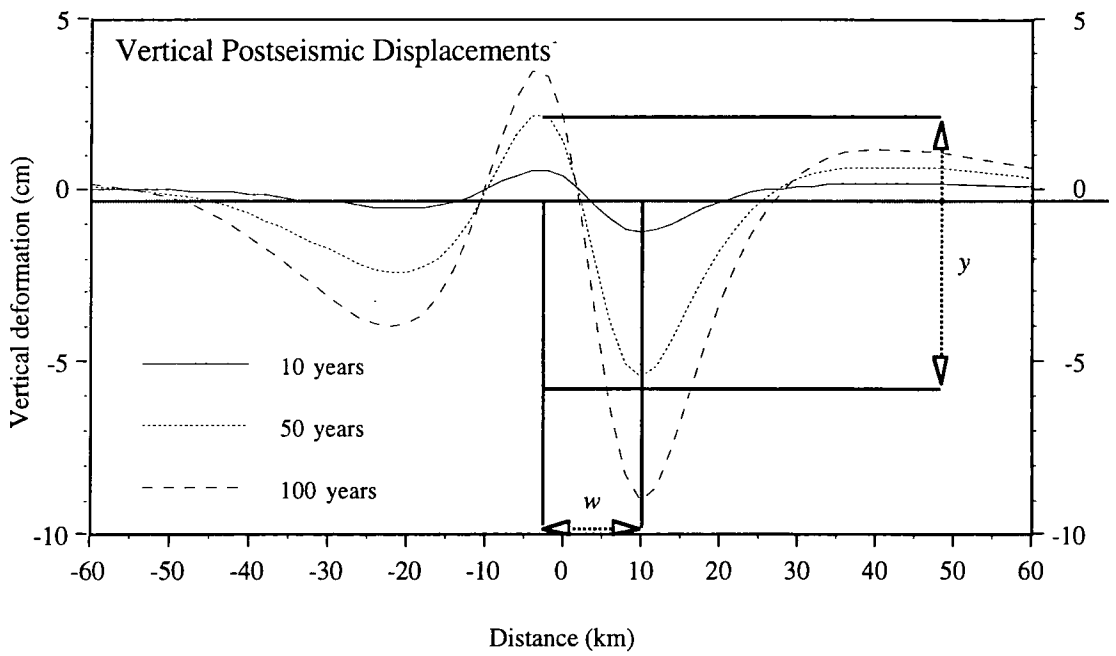


Figure 7.5 10, 50 and 100 years of cumulative, vertical, postseismic deformation following slip of 1 m on a 70°E dipping fault. The width w is the distance between the maximum and minimum displacements. The peak-to-peak amplitude y is the height difference between the points of maximum and minimum vertical uplift.

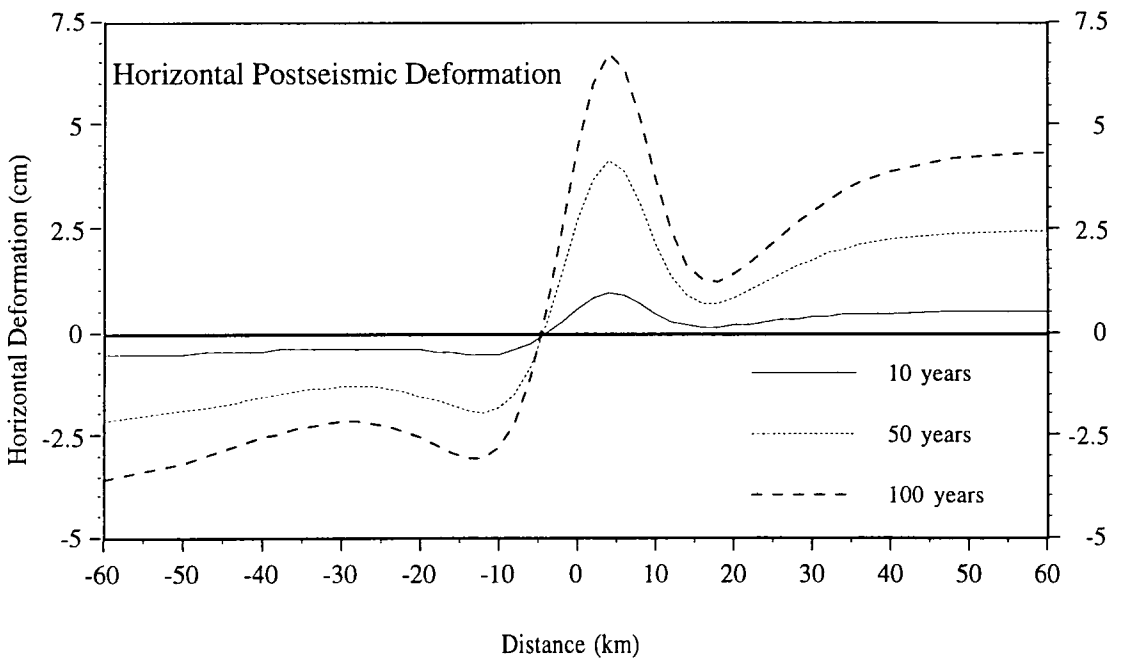


Figure 7.6 The horizontal postseismic deformation at 10, 50 and 100 years after the event.

7.4.2 Factors affecting deformation following a normal earthquake

7.4.2.1 Dependence on fault depth

The uplift following slip on a normal fault was calculated for various $D : H$ ratios (Figure 7.3a). The thickness of the elastic layer was fixed at 10 km while the fault depth was varied from 6 to 20 km. The viscosity of the lower crust was varied from 1×10^{19} Pa s to 1×10^{21} Pa s resulting in Maxwell times in the middle layer of ~ 5 years to ~ 528 years. All other parameters were as defined in Figure 7.3. One metre slip was imposed on the fault at time $t=0$ and the fault held fixed thereafter. Deformation for the 30-year postseismic period was calculated.

The peak-to-peak amplitude of the deformation decreases with increasing viscosity and is a maximum when the fault ruptures the entire elastic layer, *i.e.*, $D/H = 1$ (Figure 7.7). A transition from uplift to subsidence over the fault trace occurs when D/H is ~ 1.4 , and is independent of the viscosity of the middle layer (Figure 7.8). Therefore if a fault protrudes more than 40% into the viscoelastic layer, subsidence occurs over the fault trace in the 30 years following the earthquake. If it does not rupture the entire elastic layer then there is uplift over the fault scarp, *i.e.*, the motion over the fault scarp is in the opposite sense of the coseismic slip. This result is similar to that found by Melosh and Raefsky (1983) for a reverse faulting earthquake. The peak-to-peak amplitude cannot be used to determine D/H , *e.g.*, fault geometries with D/H ratios of 0.8 and 1.2 have approximately the same peak-to-peak amplitudes (points A and B in Figure 7.7). The two fault structures can, however, be distinguished by the *amount* of uplift over the fault scarp (Figure 7.9). Although the faults with D/H of 0.8 and 1.2 have similar peak-to-peak amplitudes the amounts of uplift over the fault trace are 1.6 cm and 0.3 cm respectively. There is no simple relation between increasing fault depth and width of the deformation field (Figure 7.10). The width of the deformation is also independent of the viscosity of the middle layer.

7.4.2.2 Dependence on the thickness of the elastic layer

To study the dependence on the thickness of the elastic layer the postseismic deformation was calculated for crustal models with increasing elastic layer thickness. Unlike the previous section, where D/H was increased by increasing the fault depth and the finite element grid was unaltered, in this case the fault depth was held fixed and the grid layers changed. As the elastic layer is made thicker the middle layer becomes thinner. The depth of the third layer was held fixed. When the fault depth is held fixed and the elastic thickness is increased the result is much the same as decreasing the fault depth (Figure 7.11). Again, the amplitude decreases with increasing viscosity and is a maximum when D/H is ~ 1 . The transition from uplift to subsidence occurs when D/H is ~ 1.4 . A smaller ratio results in uplift over the fault trace and a larger one in subsidence. While the

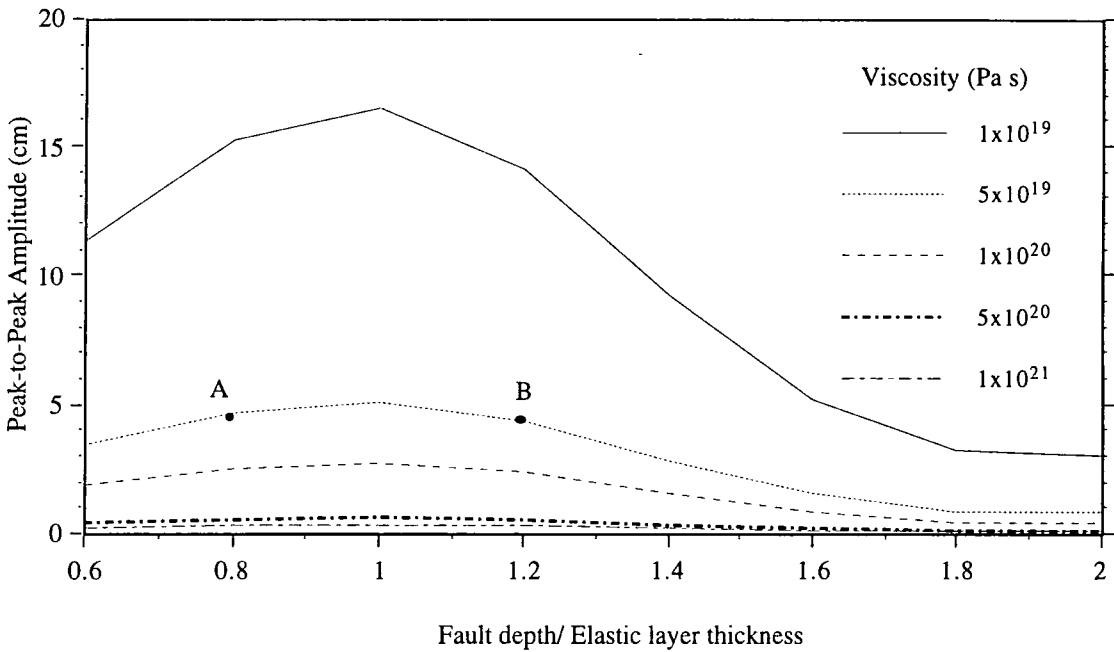


Figure 7.7 Vertical peak-to-peak amplitude of the postseismic signal 30 years after the initial elastic offsets versus the fault depth : elastic thickness ratio. Elastic thickness was fixed at 10 km while fault depth was increased. Points A and B indicate two ratios with similar peak-to-peak amplitudes.

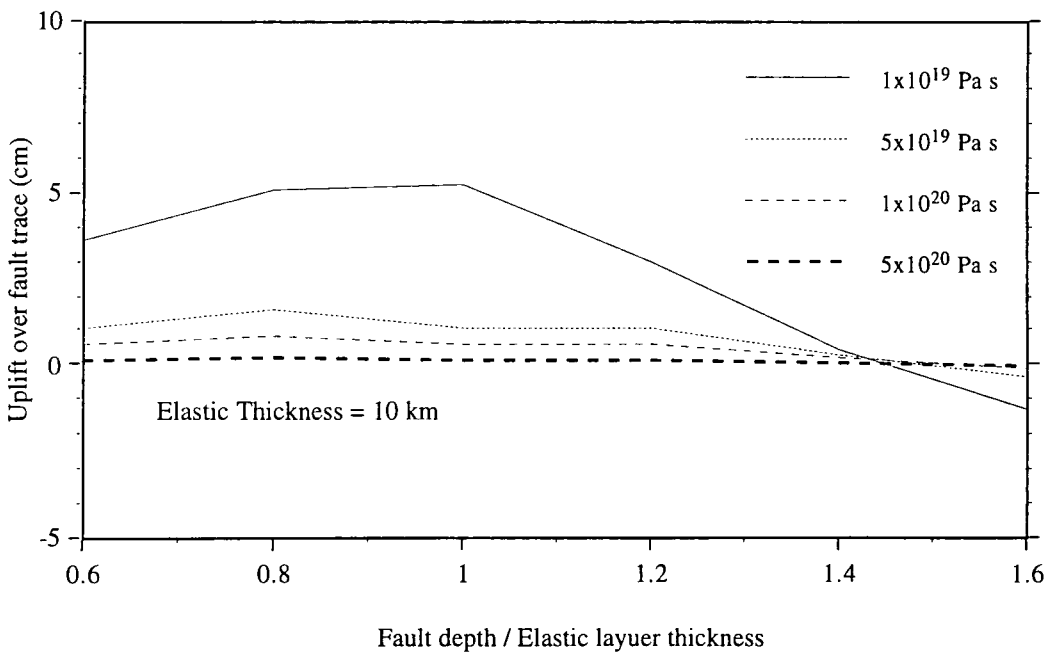


Figure 7.8 Variation of the uplift with D/H ratio over the fault scarp 30 years after the event. Elastic thickness = 10 km.

amplitude of the vertical field is almost the same regardless of whether it is the fault depth or elastic thickness that is increased, the width of the signal is dependent on the thickness of the elastic crust (Figure 7.12). It is only weakly dependent on the viscosity of the lower crust.

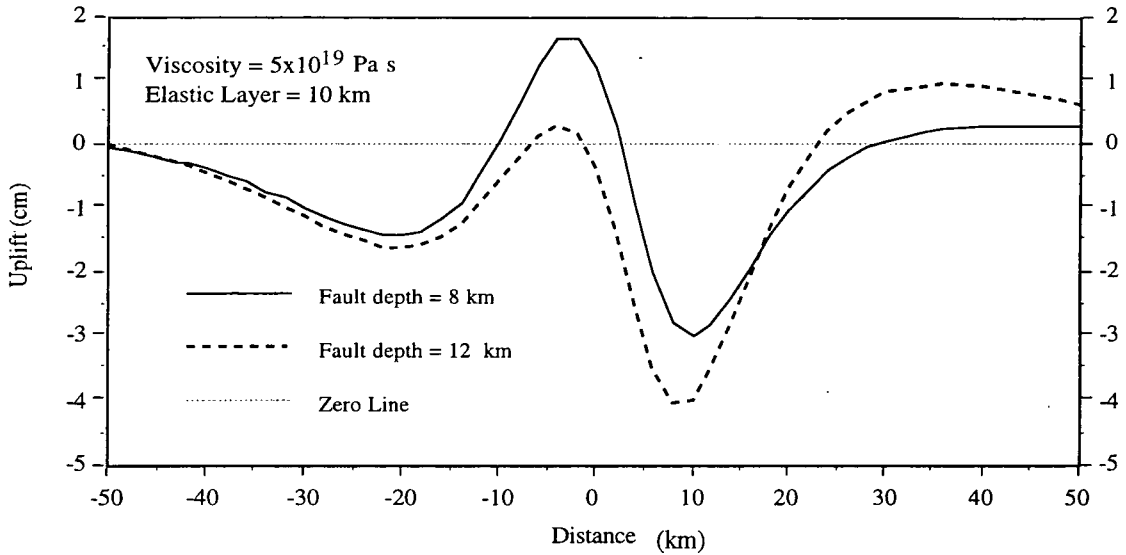


Figure 7.9 The uplift 30 years after the event for faults with 8 and 12 km depths.

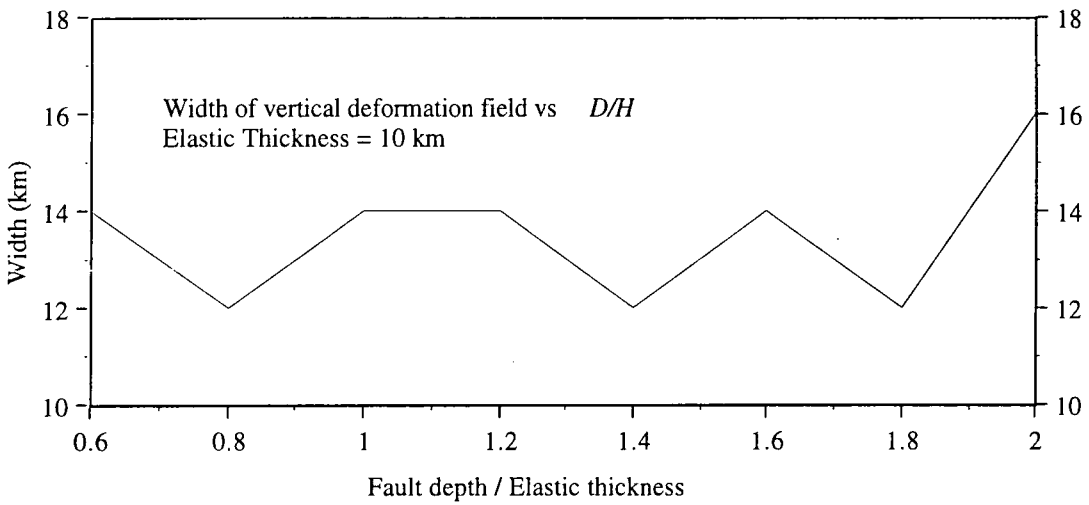


Figure 7.10 Variation of width of vertical deformation with increasing fault depth. The width is similar for viscosities ranging from 10^{19} Pa s to 10^{21} Pa s.

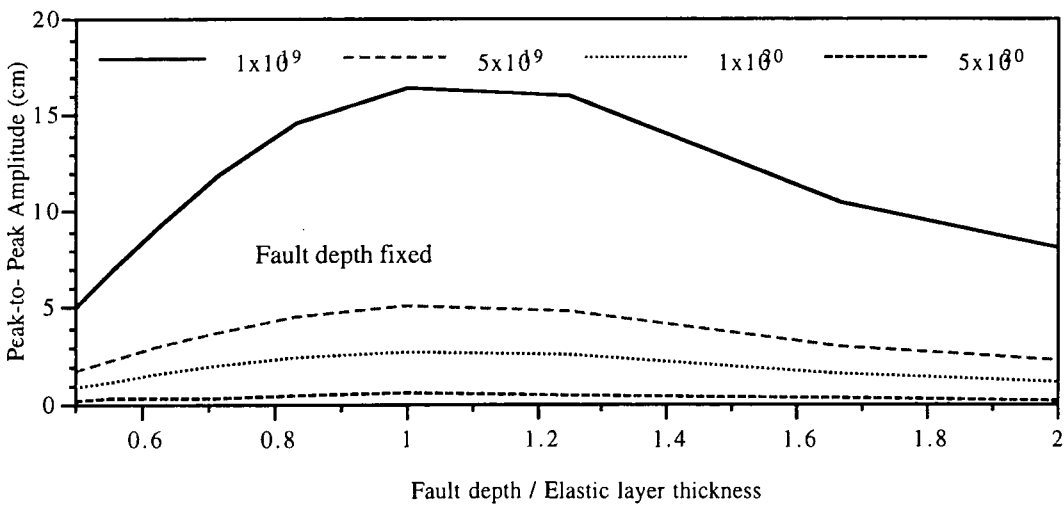


Figure 7.11 Variation in peak-to-peak amplitude with increasing elastic thickness.

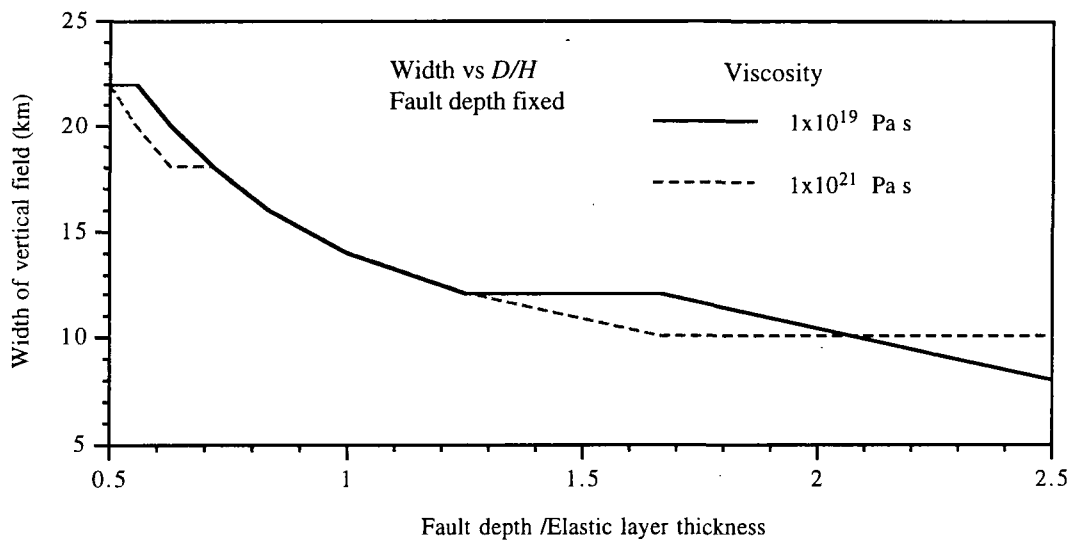


Figure 7.12 Variation in width of deformation with elastic thickness. The fault depth is fixed at 10 km. The width of the vertical field decreases with decreasing elastic thickness but is almost independent of the viscosity.

7.5 MODELLING THE DIXIE VALLEY POSTSEISMIC DEFORMATION

7.5.1 The data

After the 1954 sequence of events the levelling line along Highway 50 was remeasured in 1955, 1967, 1973, 1978 and 1986 (Chapter 4). The 1967 levelling survey was contaminated by systematic rod errors and therefore has not been used in analysis of the postseismic deformation. Between 1955 and 1986 almost 30 mm of uplift, with respect to benchmark T382, occurred over the Fairview Peak fault scarp (Figure 7.13). The elevation changes from 1955 to 1978 and 1955 to 1973 mostly are indistinguishable at the one sigma level. Only around and to the east of the West Gate fault are the differences greater than the one sigma errors. These two profiles show about 15 mm of uplift to the west of the fault with respect to T382. The postseismic deformation between 1986 and 1955 forms a well defined graben shape between benchmarks T46 and L381 (Figure 7.13). The depth of the subsidence zone *i.e.*, the difference between benchmarks T46 and X382, was 78.3 ± 11 mm in 1973, 79.5 ± 11 mm in 1978 and 87.6 ± 7.7 mm in 1986.

The subsidence zone is ~8 km wide and about 80 mm deep, and is unlikely to be caused entirely by viscoelastic relaxation because a deformation field of such a short wavelength would require a very thin brittle upper crust (Figure 7.12). Slip at depth, or creep, is also an unlikely cause as this would create a much broader signal than the sharply-defined feature observed. The most sharply-sloping parts of the anomaly (the “walls” of the graben-like feature) are coincident with the surface offsets of the Fairview Peak and West

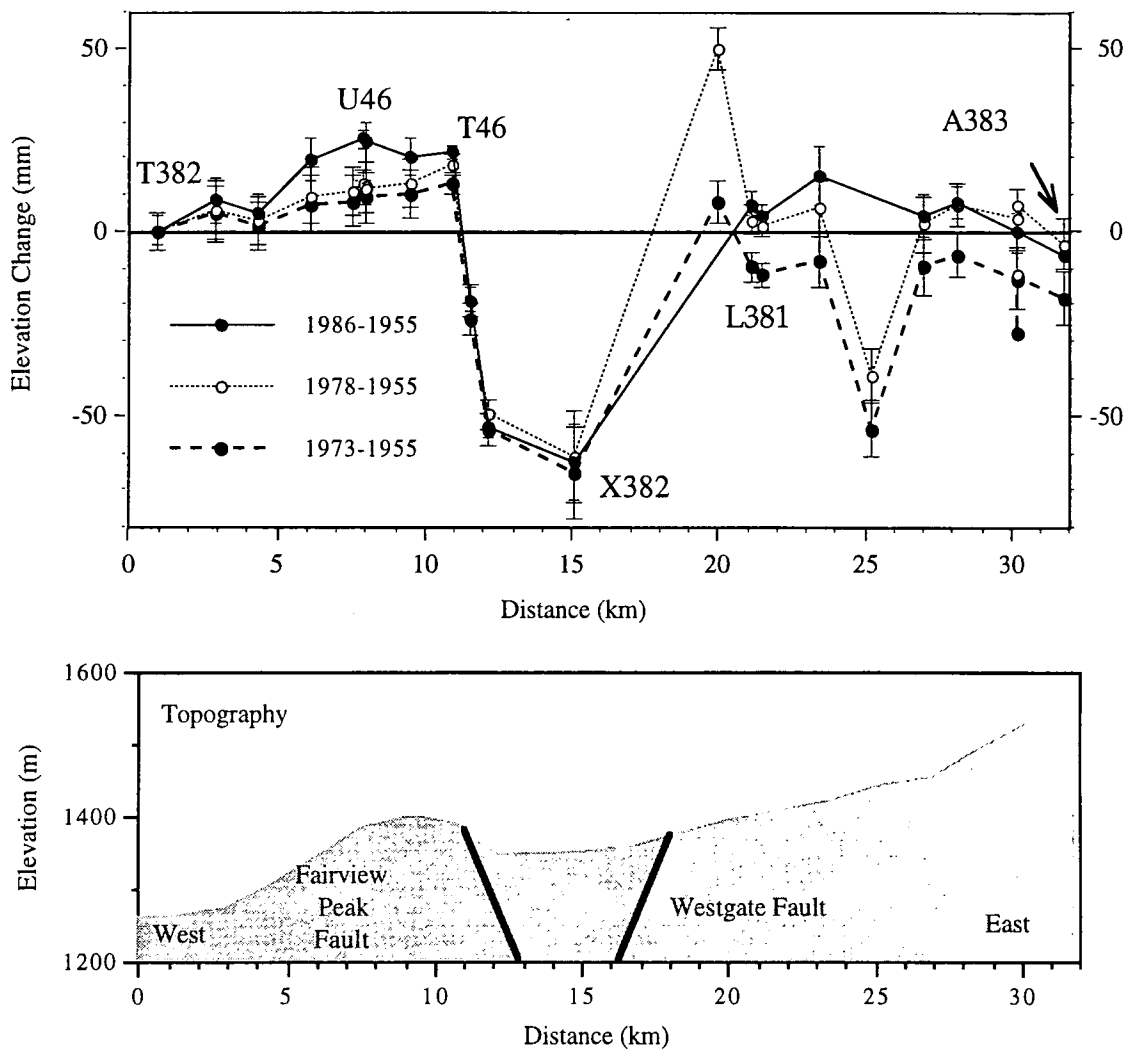


Figure 7.13 Postseismic deformation in the Fairview Peak area from levelling data taken in 1986, 1978, 1973 and 1955. The topography and position of the Fairview Peak and West Gate faults are shown in the lower figure. One sigma error bars are shown.

Gate faults. The subsidence zone is thus most likely to have been created by continued normal slip on the upper few kilometres of the Fairview Peak and West Gate faults.

Between 1986 and 1973, little deformation is detected at the one sigma level (Figure 7.14). The deformation zone shown in Figure 7.13 is also not apparent in Figure 7.14, indicating that its continued development was undetectable after 1973. The slip that created it may thus have ceased before 1973. Whether the slip happened gradually or suddenly cannot be determined from the data. There is a region of uplift over the Fairview Peak fault scarp which spans 6 benchmarks.

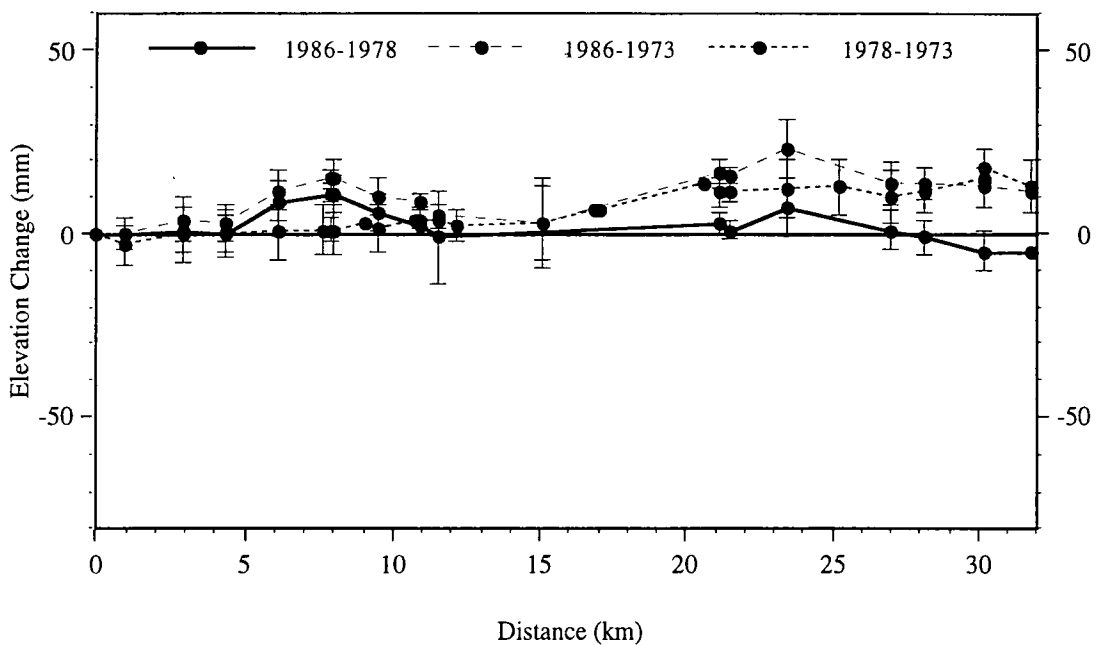


Figure 7.14 Postseismic deformation calculated by combining the 1986, 1978 and 1973 levelling data. One sigma error bars are shown.

7.5.2 Method

7.5.2.1 The modelling approach

It is assumed that the postseismic deformation that occurred from 1955 to 1986 between benchmarks T382 and A383 resulted from two processes; slip on those parts of the Fairview Peak and West Gate faults which ruptured coseismically in 1954, and longer-wavelength deformation due to creep or viscoelastic relaxation. The graben-like deformation feature in the postseismic data was created by the first process. The two effects are modelled here consecutively.

First, aseismic slip at depth is investigated using an elastic half space model. Slip is estimated on the upper 8 km of the faults which ruptured coseismically and at greater depths through a weighted least squares inversion of the 1986 - 1955 elevation changes. The inversion method used is that described in Chapter 5. The fault geometries used are those determined geodetically (Table 5.3). In the second investigation, the residual deformation after the slip estimated on the upper part of the faults has been removed is modelled using the finite element method. A three-layer crustal model is used. The modelling is a forward-modelling process where the viscosity of the middle layer is varied until a reasonable fit of the data is obtained. The fault geometry is held fixed at that determined from coseismic modelling and the geophysical properties of the crustal model, such as the elastic thickness, are those determined for the western Basin and Range province through other geophysical studies.

7.5.2.2 The finite element model of the Dixie Valley area

The finite element model consists of three layers, an upper elastic layer, a middle viscoelastic layer and a lower viscoelastic layer which is rheologically stronger than the layer which overlies it (Figure 7.3). The upper elastic layer represents the brittle upper crust, the viscoelastic layer a ductile deforming zone and the third layer, a viscoelastic layer which is stronger than the middle layer, simulates the upper mantle. This model is a simplified version of the crustal structure determined from other geophysical methods. Using seismic velocity and temperature data Catchings (1992) formed a rheological model of the Basin and Range province in Nevada. The model is based on rock-type-velocity associations and laboratory experimental results. Catchings (1992) suggested that the upper crust, with seismic velocities in the 2.5 to 6.15 km/sec range, may consist of Tertiary volcanics and rocks which are felsic in nature. It was also proposed in that study that the composition of the mid- to-lower crust may be dioritic given the temperature, 500-700°C, and the pressure, 6-8 kbars. The lower crust is likely mafic since the temperature range is about 700-1200°C and the pressures are 8-10 kbars. The upper mantle is probably ultramafic in composition. Variation in rheological properties with depth implies a variation in shear strength with depth. Assuming the different materials defined above a simplistic model of the crustal strength was developed.

The brittle upper crust is about 10 km thick beneath Dixie Valley. This depth is indicated by temperature, heat-flow, and seismic data. The seismic data show that between 10 and 30 km there are several layers of slightly different velocities indicating compositional variations. These mid-to-lower crustal layers deform in a ductile way at the temperatures involved. For simplicity these layers are modelled as one viscoelastic layer which is 20 km thick. The transition from mafic to ultramafic rocks in the upper mantle implies that the mantle defines a rheologically stronger layer than the mid- and lower-crustal layers which overlie it (Kirby, 1983). The depth to the Moho in the Basin and Range province has been estimated at between 30 and 36 km, and in the Dixie Valley area it is at ~30 km (Catchings and Mooney, 1991) (Figure 1.4). The depth to the third layer is therefore fixed at 30 km. The brittle upper layer corresponds to layers 1 to 4 of the seismic velocity model of Catchings and Mooney (1991) while the middle viscoelastic layer corresponds to layers 5 to 8 and the lower third layer corresponds to layer 9 (Figure 7.15).

Coseismic slip of 1.6 m was imposed on the Fairview Peak fault, and 0.5 m on the West Gate fault, to a depth of 8 km. The slip was tapered from there to zero at a depth of 10 km. The events are therefore modelled as rupturing the entire brittle layer. While the amount of slip imposed on the Fairview Peak fault was that determined geodetically, the slip imposed on the West Gate fault was that observed on the surface ruptures. The surface slip was used because the levelling line crosses the southern end of the West

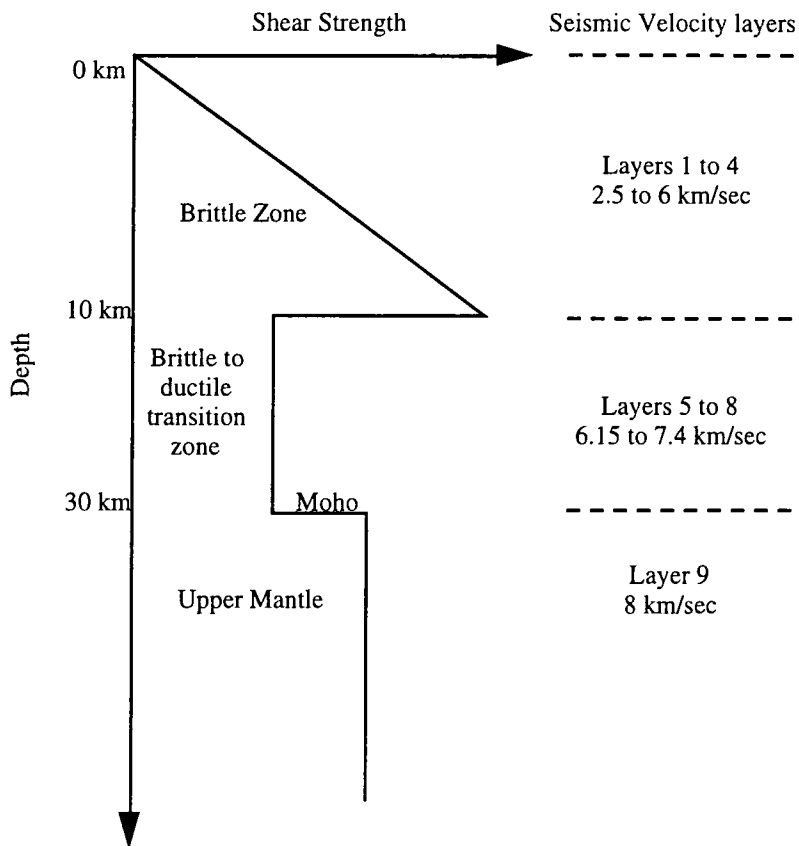


Figure 7.15 Model of shear strength versus depth for the Dixie Valley area.

Gate fault where the slip tends to zero (Figure 4.1). The average slip, determined geodetically, would therefore be an overestimate of the coseismic slip where the levelling line crosses the fault. The levelling line crosses the Fairview Peak fault near the epicentre, 1 km from where vertical offsets were largest.

7.5.3 Results

7.5.3.1 Continued aseismic slip on the fault planes.

The Fairview Peak and West Gate faults extend to depths of 8 km. The Fairview Peak fault dips 69°E while the West Gate fault dips at 59°W . The inversion of the coseismic deformation data indicated that coseismic slip was confined to 0-8 km depth. The high covariance between slip rates at adjacent depth intervals and the difficulties in resolving slip at depth required that depth intervals of at least 10 km be used for the lower depth intervals in the inversion. Large standard deviations of the slip values found reflect the high covariance and poor resolving power for deep slip. Two cases were examined; Case I, where slip was inverted for on depth intervals of 0-8 km and 8-30 km, and Case II, where slip was inverted for at the depth interval of 0-8 km (Table 7.1).

Table 7.1 Slip estimates for different fault depth intervals on the Fairview Peak and West Gate faults, 1955 to 1986. Right-lateral strike-slip motion and normal dip-slip motion are positive.

Depth (km)	Fairview Peak Fault		West Gate Fault	
	Strike-slip (cm)	Dip-slip (cm)	Strike-slip (cm)	Dip-slip (cm)
<u>Case I</u>				
0-8	35±3	1±.5	-66±52	83±37
8-30	-102±55	56±31	147±60	-82±47
<u>Case II</u>				
0-8	35±3	1±.5	-24±25	50±18

For each case the reduced chi-squared fit to the data was 1.7. The slip values determined for the depth interval 8 to 30 km in Case I are large. For the West Gate and Fairview Peak faults the average uplift rate is 2 to 2.5 cm per year. Only for the Fairview Peak dip-slip component is the sign of the slip in the two depth intervals the same. The opposite signs of the other slip components suggest that the results are counter-intuitive. The slip values obtained in Case I, and the large variances involved, thus suggest that the data are not sufficient to resolve slip at depths greater than 8 km. For these reasons the values determined by inverting for slip on the upper 8 km of the fault, Case II, are taken as the best result. The deformation calculated by forward modelling these slip values, and the difference between the calculated and measured deformation are shown in Figure 7.16.

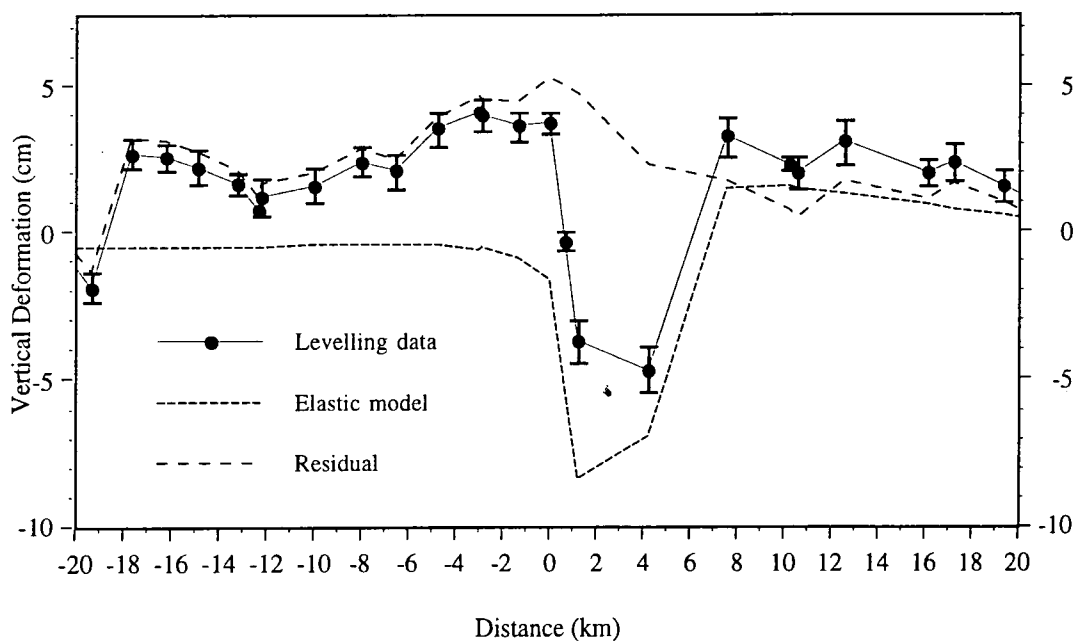


Figure 7.16 The postseismic levelling data between 1955 and 1986 is shown as a solid black line. One-sigma errors are shown. The thin dashed line (the elastic model for slip on 0 to 8 km of the faults) shows deformation caused by slip on the upper 8 km of the Fairview Peak and West Gate faults. The slip values used are those specified in Table 7.1 for Case I. The thick dashed line (Residual) is the difference between the two deformation fields.

7.5.3.2 Finite element modelling of the residual postseismic deformation

After subtracting the deformation caused by slip on the upper 8 km of the Fairview Peak and West Gate faults, (Case I), there remains as much as 4 cm of uplift over the Fairview Peak fault scarp and the uplift zone is 20 km wide (Figure 7.16). Uplift over the fault trace would imply that the fault does not protrude more than 40% into the viscoelastic layer, if at all (Figure 7.8). This places an upper limit of 14 km on the depth of the fault. This depth is independent of the viscosity of the middle layer.

The finite element grid and model used in the calculations was that described in section 7.4.1 and shown in Figure 7.3. Nodes along the bottom and sides of the grid were held fixed in the vertical direction at zero displacement and allowed to move freely in the horizontal direction. The uplift was calculated at time-step intervals of 6 months and one year. Poisson's ratio was assumed to be 0.25 and Young's Modulus to be 1.5×10^{11} Pa in each layer. The densities of the upper and middle layers were fixed at 3.0×10^3 kg m⁻³ and at 3.3×10^3 kg m⁻³ in the lowest layer (Turcotte and Schubert, 1982). The viscosity of the lower crust was varied between 1×10^{19} Pa s and 5×10^{20} Pa s. The postseismic deformation caused by the Fairview Peak event is much larger than that caused by the West Gate event, a result of the normal slip being almost three times as large on the Fairview Peak fault than on the West Gate fault. The combined effect of the two events was found by summing their deformation. The width of the combined deformation field is 12 km and the peak-to-peak amplitude is 4.5 cm (Figure 7.17).

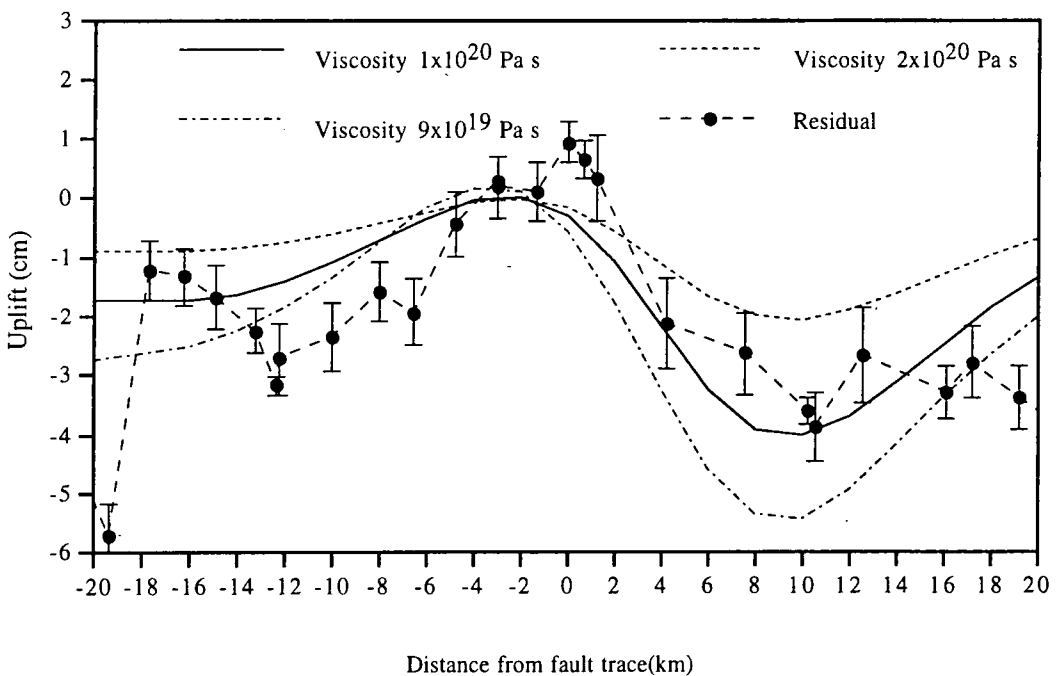


Figure 7.17 Uplift over the Fairview Peak and West Gate faults modelled using the finite element model. The dashed line is the residual signal of the postseismic deformation data after postseismic slip on the upper 8 km of the faults have been removed. The one sigma errors are shown. The solid black line is the deformation calculated using a viscosity of 1×10^{20} Pa s.

The viscosity which fits best the postseismic data, given the crustal model and fault parameters used, is 1×10^{20} Pa s. The fit is best within ± 10 km of the Fairview Peak fault scarp. The reduced chi-squared fit of the model is 2.7. If the two points at distances -12.4 km and -19.4 km are omitted the fit becomes 1.7. The point at -12.4 km has a very small associated error as the length of the levelling section is very small and the point at -19.4 km seems to be an outlier.

7.6 SUMMARY

There are two current models which have been proposed to explain postseismic deformation following an earthquake. The first proposes that the deformation is then explained by aseismic slip at depth (Savage, 1990). The surface deformation can be modelled by assigning variable slip rates to different depth intervals. The second proposes the surface deformation results from viscous flow at depth. A rheologically varied model of the Earth, where at least one layer behaves viscoelastically, is then required. The deformation observed following the Fairview Peak area is best modelled using a combination of these approaches.

The deformation was first modelled as aseismic slip on the fault plane. A reduced chi-squared fit of 1.7 was obtained. Slip was only resolvable in the depth interval 0 - 8 km. The deformation resulting from slip on the upper 8 km of the faults was then subtracted from the total deformation field and the residual modelled as resulting from viscous flow. Using a finite element approach with parameters such as the elastic thickness and depth to Moho obtained from other geophysical investigations, the residual postseismic deformation was modelled by varying only the viscosity of the crust in the 10 to 30 km depth interval. The best fitting viscosity is 1×10^{20} Pa s.

CHAPTER 8

GLOBAL POSITIONING SYSTEM SURVEYING AND CRUSTAL DEFORMATION MODELLING IN SOUTH WEST TURKEY

8.1 INTRODUCTION

In 1989 the University of Durham, in cooperation with Dokuz Eylul University (DEU), Izmir, installed and measured a 33-point GPS network in SW Turkey. The network was partially remeasured in 1992 in a project involving the University of Durham, the Massachusetts Institute of Technology (MIT), USA, the Institute für Angewandte Geodäsie (IFAG), Frankfurt, Germany and Eidgenössische Technische Hochschule (ETH), Zurich. The object of this ongoing project is to determine the distribution and rate of deformation in SW Turkey. Estimates of the horizontal extension in the Aegean and western Turkey determined from the moment tensors of earthquakes throughout the whole region vary from 30 ± 10 mm/yr to 60 ± 10 mm/yr (Jackson and McKenzie, 1988; Jackson *et al.*, 1988). However, GPS measurements made between 1988 and 1992, and Satellite Laser Ranging (SLR) measurements spanning 1985 to 1993 indicate a slower rate of 10 to 15 mm/yr relative to the Eurasian plate (Oral, 1995a; Smith *et al.*, 1994). Seismic rates agree with this slower velocity if the seismicity of SW Turkey alone is considered (Eyidogan, 1988).

The extension rate measured across the network between 1992 and 1988 was approximately 11.7 ± 5.2 mm/yr (Oral, 1995a). Since no large earthquakes occurred within the region in this period the deformation occurred aseismically. Two approaches are commonly used to model such results. First, the deformation may be described in terms of a kinematic model, *e.g.*, one involving steady plate motion. Second, the deformation may be attributed to the postseismic relaxation of the Earth's crust following earlier earthquakes in the area. The driving force behind the deformation is relaxation of deviatoric stresses in viscoelastic structural elements, following earthquakes that rupture

the brittle crust (Elsasser, 1969; Nur and Mavko, 1974). This latter approach amounts to modelling the deformation in terms of physical processes whereas the former approach is basically a simplified kinematic description of the results only.

8.2 GPS SURVEYING WITHIN SW TURKEY

8.2.1 GPS field surveys in SW Turkey

The GPS network installed and measured in 1989, herein called the SW Turkey network, consists of 28 new points spaced at 30 km intervals over an area 200 km x 250 km (Heki, 1991). Five pre-existing points were included (Figure 8.1). The network spanned the two main geological features of SW Turkey, the Gediz and the Buyuk Menderes grabens. Six of the newly-installed points and the five pre-existing points were resurveyed in 1992 (Table 8.1).

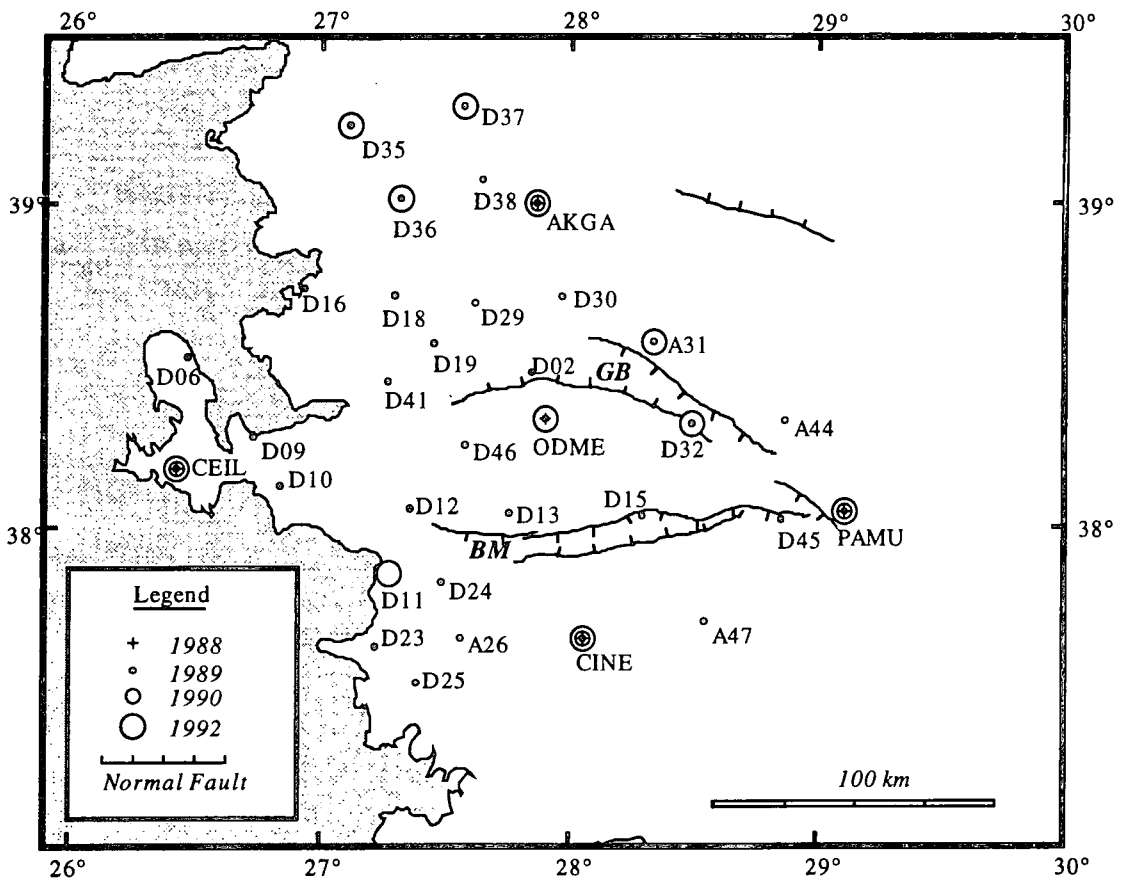


Figure 8.1 Map of the GPS network in SW Turkey, the Buyuk Menderes graben (BM) and the Gediz graben (G) are shown.

Table 8.1 Occupations of the University of Durham - MIT SW Turkey GPS network. The condition of the point refers to condition when it was resurveyed in 1992.

Point ID	1988	1989	1990	1992	Condition in 1992
AKGA	*	*	*	*	Good
CEIL	*	*	*	*	Good
CINE	*	*	*	*	Good
PAMU	*	*	*	*	Good
ODME	*	*		*	Good
DEU 02		*			
DEU06		*			
DEU 09		*			
DEU 10		*			
DEU 11		*		*	Damaged
DEU 12		*			
DEU 13		*			
DEU 15		*			
DEU 16		*			
DEU 18		*			
DEU 19		*			
DEU 23		*			
DEU 24		*			
DEU 25		*			
A 26		*			
DEU 29		*			
DEU 30		*			
DEU 31		*		*	Good
A 31		*			
DEU 32		*		*	Damaged
DEU 35		*		*	Good
DEU 36		*		*	Damaged
DEU 37		*		*	Good
DEU 38		*			
DEU 41		*			Good
A 44		*			
DEU 45		*			
DEU 46		*			
A 47		*			

The 1988 Survey: GPS surveying began in SW Turkey in 1988. From September 6 to 28, 1988, fourteen GPS points were installed and measured in west and central Turkey by MIT. As part of the survey, measurements were made at four mobile SLR stations, one on the Arabian plate, one on the Eurasian plate and two on the Anatolian plate. Measurements were made at night in six hour long sessions using TI4100 antennas and receivers. The formal uncertainties in the 1988 results were 10 mm in the north-south direction and 18 mm in the east-west direction (Oral, 1995a). The repeatability obtained was 6.4 mm and 13.5 mm in the north and east directions respectively.

The 1989 Survey: The SW Turkey network intensified the southwest part of the network installed in 1988 by MIT. Five of the GPS points installed in 1988 (CEIL, AKGA, CINE, PAMU and ODME) were included in the 1989 measurements (Figure 8.1). The survey was made simultaneously with a survey in eastern Turkey by MIT which included measurements at SLR stations on the Eurasian, Anatolian and Arabian plates. Five TI4100 receivers were used for the 16-day survey. Six satellites were observed simultaneously in an observation window of 6 hours. One point (DU19) was measured each session. The data were processed using the Bernese GPS software V3.2 (Heki, 1991). The P-code pseudorange measurements were used to estimate rough absolute point coordinates. Cycle slip detection was carried out using program MAUPRP. Ambiguities and final point coordinates were then determined using program GPSEST. Successful ambiguity resolution was achieved for almost all sessions using this technique. The best result repeatabilities were obtained by estimating orbit improvements at the parameter estimation stage (Heki, 1991). Repeatabilities of 1.7 cm in the north-south component, 2.5 cm in the east-west component and 5.8 cm in the vertical were obtained. The east-west repeatability was not as good as the north-south repeatability because of the poor satellite geometry over Turkey then. However, the good repeatability in the north-south component favours measurement in the expected direction of extension.

The GPS satellite constellation is currently greatly improved over that of 1989, and advances have also been made in field technique and data processing. A future survey of the network would be expected to yield 1σ errors of about 0.5 cm, 0.5 cm and 1cm in the north-south, east-west and vertical respectively. The combined errors of the 1989 and a future survey would then be:

$$error_{combined} = \sqrt{(error_{1989})^2 + (error_{future})^2} . \quad (8.1)$$

From this it may be concluded that, after a future survey, differencing the results with those of the 1989 survey would result in 1σ errors of 1.8, 2.6 and 5.9 cm for the north, east and vertical components of deformation respectively.

The 1990 and 1992 surveys: In 1990 four GPS sites of the 1989 network, CEIL, AKGA, CINE, and PAMU were resurveyed by MIT, IFAG and ETH as part of a ten-point GPS survey in western Turkey. Eleven points of the network, including CEIL, AKGA, CINE, and PAMU, were then remeasured in 1992 by MIT, IFAG and ETH as part of a 50-point GPS survey covering most of Turkey. The 1992 measurements were made with 10 Trimble 4000SST receivers during a 15-day survey. The data were processed at MIT using GAMIT software (Oral, 1994). Point repeatabilities in the north-south and east-west components were 0.7 cm and 1.3 cm respectively. The combined uncertainties between the 1989 and 1992 sets of measurements are about 1.8 and 2.8 cm in the north-south and east-west components. In both surveys measurements were made at SLR stations on the Eurasian, Anatolian and Arabian plates.

8.2.2 Relative plate motions in the eastern Aegean and deformation within SW Turkey, 1988-1992.

The results of the GPS measurements made in and between 1988 and 1992 in Turkey and on neighbouring plates are consistent with tectonic models proposing that W Turkey is moving westward as a whole and being extended in a north-south direction. The motion is in response to the Africa, Eurasian and Arabian plate collision and subduction at the Hellenic arc. The horizontal velocity field detected by GPS is similar to that determined with SLR measurements (Oral, 1995b). Both sets of measurements indicate that central and western Turkey and the southern Aegean move as one plate rotating anticlockwise with respect to a pole in the Nile delta. The average velocity of the Anatolian plate measured by SLR and GPS is 50 ± 20 mm/yr and 36 ± 11 mm/yr respectively (Oral, 1993; Le Pichon *et al.*, 1993). A least squares inversion of the GPS velocities gave an axis of rotation at 33.4 ± 0.5 N, 31.1 ± 1.2 W and a best fitting rate of rotation of $1.2\pm 0.2^\circ$ Ma. (Oral, 1995b). Velocities found by forward modelling the rotation deviate from the observed deformation by more than 2σ only in western Turkey and the southern Aegean (Oral, 1995a). The misfit in SW Turkey is ~ 10 mm/yr in the north-south direction increasing westwards towards the Hellenic arc. Velocities in SW Turkey are thus 10 mm/yr greater than those observed in Eastern Turkey which fit the predicted rotation velocities well. The GPS observations show that almost all the northward motion due to the Arabian collision is transferred to the North Anatolian Fault (NAF) (Oral, 1994) leaving the residual 10 mm/yr unaccounted for.

Deformation within the SW Turkey network between 1988 and 1992 is detectable at the 1σ level. The data show that aseismic north-south extension is occurring in the Bozdag Horst region (Figure 8.1). Velocities for the points CEIL, CINE, AKGA and PAMU relative to ODME were calculated using a least squares fit to the baseline measurements made in 1988, 1989, 1990 and 1992 (Oral, 1994). The north velocity of AKGA with respect to ODME is 5.2 ± 4 mm/yr, and the south velocities of PAMU, CINE and CEIL are 4.1 ± 2.3 mm/yr, 6.5 ± 4.8 mm/yr and 10.7 ± 3.3 mm/yr respectively (Figure 8.2). The north-south extension across the network was therefore 11.7 ± 5.2 mm/yr. The east-west motion is not resolvable at any of the GPS sites at the current levels of uncertainty so resolution of east-west deformation remains a research goal for the future.

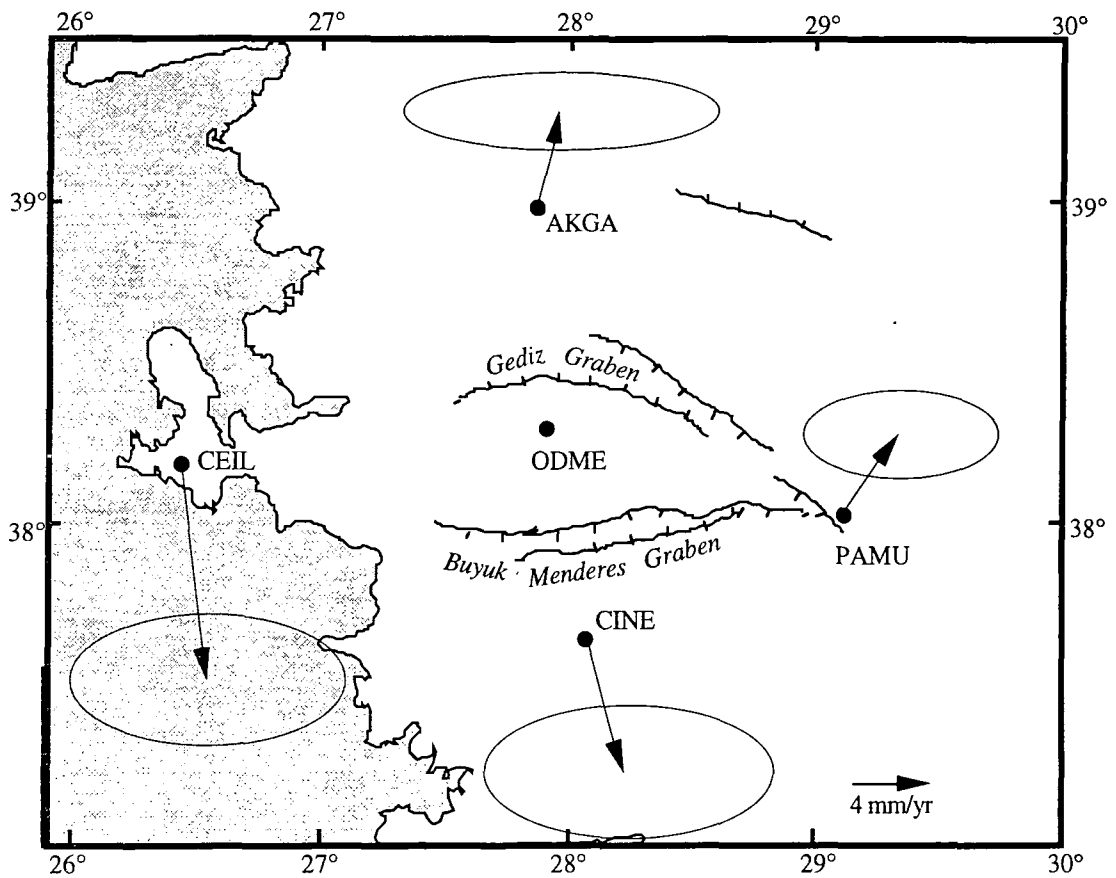


Figure 8.2 Deformation within the SW Turkey network, 1992-1988 measured using GPS. One sigma errors are shown (Oral, 1995a).

8.3 MODELLING THE DEFORMATION WITHIN SW TURKEY

8.3.1 The method and Earth structure used

The GPS and SLR measurements show that north-south extension is occurring in SW Turkey at a rate of 11.7 ± 5.2 mm/yr. The extension may be modelled as postseismic relaxation where the high strains incurred by large earthquakes are redistributed by

viscous flow in a ductile layer. This hypothesis may be tested by calculating the north-south extension caused by all $M_s \geq 6.5$ and greater earthquakes that have occurred along two north-south profiles across the Buyuk Menderes and Gediz grabens since 1899. The horizontal velocity induced by each earthquake is calculated for the epoch 1992 to 1988 and the velocities are then summed.

The finite element (FEM) program TECTON (Melosh and Raefsky, 1981) was used to calculate the time-dependent postseismic horizontal velocity field. A 2D finite element grid was constructed that consisted of 1092 quadrilateral elements. It was held fixed in the vertical direction along the bottom and sides but was free to extend in the horizontal direction (Figure 8.3). Faults are represented as lines of split nodes within the grid (see Chapter 7). The structural model of the crust consisted of three layers. The upper layer represents the Earth's upper crust and is elastic. The second is a viscoelastic layer which simulates the ductile lower crust. The third and deepest layer behaves as the upper mantle and is modelled as a viscoelastic layer with a viscosity 100 times greater than the lower crust. The depth to the upper mantle is defined by the Moho which for SW Turkey is at approximately 35 km depth (Makris, 1976; 1978). Since seismicity is confined to the upper 10-15 km (Jackson *et al.*, 1988; Eyidogan and Jackson, 1985), the brittle layer is made 10 km thick in the FEM model. Standard material properties are assumed to define the different crustal layers; Poisson's ratio is set to 0.25 and Young's Modulus 1.5×10^{11} Pa in all layers (Figure 8.3). The density of the material, ρ , varies with depth and viscosity varies with each layer.

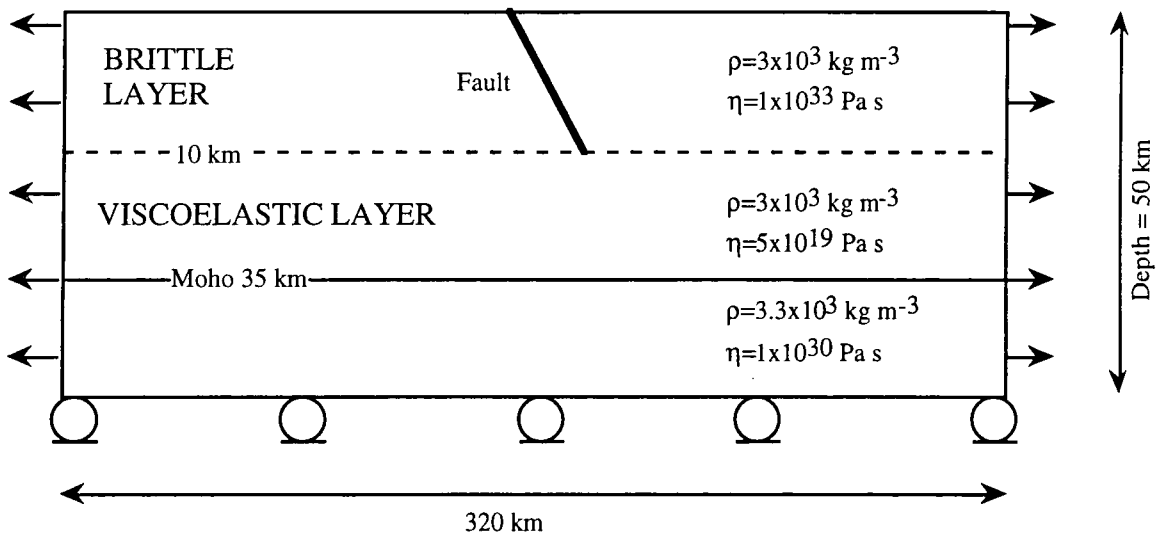


Figure 8.3 Finite element crustal model. The physical properties of each layer are given.

8.3.2 The seismicity of SW Turkey

Thirty-four earthquakes of $M_s 5.5$ and greater are known to have occurred between 1899 and 1992 in the area delimited by $26^\circ W - 30^\circ W$ and $37^\circ N - 39.5^\circ N$ (Figure 8.4). The region south of latitude $39.5^\circ N$ may be considered a separate seismotectonic region from that north of it (Crampin and Evans, 1986). Focal mechanisms suggest that the region to the north is being sheared and rotated to accommodate right-lateral motion on the NAF whereas the southern region is undergoing north-south extension through normal faulting. The earthquakes in the study area are almost all normal faulting events and not associated with movement on the NAF.

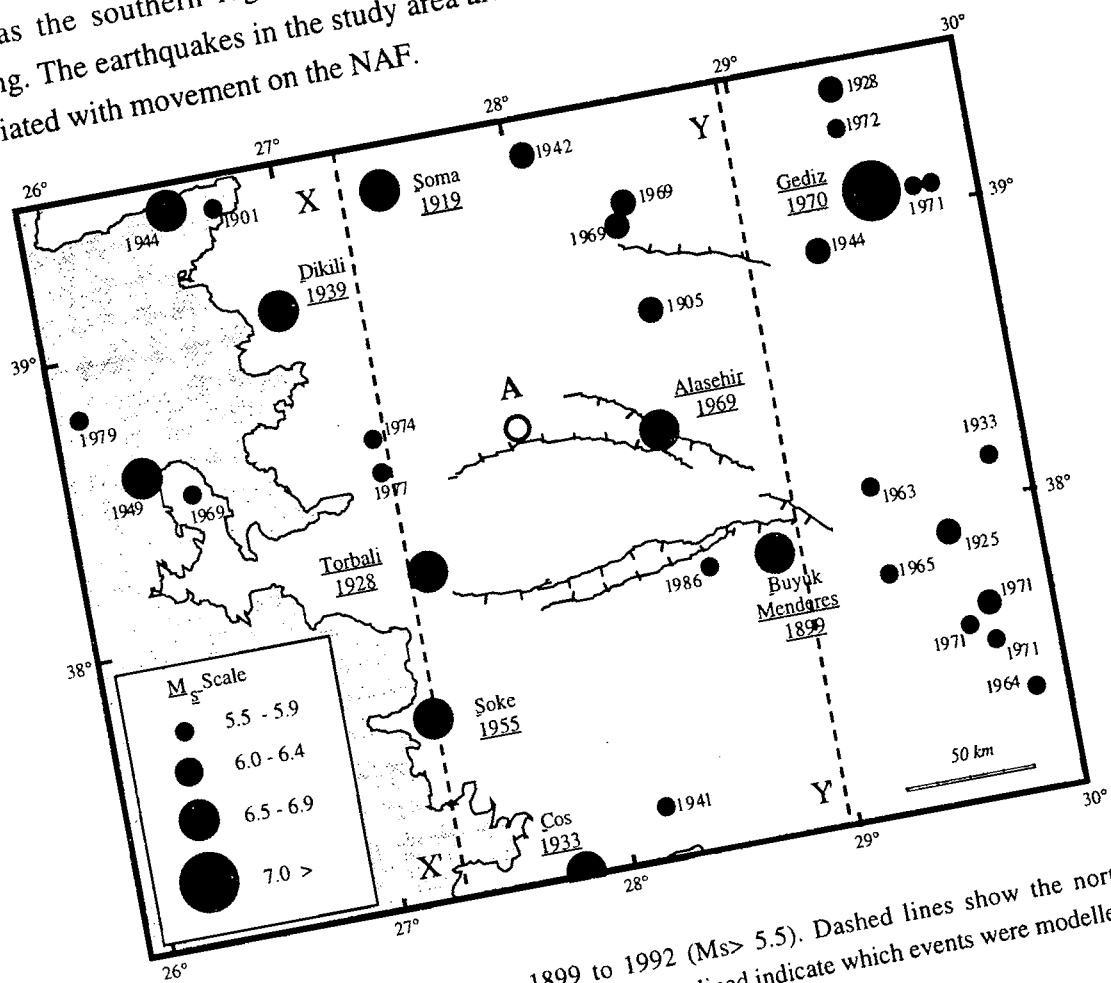


Figure 8.4 Seismicity of SW Turkey, 1899 to 1992 ($M_s > 5.5$). Dashed lines show the north-south profiles modelled using FEM analysis. Earthquakes underlined indicate which events were modelled.

Earthquake locations and magnitudes were obtained from a seismicity catalogue for all of Turkey spanning 1899 to 1986 (Ambraseys, 1988). The catalogue is based on historical reports and seismic and macroseismic data. Since the mislocation of earthquakes occurring early this century and recorded only on primitive instruments is large, positions of pre-1960 events were checked by Ambraseys (1988) with contemporary bulletins and the locations positioned in the centre of the meizoseismal areas. The surface-wave magnitudes listed in the catalogue were computed from teleseismic amplitude data. These were not recorded then the event was assigned a surface wave magnitude according to the average radii of felt intensities on the Medvedev-Sponheuer-Karnick (MSK) scale.

Post 1986 the HARVARD CMT catalogue, which spanned 1977 to 1992, was used. Focal mechanisms are only available for events after 1960. The earthquakes in the area for which the most accurate locations are available show that the seismicity is confined to the upper 10 to 15 km of the crust (Eyidogan and Jackson, 1985; Taymaz, 1993). The earthquakes occur on normal faults with dips varying from 35° to 55° and the motion is usually normal. Four of the largest events in the region, all greater than $M_s6.5$, were the Buyuk Menderes, Alasehir, Soke and Torbali earthquakes (Figure 8.4) and all were associated with slip in the Gediz and Buyuk Menderes grabens.

Since SW Turkey is a populated area it is likely that all earthquakes greater than $M_s6.5$ are listed in the catalogue. The cut-off magnitude for detection, where the linear relationship between magnitude and cumulative number of events breaks down, appears to be at about $M_s5.2$ (Figure 8.5). The ratio of cumulative number of earthquakes : magnitude, the b-value, is 0.94 ± 0.2 , calculated using the method of maximum likelihood of Page (1968). The estimated b-value is similar to the world average of 1. The 10-year earthquake thus has a magnitude of ~ 6.25 . If the seismicity this century is representative of longer periods then the maximum earthquake is likely to be less than 7.5. The frequency-magnitude curve appears to become asymptotic at magnitudes a little over 7, as would be expected for real earthquake distributions, and given that the crust is relatively thin in SW Turkey.

8.3.3 Deformation expected from a single event

8.3.3.1 The coseismic effect

Horizontal coseismic deformation would be detectable at the 1σ level within the SW Turkey network if the horizontal displacements are greater than 1.7 and 2.5 cm in the north-south and east-west directions. As an example of the coseismic displacements produced by one $M_s6.5$ event, the deformation on the northern boundary of the Bozdag Horst (the Gediz Graben) (at A in Figure 8.4), is calculated using the formulae for deformation in an elastic half-space formula (Okada, 1992).

The amount of slip required to simulate a $M_s6.5$ earthquake is determined using a surface wave magnitude - seismic moment relation based on earthquakes in western Turkey:

$$\log M_o = 1.26M_s + 10.8 \quad (8.2)$$

where M_o is the scalar seismic moment (Eyidogan, 1988) and the moment magnitude relation is:

$$M_o = \mu L W \bar{s} \quad (8.3)$$

Earthquakes in SW Turkey 1899 to 1992

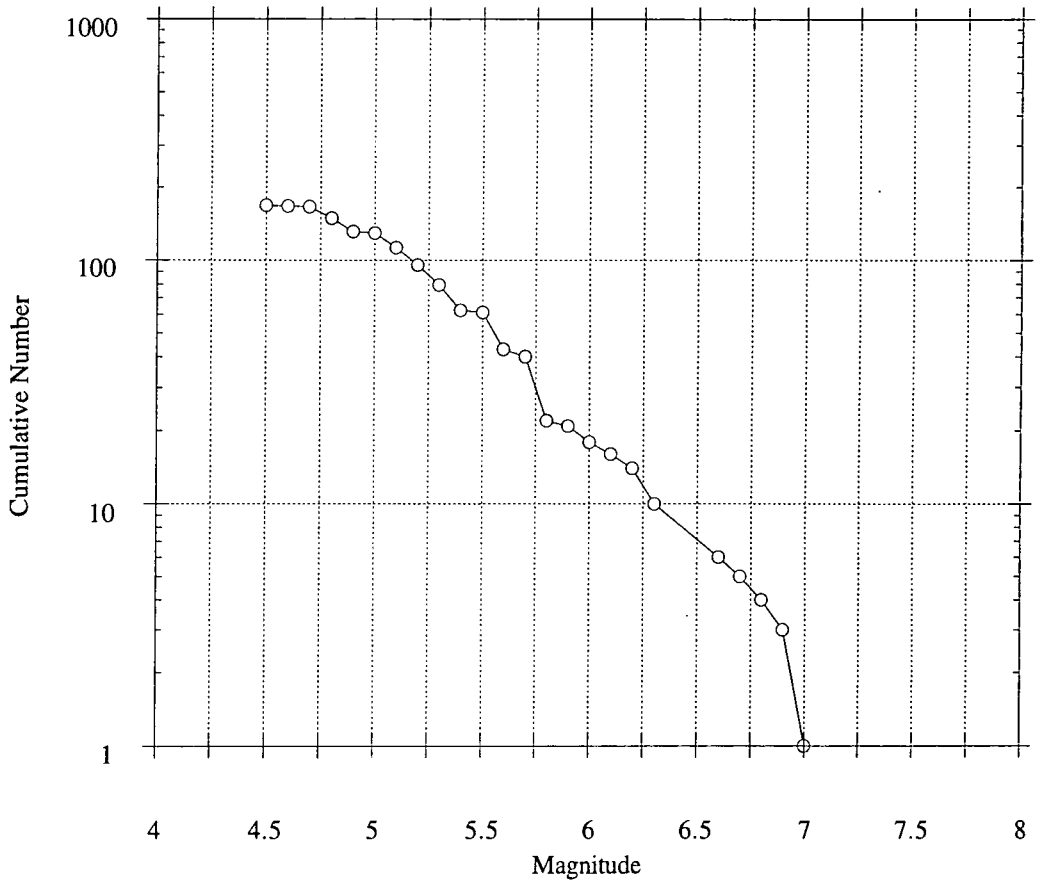


Figure 8.5 Surface wave magnitude versus the log of the cumulative number of earthquakes for the 93-years-period 1899 to 1992. Data from Ambraseys (1988) and the Harvard CMT catalogue.

where L is the length of the fault, W the width, \bar{s} is the average slip and μ the rigidity. The length L of a fault scales roughly with magnitude (Scholz *et al.*, 1986). A study of large interplate and intraplate earthquakes indicated that $M_0 \propto L^2$ or $\bar{s} = kL$ where k is the constant of proportionality. For interplate earthquakes k is $\sim 1 \times 10^{-5}$ which implies the rupture length of an $M_s 6.5$ earthquake is approximately 20 km. If the focal depth of the earthquake is 10 km then the width W is determined by the dip which is assumed to be $60^\circ N$. The rigidity is assumed to be 3×10^{11} Pa. The resulting normal slip is 1.4 m.

For an earthquake of the length, width, and amount of normal slip defined above, the predicted horizontal deformation within the network is small. Given the predicted errors for a combination of the 1989 survey and a future survey, (1.8 cm in the north-south and 2.6 cm in the east-west directions), motion in the north-south direction would be detectable at 3 of the GPS sites. Motion in the east-west and vertical directions would not be detectable at any points. The network is therefore not ideal for observing coseismic

deformation following one moderate event. However it is well positioned to observe the long-term postseismic transient which would follow this event. Occupation of the network following such an event would be necessary to monitor the cumulative effects in the Gediz and Buyuk Menderes grabens.

8.3.3.2 The postseismic effect

Postseismic deformation following an earthquake can be calculated for a rheologically-varied crustal model using the finite element method. TECTON uses a plain-strain 2-dimensional algorithm, and therefore the results will tend to be an overestimate of the true deformation since the modelled faults are effectively assumed to have infinite length. At zero time coseismic slip is imposed on a line of split nodes which represents the fault. The nodes are held fixed thereafter. The postseismic signal at time t may be calculated by subtracting the coseismic displacements from the total displacement at time t . Positive displacement on the downthrown side of the fault implies continued motion away from the fault rupture while negative displacement on the upthrown side implies continued motion in the opposite direction. The fault-normal displacements following an $M_S6.5$ normal-faulting event were calculated along a line perpendicular to the fault strike at 5, 10, 20, 40, 80 and 100 years (Figure 8.6).

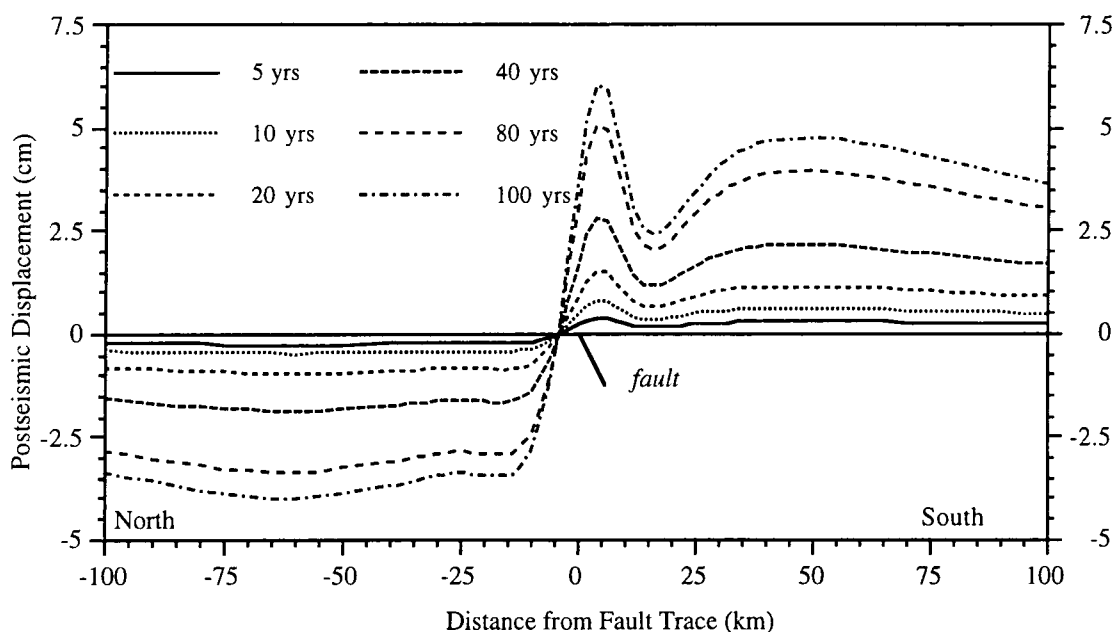


Figure 8.6 Variations in postseismic, fault-normal displacement with time following one $M_S6.5$ event.

The maximum displacement occurs over the fault trace and there is a minimum over its downward extension. Strains are large within one fault depth but tend to zero at distances greater than this with the constant displacement contributing to the overall plate velocity. The positions of the displacement maxima and minima are independent of the magnitude of the earthquake but the amplitude of displacement scales with magnitude (Figure 8.7).

The ratio of the displacement caused by M_s7 , 6.5, 6 and 5.5 events is about 1:0.5:0.1:0.02.

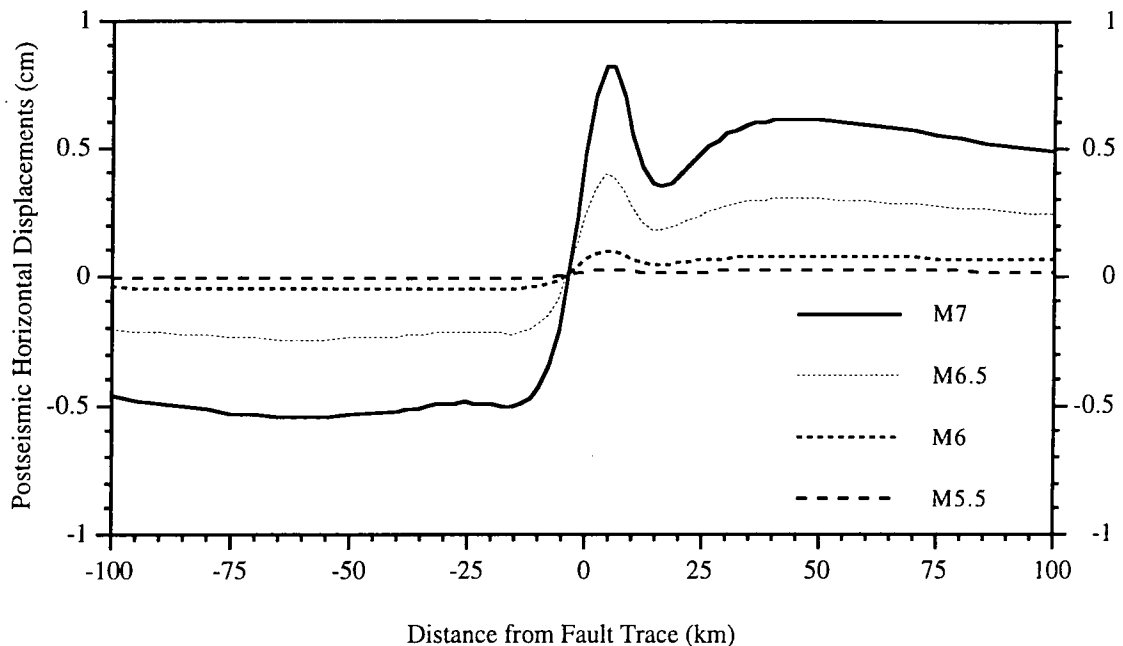


Figure 8.7 Variations in horizontal, fault-normal displacement with earthquake magnitude. Displacements correspond to a time five years after the event.

In a structure such as that used here to model SW Turkey, horizontal velocities due to postseismic motions following a single event decay slowly after the event. Five years after the event the velocity between two points 100 km on either side of the fault is about 0.1 cm/yr. One hundred years later this has decreased to 0.07 cm/yr (Figure 8.8). Not until after about 1000 years, approximately 38 times the relaxation time of the viscoelastic layer does the velocity fall to < 10 % of its early value. Such a velocity change is not detectable geodetically, and over a 100-year period the velocity may be considered constant.

8.4 MODELLING RESULTS

8.4.1 Deformation associated with repeated M_s7 events

The cumulative coseismic and postseismic deformation from earthquakes that repeatedly rupture the entire elastic plate results in steady state plate velocities. If an $M_s7.0$ earthquake repeats every 150 years then a point 50 km from the rupture reaches its steady

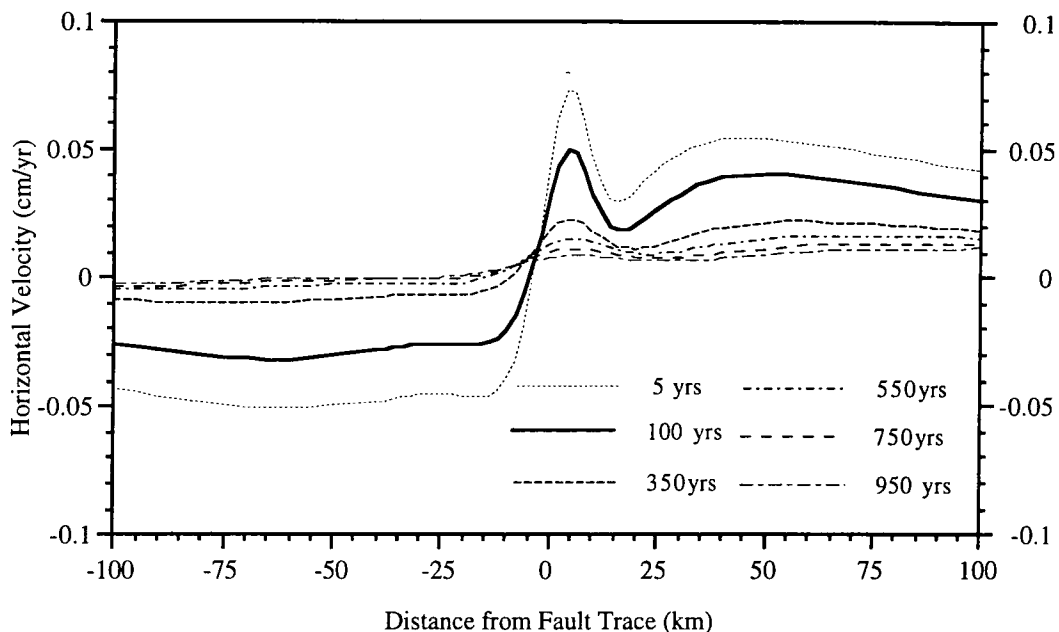


Figure 8.8 The decay in horizontal, fault-normal velocity following an $M_s6.5$ earthquake.

state velocity after ~ 1000 years (Figure 8.9). A point 50 km from the fault rupture has a steady state velocity of 2.6 mm/yr and two points lying 50 km on each side of the fault will have a velocity of 5.2 mm/yr with respect to each other. This is slower than the velocity measured by GPS between AKGA and CINE which are 100 km apart (11 ± 5 mm/yr). Incorporating smaller events in the $M_s6.5$ to 6.9 range, however, would increase this value to a range closer to that observed using GPS. Events of magnitude less than $M_s6.5$ would contribute a very small amount.

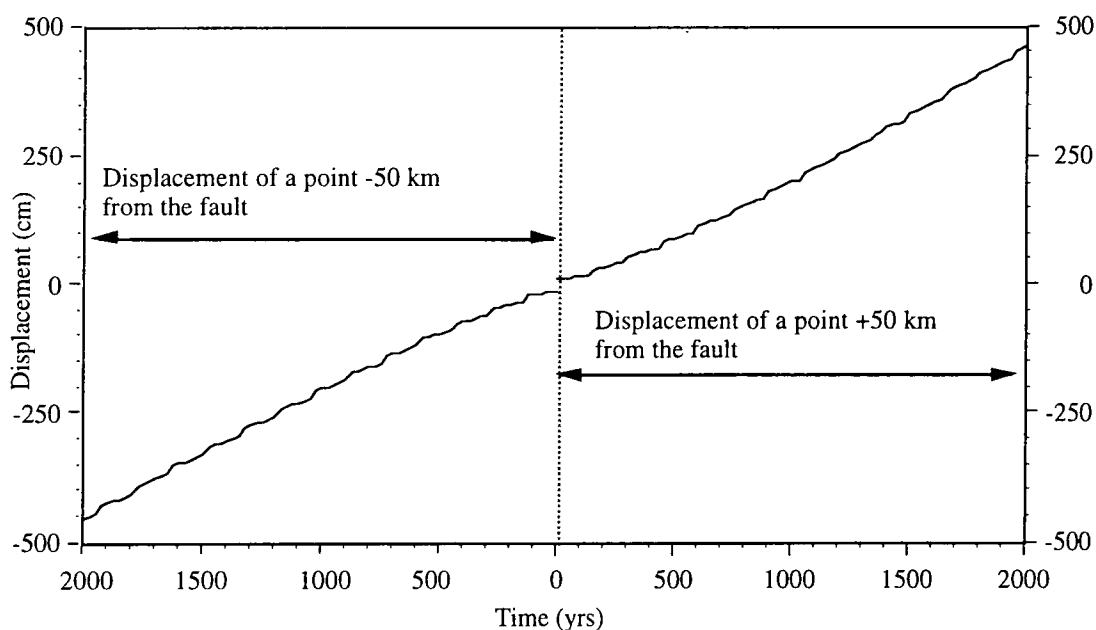


Figure 8.9 Cumulative deformation due to two thousand years of $M_s7.0$ earthquakes repeating at 100-year intervals. The steady state velocity is reached after ~ 1000 years.

During the steady state period about 30% of the total extension is due to the coseismic motion. Surveys made between large events (points A and B in Figure 8.10) yield an interseismic velocity of 1.8 mm/yr. This interseismic velocity is 30% lower than the average, long-term velocity. A GPS velocity of 11 ± 5 mm/yr measured along the baseline AKGA to CINE would suggest an average plate velocity of 17.5 ± 5 mm/yr. This velocity is below that estimated for earthquakes this century in the Aegean and Western Turkey (Jackson *et al.*, 1991) but close to that estimated from earthquakes in SW Turkey alone, of 13.5 mm/yr (Eyidogan, 1988).

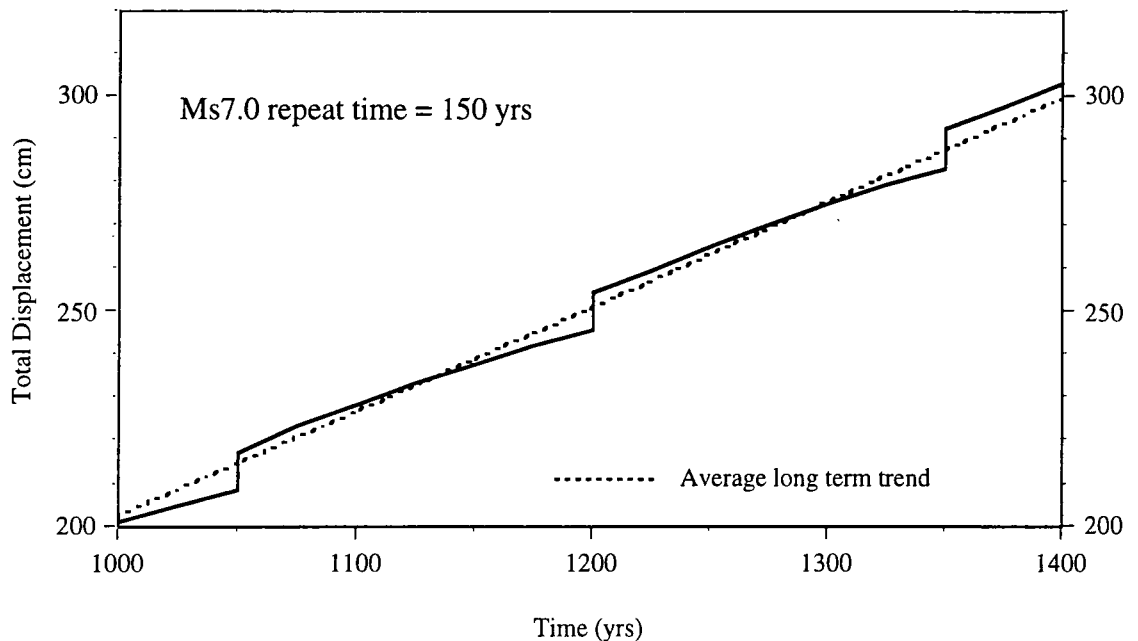


Figure 8.10 Displacements due to three $M_s7.0$ earthquakes within the steady-state period. The average, long term displacement is indicated by the dashed line. The average steady state velocity is 2.5 mm/yr. The interseismic velocity determined by making surveys at time A and B is 1.86 mm/yr.

8.4.2 Deformation associated with seismicity this century

The horizontal velocities caused by postseismic motion due to eight of the largest earthquakes that occurred in SW Turkey this century have been calculated for the period 1992 to 1988 in order to make comparisons with the GPS observations (Figure 8.2). Earthquakes smaller than about $M_s6.5$ will make little contribution to the total motion. Events were therefore selected which were greater than $M_s6.5$ and which fell within 50 km of two north-south profiles across the Bozdag Horst (XX' and YY' Figure 8.4).

To model the events it was necessary to assign a certain slip to each. This was determined from the surface wave magnitude of the event using equations 8.2 and 8.3. If the fault length was not known from independent observations then the scaling relationship of Scholz *et al.* (1986) was used. Since the dip of the fault does not greatly affect the signal more than one fault depth from the rupture, a dip of 60° was assumed for all events. It

was also assumed that each earthquake ruptured the entire brittle layer. The following events were modelled:

Buyuk Menderes, Sept. 20, 1899, Ms6.9: The 1899 earthquake in the Buyuk Menderes graben occurred on a south-dipping normal fault and created 70 km of surface rupture (Ambraseys, 1988). There was no instrumental recording of the event but it was remembered by people who lived nearby as it destroyed two villages in the area (Allen, 1975). The scarp consisted of ground cracks trending east-west along the north side of the graben following the topographic contours with vertical displacements of 1.5 to 2 m (Schaffer, 1900; Paton, 1992). Vertical offsets of 2 m were observed by local villagers (Allen, 1975) and up to 3 m were observed along the graben, although some of this displacement may have been due to an earlier large earthquake in 1655 (Ambraseys, 1988). The average observed displacement, 2 m, was used to model the event.

Soma, Nov. 18, 1919, Ms6.9: The Soma earthquake occurred on a north-dipping fault with an east-west strike (Jackson *et al.*, 1992; Ambraseys, 1988). Damage was recorded at villages up to 50 km from the epicentral area. The moment-magnitude relation for SW Turkey (Equation 8.1) predicts that this event had a seismic moment of 3×10^{19} N m. Since the length of fault rupture is not recorded, a length of 50 km was assumed. This implies 1.73 m of normal slip.

Torbali, March 31, 1928, Ms6.5: The destructive Torbali earthquake occurred southwest of Izmir on an east-west, south-dipping fault, inferred from nearby active faults (Jackson *et al.*, 1988). The shock was felt as far as the Sea of Marmara and the Aegean Islands and damage was recorded to a railway 70 km away. Using the scaling relations, the event was assigned a seismic moment of 9.77×10^{18} N m and a length of 20 km. The average normal slip is then 1.41 m.

Cos, April 23, 1933, Ms 6.5: The Cos earthquake occurred offshore. The focal mechanism of a smaller earthquake that occurred on the same fault in 1968 indicated a south-dipping fault (Jackson *et al.*, 1988). This event was assigned the same length and moment as the Torbali earthquake of the same magnitude since its length was not known. A normal slip of 1.41 m is then predicted.

Dikili, Sept. 22, 1939, Ms 6.5: The Dikili earthquake occurred on an east-west, north-dipping fault (Jackson *et al.*, 1988). Like the Torbali and Cos earthquakes, the rupture length was not recorded. It was assigned a seismic moment of 9.77×10^{18} N m, a length 20 km and slip of 1.41 m.

Soke, July 16, 1955, Ms6.8: The Soke event was located in the western extremity of the Buyuk Menderes graben on a south-east dipping fault. The earthquake is thought to have occurred on the northern boundary of the Buyuk Menderes graben (Paton, 1992). The moment magnitude of the earthquake was 24.75×10^{18} N m (Eyidogan, 1988). A length of 45 km was assumed, resulting in an average slip of 1.66 m.

Alasehir, March 28, 1969, Ms6.6: The Alasehir earthquake created 36 km of north to north-west striking surface faulting. The scarp ran along the southern side of the Gediz graben with the northeast side of the fault downthrown. The first motion fault plane solution reveals a normal faulting earthquake on a 32° NNE dipping fault striking at $N79^\circ$ W (Eyidogan and Jackson, 1985). Body-wave modelling indicated the event consisted of 4 discrete subevents. The first and second subevents occurred within 3.8 seconds of each other and the second subevent 11.4 km east-south-east of the first. These two events had sufficient moment, 10.6×10^{18} N m, to account for the surface rupture. Their hypocentral depths were well constrained at 6 km. The third and fourth subevents were deeper and appeared to occur on very shallow dipping faults. The average slip is calculated to be 0.86 m.

Gediz, March 28, 1970, Ms 7.0: The Gediz earthquake struck almost one year after the Alasehir event. The 45-km fault scarp associated with the event was not a simple feature. It trended north-northwest and east-west with the downthrown side to the east and north of the fault scarps. The event consisted of 5 subevents and the 45 km of surface faulting is associated with the first two subevents which nucleated at 10 km depth. The total moment of all the events was 87.5×10^{18} N m (Eyidogan and Jackson, 1985). An average normal slip of 5.31 m was calculated for this event.

A velocity profile for events this century along the western extremity of the Bozdag Horst (XX' Figure 8.4) was calculated by summing the deformation caused by the 1919 Soma, 1928 Torbali, 1933 Cos, 1939 Dikili and 1955 Soke earthquakes. The velocity between AKGA and CINE predicted from events this century is 0.15 cm/yr (Figure 8.11). The velocity profile along the eastern extremity (YY', Figure 8.4), was calculated by summing the deformation caused by the 1899 Buyuk Menderes, 1969 Alasehir and 1970 Gediz earthquakes. The predicted result is a velocity of 0.1 cm/yr between AKGA and CINE (Figure 8.12). Ten percent of the measured motion only can therefore be attributed to seismicity this century.

Assuming this century's seismicity is approximately representative of previous centuries then the deformation due to 1000 years of earthquakes can be calculated by summing the deformation caused by this century's events over several centuries. According to the

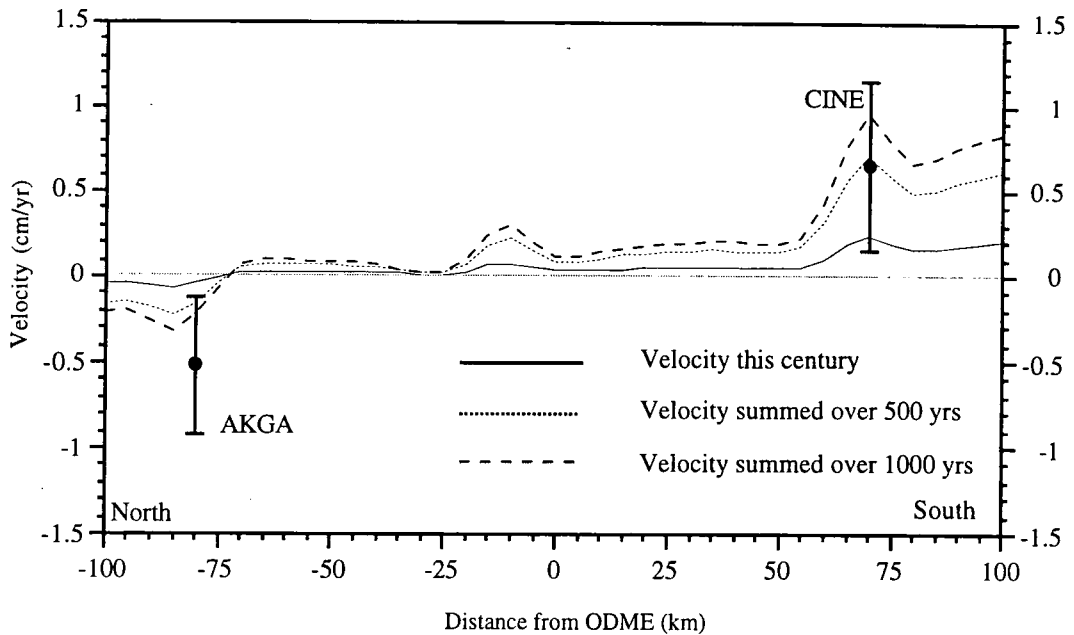


Figure 8.11 Velocity along the western extremity of the Bozdag Horst, contributed by the postseismic effect of earthquakes this century, *i.e.*, the:1919 Soma, 1928 Torbilli, 1933 Cos, 1939 Dikili and 1955 Soke events.

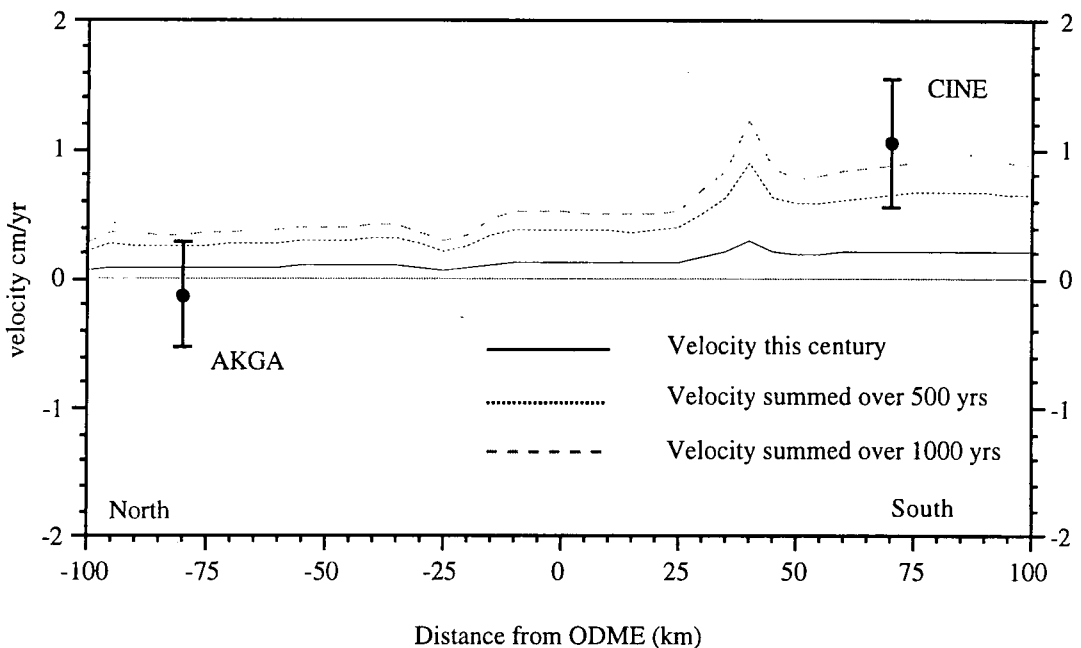


Figure 8.12 Velocity along the eastern extremity of the Bozdag Horst, contributed by the postseismic effect of earthquakes this century, *i.e.*, the 1899 Buyuk Menderes, 1969 Alasehir and 1970 Gediz events.

velocity-decay curve shown in Figure 8.8, after 100 years the motion due to a set of events will have decayed by about 21% and after 1000 by about 83%. Thus, 21% of the postseismic signal is added to that calculated to represent the deformation caused by 200 years of seismicity. When deformation over the past 1000 years is summed in this way

then the velocities along the eastern and western profiles are 6 mm/yr and 11 mm/yr respectively (Figures 8.11 and 8.12). The irregularities on the profiles would be smoothed out if earthquakes were spread out spatially rather than assuming they occurred on the same fault segment each time. These calculated velocities are consistent with those observed geodetically. The opening rate of the Buyuk Menderes and Gediz grabens is predicted to be almost twice as fast towards the west than the east. This result is consistent with geomorphological data from the grabens, *i.e.*, that the grabens are wider and deeper to the west than to the east. The result suggests that the seismicity in SW Turkey this century is representative of the long-term average and that the seismic record is complete for events greater than $M_s 6.5$ this century.

8.5 SUMMARY

The ongoing GPS project in western Turkey is yielding information on how crustal deformation is occurring in the region. Measurements made between 1988 and 1992 show that the Anatolian plate is being extruded at a rate of 50 mm/yr and rotating anticlockwise about a pole in the Nile delta at a rate of $1.2^\circ/\text{Ma}$. Subtraction of this rotational motion from the GPS determined motions of points in SW Turkey shows a residual deformation in the form of north-south extension in that area (Oral, 1995a). The measured north-south extension is 11.5 mm/yr and is occurring in a direction perpendicular to two major grabens which trend for 150 km in an east-west direction across western Turkey. Given that the errors of the 1989 survey combined with those of future surveys will be of the order of 2 cm in the horizontal components, then reoccupation of the SW Turkey network at 6 to 8 year intervals should reveal motion which is above the 3σ noise level.

An $M_s 6.5$ or greater earthquake within the Gediz or Buyuk Menderes grabens will yield deformation within the network which is detectable at the one-sigma level at about 3 of the points within the SW Turkey network. Reoccupation of the network would, after such an event, establish an initial postseismic survey with which later surveys could be referenced. Twenty years after an $M_s 6.5$ earthquake the horizontal deformation will be about 2 cm across the network and detectable by GPS.

The deformation measured between 1988 and 1992 occurred aseismically and may be attributed to the postseismic redistribution of stress in the viscoelastic lower crust. Assuming a rheologically-varied model of the Earth's crust and upper mantle, and using finite element modelling it is possible to simulate this deformation. Following a normal faulting earthquake, the calculated displacements show that strains within one fault depth

are high but that they tend to zero at distances greater than this. Displacements are greatest over the downthrown side of the fault. The horizontal velocities decay slowly after the event, taking 1000 years (38 times the Maxwell relaxation time of the viscoelastic layer) to decay to 10% of the signal 5 years after the event.

The overall extensional velocity, calculated by summing the deformation due to an $M_s 7.0$ earthquake which repeats every 150 years is about 5mm/yr, somewhat lower than the extension rates measured by GPS and those calculated using seismic moment tensors from SW Turkey. The discrepancy could be a result of ignoring smaller earthquakes. This indicates that the secular strain can be modelled as stress redistribution in the viscoelastic lower crust, following the sudden release of stress in the Earth's crust brittle upper crust through earthquakes. Summing the extension caused by five earthquakes along a north-south profile at the western extremity of the Buyuk Menderes and Gediz grabens, and three earthquakes along a north-south profile at the eastern extremity, gives modelled north-south extensional velocities of 6 and 11 mm/yr respectively. Assuming this century's seismicity is representative of the past 1000 years of earthquakes, and summing the calculated velocities over that period, modelled velocities which are compatible with GPS measurements are achieved.

CHAPTER 9

DISCUSSION

9.1 GPS SURVEYING IN THE HENGILL TRIPLE JUNCTION

9.1.1 The 1991 survey

A 23-point, 30 x 25 km, GPS geodetic network was established in the Hengill ridge-ridge-transform triple junction in 1991. After processing the data with the Bernese V3.2 software the best solution obtained was the ambiguity-fixed solution which yielded scaled formal errors of less than 1 cm in the horizontal and about 1 cm in the vertical. The effect of ocean loading on the vertical component of the measurements was negligible compared to other errors. Whereas the ocean loading effect was predicted to cause a daily variation of 6 mm in the vertical, the measured diurnal variations were 50 to 70 mm. Thus, within GPS surveys the size of the Hengill 1991 survey the ocean loading effect may be ignored. However, for larger surveys, where lines span over 100 km, and for higher-accuracy work, the ocean loading effect may need to be considered.

The relatively large diurnal variation in the vertical component when compared with the formal errors calculated illustrates how that measure underestimates the true errors. The shortness of the sessions and lack of fixed ambiguities are probably largely responsible for the scatter in the results. In particular, the SV geometries of the two-hour time windows varied considerably. Additional sources of error include unmodelled ionospheric or tropospheric variations and variations in orbit quality.

9.1.2 Possible future tectonic activity in the Hengill triple junction

The Hengill GPS network lies in a region where there are persistently high levels of seismicity and occasional earthquakes of up to magnitude 7. Within the Hengill volcanic system, tectonic activity could occur through inflation of magma chambers or through rifting events similar to the Krafla event of 1975 to 1985. The last such event in the

Hengill system was in 1789. The activity was reportedly accompanied by an M6.5 earthquake. Volcanic activity has been limited within the Hromundartindur system since 10 Ka and there has been little spreading in that zone. Tectonic deformation in the Hromundartindur system is thus likely to be limited to uplift associated with magmatism. The third volcanic system which the network encompasses, the Grensdalur system, is believed to be extinct and thus deformation caused by magmatism from that volcano or rifting is not expected.

The Hengill GPS network is ideally placed to study the tectonics of a ridge-ridge transform triple junction. Volcanism or rifting within the EVZ or WVZ could trigger a large earthquake within the SISZ. For example, the earthquake sequence in 1784 was preceded by the 1784 Laki eruption in the EVZ and the 1789 Hengill rifting event followed after only 5 years. Recently, activity has been concentrated in the eastern part of the SISZ with the 1991 Hekla eruption and the 1987 Ms5.8 Vatnajokull earthquake.

Earthquakes are known to repeat in the SISZ at 100 to 150 year intervals and tectonic activity appears to propagate from east to west. In 1896 five events of magnitude 6 to 7 occurred on different faults within the zone and between 1784 and 1789 three events of magnitude 6.5 to seven occurred (Stefansson and Halldorsson, 1987). The proximity of the earthquakes, and the time period involved, suggest the earthquake sequences may be influenced by increases in static stresses just as the Rainbow Mountain-Fairview Peak and Dixie Valley earthquakes seem to have been. Triggered earthquakes are therefore not confined to the continental crust.

Small earthquake activity recently increased greatly within the Hengill triple junction and because a moderate to large earthquake is expected soon in SW Iceland, the Hengill GPS network should be measured regularly to monitor strain accumulation. In the event of an earthquake within the SISZ the Hengill GPS network and the south Iceland GPS network should be remeasured immediately. Measurements of the surface coseismic deformation can be used to infer the subsurface geometry and coseismic slip on the SISZ fault which failed. The subsurface fault geometry and the coseismic slip inferred from the GPS measurements could then be used to calculate where moderate to large earthquakes are likely to be triggered by increases in the static stresses.

9.1.3 Recent partial measurement of the network

Since the 1991 survey, points within the Hengill network have been remeasured twice. In May 1995, five of the Hengill network points were remeasured in response to seismic unrest in the area, and in August 1995 three of the points were remeasured as part of a GPS experiment to densify the South Iceland GPS network. The measurements were made by the Nordic Volcanological Institute. Between 1991 and 1995 vertical

deformation was at the cm level (Table 9.1) and the largest horizontal displacement vector was 1.5 cm after the displacements between the surveys have been minimised (Sigmundsson, 1995, personal communication). These results may indicate inflation beneath the Hromundartindur system. Thus, the network has already proved valuable in monitoring tectonic activity in the area.

Table 9.1 Points within the Hengill network remeasured in May 1995 (Sigmundsson, 1995, pers. comm.).

Station Name	Latitude (dd mm ss)	Longitude (dd mm ss)	Height (m)
OS-1985-7143	64 0 8.28848	- 21 14 56.66970	368.5593
OS-1991-DU07	64 1 5.02250	- 21 11 34.32983	157.4429
OS-1991-DU18	64 2 52.75375	- 21 13 49.05516	407.1400
OS-1991-DU25	64 4 37.61887	- 21 10 10.75448	421.3560
OS-1985-7331	64 5 6.44359	- 21 15 28.40928	374.1991

9.2 MODELLING OF DEFORMATION ASSOCIATED WITH THE 1954 RAINBOW MOUNTAIN - FAIRVIEW PEAK AND DIXIE VALLEY EARTHQUAKES

9.2.1 Geodetic data analysis

After systematic errors were corrected, and non-tectonic deformation was subtracted from the 1908 to 1986 geodetic data, the coseismic deformation associated with the Rainbow Mountain, Fairview Peak and Dixie Valley earthquakes, and the postseismic deformation in the Fairview Peak area were well constrained. The systematic error which contaminated the levelling data was an incorrect miscalibration correction applied to data from three levelling surveys made in 1967. The non-tectonic deformation detected was that of water withdrawal in the Fallon area. After an assessment of data quality, α values assigned to the levelling data ranged from 1 to 4 mm/km^{1/2}. Hence, the error in elevation change between 2 benchmarks 1 km apart ranged from 1 to 4 mm. The errors assigned to the triangulation data were on average 0.86 to 1.05 arcseconds. These terrestrial geodetic data thus tightly constrain deformation in the region.

Although a rod miscalibration error does explain the anomalous signal in the Dixie Valley postseismic data set there are still peculiarities associated with the 1967 survey along the Dixie 1 route. The survey was double run, *i.e.*, each level section was measured twice, once in the forward direction and once in the backward direction (Section 4.2.1.1). When

these measurements are summed instead of being zero, the total is 140 mm. This suggests that a systematic error may still contaminate the 1967 levelling data.

The type of analysis involved in isolating systematic errors and non-tectonic deformation in levelling and geodetic data sets may become increasingly important in analysing the earthquake cycle, in particular the postseismic stage. Comparison of historical geodetic sets, such as the one used in this study, with GPS measurements made today and in the future will yield valuable information on the interseismic strain build up between earthquakes. Another benefit of studying an earthquake which occurred several decades ago is that its function in transferring stress to neighbouring faults may be studied. Calculating the static stress associated with such events and comparison with the following seismicity, may illuminate areas of higher or lower seismic risk. The disadvantage in using historical geodetic data is that it is of lower quality than current space-based geodetic measurements and the associated errors are larger. Systematic errors may be large, such as the rod miscalibration in the 1967 levelling data in the Dixie Valley data. It is important that at least three sets of measurements of the geodetic network exist so the consistency of data can be examined and systematic errors be identified.

9.2.2 Modelling of coseismic deformation

The geodetic data which constrain the coseismic deformation are modelled well by planar faults dipping at 50° to 80° and extending to depths of 5 to 14 km, *i.e.*, with geometries similar to those determined for other Basin and Range faults. The elevation changes caused by the M7.3, 1959, Hebgen Lake, Montana, and the M6.9, 1983, Borah Peak, Idaho, earthquakes indicated slip extending to depths of 7 to 12 km and 6 to 14 km respectively on faults which dip at 45° to 50° (Barrientos and Stein, 1987). Teleseismic body-wave modelling of the M6.9, 1915, Pleasant Valley, the M6.1, 1930, Excelsior Mountain and the M6.7, 1932, Cedar Mountain earthquakes, indicate similar source parameters. The Pleasant Valley earthquake, which occurred 100 km from the Dixie Valley earthquake (Figure 1.5), occurred on a $44 \pm 8^\circ$ dipping fault at a depth of 9 ± 5 km (Doser, 1988). The Cedar Mountain event, 45 km south of Dixie Valley (Figure 1.5), occurred on a $72 \pm 7^\circ$ dipping fault at 14 ± 2 km depth and the Excelsior Mountain earthquake, 200 km south of Dixie Valley, was on a fault dipping at $40 \pm 8^\circ$ at a depth of 14 ± 10 km (Doser, 1988). The dip of the Fairview Peak fault is similar to that of the Cedar Mountain fault while the dip of the Dixie Valley fault is in the same range as that of the Hebgen Lake, Borah Peak, Pleasant Valley and Excelsior Mountain faults. The dips of the other faults in the 1954 sequence are poorly determined.

The ranges of error in the fault geometries reflect the noise and possible non-tectonic signals in the data. The quality of the data, however, was carefully assessed and each coseismic elevation or angle change was appropriately weighted given the accuracy of the

survey involved and the misclosure of the leveling or triangulation surveys. The factors which have greatest impact on the range of the errors involved are the assumptions of uniform slip on rectangular dislocations and weaknesses in the geodetic network. The ranges of errors in the fault geometries are also affected by uncertainty in the position of the faults. This effect was reduced by searching for the position of the faults simultaneously with the dips and depths in a gradient search of parameter space.

In this study, the coseismic vertical and horizontal slip values determined geodetically are either similar to, or greater than, the maximum displacements observed at the surface. The only exceptions are: vertical motion on the Fairview Peak fault, which is much smaller than that observed at the surface, and the displacements determined on the Rainbow Mountain fault. The vertical and horizontal offsets calculated on the Rainbow Mountain fault agree reasonably well with those on the surface. Vertical slip calculated on the Dixie Valley fault is about twice that observed at the surface and the vertical slip calculated on the combined West Gate and Gold King fault is 50% larger than the maximum offset observed along the surface ruptures.

Along the Gold King, West Gate and Dixie Valley scarps, little or no horizontal slip is observed at the surface while 1 - 3 m of right-lateral motion is determined geodetically. Recent mapping of the east side of Dixie Valley has revealed a previously unknown fault, the Lauderback Mountain fault, on which as much as 2 m of right lateral slip may have occurred in the 1954 sequence (Caskey *et al.*, 1996). The Lauderback Mountain fault lies ~ 3 km west of and parallels the West Gate and Gold King faults. The right-lateral motion of 3.35 metres determined through the geodetic inversion for the combined Gold King and West Gate fault is therefore probably a result of slip on these three faults. If this is the case, then the geodetically determined slip of 3.5 meters is very close to the sum of the observed maximum right-lateral motion on the Lauderback Mountain West Gate and Gold King faults, which is 3.2 m. Lateral motion along the Dixie Valley fault is very poorly resolved due to the lack of data in Dixie Valley. There is no significant change in the model-to-data fit when zero slip is imposed on the fault or when 1.58 m of slip is imposed on it. This reflects the uncertainty associated with the right-lateral slip determined on the fault. Given the weakness of the triangulation network in Dixie Valley it is possible that slip which occurred on the Lauderback Mountain fault has been put on the Dixie Valley fault in the modelling process. However, it is more likely that slip which occurred on the Lauderback Mountain fault has been incorporated into motion on the West Gate and Gold King combined fault. The other possibility is that the right-lateral slip determined geodetically on the Dixie Valley fault occurred at depth.

A mismatch between observed surface offsets and calculated slip has been found for other events. The calculated vertical slip for the Hebgen Lake earthquake (7-8 m) was more

than twice that observed at the surface (3 m) and the calculated vertical slip for the Borah Peak earthquake was 1.4 times greater (Barrientos and Stein, 1987). Source parameters of the Pleasant Valley earthquake derived from body-wave modelling suggest 3.3 m of vertical slip occurred on that fault (Doser, 1988) compared to observed vertical surface offsets of 2 m and little horizontal displacement (Wallace, 1984). The extent of strike-slip motion calculated for the Cedar Mountain event through body-wave modelling is also not evident at the surface (Doser, 1988). Another example of the mismatch of surface slip and geodetically-determined slip comes from the M6.6, 1979, Imperial Valley, California earthquake. The vertical deformation created by that event was modelled by assuming a variable slip distribution for vertical and lateral motion. Again, the data were best fitted by assuming a greater amount of strike-slip motion at depth than observed at the surface. Whereas the maximum right-lateral offset at the surface was 0.7 m the strike-slip motion determined at a depth of 8 to 10 km was 1 to 1.4 m (Reilinger and Larsen, 1986).

Since the recurrence interval is calculated as the amount of coseismic slip divided by the long-term average rate of slip then recurrence intervals for earthquakes based on surface offsets may be underestimated. Wallace and Whitney (1984) calculated that reoccurrence interval on fault scarps to the north of the Dixie Valley fault within the Stillwater range to be between 2,800 and 7,000 years. This estimate was based on an uplift rate of 0.26 mm/yr determined through Pleistocene shoreline deposits and coseismic slip estimates of 1 to 2 metres which were deduced from Holocene fault scarps. Based on the coseismic slip values found in this study the reoccurrence interval on the Fairview Peak fault is close to 7000 years while on the Dixie Valley fault it is about 14,000 years.

9.2.3 Stress transfer between normal faults

The changes in static stresses caused by the 1954 Rainbow Mountain-Fairview Peak-Dixie Valley, Nevada, earthquakes show that each event in the sequence was preceded by a positive static stress change on some part of the fault which failed. The calculated magnitude of the stress increases ranged from 10^4 Pa to over 10^5 Pa. These changes are typical of those that appear to trigger earthquakes. Harris *et al.* (1995) found that $M \geq 5.5$ earthquakes which caused stress increases of $\geq 10^4$ Pa on another fault plane were usually followed by rupture of that plane within 1.5 years. Also, the increase in stress along the Landers fault caused by four events in the region in the 24 years preceding the M7.4, 1992 event was about 10^5 Pa (King *et al.*, 1994).

The Fairview Peak fault received a positive stress change of 10^4 Pa from the Rainbow Mountain events. The Dixie Valley fault received a larger stress increase of up to 10^5 Pa. The northern half of the fault, where the rupture began, received the largest positive stress change. The static stress change calculations can therefore explain why rupture began at the northern end of the fault rather than the southern end which was closer to the Fairview

Peak epicentre. The Rainbow Mountain earthquakes caused a smaller stress increase on the Fairview Peak fault than on the Dixie Valley fault. It is therefore puzzling that the Fairview Peak fault failed first. There are two possible explanations for this, the West Gate and Gold King faults failed before the Fairview Peak earthquake or, the Fairview Peak fault was already close to failure.

The West Gate and Gold King faults, which received stress increases of 7×10^4 Pa may have begun to slip before the Fairview Peak event and triggered that event. No times or focal mechanisms have been determined for the West Gate or Gold King events but the faults associated with these events are assumed to have ruptured with the Fairview Peak event (Doser, 1986). Although these faults are smaller and less dominant in the geomorphology of the area than the Fairview Peak, Dixie Valley and Rainbow Mountain faults, they may thus have an important role in transferring stress between major range-bounding faults. The second possibility is that the order in which the Fairview Peak and Dixie Valley faults failed was influenced by the 1932, M6.7, Cedar Mountain earthquake (Figure 1.5). The Cedar Mountain earthquake involved almost pure strike-slip motion on a near-vertical fault 60 km from the Fairview Peak fault (Doser, 1988). That event increased the static stresses on the Fairview Peak fault by up to 1.7×10^4 Pa while the stress increases on the Dixie Valley fault were, at most, 5×10^3 Pa. The Fairview Peak fault may thus have been closer to failure than the Dixie Valley fault when the Rainbow Mountain events occurred. The 1915, M6.9, Pleasant Valley earthquake, which occurred 90 km from the Dixie Valley epicentre (Figure 1.5) had a very small effect on the Dixie Valley and Fairview Peak faults. Right-lateral slip was encouraged by stress changes of 8×10^3 Pa and 4×10^3 Pa on the Dixie Valley and Fairview Peak faults respectively. At stress changes of $< 10^4$ Pa the correlation of seismicity and positive static stress changes is weak (Reasenberg and Simpson, 1992).

After the 1954 sequence, about one fault depth away from the ruptured faults, stresses were generally relaxed on optimally-orientated faults by stress changes of 10^5 Pa (Figure 6.13). Given that the rate of extension in the Dixie Valley area has been 0.5 mm/yr over the past 8 to 10 Ma (Okaya and Thompson, 1985) then the average stress rate in Dixie Valley is about 1.5×10^3 Pa/yr. Thus, the earthquake sequence released about 66 years of the time-averaged accumulated stress, and, it could be argued, delayed the next event by this amount of time.

The combination of fault orientations and current regional stress field may explain the northeast-southwest trend of seismicity through the Central Nevada Seismic Zone (Figure 1.5). The static stress changes induced by the 1954 earthquake sequence encourage earthquakes to occur to the northeast or southwest of the Dixie Valley area. As is seen in Figures 6.8 and 6.11, lobes of high stress change tend to fall to the northeast and

southwest of northeasterly-orientated faults, while lobes of negative stress change tend to fall to the northwest and southeast of the faults. This is a result of the orientation of the regional stresses. The present-day northwest orientation of the least principal stress is probably caused by the distribution of strike-slip motion between the Pacific and North American plates inland from the San Andreas fault. The trend of seismicity in western Nevada is therefore influenced not only by current but also by past tectonism since the orientation of the western Basin and Range faults results from the extensional regime which existed between 17 to 10 Ma. This study also shows that the current heightened seismicity within the zone and the trend of the zone could be attributed to processes within the brittle crust and not solely to process in the lower crust such as a narrow zone of localized extension at depth as proposed by Wallace (1984).

The 1954 sequence of earthquakes involved the transfer of stress between faults which were not continuous in strike and did not join at depth. No decollement feature or listric-type fault was required to transfer sufficient amounts of stress to encourage failure. The faults which ruptured did so in regions of static stress increases and were favourably oriented for failure given the existing extensional regional stress regime. Patterns of normal faulting events similar to the Fairview Peak-Dixie Valley events have been observed in other regions. In SW Turkey three normal faulting events of M_s 5.9, 6.5 and 7.2 occurred within 100 km of each other in 1969 and 1970 (Eyidogan and Jackson, 1985). The time intervals between the events were 5 days and one year. The faults were orientated east-west in a north-south extensional regime. In 1981 three earthquakes of M_s 6.7, 6.4 and 6.4 occurred in the easternmost part of the Gulf of Corinth (Jackson *et al.*, 1982). The events occurred on normal faults which were within 30 km of each other. The first two events were separated by 2 hours and the second and third events by 7 days. Again, these faults were favourably orientated for failure in an extensional regime. The Wasatch fault zone is a 370 km north-south trending fault zone in western Utah. There have been no major earthquakes in this zone in historic time but paleoseismological evidence suggests that M_s 6.5 to 7 earthquakes repeatedly occur along it (Schwartz and Coppersmith, 1984). It appears that most of the fault zone ruptured between 1000 and 500 years ago, suggesting that seismicity may have propagated through it in a manner similar to that occurring now in the Central Nevada Seismic Zone.

Normal faulting earthquakes accommodate regional extensional stresses within an area, and when a fault fails stresses are transferred to regions away from the fault. If there are favourably orientated faults within the region of increased stresses then a sequence of normal faulting earthquakes may be 'triggered', as appears to have happened in Dixie Valley, SW Turkey and Greece. Such sequences therefore result from the orientation of the regional stress field and the existence of faults favourably orientated for failure.

It is not clear why there is a time lapse between the increases in static stress on a fault and the triggered earthquake occurring. There is a lack of correlation between the time period between the triggered earthquake and the magnitude of static stress increase. For example, the Dixie Valley earthquake followed the Rainbow Mountain earthquake by 4 months while the 1992, M5.5 Big Bear earthquake in southern California which received a comparable stress increase from the 1992 M7.2 Landers earthquake, occurred 30 minutes after that event. Future work on the study of triggered earthquakes should address this issue. Factors which may contribute to the delay between the triggering and triggered earthquakes include; creep, the strain rate of the area and ductile flow in the lower crust. Another possible explanation may lie in the redistribution of groundwater fluids. If, during an earthquake, the pore pressure drops then earthquakes will be “discouraged” since the normal stresses are effectively increased. An earthquake may only occur in the area when the pore pressure has resumed its normal level in the area, or at least when the effective normal stress is again low enough to permit slip. Knowledge of the factors involved in controlling the time between the triggering and triggered earthquake is essential to seismic hazard assessment.

9.2.4 Modelling of postseismic deformation

Postseismic deformation measured at the Earth’s surface can be modelled by assuming aseismic slip on planes in an elastic half space or by distributed deformation in viscous elements of a rheologically-varied Earth. The postseismic deformation following the 1954 Fairview Peak and West Gate earthquakes was modelled here using both methods. An investigation of the possibility of aseismic slip on a downward extension of the fault to upper mantle depths, as proposed by Savage (1990) yielded questionable results. The slip values determined on downward extension of the faults were in the opposite direction to slip resolved on the upper section of the faults (Section 7.5.3.1). The associated variances were also relatively large and suggest that the surface data are not sufficient to resolve slip at depth. Also, there are geophysical and geometric reasons for doubting that the faults extend to these depths. If the faults extend to 30 km they would underlie neighbouring ranges and intersect other faults. Seismic refraction profiles in western Nevada show that planar faults do not extend below 10 to 15 km (Catchings and Mooney, 1991) and temperature data show that the brittle-ductile transition is at 10 km depth in Dixie Valley (Blakely, 1988). It is therefore likely that the faults either terminate or flatten at depths of 10 to 15 km. Aseismic slip at depth, such as proposed by Savage (1990) could only be accommodated if the fault flattens at depths of 10-15 km and the slip vector becomes more horizontal. This might occur on low angle detachment faults in the Basin and Range province which could creep aseismically.

For these reasons, the results obtained by modelling the broad-scale postseismic deformation assuming a rheologically varied model of the Earth and viscous flow are

favoured here. After allowing for shallow slip on the upper parts of the faults, which created a well-defined, local subsidence feature, the remaining deformation can be reasonably well modelled assuming a three-layer model with a weak middle layer. It is notable though, that although the long-wavelength postseismic deformation was best modelled in this way, it was necessary to assume the local feature had been formed through aseismic slip which was modelled assuming an elastic half-space. Thus, both postseismic deformation models were required by the data in this case.

Postseismic deformation can be used to infer the rheological properties of the Earth and fault geometry. The peak-to-peak amplitude of the vertical deformation is dependent on the viscosity of rocks at mid-crustal depths and the ratio of the fault depth and thickness of the brittle upper crust. The amplitude is greatest when this ratio is about 1, *i.e.*, when the entire brittle layer is ruptured (Figure 7.7). If more than 40% of the fault protrudes into the middle layer then subsidence occurs over the fault trace following a normal faulting earthquake, otherwise uplift occurs. This is independent of the viscosity of the viscoelastic layer (Figure 7.8). The width of the postseismic deformation field is largely dependent on the thickness of the brittle upper crust and is independent of the viscosity of the middle viscoelastic layer. If the thickness of the brittle upper crust is known then an upper limit can be placed on the depth of the fault if it can be established whether subsidence or uplift occurred following a normal faulting earthquake. In the Fairview Peak area several independent geophysical surveys indicate the brittle layer is about 10 km thick, and since uplift occurred over the fault trace then the Fairview Peak fault can extend no deeper than 14 km. This depth is consistent with geodetic and seismic estimates of the fault depth.

Using data from geophysical surveys to constrain the structure wherever possible, the postseismic deformation in the Fairview Peak area was best fitted with a viscosity of 1×10^{20} Pa s at depths of 10 to 30 km. This viscosity is similar to estimates made from Pleistocene shoreline deposits in the eastern Basin and Range province (Bills *et al.*, 1994). In that study the best fitting viscosities ranged from 1.8×10^{19} to 2×10^{20} Pa s. The range of values may be a result of the three different epochs the data sets spanned, the Bonneville epoch (17 Ka), the Provo epoch (16 Ka) and the Gilbert epoch (12 Ka). Data from the Bonneville epoch are best fit with a viscosity of $\leq 10^{20}$ Pa s, the Provo epoch data with a viscosity 10^{19} to 10^{20} Pa s and the Gilbert data with a viscosity of 2×10^{20} Pa s. A viscosity of 1×10^{20} Pa s is higher than that determined from the postseismic deformation following the M7.3, Hebgen Lake earthquake (Reilinger and Larson, 1986). That study suggested a value of 10^{19} Pa s. This lower value is probably a result of the thick elastic layer (30-40 km) used in the analysis compared to the 10 km thick elastic layer assumed in this study.

The viscosity of 1×10^{20} Pa s is an order of magnitude lower than suggested for the global average estimated from glacial rebound studies. This may be due to the anomalously high heat flow in the Basin and Range province. Bills *et al.* (1995) suggested that if the relation between strain rate and stress is nonlinear, the viscosity will be dependent on the preexisting tectonic stresses. A region such as the Basin and Range province which has been subjected to large scale extensional tectonics would then be expected to exhibit a lower viscosity than a region which was not subjected to such stresses.

Modelling the postseismic deformation using a two-dimensional finite element code has limitations. It is assumed that the fault is finite, and a plain-strain algorithm is used. In the case of the Fairview Peak earthquake the assumption of a finite fault is not too great a simplification since the levelling line crosses the fault and lies a few kilometres from the end points. The plain-strain assumption will have the result of overestimating motion since motion in the out-of-plane direction is not allowed. Future work in analysis of the postseismic deformation field in the vicinity of the Fairview Peak fault would be to study the horizontal postseismic signal using a three-dimensional finite element program. This would allow the right-lateral slip associated with the earthquake to be modelled also. Using both vertical and horizontal data may allow the structure of the crust to be studied, *i.e.*, the thickness of the brittle layer and the depth to the Moho.

9.3 EXTENSIONAL DEFORMATION IN SW TURKEY

The GPS network in SW Turkey is ideal to monitor the long-term strain of the Earth's crust there. GPS measurements made between 1988 and 1992 shows that north-south extension within SW Turkey is occurring at rates of 11.7 ± 5 mm/yr. The measured GPS velocities are much slower than those estimated from the total seismicity of the Aegean area. They are however, similar to those determined from summation of the moments of earthquakes in SW Turkey alone, which predicts north-south extensional rates of 13.5 mm/yr (Eyidogan, 1988). GPS measurements of crustal deformation rates are superior to estimates derived from kinematic models or seismicity data since no assumptions are made about the source mechanisms of earthquakes or focal depths. The similarity though, of the measured deformation and the extension rates determined in the study of SW Turkey earthquakes by Eyidogan (1988) show that the seismic record can yield a close estimate of the rate measured geodetically.

The deformation of the SW Turkey network in the period 1988 to 1992 occurred aseismically and was modelled here as 2-dimensional north-south profiles using the finite element method. The 3-layer model of the Earth used was similar to that used for the

Basin and Range province. Following a normal-faulting earthquake, extensional strains are large within a horizontal distance of one fault depth but tend to zero at greater distances. The maximum displacements occur over the fault trace and a local minimum occurs over the downward extension of the fault. The displacements propagate away from the fault rupture with time and the direction of motion is always away from the fault. The horizontal velocities following an $M_s 6.5$ normal faulting earthquake are less than 1 mm/yr within 10 km of the fault, where the velocities are greatest.

The horizontal velocities decay relatively slowly with time being about 70% of the initial extension rate 100 years, or 4 times the relaxation time of the viscoelastic layer, after the earthquake. Thus, for earthquakes with a repeat time of 10 to 100 years, and for structures such as that modelled here, immediate postseismic strain rates will not be much higher than the immediate pre-seismic rates, and little variation in deformation rate is predicted throughout the earthquake cycle (Figure 8.10). This has been observed elsewhere by VLBI measurements. The postseismic transients, the differences between the pre- and post-seismic deformation rates, were found to be very small following two $M_s 7.6$ earthquakes in the Gulf of Alaska (1987 and 1988) and the $M_s 7.1$, 1989, Loma Prieta event (Argus *et al.*, 1994). After the Loma Prieta event the rate of motion was 4 ± 3 mm/yr faster than the preseismic, and after the Alaska earthquakes the postseismic velocity was 3 ± 4 mm/yr faster than the preseismic.

The modelled north-south extension caused by five earthquakes at the western extremity of the Buyuk Menderes and Gediz grabens, and from three earthquakes easterly in the grabens, are 1.5 and 1 mm/yr respectively. Thus, seismicity this century accounts for 10% of the extension measured in the 1989 to 1992 period. When the contributions of past earthquakes are added, assuming the appropriate velocity decay rates, and assuming that the seismicity of this century is representative of previous centuries, the calculated opening rate is 11 mm/yr along the western end of the graben and 5 mm/yr along the eastern end. These rates are similar to those measured by GPS. Modelling this aseismic extensional deformation predicts that the western extremity of the Bozdag Horst is opening at almost double the rate of the eastern end, suggesting the Bozdag Horst region is opening in a 'fan' like manner. This result is supported by the geomorphology of the area. The Gediz and Buyuk Menders grabens are wider to the west and narrower and shallower to the east (Paton, 1992). The probable cause of this laterally-varying strain field is that north-south extensional forces are greater towards the west, closer to the Hellenic subduction arc. The combined errors of the 1989 survey and that of a complete future resurvey will be at the 2 cm level in the horizontal component. Thus, reoccupation of the network around the year 2000 would yield a clear regional strain field.

9.4 CRUSTAL EXTENSION IN OCEANIC-TYPE AND CONTINENTAL-TYPE ENVIRONMENTS

Crustal extension in oceanic environments is characterised by episodic rifting events. In Iceland these events occur at intervals of 100 to 150 years and several metres of extension may occur in a spreading segment during one event. Modelling of the postseismic deformation field measured by GPS around the Krafla volcanic zone has given an insight to the role of aseismic extension in oceanic crustal growth. Assuming an elastic over viscoelastic crustal model, the GPS data there suggest that the viscosity of the lower crust is about 1.1×10^{18} Pa s (Hofton, 1995). The implications of modelling the anelastic deformation as a process through which the coseismic stresses in the Earth's crust are redistributed through ductile flow are: 1) the event will be followed by large postseismic transients, and 2) extension will be episodic over a zone a few 100's of km wide (Hofton, 1995). The GPS data from north Iceland, which span about 5 years are modelled reasonably well using this model. Strain rates of up to 6 cm/yr, about three times the NUVEL-1A predicted spreading rate, are observed close to the rift zone (Hofton, 1995; DeMets *et al.*, 1994).

Extensional crustal deformation in continental environments, such as the Basin and Range province and SW Turkey is accommodated mainly through normal faulting. Seismicity is diffuse, occurring over regions 100 km or more wide and, compared to rifting episodes in Iceland, earthquakes occur relatively continuously. The postseismic deformation following a normal faulting earthquake was calculated using the finite element method and assuming a three-layer crustal model with physical parameters such as the seismogenic depth derived from geophysical data. Modelling the vertical postseismic deformation associated with the 1954 Fairview Peak earthquake suggests the viscosity of the lower crust (1×10^{20} Pa s) may be as much as two orders of magnitude greater than that in an oceanic crustal environment. Following one event the postseismic transients are predicted to be small. Horizontal extensional velocities decay slowly with time and the rapid diffusion of stress predicted to follow oceanic rifting events do not occur in the continental crust. Thus, the extensional process within the continental crust tends to be more continuous in nature. The difference between the two extensional processes lies in the difference in crustal structure. The higher viscosity of the continental lower crust results in relaxation times on the order of decades compared to relaxation times of the order of years in the oceanic crust.

9.5 CONCLUSIONS

- First epoch coordinates have been determined for the Hengill GPS geodetic network. The scaled formal errors associated with these coordinates are sub-centimetre in the horizontal components and at the 1 cm level in the vertical.
- The effect of ocean loading is negligible compared with other error sources for GPS surveys of the type of the Hengill 1991 survey.
- The systematic error in the Rainbow Mountain, Fairview Peak and Dixie Valley postseismic levelling data was caused by a miscalibration of levelling rods 312-347 and 312-383 used in three surveys of the area in 1967 by a factor of 150 ± 30 ppm. Non-tectonic deformation caused by water withdrawal in the Fallon area was detected by comparing levelling surveys made between 1955 and 1986.
- The faults which best fit the combined levelling and triangulation data extended to depths of 8 to 14 km and dipped between 50° to 80° . All the earthquakes contained a significant component of right-lateral slip which was generally as large as, or greater than, that observed at the surface.
- Static stresses may have played a role in triggering the 1954 Nevada earthquake sequence. Each earthquake was preceded by a static stress increase of 10^4 to 10^5 Pa on some part of the fault.
- Each of the faults involved in the 1954 sequence was optimally orientated for failure given the regional stress regime. Extensional tectonism within the Basin and Range province is therefore influenced by the tectonic regime which existed several million years ago.
- The vertical postseismic deformation which followed the 1954 Fairview Peak earthquake can be explained by modelling aseismic slip on the part of the fault which ruptured coseismically and by stress redistribution in the Earth's crust through viscous flow in the lower crust. The former process caused the short-wavelength deformation and the latter the longer-wavelength deformation. The two processes which have been proposed to explain postseismic deformation, aseismic slip and viscous flow thus both occur.
- The viscosity of the lower crust beneath the Dixie Valley area is about 1×10^{20} Pa s.

- Reoccupation of the SW Turkey GPS network in the year 2000 will yield clearly the regional strain within the network given the errors of the 1989 survey.
- The postseismic deformation created by eight earthquakes of $M_s \geq 6.5$ and greater within SW Turkey this century accounts for 10% of the north-south extension rate measured between 1989 and 1992 by GPS. If the seismicity across the network this century is representative of the past thousands of years of seismicity then the predicted extension rates across the Bozdag Horst range from 11 mm/yr in the west to 5 mm/yr in the east. These rates are comparable to 11.7 ± 5 mm/yr measured by GPS.
- Although the coseismic deformation associated with a normal-faulting earthquake may be confined to within a few fault depths of the fault after the event, the strain induced coseismically propagates out away from the fault rupture with time. Thus, through the postseismic redistribution of stress earthquakes in plate interiors contribute to the overall extension of the region.
- Extensional deformation in the continental crust differs from extensional deformation in an oceanic environment in that there are very small postseismic transients and the redistribution of stress occurs at rates of one or two orders of magnitude slower. This is a result of the higher viscosity of the continental lower crust.

9.6 FUTURE WORK

- Remeasurement of the Hengill triple junction and south Iceland GPS networks at regular intervals will provide information on the strain buildup in the western part of the SISZ which is relatively densely populated and considered an area of high seismic hazard.
- In the event of an earthquake within the SISZ, the Hengill and south Iceland GPS networks should be remeasured and the coseismic slip vectors and fault geometries calculated. These parameters should then be used to identify regions where the static stress changes are positive and triggered earthquakes are likely to occur.
- The 1954 Rainbow Mountain - Fairview Peak - Dixie Valley earthquakes were part of a much larger sequence of earthquakes that have occurred in the western Basin and Range province this century. Future work could involve determining the fault geometries and coseismic slip vectors associated with other earthquakes in western Nevada this century. It has been proposed that the Eastern Californian Shear Zone

extends into western Nevada if this is the case then it would be expected that these other earthquakes have significant right-lateral components. This motion would be a result of the influence of the motion between the Pacific and North American plates.

- Future study of triggered earthquakes should aim to explain the time lapse between the increase in static stress and a triggered earthquake occurring. The change in ground water flow, creep, or viscoelastic relaxation are possible factors which may affect the timing of triggered earthquakes.
- Reoccupation of the SW Turkey network in the year 2000 will constrain better the regional deformation field, particularly variation in the extension rate from east to west. If an $M_s 6.5$ earthquake occurs in the area then the network should be remeasured shortly afterwards to establish an initial postseismic survey. Two centimetres of extension should occur across the network in the following 20 years assuming the structural model used in this thesis.
- The SW Turkey GPS network is ideally placed and designed to measure the regional strains within the area. The usefulness of the network in studying crustal extension would be greatly increased if it were densified. Then, if an earthquake was to occur within the network, measurements of the surface deformation could be used to study the subsurface structure of the faults in the area as was done for the Rainbow Mountain-Fairview Peak and Dixie Valley faults. With such coseismic deformation it may be possible to distinguish whether listric or normal faulting occurred. Postseismic surveys of the area could also yield information on the viscosity of the lower crust and crustal structure.

REFERENCES

- Allen, C. R., 1975, Geological criteria for evaluating seismicity, *Geol. Soc. Am. Bull.*, 86, 1041-1057.
- Allmendinger, R. W., T. A. Hauge, E. C. Hauser, C. Potter, S. L. Klemperer, K. D. Nelson, P. Kneupfer and J. Oliver, 1987, Overview of the COCORP 40N transect, western United States: The fabric of an orogenic belt, *Geol. Soc. Am.*, 98, 308-319.
- Ambraseys, N. N., 1988, Engineering seismology, *Earthquake engineering and structural dynamics*, 17, 1-105.
- Anderson, R. E., 1989, Tectonic evolution of the Intermontane System; Basin and Range, Colorado Plateau, and High Lava Plains, in *Geophysical Framework of the Continental United States*, edited by L. C. Pakiser and W. D. Mooney, The Geological Society of America, Memoir 172, 163-176.
- Anderson, R. E., M. L. Zoback and G. A. Thompson, 1983, Implications of selected subsurface data on the structural form and evolution of some basins in the northern Basin and Range Province, Nevada and Utah, *Geol. Soc. Am. Bull.*, 94, 1055-1072.
- Argus, D. and G. Lyzenga, 1994, Site velocities before and after the Loma Prieta and Gulf of Alaska earthquakes determined from VLBI, *Geophys. Res. Lett.*, 21, 333-336.
- Atwater, T., 1970, Implications of plate tectonics for the Cenozoic evolution of western North America, *Geol. Soc. Am. Bull.*, 81, 3513-3536.
- Backus, G. and F. Gilbert, 1968, The resolving power of gross earth data, *Geophys. J. Roy. Astron. Soc.*, 16, 169-205.
- Bahe, K. J., 1982, *Finite element procedures in engineering analysis*, Prentice-Hall, New-Jersey, 735 pp.
- Barka, A. A. and K. Kadinsky-Cade, 1988, Strike-slip fault geometry in Turkey and its influence on earthquake activity, *Tectonics*, 7, 663-684.
- Barrientos, S. E., R. S. Stein and S. N. Ward, 1987, Comparison of the 1959 Hebgen Lake, Montana, and the 1983 Borah Peak, Idaho, earthquakes from geodetic observations, *Bull. Seismol. Soc. Am.*, 77, 784-808.
- Beanland, S. and M. Clark, 1994, The Owens Valley fault zone, eastern California, and surface faulting associated with the 1872 earthquake, *U. S. Geological Survey Bulletin*, B 1982, pp29.
- Beblo, M., A. Bjoernsson, K. Arnason, B. Stein and P. Wolfgram, 1980, Electrical conductivity beneath Iceland; constraints imposed by magnetotelluric results on temperature, partial melt, crust- and mantle structure, *Zeitschrift fur Geophysik*, 53, 16-23.
- Bedinger, M. S., J. R. Harril and J. M. Thomas, 1984, Maps showing ground-water units and withdrawal, Basin and Range Province, Nevada, *Water-Resources Investigation*, No. 83-4119-A, 10 pp.
- Bell, J. W. and T. Katzer, 1987, Surficial geology, hydrology, and late Quaternary tectonics of the IXL Canyon area, Nevada, as related to the 1954 Dixie Valley earthquake, *Mackay School of Mines, Nevada Bureau of Mines and Geology, Bulletin* 102, pp 50.
- Bell, J. W. and T. Katzer, 1991, Timing of late Quaternary faulting in the 1954 Dixie Valley earthquake area, central Nevada, *Geology*, 18, 622-625.

- Beutler, C., I. Bauersima, W. Gurtner, M. Rothacher, T. Schildknecht and A. Geiger, 1987a, Atmospheric reflection and other important biases in GPS carrier phase observations, XIX General Assembly of IUGG, Vancouver.
- Beutler, G. I., I. Gurtner, W. Bauerisma, M. Rothacher and T. Schildknecht, 1987b, Evaluation of the 1984 Alaska Global Positioning System campaign with the BERNESE GPS software, *J. Geophys. Res.* 92, 1295-1303.
- Bilham, R., 1991, Earthquakes and sea-level: Space and terrestrial metrology on a changing planet, *Rev. Geophys.*, 29, 1-29.
- Bills, G. B., D. R. Currey and G. A. Marshall, 1994, Viscosity estimates for the crust and upper mantle from patterns of lacustrine shoreline deformation in the Eastern Great Basin, *J. Geophys. Res.*, 99, 22059-22086.
- Björnsson, A., K. Sæmundsson, P. Einarsson, E. Tryggvason and K. Grönvold 1977. Current rifting episode in North Iceland, *Nature*, 266, 318-323.
- Blakely, R. J., 1988, Curie temperature isotherm analysis and tectonic implication of aeromagnetic data from Nevada, *J. Geophys. Res.*, 93, 11817-11832
- Blewitt, G., 1989, Carrier phase ambiguity for the Global Positioning System applied to geodetic baselines up to 2000 km, *J. Geophys. Res.*, 94, 10187-10283.
- Blewitt, G., 1993, Advances in Global Positioning System, technology for geodynamics investigations: 1978-1992, in *Contributions of Space Geodesy to Geodynamics: Crustal Dynamics*, edited by Smith, D. E. and D. L. Turcotte, American Geophysical Union, Washington, D.C., 195-213.
- Bomford, G., 1971, *Geodesy*, Oxford University Press, New York, 885 pp.
- Brace, W., 1966, Brittle fracture of rocks, Conference Proc. *State of stress in the earth's crust, Santa Monica, Calif. 1963*, 100-178.
- Brace, W. F. and J. D. Byerlee, 1966, Stick-slip as a mechanism for earthquakes, *Science* 153, 990-992.
- Brace, W. F. and D. L. Kohlstedt, 1980, Limits on lithospheric stress imposed by laboratory experiments, *J. Geophys. Res.*, 85, 6248-6252.
- Burchfiel, D. B., 1979, Geological history of the western United States, *Nevada Bureau of Mines and Geology Report*, 33, 1-11.
- Byerlee, J., 1978, Friction of rocks, *Pure and Appl. Geophysics*, 116, 615-626.
- Caskey, S. J., S. G. Wesnousky, P. Zhang, and D. B. Slemmons, 1996, *Bull. Seis. Soc. of Amer.*, in press.
- Catchings, R., 1992, A relation among geology, tectonics, and velocity structure, western to central Nevada Basin and Range., *Geol. Soc. of Amer. Bull.*, 104, 1178-1192.
- Catchings, R. D. and W. Mooney, 1991, Basin and Range crustal and upper mantle structure, northwest to central Nevada, *J. Geophys. Res.*, 96, 6247-6267.
- Chen, W. P. and P. Molnar, 1983, Focal depths of intracontinental and intraplate earthquakes and their implications for the thermal and mechanical properties of the lithosphere, *J. Geophys. Res.*, 88, 4183-4214.
- Chi, S. C. and R. E. Reilinger, 1984, Geodetic evidence for subsidence due to ground water withdrawal in many parts of the United States of America, *Journal of Hydrology*, 67, 155-182.

- Chinnery, M. A., 1961, Deformation of the ground around surface faults, *Bull. Seismol. Soc. Amer.*, 41, 355-372.
- Corneau, I., 1975, Numerical stability in quasi-static elasto/visco-plasticity, *International Journal for Numerical Methods in Engineering*, 9, 109 - 127.
- Crampin, S. and R. Evans, 1986, Neotectonics of the Marmara Sea region of Turkey, *J. Geol. Soc. London*, 243, 343-348.
- Craymer, M. R. and P. Vaniceck, 1986, Further analysis of the 1981 Southern California field test for levelling refraction, *J. Geophys. Res.*, 9045-9055.
- Das, S. and C. H. Scholz, 1983, Off-fault aftershock clusters caused by shear stress increase?, *Bull. Seismol. Soc. Amer.*, 71, 1669-1675.
- DeMets, C., R. G. Gordon, D. F. Argus and S. Stein, 1990, Current plate motions, *Geophys. J. Int.*, 101, 425-478.
- DeMets, C., R. G. Gordon, D. F. Argus and S. Stein, 1994, Effect of recent revisions to the magnetic reversal time scale on estimates of current plate motion, *Geophys. Res. Letts.*, 21, 2191-2194.
- Dixon, T. H., 1991, An introduction to the Global Positioning System and some geological applications, *Rev. Geophys.*, 29, 249-276.
- Dong, D. and Y. Bock, 1989, GPS network analysis with phase ambiguity resolution applied to crustal deformation studies in California, *J. Geophys. Res.*, 94, 3949-3966.
- Doser, D. I., 1986, Earthquake processes in the Rainbow Mountain-Fairview Peak-Dixie Valley, Nevada Region 1954-1959, *J. Geophys. Res.*, 91, 12572-12586.
- Doser, D., 1988, Source parameters of earthquakes in the Nevada Seismic Zone, 1915-1943, *J. Geophys. Res.*, 93, 15,001-15,015.
- Einarsson, P., 1988, On the propagation velocity of the eastern rift zone in Iceland. Paper presented at the Symposium on volcanic activity in Iceland. Reykjavik, Iceland.
- Einarsson, P., 1991, Earthquakes and present-day tectonism in Iceland, *Tectonophysics*, 189, 261-279.
- Elsasser, W. M., 1969, Convection and stress propagation in the upper mantle, in *The Application of Modern Physics to the Earth and Planetary Interiors*, edited by S. K. Runcorn, Wiley, New York, 223-246 pp.
- Eyidogan, H., 1988, Rates of crustal deformation in western Turkey as deduced from major earthquakes, *Tectonophysics*, 83-92.
- Eyidogan, H. and D. Jackson, 1985, A seismological study of normal faulting in the Demirci, Alasehir and Gediz earthquakes of 1969-70 in Western Turkey: implications for the nature and geometry of deformation in the continental crust., *Geophys J. R. Astr. Soc.*, 81, 569-607.
- Ezen, U., 1991, Crustal structure of western Turkey from Rayleigh wave dispersion, *Bull. Int. Inst. Seism. and Earthquake Engineering*, 25, 1-21.
- Fara, H. D., 1964, A new catalogue of earthquake plane solutions, *Bull. Seismol. Soc. Amer.*, 54, 1491-1518.
- Farrel, W. E., 1972, Deformation of the earth by surface loads. *Rev. Geophys.*, 10, 761-797.
- Foulger, G., R. Bilham, W. J. Morgan and P. Einarsson, 1987, The Iceland GPS geodetic field campaign 1986, *EOS*, 68, 1809-1818.

- Fiero, B., 1986, *Geology of the Great Basin*, University of Nevada Press, Reno, 198 pp.
- Foulger, G., 1988a, The Hengill triple junction, SW Iceland: 1. Tectonic structure and the spatial and temporal distribution of local earthquakes. *J. Geophys. Res.*, 93, 13493-13506.
- Foulger, G., 1988b, The Hengill triple junction, SW Iceland: 2. Anomalous earthquake focal mechanisms and implications for process within the geothermal reservoir and at accretionary plate boundaries, *J. Geophys. Res.*, 93, 13507-13523.
- Foulger, G. R., C. H. Jahn, G. Seeber, P. Einarsson, B. R. Julian and K. Heki, 1992, Post-rifting stress relaxation at the divergent plate boundary in Northeast Iceland, *Nature*, 358, 488-358.
- Foulger, G., G. Beutler, R. Bilham, P. Einarsson, S. Fankhauser, W. Gurtner, U. Hugentobler, W. J. Morgan, M. Rothacher, G. Thorbergsson, and U. Wild, 1993, The Iceland 1986 GPS geodetic survey: Tectonic goals and data processing results, *Bull. Geodetica*, 67, 148-172.
- Foulger, G. R., 1995, The Hengill geothermal area, Iceland; variation of temperature gradients deduced from the maximum depth of seismogenesis, *J. Volcan. and Geoth. Res.*, 65, 119-133.
- Frank, F. C., 1966, Deduction of earth strains from survey data, *Bull. Seismol. Soc. Am.*, 56, 35-42.
- Gosset, F. R., 1952, *Manual of Geodetic Triangulation*, Washington, DC., 205 pp.
- Gudmundsson, A., 1987, Tectonics of the Thingvellir fissure swarm, *J. of Struct. Geol.*, 9, 61-69.
- Hackman, C., 1991, A study of crustal deformation in Iceland using boundary element modelling and the GPS system, *Ph.D. Thesis*, University of Colorado, 308 pp.
- Hager, B., R. W. King and M. H. Murray, 1991, Measurement of crustal deformation using the GPS system, *Ann. Rev. Planet Sci.*, 19, 351-382.
- Harris, R. A. and R. W. Simpson, 1992, Changes in static stress on southern California faults after the 1992 Landers earthquake, *Nature*, 360, 251-254.
- Harris, R. A. and R. W. Simpson, 1993, In the shadow of 1857: an evolution of the stress changes generated by the M8 Ft. Tejon, California, earthquake, *EOS*, Fall AGU abstracts, 74, No. 43, p 427.
- Hatzfield, D., A. Christodoulou, E. Scordilis, D. Panagiotopoulos and P. Hatzidmitriou, 1987, A microearthquake study of the Mygdonian graben (N. Greece), *Earth and Planet. Sci. Lett.*, 81, 379-396.
- Haskell, N. A., 1935, The motion of a viscous fluid under a surface load, *Physics*, 6, 265-269, 1935.
- Heki, K., G. Foulger, O. Alp and M. Ergun, 1989, GPS Campaign in Southwest Turkey- data analysis, *University of Durham-Internal Report*, 1991.
- Heki, K., 1992, A network adjustment program for the Bernese Global Positioning System data analysis software, *J. Geod. Soc. Jap.*, 38, 309-312.
- Heki, K., G. R. Foulger, B. Julian and C. H. Jahn, 1993, Plate dynamics near divergent boundaries: Geophysical implications of post-rifting crustal deformation in NE Iceland., *J. Geophys. Res.*, 14, 14279-14297.
- Hill, D. P., P. A. Reasenber, A. Michael, W. J. Arabaz, G. Beroza, D. Brumbaugh, J. N. Brune, R. Castro, S. Davis, D. dePolo, W. L. Ellsworth, J. Gomberg, S. Harmsen, L. House, S. M. Jackson, M. J. S. Johnston, L. Jones, R. Keller, S. Malone, L. Munguia, S. Nava, J. C. Pechmann, A. Sanford, R. W. Simpson, R. B. Smith, M. Stark, M. Stickney, A. Vidal, A. Walter, V. Wong, J.

- Zollweg, 1993, Seismicity remotely triggered by the Magnitude 7.3 Landers, California, earthquake, *Science*, 260, 1617-1623, 1993.
- Holdahl, S. R., 1981, A model of temperature stratification for correction of levelling refraction, *Bull. Geod.*, 55, 231-249.
- Holdahl, S. R., 1982, Recomputation of vertical crustal motions near Palmdale, California, *J. Geophys. Res.*, 87, 9374-9388.
- Hofton, M. A., 1995, Anelastic surface deformation in Iceland detected using GPS, with special reference to isostatic rebound and the 1975-1985 Krafla rifting episode, Ph. D. thesis, University of Durham, 259 pp.
- Hughes, T. J. R. and R. L. Taylor, 1978, Unconditionally stable algorithms for quasi-static elasto/viscoplastic finite element analysis., *Comput. Struct.*, 8, 169-173.
- Jackson, D. D., 1972, Interpretation of inaccurate, insufficient and inconsistent data., *Geophys. J. R. Astron. Soc.*, 28, 97-109.
- Jackson, J. A., J. Gagnepain, G. Houseman, G. C. P. King, P. Papadimitriou, C. Soufleris and J. Virieux, 1982, Seismicity, normal faulting, and the geomorphological development of the Gulf of Corinth (Greece): the Corinth earthquakes of February and March 1981, *Earth Planet. Sci. Lett.*, 57, 377-397.
- Jackson, J. and D. McKenzie, 1983, The geometrical evolution of normal fault systems, *J. of Structural Geology*, 5, 471-482.
- Jackson, J. and D. McKenzie, 1988, The relationship between plate motions and seismic moment tensors, and the rates of active deformation in the Mediterranean and Middle East, *Geophys. J. Int.*, 93, 45-73.
- Jackson, J., J. Haines and W. Holt, 1988, The horizontal velocity field in the deforming Aegean Sea region determined from the moment tensors of earthquakes, *J. Geophys. Res.*, 93, 17,657-17,684.
- Jackson, J. A. and N. White, 1989, Normal faulting in the upper continental crust: observations from regions of active extension, *J. of Struct. Geol.*, 11, 15-36.
- Jacobson, R. S. and P. R. Shaw, 1991, Using the F-test for eigenvalue decomposition problems to find the statistically 'optimal' solution., *Geophys. Res. Letters*, 18, 1075-1078.
- Jahn, C. H., G. Seeber, G. R. Foulger and P. Einarsson, 1994, GPS epoch measurements across the mid-Atlantic plate boundary in northern Iceland 1987-1990. Proceedings, IUGG XX General Assembly, Vienna, 11-24th August 1991.
- Jahn, C.-H., G. Seeber, G.R. Foulger and A. Bjornsson, 1989, A GPS survey in the north-east volcanic zone of Iceland 1987. First results. Proceedings, International Association of Geodesy, Symposium 101, Edinburgh, Scotland, 173-181.
- Jaumé, S. C. and L. R. Sykes, 1992, Change in the state of stress on the southern San Andreas fault resulting from the California earthquake sequence of April to June, *Science* 258, 1325-1328.
- King, G. C. P., R. S. Stein and J. Lin, 1994, Static stress changes and the triggering of earthquakes, *Bull. Seismol. Soc. Amer.*, 84, 935-953
- Kuo, J. T., R. C. Jachens, M. Ewing and G. White, 1970, Transcontinental tidal gravity profile across the United States, *Science*, 168, 968-971.

- Kirby, S. H., 1983, Rheology of the lithosphere, *J. Geophys. Res.*, 89, 3177-3192.
- Kissel, C. and C. Laj, 1988, The Tertiary geodynamical evolution of the Aegean arc; a paleomagnetic reconstruction, *Tectonophysics*, 146, 183-201.
- Lachenbruch, A. H. and J. H. Sass, Models of an extending lithosphere and heat flow in the Basin and Range province, in *Cenozoic tectonics and regional geophysics of the western cordillera*, edited by R. B. Smith and J. P. Eaton, Geological Society of America, 209-250.
- Lanczos, C., 1961, *Linear Differential Operators*, D. Van Nostrand, Princeton, 564 pp.
- Larson, K. and D. Agnew, 1991, Application of the Global Positioning System to Crustal Deformation Measurement, 1, Precision and Accuracy, *J. Geophys. Res.*, 96, 16,547-16,566.
- Le Pichon, X. and J. Angelier, 1978, The Hellenic arc and trench system; a key to the neotectonic evolution of the eastern Mediterranean area, *Tectonophysics*, 60, 1-42.
- Le Pichon, X., N. Chamot-Rooke, P. Huchon and P. Luxey, 1993, Implications des nouvelles mesures de géodesie spatiale en Grèce et en Turquie sur l'extrusion latérale de l'Anatolie et de l'Egée, *C. R. Acad. Sci. Paris, t. 316, Série II*, 983-990.
- Lisowski, M., J. C. Savage and W. H. Prescott, 1991, The velocity field along the San Andreas fault in central and southern California, *J. Geophys. Res.*, 96, 8369-8389.
- Lyzenga, G. A., A. Raefsky and S. G. Mulligan, 1991, Models of recurrent strike-slip earthquake cycles and the state of crustal stress, *J. Geophys. Res.*, 96, 21,623-21,640.
- Makris, J., 1976, A dynamical model of the Hellenic Arc deduced from geophysical data, *Tectonophysics*, 36, 339-346.
- Makris, J., 1978, Some geophysical considerations on the geodynamic situation in Greece, *Tectonophysics*, 46, 251-268.
- Marshall, G. A., R. S. Stein and W. Thatcher, 1991, Faulting geometry and slip from coseismic elevation changes: The 18 October 1989, Loma Prieta, California, earthquake, *Bull. Seismol. Soc. Amer.*, 81, 1660-1693.
- Mansinha, L. and D. E. Smylie, 1971, The displacement fields on inclined faults, *Bull. Seismol. Soc. Amer.* 61, 1,433-1,440.
- McKenzie, D., 1978, Active tectonics of the Alpine-Himalayan belt: the Aegean Sea and surrounding regions, *Geophys. J.R. Astr. Soc.*, 55, 217-54.
- Meister, L. J., 1967, Seismic refraction study of Dixie Valley Nevada,, in *Geophysical study of Basin-Range Structure, Dixie Valley Region, Nevada*, edited by G. A. Thompson, U.S. Air Force Cambridge Res. Lab. Spec. Rep. 66-848, 1-72.
- Melosh, H. J. and A. Raefsky, 1980, The dynamical origin of subduction zone topography., *Geophysics J.R. Astr. Soc.*, 60, 333-354.
- Melosh, H. J. and A. Raefsky, 1981, A simple and efficient method for introducing faults into finite element computations, *Bull. Seismol. Soc. Amer.*, 71, 1391-1400.
- Melosh, J. and A. Raefsky, 1983, Anelastic response to a dip-slip earthquake, *J. Geophys. Res.*, 88, 515-526,.
- Menke, W., 1984, *Geophysical Data Analysis: Discrete Inverse Theory*, Academic Press Inc., 260 pp.

- Miller, R. W., 1967, Earthquake movement study in the vicinity of Fallon, Nevada, *U.S. Coast and Geodetic Survey*, Report 564, 45 pp.
- Minster, J. B. and T. H. Jordan, 1987, Vector constraints on western U.S. Deformation from space geodesy, neotectonics, and plate motions, *J. Geophys. Res.*, 92, 4798-4804.
- Moffitt, F. H. and H. Bouchard, 1987, *Surveying*, Harper Collins, New York, pp 876.
- Möller, D. and B. Ritter, B 1980, Geodetic measurements and horizontal crustal movements in the rift zone of NE-Iceland, *J. Geophys.*, 47, 110-119.
- Murray, M. H., J. C. Savage, M. Lisowski and W. K. Gross, 1993, Coseismic displacements: 1992 Landers, California, earthquake, *Geophys. Res. Lett.*, 20, 623-626.
- Noomen, R. B., A. C. Ambrosius and K. F. Wakker, Crustal motions in the Mediterranean region determined from laser ranging to LAGEOS, in *Contributions of Space Geodesy to Geodynamics: Crustal Dynamics*, edited by Smith, D. E. and D. L. Turcotte, American Geophysical Union, Washington, D.C., 331-346.
- Nur, A. and G. Mavko, 1974, Postseismic viscoelastic rebound, *Science*, 183, 204-206.
- Okada, Y., 1992, Internal deformation due to shear and tensile faults in a half-space, *Bull. Seismol. Soc. Amer.*, 82, 1018-1040.
- Okaya, D. A. and G. E. Thompson, 1985, Geometry of Cenezoic extensional faulting: Dixie Valley, Nevada, *Tectonophysics*, 4, 107-125.
- Oppenheimer, D. H., P. A. Reasenberg and R. W. Simpson, 1988, Fault plane solutions for the 1984 Morgan Hill, California, earthquake sequence: Evidence for the state of stress on the Calaveras fault, *J. Geophys. Res.*, 93, 9007-9026.
- Oral, B., R. E. Reilinger, N. Toksoz, A. A. Barka and I. Kinik, 1993, Preliminary results of 1988 and 1990 GPS Measurements in Western Turkey and their Tectonic Implications, in *Contributions of Space Geodesy to Geodynamics: Crustal Dynamics*, edited by Smith, D. E. and D. L. Turcotte, American Geophysical Union, Washington, D.C., 407-416
- Oral, B. M., 1995a, Global Positioning System (GPS) measurements in Turkey (1988-1992): Kinematics of the Africa-Arabia-Eurasia Plate collision zone, Ph.D. Thesis, M.I.T., 344 pp.
- Oral, B. M., R. E. Reilinger, M. N. Toksoz, R. W. King, A. A. Barka, I. Kinik and O. Lenk, 1995b, Global Positioning System offers evidence of plate motions in the eastern Mediterranean, *EOS Trans. AGU*, 76, 9-1.
- Page, B. M., 1965, Preliminary geologic map of part of the Stillwater Range, Nevada: Map 28.
- Palmason, G., 1971, Crustal structure of Iceland from explosion seismology, *Soc. Sci. Islandica*, 40, 187 pp.
- Paton, S., 1992, Active normal faulting, drainage patterns and sedimentation in southwestern Turkey, *Jour. of the Geol. Soc. of London*, 149, 1031-1044.
- Press, F., 1965, Displacements, strains and tilts at tele-seismic distances, *J. Geophys. Res.*, 70, 2395-2412.
- Proffet, J. M., Jr., 1977, Cenozoic implications of the Yerington district, Nevada, and implications for the nature and origin of Basin and Range faulting, *Geol. Soc. Am. Bull.*, 88, 247-266.

- Reasenber, P. A. and R. W. Simpson, 1992,. Response of regional seismicity to the static stress change produced by the Loma Prieta earthquake, *Science*, 255, 1687-1690.
- Reilinger, R., 1984, Coseismic and postseismic vertical movements associated with the 1940 M7.1 Imperial Valley, California, earthquake, *J. Geophys. Res.*, 89, 4531-4537.
- Reilinger, R., 1986, Evidence for postseismic viscoelastic relaxation following the 1959 M=7.5 Hebgen Lake, Montana, Earthquake, *J. Geophys. Res.*, 91, 9488-9494.
- Reilinger, R. and S. Larsen, 1986, Vertical crustal deformation associated with the 1979 M=6.6 Imperial Valley, California earthquake: Implications for fault behavior, *J. Geophys. Res.*, 91, 14044-14056.
- Rice, J. R., 1992, Fault stress states, pore pressure distributions, and the weakness of the San Andreas fault, in *Fault Mechanics and Transport Properties of Rock*, B. Evans and T.-F. Wong, Academic Press, London, 475-503.
- Roeloffs, E. A., 1988, Fault stability changes induced beneath a reservoir with cyclic variations in water level, *J. Geophys. Res.*, 93, 2107-2124.
- Rocken, C., 1988, The Global Positioning System: A new tool for tectonic studies., *Ph.D. Thesis*, University of Colorado,
- Romney, C., 1957, Seismic waves from the Dixie Valley-Fairview Peak earthquakes, *Bull. Seismol. Soc. Am.*, 47, 301-309.
- Rothacher, M., G. Beutler, T. Schildknecht and U. Wild, 1990, *Bernese GPS Software Version 3.2*, University of Bern.
- Sæmundsson, K., 1986, Subaerial volcanism in the western north Atlantic. In *The western North Atlantic region, The Geology of North America*, edited by Vogt P. R. and B. E. Tucholke, 69-84.
- Savage, J. C. and R. O. Burford, 1970, Accumulation of tectonic strain in California, *Bull. Seismol. Soc. Amer.*, 60, 1877-1896.
- Savage, J. C. and J. P. Church, 1974, Evidence for postearthquake slip in the Fairview Peak, Dixie Valley, and Rainbow Mountain Fault Areas of Nevada, *Bull. Seismol. Soc. Amer.*, 64, 687-698.
- Savage, J. C. and W. H. Prescott, 1978, Geodimeter measurements and the Southern California uplift, *Earthquakes and Volcanoes*, 10, 131-135.
- Savage, J. C. and L. M. Hastie, 1969, A dislocation model for the Fairview Peak, Nevada, earthquake, *Bull. Seismol. Soc. Amer.*, 59, 1937-1948.
- Savage, J. C., 1983, A dislocation model of strain accumulation and release at a subduction zone, *J. Geophys. Res.*, 88, 4984-4996.
- Savage, J. C., 1990, Equivalent strike-slip earthquake cycles in half-space and lithosphere-asthenosphere earth models, *J. Geophys. Res.*, 95, 4873-4879.
- Savage, J. C., M. Lisowski, W. Prescott and M. A. Pitt, 1993, Deformation from 1973 through 1987 in the epicentral area of the 1959 Hebgen lake, Montana, earthquake ($M_s=7.5$), *J. Geophys. Res.*, 98, 2145-2153.
- Schaffer, F., 1900, Das Meanderthalen vorn 20 September 1899, *Mittewist Klass Geographische Gestalt*, 43, 221-231.
- Schuh, H. and L. Moehlmann, 1989, Ocean loading station displacements observed by VLBI, *Geophys. Res. Lett.*, 16, 1105-1108.

- Scholz, C. H., C. Aviles and S. Wesnousky, 1986, Scaling differences between large intraplate and interplate earthquakes, *Bull. Seismol. Soc. Amer.*, 76, 65-70.
- Scholz, C. H., 1990, *The Mechanics of Earthquakes and Faulting*, Cambridge University Press, 439 pp.
- Schwartz, D. P. and Coppersmith, K. J., 1984, Fault behavior and characteristic earthquakes; Examples from the Wasatch and San Andreas fault zones, *J. Geophys. Res.*, 89, 5681-5698.
- Schwiderski, E. W., 1980, Ocean tides, parts 1 and 2: Global ocean tidal equations, *Marine Geodesy*, 3, 161-255.
- Seiler, R. L. and K. K. Allander, 1993, Water-level changes and directions of ground-water flow in the shallow aquifer, Fallon area, Churchill County, Nevada, *USGS Water-Resources Investigation*, No. 93-4118.
- Sengor, A. M. C., N. Gorur and F. Saroglu, 1985, Strike-slip faulting and related basin formation in zones of tectonic escape: Turkey as a case study, in *Strike-slip Faulting and Basin Formation*, *Soc. Econ. Paleontol. and Mineral*, edited by K. T. Biddle and N. Christie-Blick, vol. Spec. Pub. 37, 227-64.
- Sigmundsson, F., P. Einarsson and R. Bilham, 1992, Magma chamber deflation recorded by the Global Positioning System - the Hekla 1991 eruption, *Geophys. Res. Lett.*, 14, 1483-1486.
- Sigmundsson, F., P. Einarsson, R. Bilham and E. Sturkell, 1995, Rift-transform kinematics in south Iceland: Deformation from Global Positioning System measurements, 1986 to 1992, *J. Geophys. Res.*, 100, 6235-6248.
- Simpson, R. W. and P. A. Reasenber, 1994, Static stress changes on central California faults produced by the Loma Prieta earthquake, *U.S. Geol. Surv. Prof. Paper* P 1550-F, F55-F89.
- Slemmons, D. B., 1957, The Dixie Valley - Fairview Peak, Nevada, earthquakes of December 16, 1954: geological effects., *Bull. Seismol. Soc. Amer.*, 47, 353-376.
- Smith, D. E., R. Kolenkiewicz, J. W. Robbins, P. Dunn and M. H. Torrence, 1994, Horizontal crustal motion in the central and eastern Mediterranean inferred from Satellite Laser Ranging measurements, *Geophys. Res. Letters*, 21, 1979-1982.
- Smith, R. B. and R. L. Bruhn, 1984, Intraplate extensional tectonics of the eastern Basin and Range; Inferences on structural style from seismic reflection data, regional tectonics, and thermal-mechanical models of brittle/ductile deformations, *J. Geophys. Res.*, 89, 5733-5762.
- Smith, R. B., W. C. Nagy, K. A. Julander, J. J. Viveiros, C. A. Barker and D. G. Gants, 1989, Geophysical and tectonic framework of the eastern Basin and Range-Colorado Plateau-Rocky Mountain transition, in *Geophysical Framework of the Continental United States*, edited by L. C. Pakiser and W. D. Mooney, The Geological Society of America, Memoir 172, 205-234.
- Snay, R., M. W. Cline and E. L. Timmerman, 1985, Dislocation models for the 1954 earthquake sequence in Nevada, *USGS Open File Report*, No. 85-290.
- Sovers, O. J., 1994. Vertical loading amplitudes from VLBI measurements, *Geophys. Res. Lett.*, 21, 357-360.
- Stefansson, R. and P. Halldorsson, 1987, Strain release and strain build-up in the south Iceland seismic zone, *Tectonophysics*, 152, 276-276.

- Stein, R. S., 1981, Discrimination of tectonic displacement from slope-dependent errors in geodetic levelling from southern California, 1953-1979, in *Earthquake Prediction - An International Review*, D. W. Simpson and P. G. Richards, Maurice Ewing Series 4, AGU, 441-456.
- Stein, R. S. and M. Lisowski, 1983, The 1979 Homestead Valley earthquake sequence, California: Control of aftershocks and postseismic deformation, *J. Geophys. Res.*, 88, 6477-6490.
- Stein, R. S. and S. E. Barrientos, 1985, Planar high-angle faulting in the Basin and Range: Geodetic analysis of the 1983 Borah Peak, Idaho, earthquake, *J. Geophys. Res.*, 86, 11,355-11,366.
- Stein, R. S., C. T. Whalen, S. R. Hodhal, W. E. Strange and W. Thatcher, 1986, Saugus - Palmdale, California, field test for refraction error in historical levelling surveys, *J. Geophys. Res.*, 91, 9031 - 9044.
- Stein, R. S., G. C. P. King and J. Lin, 1992, Change in failure stress on the southern San Andreas fault system caused by the 1992 Magnitude = 7.4 Landers earthquake, *Science*, 258, 1328-1332.
- Steketee, J.A., On Volterra's dislocations in a semi-infinite elastic medium, *Can. J. Phys.*, 36, 192-205.
- Stewart, J. H., Basin and Range structure: A system of horsts and grabens produced by deep-seated extension, *Geol. Soc. Am. Bull.*, 82, 1019-1044, 1971.
- Stock, J. M. and J. H. Healy, 1988, Stress field at Yucca Mountain, Nevada, *U.S. Geol. Surv. Bull.*, 87-93.
- Taymaz, T., J. Jackson and D. McKenzie, 1991, Active tectonics of the north and central Aegean Sea, *Geophys. J. Int.*, 106, 433-490.
- Taymaz, T., 1993, The source parameters of the Cubukdag (W. Turkey) earthquake of 1986 October 11, *Geophys. J. Int.*, 113, 260-267.
- Thatcher, W., 1979, Systematic inversion of geodetic data in central California, *J. Geophys. Res.*, 84, 2283-2295.
- Thatcher, W., T. Matsuda, T. Kato and J. Rundle, 1980, Lithospheric loading by the 1896 Riku-U earthquake, Northern Japan: Implications for plate flexure and asthenospheric rheology., *J. Geophys. Res.*, 85, 6429-6435.
- Thatcher, W. and J. B. Rundle, 1984, A viscoelastic coupling model for the cyclic deformation Due to periodically repeated earthquakes at subduction zones, *J. Geophys. Res.*, 89, 7631-7640.
- Thatcher, W., 1990, Present-day crustal movements and the mechanics of cyclic deformation, in *The San Andreas fault System, California*, edited by R. E. Wallace, U.S. Geol. Surv. Prof. Paper, 1515, 189-206.
- Thompson, G. A., 1966, The rift system of the western United States, in *The World Rift System*, Geological Survey of Canada, Paper 66-14, 280-290.
- Thompson, G. A. and D. B. Burke, 1973, Rate and Direction of spreading in Dixie Valley, Basin and Range Province, Nevada, *Geol. Soc. Am. Bull.*, 84.
- Thompson, G. A., R. Catchings, E. Goodwin, S. Holbrook, C. Jarchow, C. Mann, G. McGarthy and D. Okaya, Geophysics of the western Basin and Range Province, 1989, in *Geophysical Framework of the Continental United States*, The Geological Society of America, edited by L. C. Pakiser and W. D. Mooney, Memoir 172, pp.

- Tocher, D., 1956, Geologic setting of the Fallon-Stillwater earthquakes of 1954, *Bull. Seismol. Soc. Amer.*, 10-14.
- Tryggvason, E., 1982, Recent ground deformation in continental and oceanic rift zones, in *Continental and Oceanic Rifts*, edited by Palmason, G., Geodynamics Series, 8, 17-29.
- Tryggvason, E., 1984, Widening of the Krafla fissure swarm during the 1975-1981 volcano-tectonic episode, *Bull. Volcanologique*, 47, 47-69.
- Tryggvason, E., 1990, Displacement of the Almanagja fault, in Icelandic, *Nord. Volcanol. Inst.*, No. 9001.
- Turcotte, D. L. and G. Schubert, 1982, *Geodynamics, Applications of continuum physics to geological problems*, John Wiley & Sons, Inc., 450 pp.
- Wallace, R. E., 1984, Patterns and timing of late Quaternary faulting in the Great Basin province and relation to some tectonic features, *J. Geophys. Res.*, 89, 5763-5769.
- Wallace, R. E. and R. A. Whitney, 1984, Late quaternary history of the Stillwater Seismic Gap, Nevada, *Bull. Seismol. Soc. Amer.*, 74, 301-314.
- Ward, S., 1990, Pacific-North America plate motions: New results from Very Long Baseline Interferometry, *J. Geophys. Res.*, 95, 21,965-21,981.
- Wells, D., 1987, Guide to GPS Positioning, *Canadian GPS Associates*, Fredericton, New Brunswick.
- Wernicke, B. and B. C. Burchfiel, 1982, Modes of extensional tectonics, *J. Struct. Geol.*, 4, 105-115.
- Whitten, C. A., 1957, Geodetic measurements in the Dixie Valley area, *Bull. Seismol. Soc. Amer.*, 47, 321-325.
- Willden, R. and R. Speed, 1974, Geology and mineral deposits of Churchill County, Nevada, Map.
- Zoback, M. L., 1989, State of stress and deformation in the northern Basin and Range Province, *J. Geophys. Res.*, 94, 7105-7128.
- Zoback, M. L. and M. D. Zoback, 1980, State of stress in the conterminous United States, *J. Geophys. Res.*, 85, 6113-6156.

APPENDIX 1

HENGILL GPS POINT DESCRIPTIONS

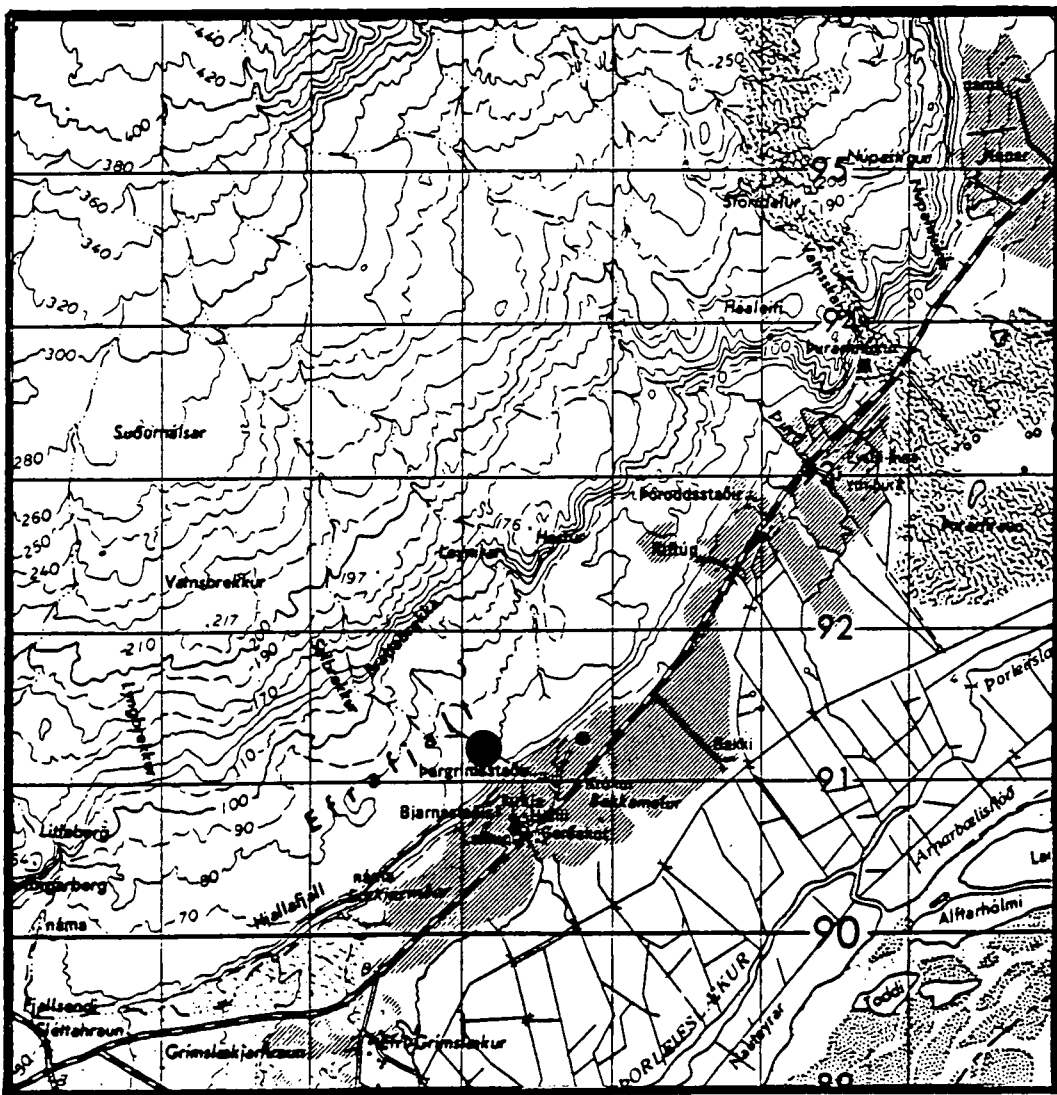
NAME: BJARNASTADIR

POINT INSCRIPTION: OS - 1991 - DU02

WGS 84 CO-ORDINATES: Lat: 63 56 44.58386
Long: -21 18 8.82331
Height: 120.1438 m

DESCRIPTION: From Reykjavik go east on #1 to Hveragerdi. Turn right, to the south, on #38 and drive 8.5 km to a signpost to Laekur and Bjarnistadir. Take the fork signposted Laekur. Walk to the top of the cliff along a path then go about 270 m north. The point is in flat outcrop in a stream bed which is dry in August. A cairn is built over the point.

ACCESSIBILITY: Two wheel drive + 25 minute walk



1 cm = 500 m

NAME : **BRAEDRABOL**

POINT INSCRIPTION: OS - 1991 - DU03

WGS 84 CO-ORDINATES: Lat: 63 57 5.26230
Long: -21 6 21.75426
Height: 120.1444 m

DESCRIPTION: Follow the lane leading to the farmhouse Braedrabol from #1. The point is on a small hill opposite the farmhouse, on the other side of the track. The hill is 50m from the track and has a distinct shape of two peaks. The point is placed between the two peaks on flat bedrock. It is marked by a small cairn.

ACCESSIBILITY: Two wheel drive + 100 m walk

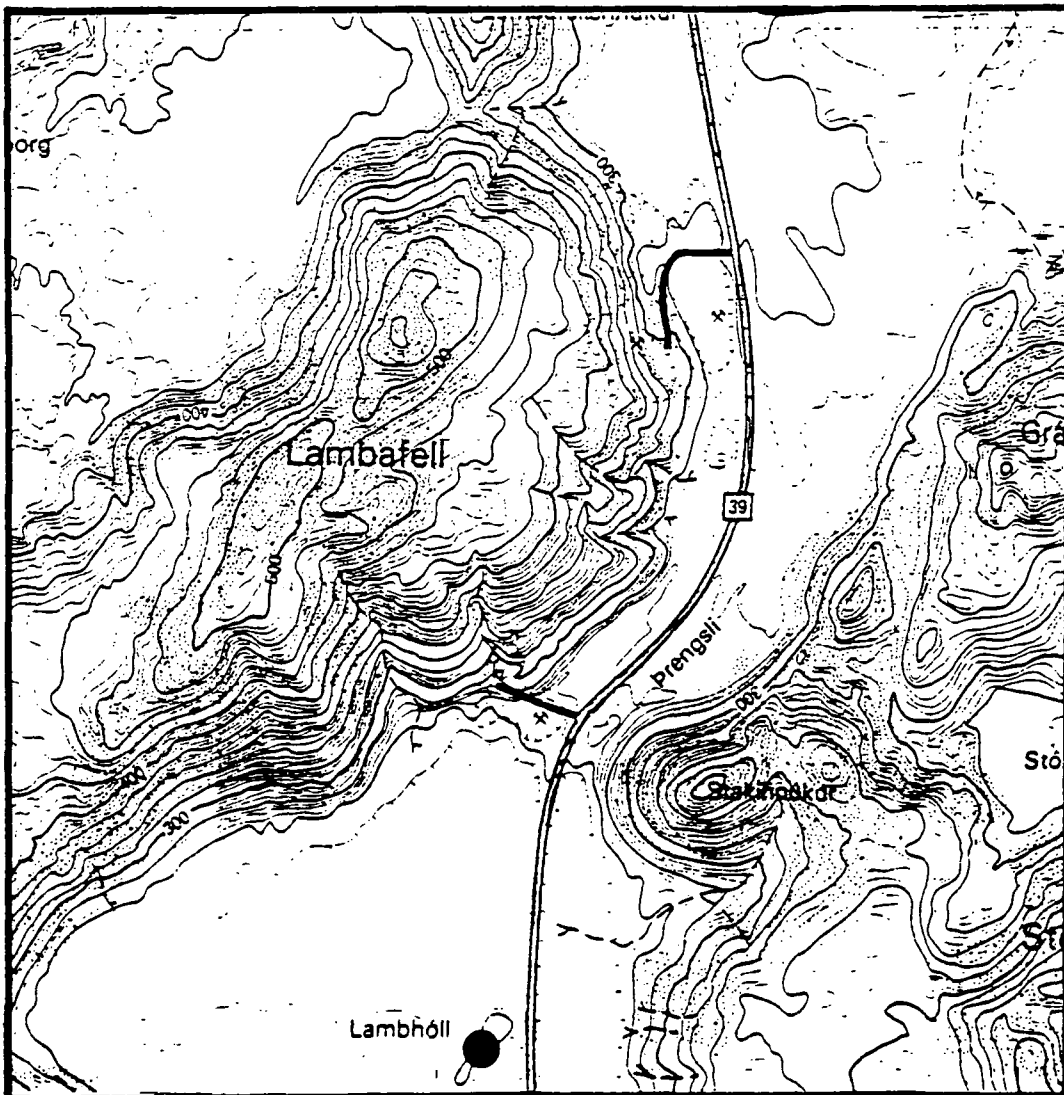


1 cm = 500 m

NAME: LAMBAFELL
POINT INSCRIPTION: OS - 1991 - DU04
WGS 84 CO-ORDINATES: Lat: 64 0 3.53248
Long: -21 27 48.55570
Height: 332.2599 m

DESCRIPTION: The point is placed on the south-west end of a hill called Lambaholt, which is 3 km along #39 from the junction of #1 and #39, and, 150m's to the west of #39. It is placed in tuff on the southerly brow of the hill and marked with a cairn.

ACCESSIBILITY: Two wheel drive + 50 m walk



1 cm = 210 m

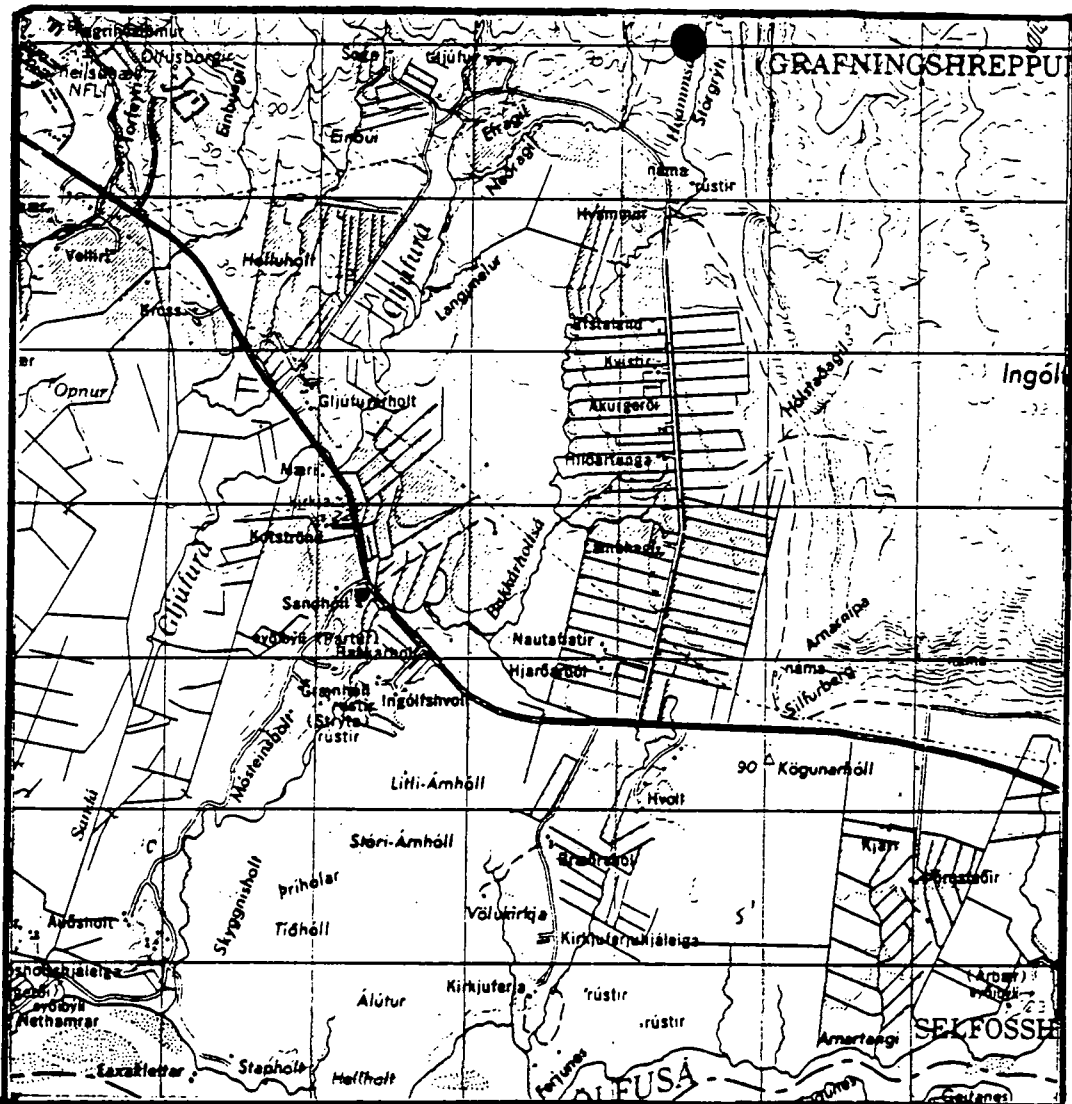
NAME: **AEDAGIL**

POINT INSCRIPTION: OS - 1991 - DU06

WGS 84 CO-ORDINATES: Lat: 63 59 54.38761
Long: -21 5 46.08683
Height: 186.1043 m

DESCRIPTION: Follow #374 off #1 from Reykjavik, north past the farm Gljufur. As the road bends south-east there is a small track which enters a field and runs northwards over Grafningshals. Drive 0.7 km along the track and uphill. The point is placed on the first bedrock outcrop on the hillside. It is 30 m to the east of the track and marked by small cairn.

ACCESSIBILITY: Four wheel drive



1 cm = 500 m

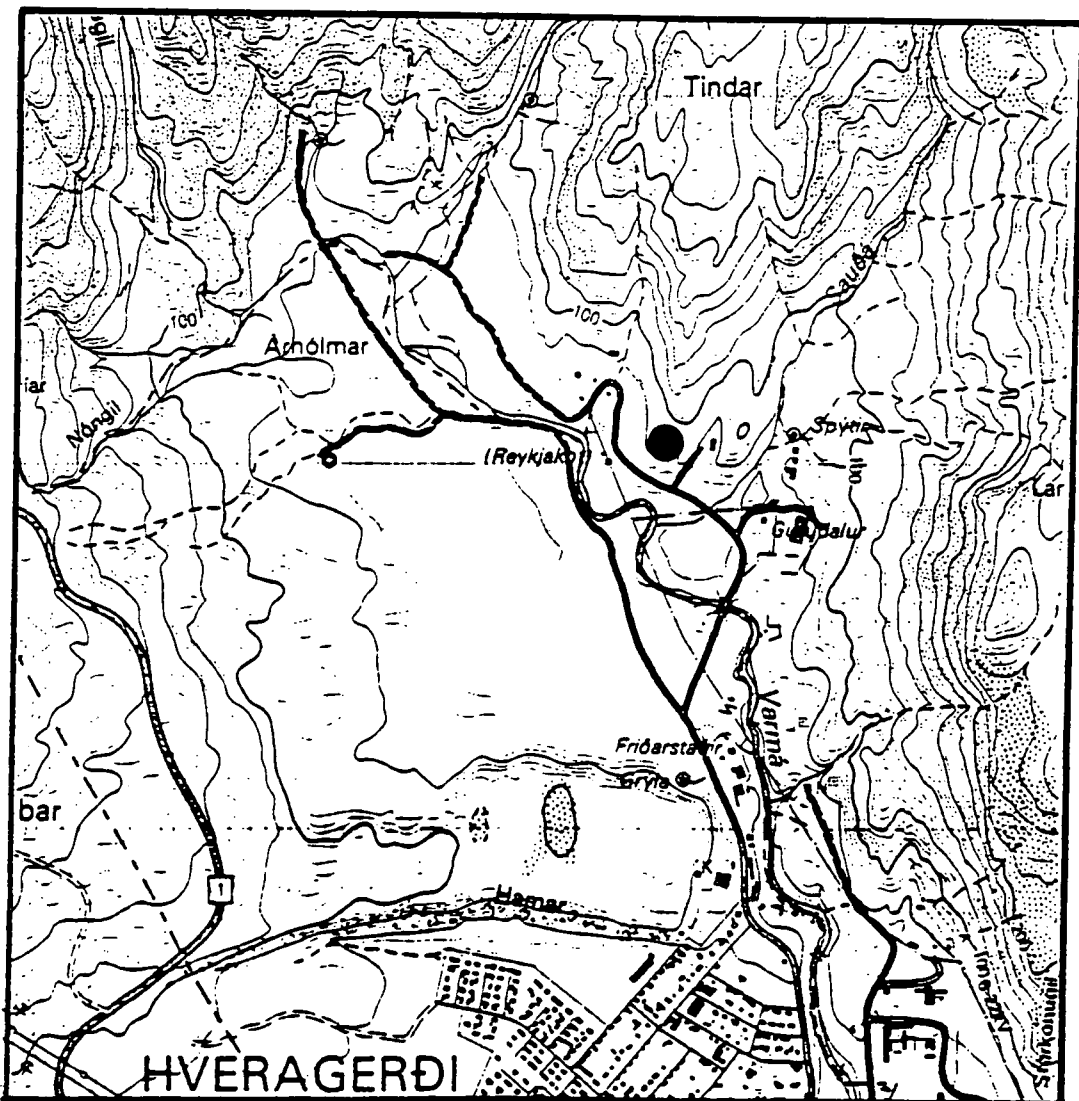
NAME: TINDAR

POINT INSCRIPTION: OS - 1991 - DU07

WGS 84 CO-ORDINATES: Lat: 64 1 5.01438
Long: -21 11 34.37055
Height: 155.2207 m

DESCRIPTION: From Hveragerdi take the road which leads to Gufudalur crossing the river Varma. After passing the turn off to Gufudalur take the next turn off to the right. This track leads to a chicken house. Climb the steep hill to the west beside the wire fence and continue for another 75 m. The point is marked by a cairn.

ACCESSIBILITY: Two wheel drive



1 cm = 210 m

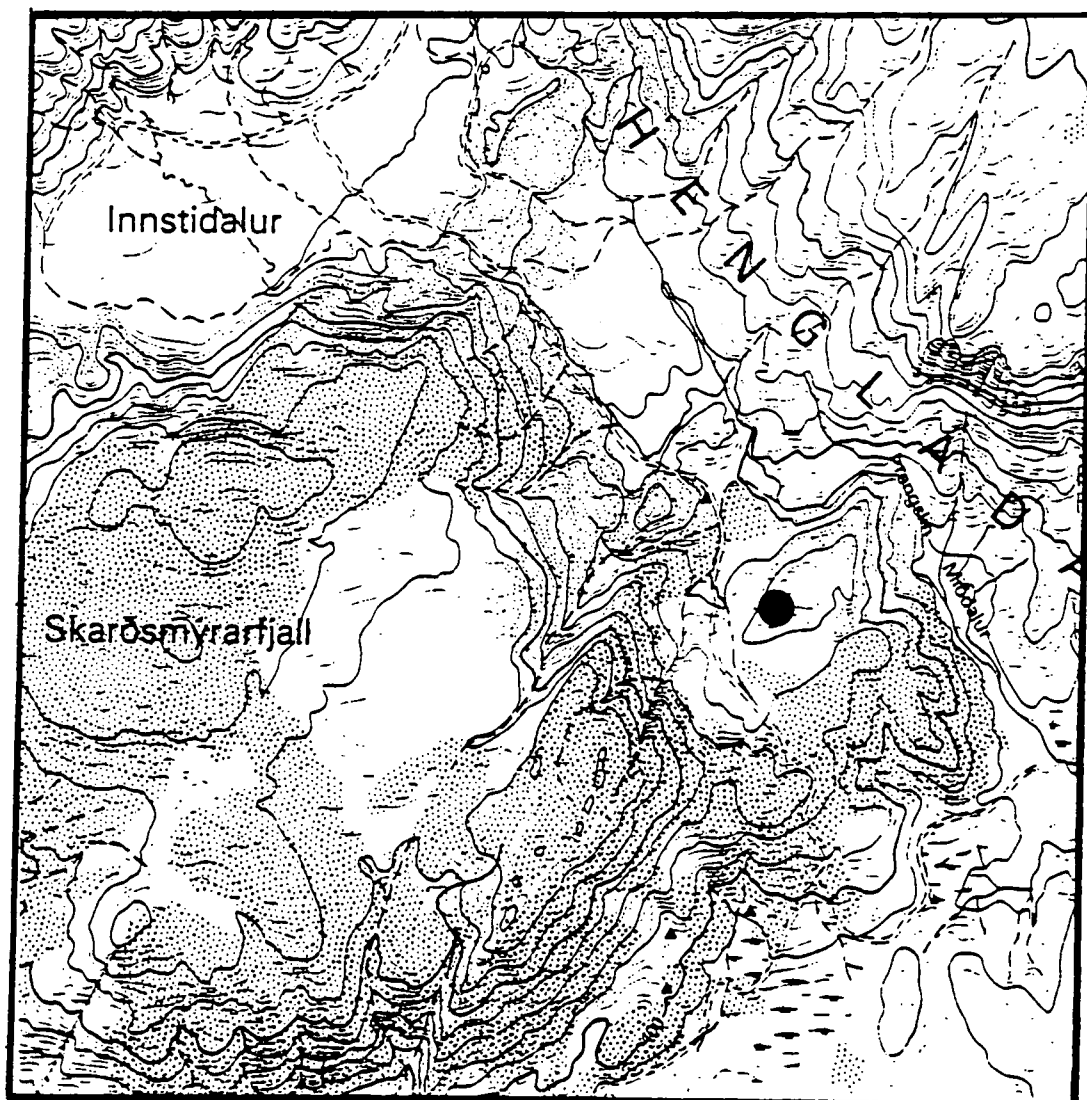
NAME: SKARDSMYRAFJALL

POINT INSCRIPTION: OS - 1991 - DU13

WGS 84 CO-ORDINATES: Lat: 64 3 12.52612
Long: -21 18 57.20390
Height: 516.4662 m

DESCRIPTION: Join the "Vegur milli hrauns og Hida ", at the Ski-lodge in Hveradalir (Skidaskali i Hveradolum). Travel along this road for 6.2 km. You will reach an electricity pylon after 3.4 km and a junction after another 2.8 km. At this junction take the track to the left, (the other leads to Fremstadalur). Drive 0.8 km along this road into a small valley. The point is approximately 165m to the right up a steep hill, this is the highest hill in the valley. It is 5m from the highest peak of the hill and is marked by a cairn.

ACCESSIBILITY: Four wheel drive



1 cm = 210 m

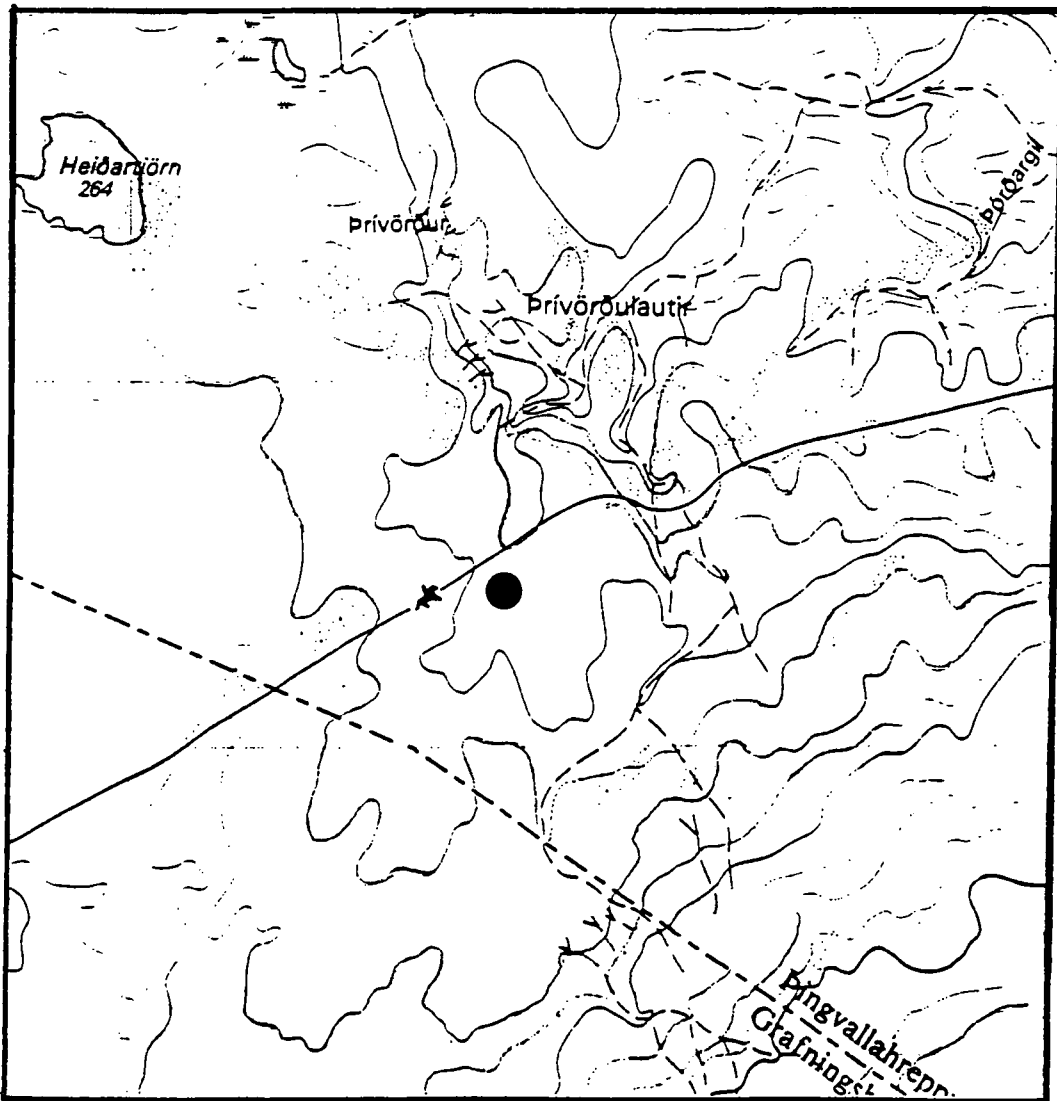
NAME: **THRIVORDUR**

POINT INSCRIPTION: OS - 1991 - DU15

WGS 84 CO-ORDINATES: Lat: 64 11 28.56094
Long: -21 19 56.84229
Height: 324.7884 m

DESCRIPTION: Take the south-west running track which leaves the #360 1.25 km after passing the road to Heidarbeal. Travel along this track in a south-west direction for 2.4 km, the track then veers north-west but continue on a smaller track for another 3.3 km in a south-west direction. After 3.3 km you will reach a 1.5 m high cairn which is unique in that a brick sticks out at right angles about 1 m up. The point is 110 m past this and 6 m from the road on the right. It is on a flat round basalt outcrop which is 3 m in diameter.

ACCESSIBILITY: Four wheel drive



1 cm = 210 m

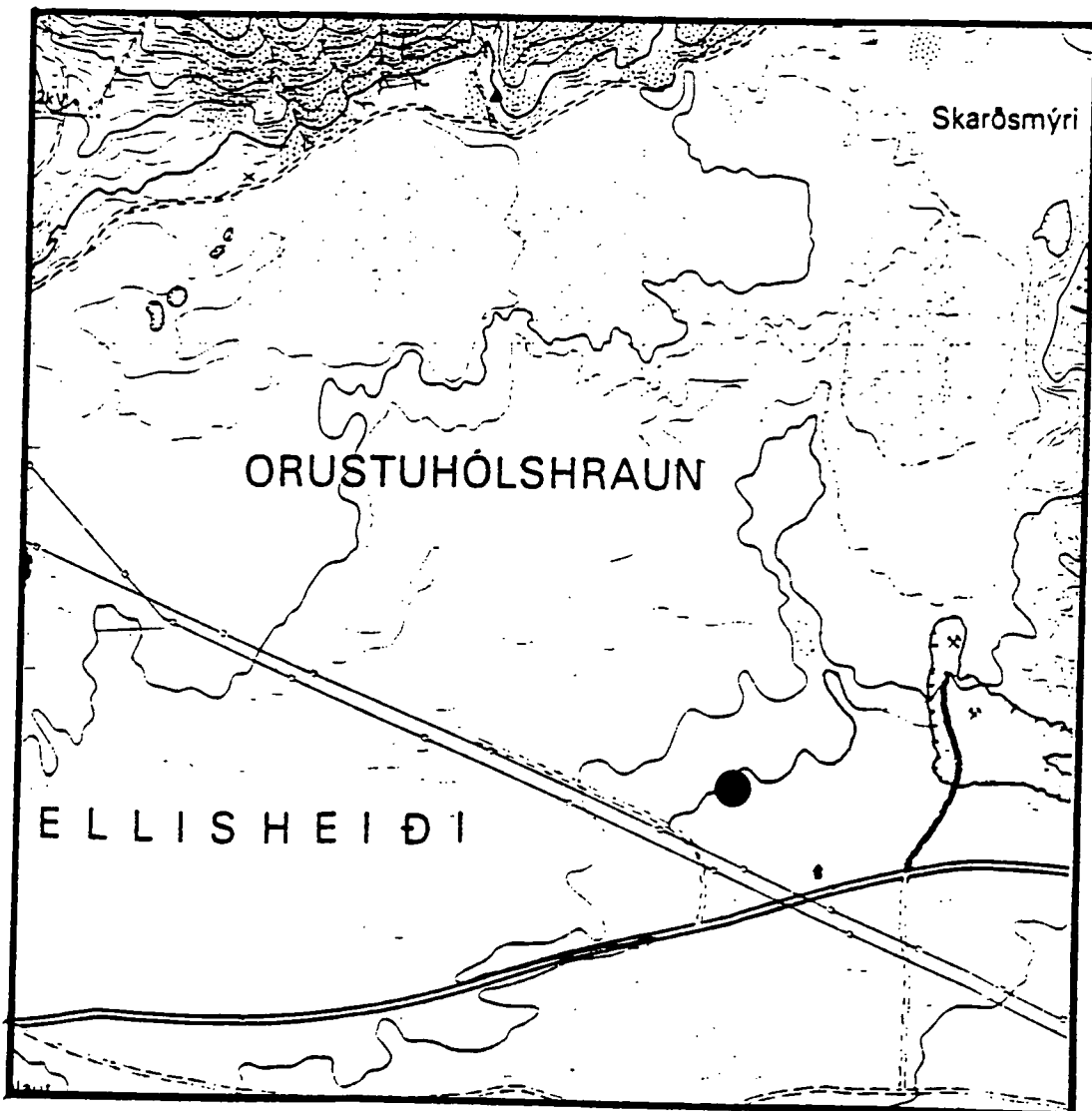
NAME: HELLISHEIDI

POINT INSCRIPTION: OS - 1991 - DU16

WGS 84 CO-ORDINATES: Lat: 64 1 28.80673
Long: -21 19 9.79677
Height: 421.3098 m

DESCRIPTION: Drive east on #1 along Hellisheidi until you reach a rescue hut on the north side of the road, The power lines cross the road here. There are two lines of tall cairns one trending northerly, the other trending north-easterly. Walk along the northerly line until you arrive at the seventh cairn. The point is 45 m further north and then 14 m west on a flat outcrop of pahoehoe lava. The point is marked with a small cairn.

ACCESSIBILITY: Two wheel drive + 200 m walk



1 cm = 210 m

NAME:

GIGIR

POINT INSCRIPTION:

OS - 1991 - DU17

WGS 84 CO-ORDINATES:

Lat: 64 1 58.98692

Long: -21 21 59.67744

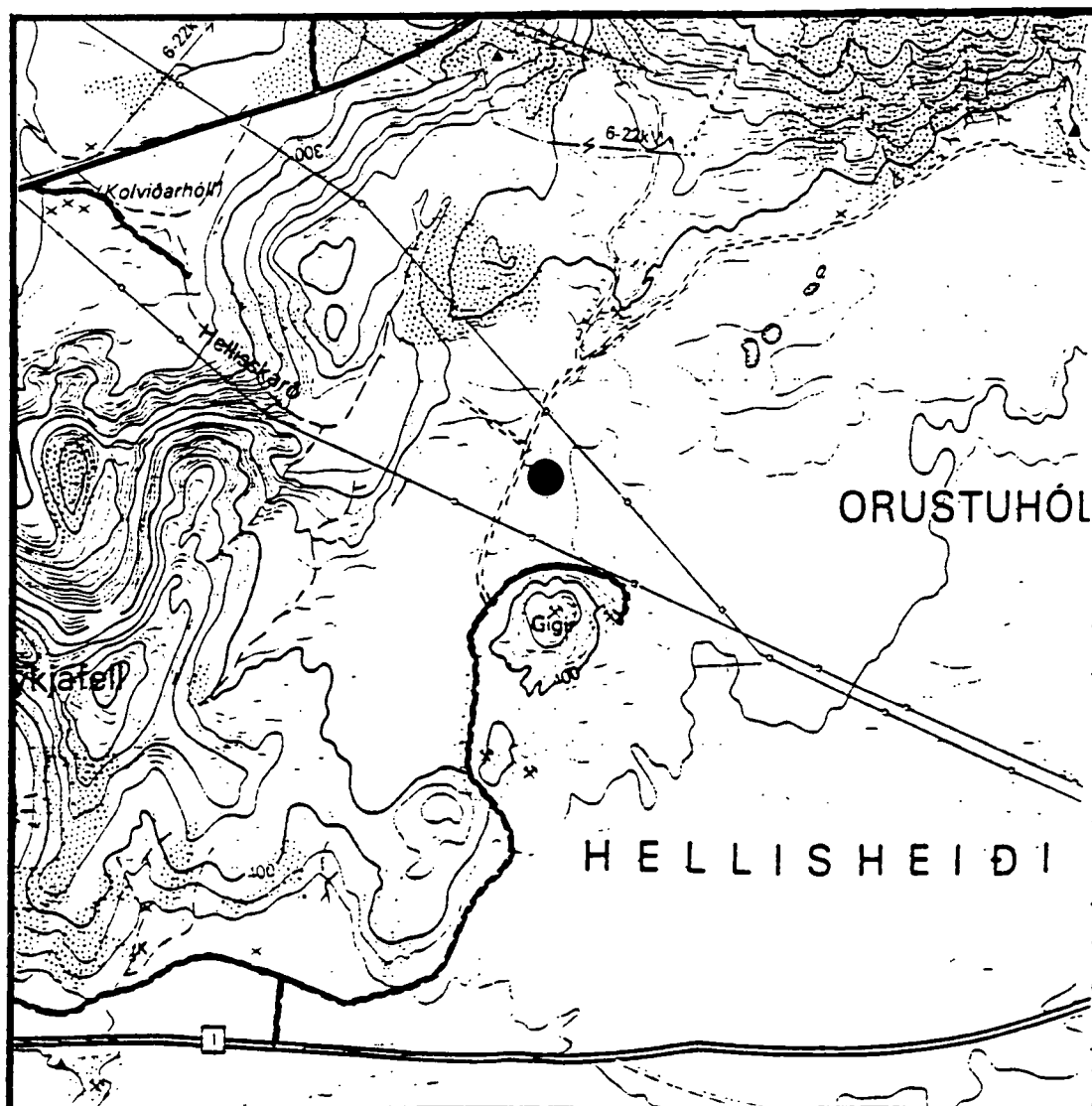
Height: 453.8239 m

DESCRIPTION:

Take #1 from Reykjavik. After the turn off for #417 continue along #1 for 12 km. Join the "vegur milli hrauns og Hida" at the ski lodge in Hveradalir (Skidaskalinn i Hveradolum). Drive 3.3 km along the road until you reach a junction which is 120 m before an electricity pylon. Turn off the road down the track to the right, going eastwards, and go 25 m along the track. The point is placed 6m south of the track on a 1.5 m high lava hillock which is to the left of a larger lava dome. It is marked by a cairn.

ACCESSIBILITY:

Four wheel drive



1 cm = 210 m

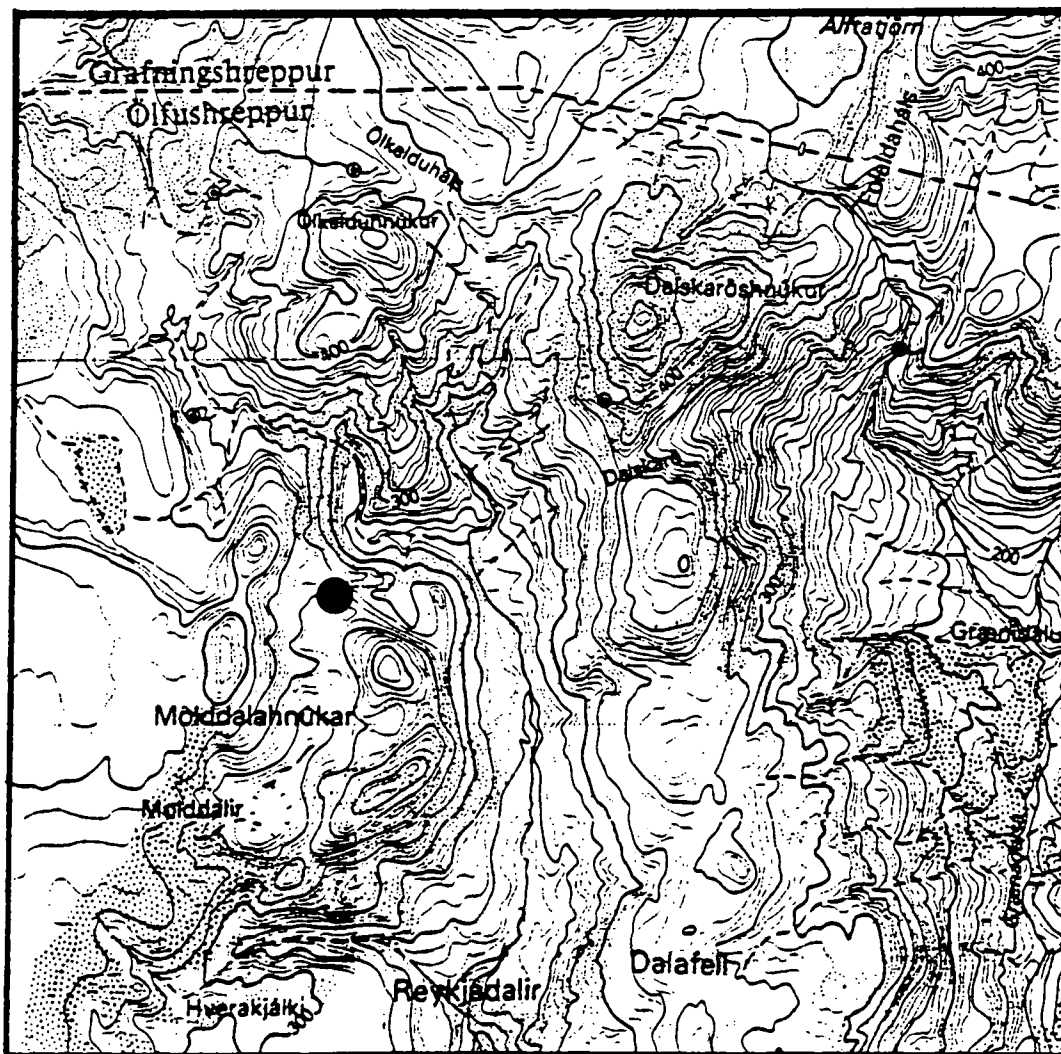
NAME: KLAMBRAGIL

POINT INSCRIPTION: OS - 1991 - DU18

WGS 84 CO-ORDINATES: Lat: 64 2 52.74540
Long: -21 13 49.09403
Height: 404.9480 m

DESCRIPTION: Take #1 from Reykjavik. After the turn off for #417 continue along #1 for 12 km. Join the "vegur milli hrauns og Hida" at the ski lodge in Hveradalir (Skidaskalinn i Hveradolum). Drive 7 km along this road to the turn off for Skardsmyrafjall. Drive another 4.6 km, the road enters a plain and crosses the river Hengladalsa as it flows south. After crossing the river follow the track until you reach a cairn. From the cairn follow the track which runs east along the edge of Bitra for 2 km, the road leads to the hill Moldahnukar. Walk along the westerly face of this hill and go between the pass of this and the neighbouring hill. The point is on a flat outcrop about 4m from the edge of the cliff which overlooks the gorge Klambragil. It is marked by a cairn.

ACCESSIBILITY: Four wheel drive + 2 km walk



1 cm = 210 m

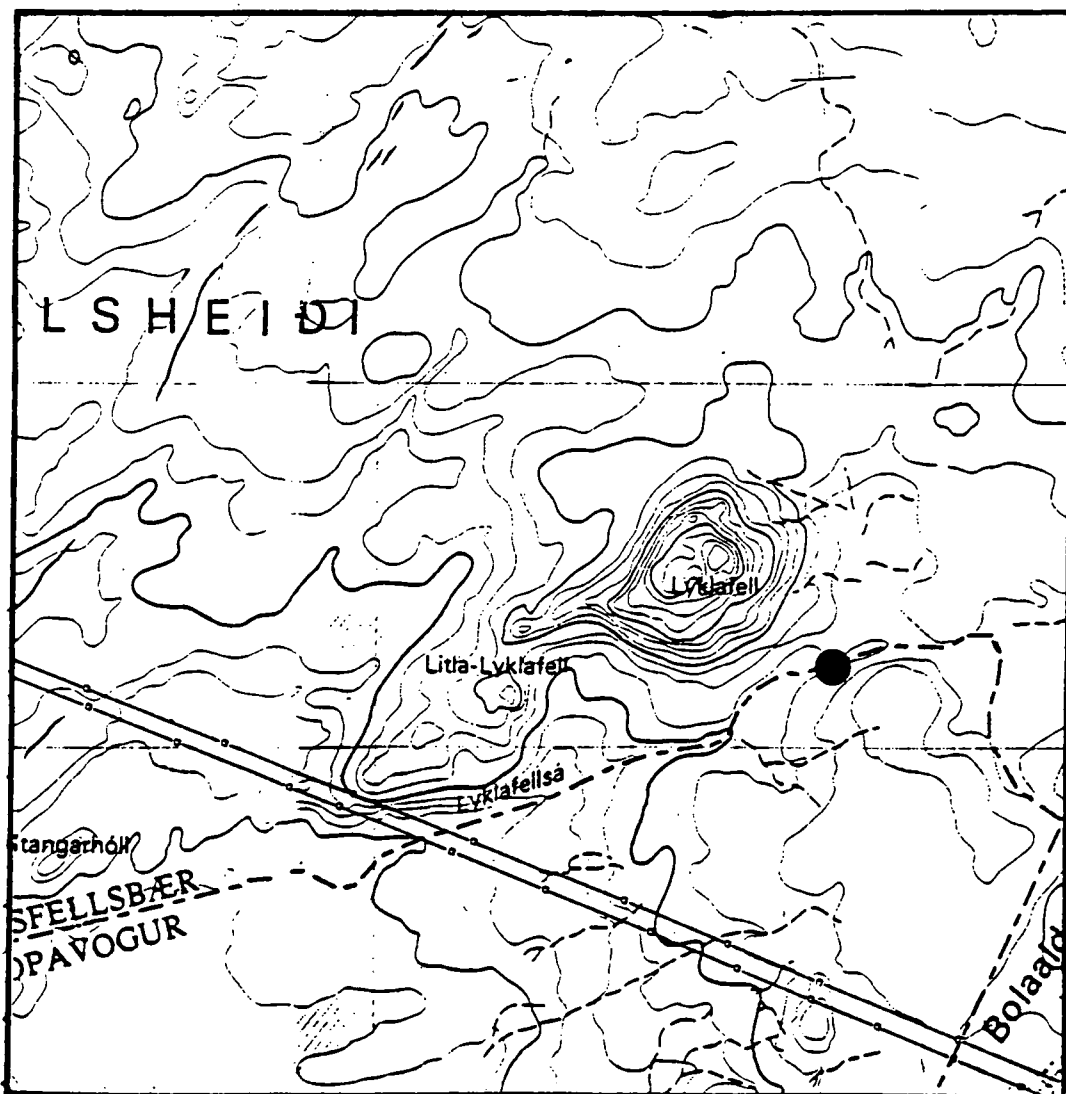
NAME: LYKLAFELL

POINT INSCRIPTION: OS - 1991 -DU20

WGS 84 CO-ORDINATES: Lat: 64 4 52.46037
Long: -21 31 38.19600
Height: 268.9407 m

DESCRIPTION: The hill Lyklafell is accessed by a track which leads off #1 from Reykjavik. The track runs north along the east side of Lyklafell. Drive along this track for 3.9 km to the most northerly crag. The point is 50 m to the east of the track. It is on a basalt pavement with glacial scratch marks. The pavement runs along a river bed.

ACCESSIBILITY: Two wheel drive + 30 m walk



1 cm = 210 m

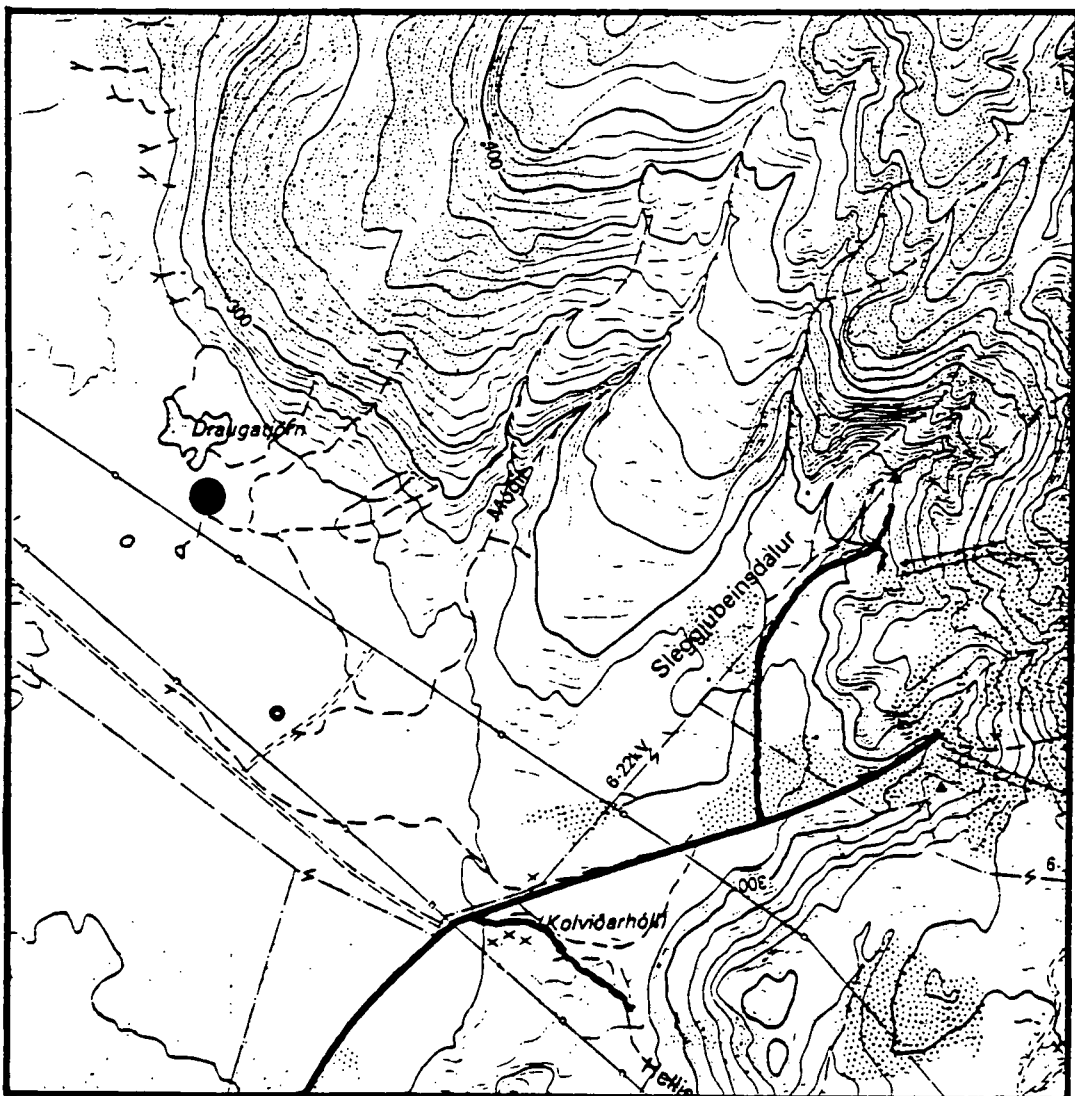
NAME: DRAUGATJORN

POINT INSCRIPTION: NE - 79 - 037

WGS 84 CO-ORDINATES: Lat: 64 3 0.33790
Long: -21 24 43.08658
Height: 320.4250 m

DESCRIPTION: Turn off #1 from Reykjavik to follow the road which runs along Stora-Reykjafell. After 2.2 km, just before you reach an electricity pylon, take the road which runs north-west parallel to the line of electricity pylons. After 1.5 km turn onto a northward running track which leaves the road between the fifth and sixth pylons. The track veers to the west after passing under the overhead power lines, leave the track at this point and continue 100 m north until you reach a hillock of pahoehoe lava. The point is placed here and is marked by a cairn, which is easily visible from 100 m.

ACCESSIBILITY: Two wheel drive



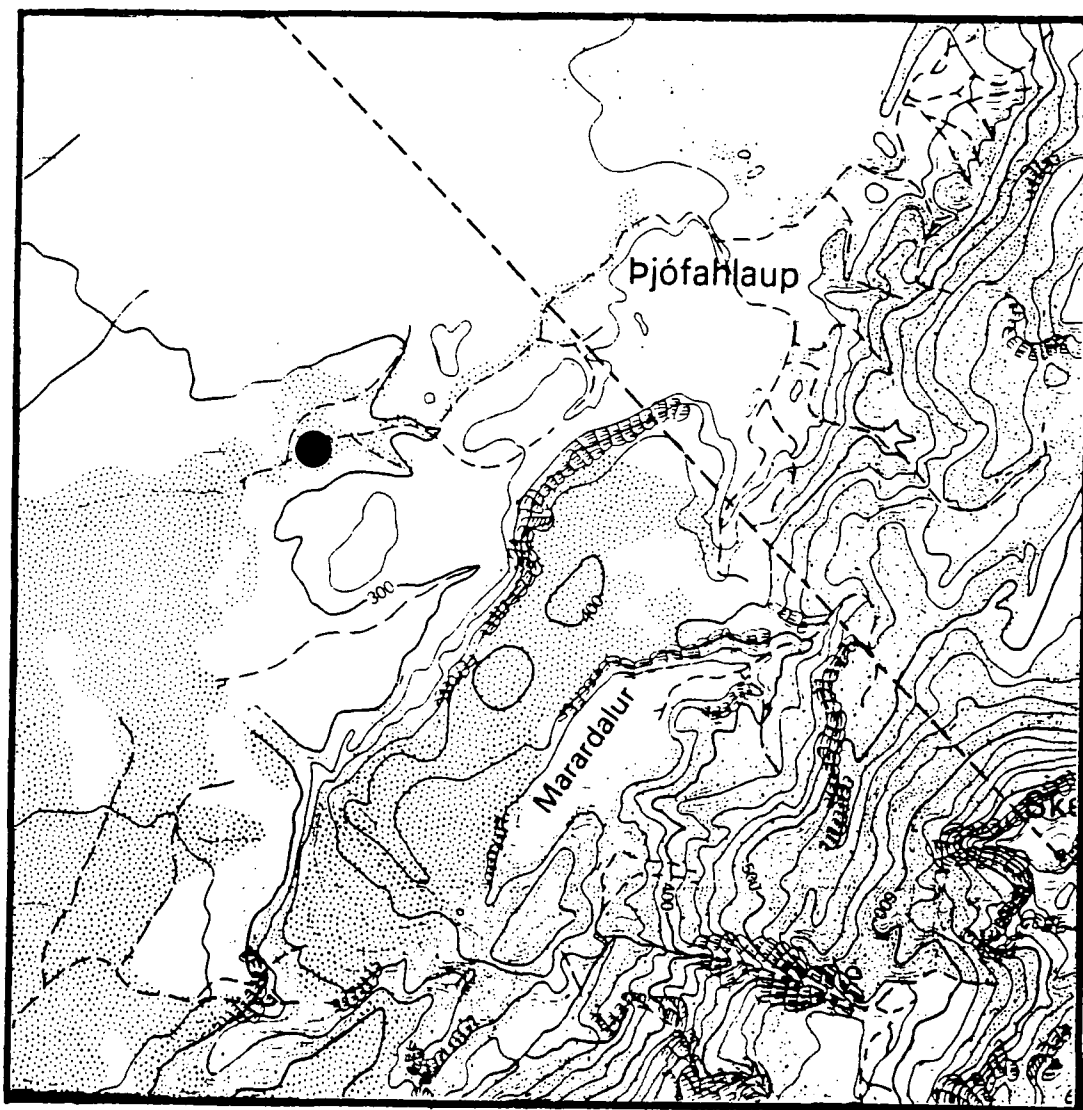
NAME: MARADULAR

POINT INSCRIPTION: OS - 1991 - DU21

WGS 84 CO-ORDINATES: Lat: 64 6 0.57519
Long: -21 21 40.41254
Height: 362.0413 m

DESCRIPTION: Take #431 off #1 from Reykjavik after 4.5 km along this road you will come to a junction. A signpost points to Hafravatnsleid, Mosfellsheidi, and Geithals. Take the road to Mosfellsheidi, drive along this road parallel to the pipeline for 15.3 km. Stop about 30 m before you come to the part of the pipe where snow mobiles can cross, marked by orange signposts. The point is marked by a cairn.

ACCESSIBILITY: Two wheel drive + 3 km walk.



1 cm = 210 m

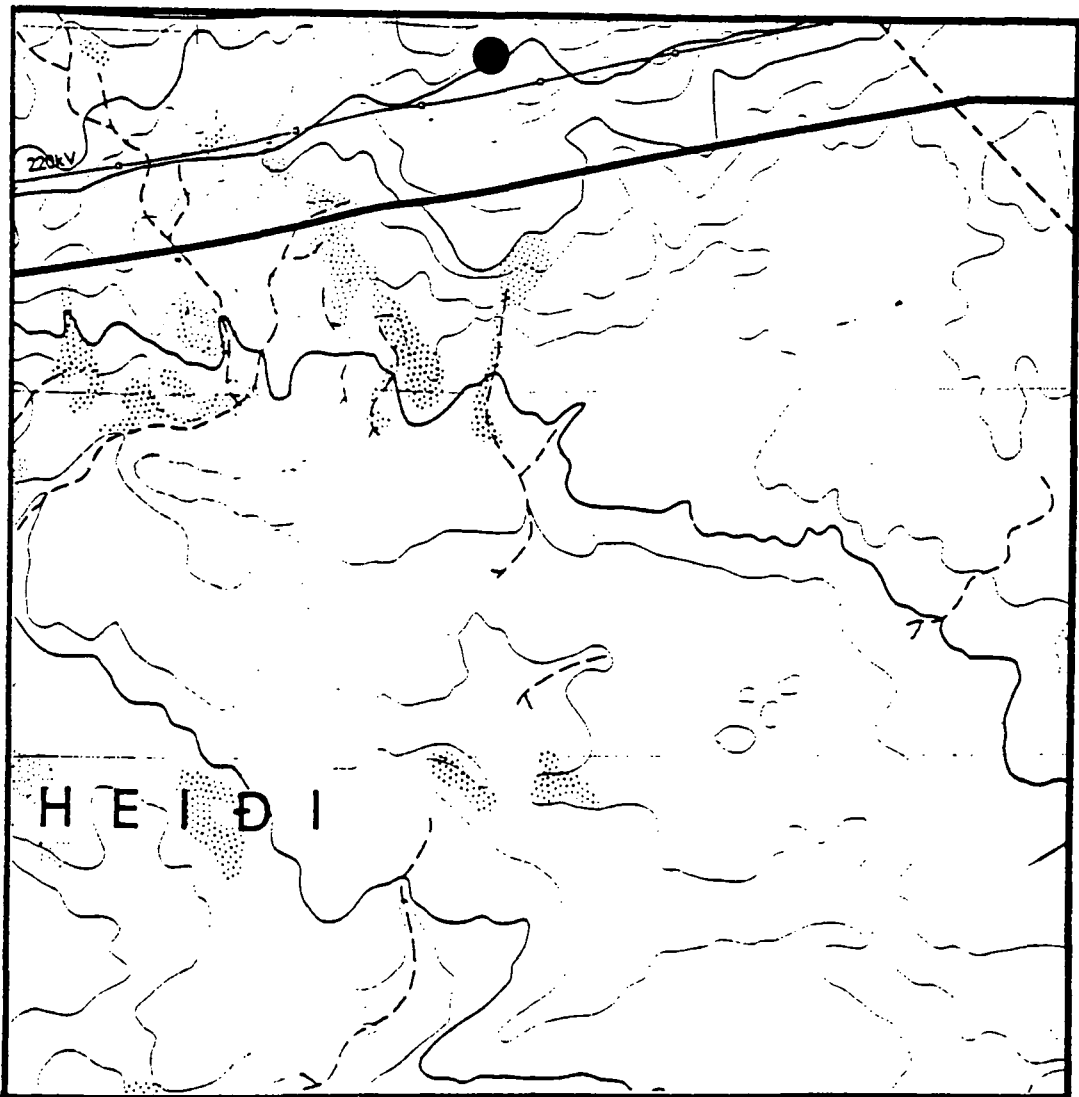
NAME: EITURHOLL

POINT INSCRIPTION: OS - 1991 - DU22

WGS 84 CO-ORDINATES: Lat: 64 7 16.39491
Long: -21 24 57.74655
Height: 392.5632 m

DESCRIPTION: Take #431 off #1 from Reykjavik after 4.5 km along this road you will come to a junction. A signpost points to Hafravatnsleid, Mosfellsheidi, and Geithals. Take the road to Mosfellsheidi, drive along this road, parallel to the pipeline for 12.1 km. Park by a large dog kennel shaped hut built over the pipeline. The point is 50 m north of the pipeline on the highest point of 1 m high basalt outcrop which can be seen from the road.

ACCESSIBILITY: Two wheel drive + 30 m walk



1 cm = 210 m

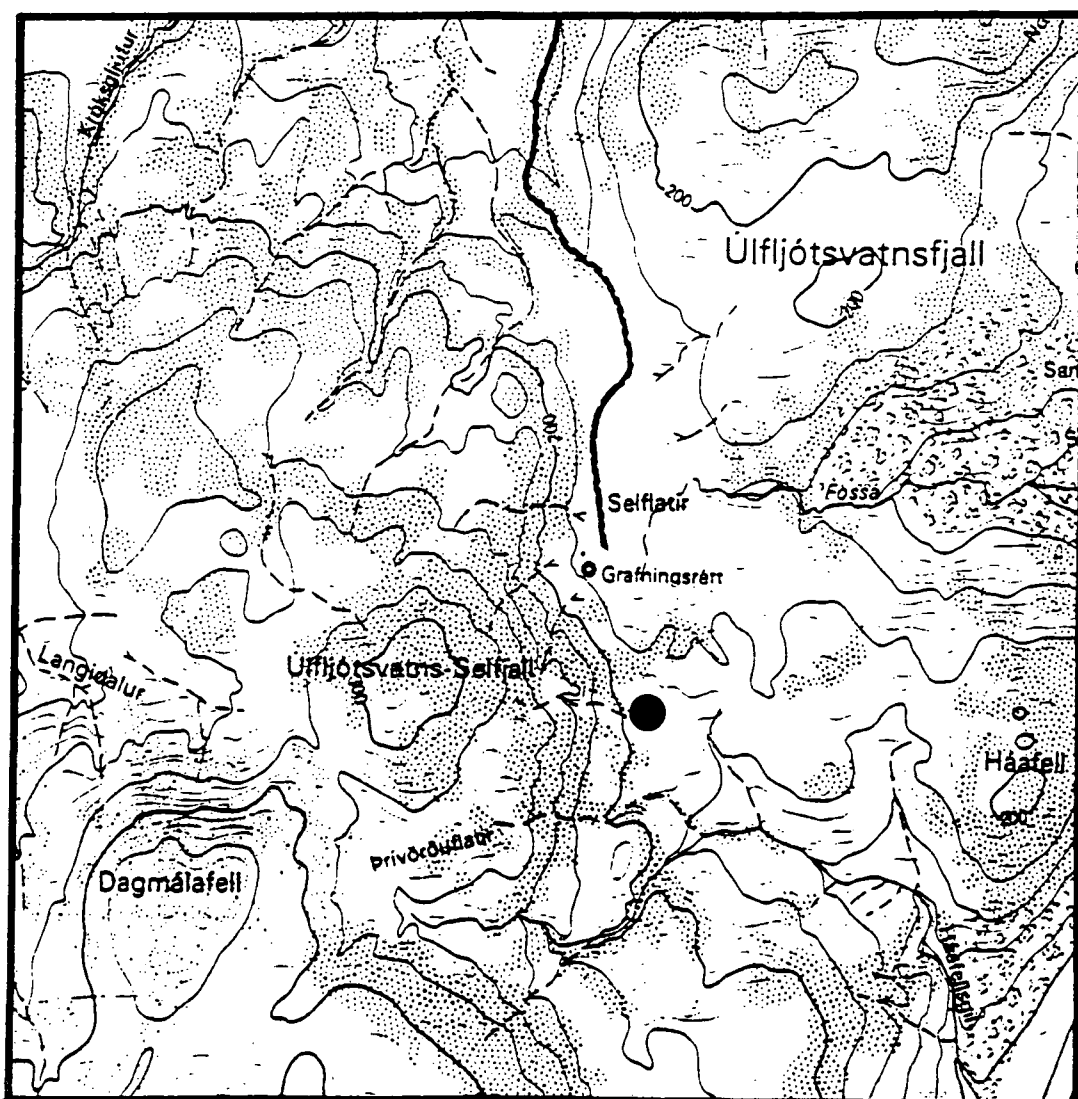
NAME: SELFLATIR

POINT INSCRIPTION: OS - 1991 -DU26

WGS 84 CO-ORDINATES: Lat: 64 4 35.65922
Long: -21 5 12.13848
Height: 271.5341 m

DESCRIPTION: From #360 take the track which leads to the Grafningsrett sheepfold and drive 3.3 km. You will reach the sheep fold and hut. Go through a gate and continue driving south along the track for 0.4 km. Park at the bottom of a dirt gully. The point is 125 m west of the track on the southerly end of a 50 m long north-south trending hill. A cairn is built to mark the site.

ACCESSIBILITY: Four wheel drive.



1 cm = 210 m

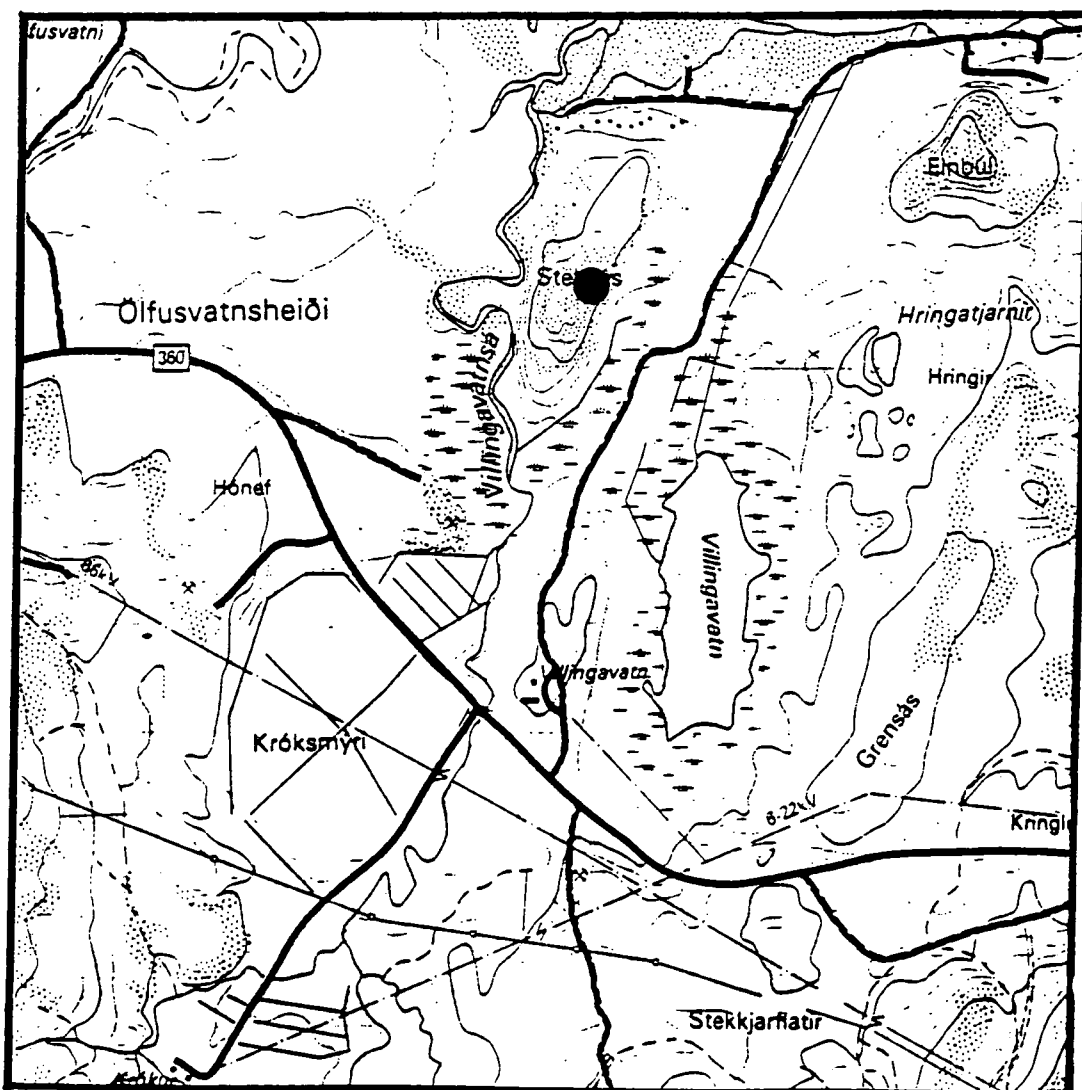
NAME: VILLINGAVATN

POINT INSCRIPTION: OS - 1991 - DU27

WGS 84 CO-ORDINATES: Lat: 64 7 5.59779
Long: -21 5 30.04738
Height: 193.5497 m

DESCRIPTION: Take the lane to Villangavatn from #360. Drive 1.6 km along this lane. It then bends to the right but you must continue into the field in front. Parallel to the road, to the western side, are 20 m high cliffs of the hill Stekkas. The northerly part of the eastern face is a grassy slope, climb the grassy slope and about 10 m to the south-west are 2 m high boulders. These are the highest points on this part of the hill. The point is 10m due west of these boulders. It is on a flat smooth whale-back shaped bedrock which is 2 m in diameter. It is marked by a cairn.

ACCESSIBILITY: Four wheel drive + 50 m walk



1 cm = 210 m

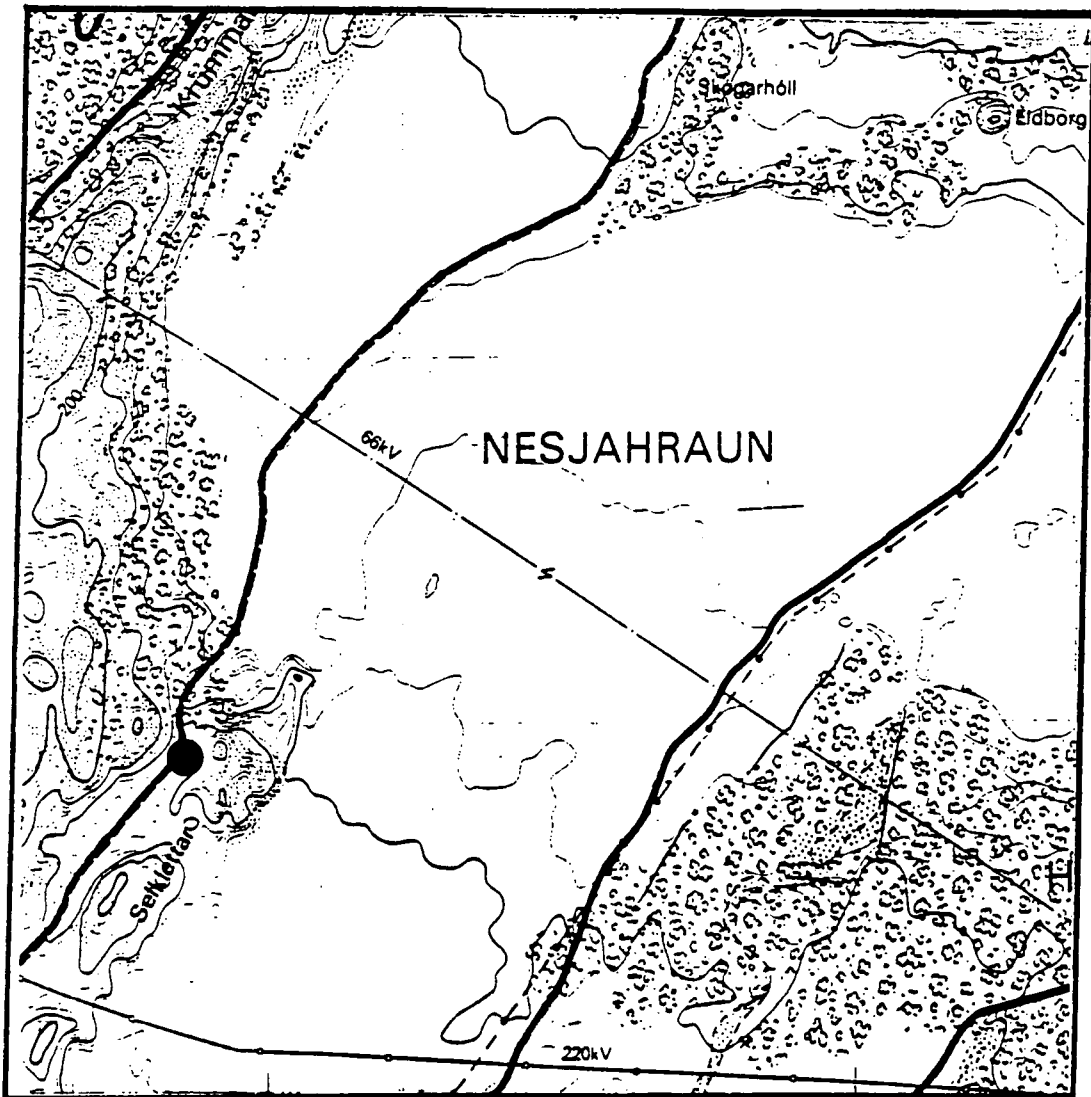
NAME: NESJAHRAUN

POINT INSCRIPTION: OS - 1991 - DU28

WGS 84 CO-ORDINATES: Lat: 64 8 1.18846
Long: -21 14 14.6180
Height: 222.8381 m

DESCRIPTION: This point is placed along side #360 from Selfoss. It is approximately 2.37 km after the turn off to the power station and is overshadowed by the hill Selklettan. It is located in bedrock where the road curves sharply and is marked by a cairn.

ACCESSIBILITY: Two wheel drive



1 cm = 210 m

NAME: **JORUGIL**

POINT INSCRIPTION: OS - 1991 - DU30

WGS 84 CO-ORDINATES: LAT: 64 9 1.11684
Long: -21 16 19.32870
Height: 303.4312 m

DESCRIPTION: From #360 turn off up a track which runs west towards the hill Jorugil. After 0.3 km along the track you will pass a summer house, continue for another 1.2 km. The track runs west then north becoming steeper as it rises up the side of the hill Jorutindur. The track leads to a large open flat area. The point is 22m from the track to the east and is marked by a cairn.

ACCESSIBILITY: Four wheel drive



1 cm = 210 m

